Generation of Postured Voxel-based Human Models Used for Electromagnetic Applications

Vom Fachbereich Elektrotechnik und Informationstechnik
der Technischen Universität Darmstadt

zur Erlangung
der Würde eines Doktor-Ingenieurs (Dr.-Ing.)
genehmigte

DISSERTATION

von
Jing Gao, M.Sc.
geboren am 22. Dezember 1982 in Handan, China
Darmstadt 2012

Referent:	Prof. Dr.-Ing. Thomas Weiland
Korreferent:	Prof. Dr.-Ing. Irina Munteanu
	Prof. Dr.-Ing. Reiner Anderl

Tag der Einreichung:	06.07.2011
Tag der mündlichen Prüfung:	11.01.2012

D 17
Darmstädter Dissertation

Generation of postured voxel-based human models used for electromagnetic applications

Jing Gao

Generation of Postured Voxel-based Human Models Used for Electromagnetic Applications

Abstract

The main contribution of this dissertation is the development of a poser program package, which can deform a voxel-based human body model named HUGO to allow the generation of common postures that people often use in normal life. To illustrate the usefulness of this poser program, two electromagnetic applications are presented. As a low frequency application example in electrical engineering, the first one simulates and analyzes the step voltage due to a lightning strike in detail with the help of two postured human body models. The second one studies the influence of human's posture on specific absorption rate (SAR) calculation as a high frequency electromagnetic application example.

With the development of medical technique, computer graphics and computational electromagnetics, high resolution and anatomically realistic whole-body voxel-based human models have been recently developed and widely used in computation of induced electromagnetic fields and SAR in the human body. However, voxel models' unchangeable posture strongly limits related researches when simulating a realistic scenario in which people have a lot of different postures. In this dissertation, a poser program package, which is an improved version of the well known free form deformation (FFD) technique in computer graphics, was developed to overcome this problem. The poser program can import and render the original voxel dataset, set rotation angles of different joints with a simplified human model, generate postured human models, and export the postured human models as new voxel dataset files. With its help, the original voxel-based human model can be deformed smoothly, continuity of internal tissues and organs can be maintained, and masses of different tissues and organs can be conserved at a reasonable level. In order to generate a postured human model with correctly anatomic structure, a segmentation approach was developed to separate arms away from the trunk. Deformation of the knee joint was dealt with separately to avoid unreasonable deformation of the femur and tibia, and to realize movement and rotation of the patella when the knee joint is bent.

As a typical application of the postured human models, internal electromagnetic fields in the walking and standing human body shocked by the step voltage caused by broken power line or lightning strike were simulated. In order to get a much longer stable time step than the value specified by the Courant limit for stability, the reduced *c* technique was applied for the first time to these electro-quasistatic simulations, after a thorough study. At last, because human's posture can significantly affect the way in which the human body absorbs electromagnetic radiation, whole body averaged SAR and localized SAR distribution of a sitting human model were calculated and compared to that of the standing human model for various incidence angles of the electromagnetic wave and for different environmental conditions.

Erstellung voxelbasierter Menschmodelle in beliebiger Körperhaltung für elektromagnetische Simulationen

Kurzfassung der Arbeit

Der wichtigste Beitrag dieser Dissertation ist die Entwicklung des Computerprogramms „Poser“. Mit Hilfe dieses Programms lässt sich ein Voxel-basiertes HUGO-Modell des menschlichen Körpers verformen, um Simulationsmodelle der im Alltagsleben üblichen Körperhaltungen zu ermöglichen. Um die Nützlichkeit des Poser-Programms zu verdeutlichen, werden im Rahmen dieser Arbeit zwei elektromagnetische Anwendungsbeispiele vorgestellt. Als ein Anwendungsbeispiel im niedrigen Frequenzbereich in der Elektrotechnik wird die durch einen Blitzschlag induzierte Schrittspannung beim ersten Beispiel mit Hilfe von zwei posierten Menschmodellen ausführlich simuliert und analysiert. Das zweite Beispiel dreht sich um die Simulation im Hochfrequenzbereich. Dabei wird der Einfluss der menschlichen Körperhaltung auf die spezifische Absorptionsrate untersucht.

Mit der Entwicklung der medizinischen Technik, Computergrafik und numerischen elektromagnetischen Feldberechnung, wurden voxel-basierte Menschmodelle mit feiner Auflösung und anatomisch realistischem Ganzkörper entwickelt und viel benutzt, um die induzierten elektromagnetischen Felder und die spezifische Absorptionsrate (SAR) im menschlichen Körper zu berechnen. Die unveränderbare Körperhaltung des Voxel-modells aber schränkt die anschließenden Forschungen sehr stark ein, denn zur Simulation eines realistischen Szenarios benötigt man Menschmodelle in ganz unterschiedlichen Körperhaltungen. Um das Problem zu beheben, wurde ein Poser-Programmpaket, das eine verbesserte Version des wohlbekannten Freiform-Deformation (FFD) Verfahrens in der Computergrafik ist, in dieser Dissertation entwickelt. Das Poser-Programm kann die ursprüngliche Voxel-Datei des Menschmodells importieren und rendern, die Drehwinkel von verschiedenen Gelenken mit einem vereinfachten Menschmodell einstellen, die posierten Menschmodelle erzeugen und diese Modelle in eine neue Voxel-Datei exportieren. Dadurch kann das originale Voxel-basierte Menschmodell problemlos verformt werden. Dabei bleibt die Stetigkeit der inneren Gewebe und Organe erhalten und auch die Massenerhaltung der unterschiedlichen Organe wird bis auf wenige Prozent erfüllt. Zur Erstellung der posierten Menschmodelle mit korrekter anatomischer Struktur wurde eine Segmentierungsmethode entwickelt, um die Arme vom Rumpf zu trennen. Die Verformung des Kniegelenks wurde getrennt behandelt, um einerseits die Bewegung und Rotation der Patella bei der Beugung des Gelenks zu realisieren, andererseits aber den Oberschenkelknochen und das Schienbein nicht zu verformen.

Als ein typisches Anwendungsbeispiel für das posierte Menschmodell wurde die Schrittspannung, welche durch eine beschädigte Stromleitung oder einen Blitzschlag ausgelöst wird, und die induzierten elektromagnetischen Felder im gehenden und

stehenden menschlichen Körper zu simulieren. Um einen Zeitschritt zu erhalten, der deutlich länger stabil ist als der Wert, der durch das Courant-Limit für Stabilität festgelegt ist, wurde das Reduced *c* Verfahren zum ersten Mal auf diesen elektromagnetischen Simulationen nach einer umfassenden Untersuchung angewendet. Da die menschliche Körperhaltung die Absorption elektromagnetischer Strahlung signifikant beeinflusst, wurden die gemittelten Ganzkörper SAR und die lokalen SAR-Verteilungen eines sitzenden Menschmodells ermittelt und mit der SAR und SAR-Verteilung des stehenden Menschmodells für die unterschiedlichen Einfallswinkel der elektromagnetischen Welle und die verschiedenen Umgebungsbedingungen verglichen.

Contents

1. Introduction

1.1. Motivation and History

The concern of mankind to its self being has never been reduced since civilization. In the last decades, with the fast development of computer science and medical technique, building accurate human body models in computer's virtual environment is one of the highlights of related research domains. To be precise, computational models of human anatomy are mathematical representations of the external envelope of the human body shape together with the boundaries of the internal organs and tissues [1]. Until now there are already several kinds of computational human models developed mainly by combining some basic mathematical shapes together. However, because human body has a very complex internal structure and the outer surfaces of most organs are very complicated, none of these models can express a completely accurate anatomical structure.

Since coming into being, medical imaging technique has developed rapidly. Nowadays it allows the construction of digital three-dimensional computational models based on the actual anatomy of individual humans by scanning a real person with the computer tomography (CT) or the magnetic resonance imaging (MRI) technique. The usefulness of these so called voxel-based human body models lies in their faithful representation of human anatomy. Until now there are already more than twenty voxel-based human models reported including different ethnicities, ages, sizes, heights and genders.

In recent years, with continuous spread of different kinds of electric devices in daily life, the interaction of electromagnetic fields with biological tissues raises increasing concern in public discussion. Any human being who directly touches an object at a different electric potential from that of its body will have conductive current in his or her own body. Moreover, the direct exposure of the human body to electromagnetic radiation will result in induced electromagnetic fields in the weakly conductive biological tissues. All of these effects are relevant to some health issues. Because it's almost impossible to measure internal electromagnetic fields inside the human body directly, since the mid 1980s, the approach for the evaluation of electromagnetic fields in the human body is to solve Maxwell's equations numerically in the high resolution voxel-based human body models. The finite integration technique (FIT), proposed by Weiland in 1977 [2] [3], is an appropriate method to accomplish this meaningful task.

However, while the voxel-based human models were being built, almost all of the cadavers, volunteers or patients, which they were constructed from, were arranged to stand on the ground or lie on an experimental table. As a result, all these digital human models also use these two similar postures, which significantly limit related research activities in a realistic scenario where postured human bodies must be considered. In order to solve this problem, several deformed voxel-based human models have already been developed based on the initial upright-posture models. Among them are the sitting human models developed by Dawson [4], Allen [5] [6], Findlay and Dimbylow [7] [8] et al; the deformed human model with outstretched or forward stretched arms developed by Dawson [4] [9], Findlay and Dimbylow [7]; and the deformed human models with several different postures developed by Nagaoka and Watanabe [10]. Until now most of these postured human models were developed by cutting, rotating and re-attaching the limb to the trunk, and then adding manual editing around the joint attachment areas to ensure tissue continuity. However, developing a deformed human model from the heterogeneous voxel model with a manual editing procedure is very time-consuming, and in reality people may be in various different postures. So, it's necessary to develop a software tool which can be used to generate different kinds of postured human models conveniently and conserve continuity of original model's tissues and mass preservation.

The voxel-based human model studied in this dissertation is even more challengeable, because its two arms are originally bent before the abdomen and touch the trunk as Fig. 1 shows. A special approach must be developed to separate the arm voxels away from the trunk. Apart from that, because of complicated anatomical structure of human's knee joint, movement and rotation of the patella has to be adjusted automatically when the knee joint is bent, which has not been realized by existing algorithms. At last, most of the present software tools use the cuberille method to render the voxel model. As a result, they can check the configuration of the deformed human model only after a new voxel dataset is generated, which will maybe consume researchers more time than necessary. If the deformed human model is not satisfactory, much more time must be spent to generate another, better one.

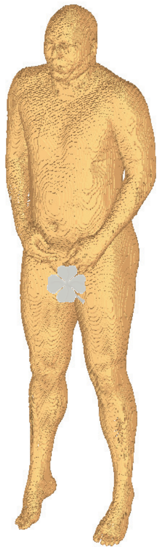
Fig. 1 Voxel-based human model studied in the dissertation

1.2. Overview

This dissertation is organized as follows: after introducing the motivation and development history of the postured voxel-based human body models used for electromagnetic applications in Chapter 1, Chapter 2 will give a review of several different kinds of computational human models especially the history of the voxel-based human body model. The development method and procedure of the voxel-based human model named HUGO from the Visible Human Project® (VHP), which is used in this dissertation, will be explained in detail. Chapter 3 explains the working principles of the most important three algorithms used in the dissertation: three-dimensional deformation technique: free form deformation (FFD); three-dimensional rendering technique: marching cubes algorithm (MC); and numerical computation algorithm for electromagnetic fields: Finite Integration

Technique (FIT). Apart from the basic working principles, some important properties and several simple application exercises of these algorithms will be introduced too. At last, in order to avoid very small time step while using the FIT to solve low frequency simulation problems, the use of the reduced *c* technique will be also explained to speedup quasistatic simulations.

In Chapter 4, a poser program package based on the FFD technique is described, which was developed in order to posture the most popular voxel-based human model HUGO. With the help of this poser program package, the HUGO model can be deformed smoothly, continuity of the internal tissues and organs can be maintained, and masses of different tissues and organs can be conserved at a reasonable level. Compared with previous methods or other existing software tools, this poser program includes a special method developed to separate arm voxels away from the trunk, which can also avoid the possible errors caused by the direct cutting method [10]. Apart from that, the deformation of the knee joint was dealt with separately to avoid unreasonable deformation of the femur and tibia, and to rotate the patella into correct position when the knee joint is bent. With combination of the MC algorithm and the FFD technique, this software package can show the deformed human model before exporting it as a new voxel dataset. Because exporting a new voxel dataset file is the most time consuming step in the whole working procedure, checking the deformed human body model before exporting it as a new voxel dataset can save researchers a lot of time and ensure validity of the deformed human model as early as possible. The most important step of the FFD technique while applying it to deform the voxel-based human model: how to define and operate FFD control lattices is also explained in detail here. Mass conservation results of the postured human model, which will be used in following application examples, were also calculated and compared with the original HUGO model.

With two postured human body models, Chapter 5 studies the step voltage, which is a very common phenomenon in electrical engineering. Because the step voltage can be caused by different reasons, the first application example is simulation of the step voltage caused by downed power lines, which can be analyzed from a stationary current calculation. The time-domain current signal, which excites the step voltage in the second application example, is a lightning current. The lightning current signal used in this dissertation has very low frequency spectrum, and then the simulation itself turns out to be an electro-quasistatic problem. In order to consider the dispersive nature of the biological tissues, full-wave simulations were performed to analyze this problem. The reduced *c* technique, which was often used to speedup magneto-quasistatic simulations before, was studied to be applied into this electro-quasistatic simulation. After a detailed error analysis on two simulation models, all the simulations about the lightning current can be then speeded up around twenty times with a much larger stable time-step than the value specified by the Courant limit for stability. Simulation results show all dangerous areas in the human body shocked by the step voltage, and are compared with some existing safety criterions. All results in this chapter are very useful references for designing, manufacturing and optimizing the lightning protection equipments.

Chapter 6 studies the influence of human’s posture and irradiation direction of the incident electromagnetic wave on the specific absorption rate (SAR) of the human body. Both the whole-body averaged SAR and the localized SAR distribution were computed, analyzed and compared with the restriction values of the guidelines of the International Commission on Non-ionizing Radiation Protection (ICNIRP) [11]. In order to simulate a real scenario including human being, a sitting human body model was generated and placed into a car model as a driver model, and then the distribution situations of the electric field, internal current density field and local SAR of this driver-car model were simulated and analyzed when the whole model is exposed to a high frequency electromagnetic wave and struck by a lightning current respectively.

The dissertation is concluded with a summary in Chapter 7.

2. Computational Human Models

As defined above, computational models of human anatomy are mathematical representations of the external envelope of the human body shape together with the boundaries of the internal organs and tissues. Until now there are several kinds of computational human models developed including mathematical model, stick model, surface model, multi-layer model, voxel-based human model, etc., in computer graphics and electromagnetic simulation domain. In this chapter, all of these human models will be introduced and compared with each other to show the advantages and disadvantages of the voxel-based human model. In the second part, the voxel-based human model HUGO used in this dissertation will be introduced in detail.

2.1. Development History of Computational Human Models

The human body has a very complex internal structure and significant inhomogeneity. Modeling a human body is a great challenge if the numerous parts needed to compose a body must be considered. In the early days, the human body was modeled by simple geometrical structures. The first set of computational human models in history are the "mathematical" models of adults and children from Oak Ridge National Laboratory [12] [13] [14] [15]. Equations of planes, spheres, cylinders, cones, ellipsoids and elliptical cylinders were used to represents internal organs. All of these shapes were fitted into an elliptical cylinder which stands for trunk. The models also include head, neck, arm, legs, etc. External dimensions, internal organ dimensions and masses were designed to be close to the "Reference Man" [16]. However, simple geometrical volumes described by equations do not accurately conform to the shape of real organs and do not fit alongside each other in the way human organs do. Furthermore, the constraints imposed by fitting the defined shapes within an elliptical cylinder mean that their positioning is not anatomically realistic.

In the computer graphics domain, the problems involved in the simulation of human beings could be divided into two major steps: the creation of the human appearance and the motion of the skeleton. The research on human animation started in the seventies of last century with the representation of humans by stick figures with only a few articulations joining the segments animated by a kinematic model [17]. Concerning the body modeling, many efforts have been devoted to represent and deform the human body shape. The models until now can be classified into following categories: stick models, surface models and multi-layer models.

A system using stick models consists of a hierarchical set of rigid segments (limbs) connected at joints. These models, called articulated bodies, may be more or less complex, depending on the number of limbs and joints involved. Surface models are conceptually simple, containing a skeleton and an external shape, the skin, such as the human skin model developed by Komatsu [18]. This model has a skeleton structure, and uses Bezier surfaces jointed smoothly to each other to cover the skeleton just like the skin. The model permits continuous variation of every component of the skeleton according to actions. During such movement, the skin remains smooth and natural because of the good properties of the Bezier surfaces. Because the deformation of the Bezier surfaces is also controlled by control points, the definition and operation method of the control points used in this model are very good references for the control points of the FFD technique used in this dissertation. Finally, multi-layer models contain the skeleton layer, intermediate layers to simulate the body volume (muscles, fat, bones and so on) and the skin layer, such as the model developed by Nedel [19]. This model is divided into three different layers: the rigid body built from a real skeleton, the muscle design and deformation based on physical concepts, and the skin generation.

Surface models or multi-layer models can approximate outer surfaces and shapes of important organs and tissues of the human body very well and also satisfy most human dynamic researches. As a result, these models have good performance in computer graphics applications such as computer game, movie, animation video, etc. However, they cannot be used for electromagnetic simulations because it's still very difficult to model so many internal tissues and organs.

In recent decades, rapid advancement and increased use of the medical imaging technology, specifically the computed tomography (CT) and the magnetic resonance imaging (MRI) has provided high resolution cross-sectional digital images of internal anatomy such as Fig. 2 [20] shows. The two-dimensional pixel data from such images, when extended into the third dimension, become cuboid volume elements called voxels (volume pixels). These data can be used to create a three-dimensional digital representation of the shape, volume and composition of human organs as Fig. 3 shows. Each voxel is defined so that it contains a uniform medium and is assigned an ID number that identifies it as belonging to a particular organ or tissue. These computational human models have also been called tomographic models, voxel models and voxel phantoms.

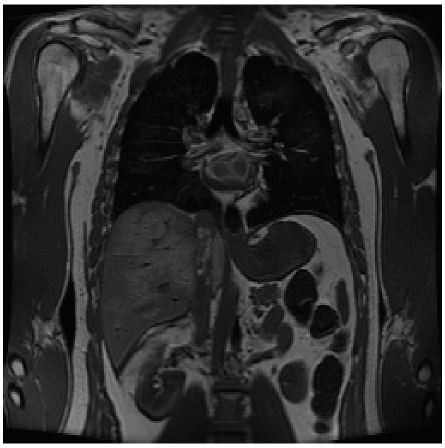

Fig. 2 MR images at trunk level [20]

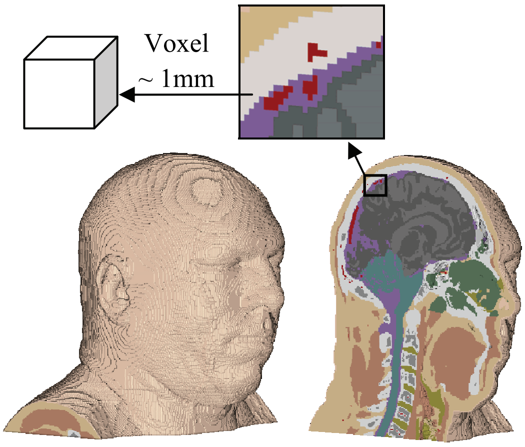

Fig. 3 3D voxel-based human head model

The first voxel model, a representation of a head and trunk from CT scans of a female cadaver was reported in 1984 and used for the calculation of effective dose from dental radiography [21]. At present there are more than 20 partial or whole-body tomographic models reported [1] and much more are in preparation. The reason behind the continuing development of the voxel models is the hope that the smaller voxel size can realize greater realism, with which human anatomy represented in the voxel computational models will allow for more accurate organs and tissues shapes.

These models already have a lot of applications. Whole body voxel tomographic models have been used with the finite difference time domain (FDTD) calculations to determine the SAR from exposure to non-ionizing electromagnetic fields [5] [6] [22] [23] [24] and induced current densities from low frequency magnetic fields [25] [26]. Radiotherapy treatment planning involves making a small voxel model, limited to the region of interest, from CT images of the relevant body section of each individual patient [27]. A combination of the Monte Carlo techniques and the voxel model has been used to calculate absorbed dose to human organs and tissues irradiated with ionizing radiation in radiography, for radiation protection purpose and for dosimetry of procedures involving internal radioactive sources [28] [29].

2.2. Characteristics of Voxel-based Human Models

Voxel models are the most faithful representation of human anatomy currently available as they are designed from real anatomy. When a more extensive range of the voxel models which vary in ages, genders, ethnicities, sizes and heights becomes available, they will allow a close match between a computational human model and an individual patient to be studied. Apart from that they also have the flexibility of being able to be scaled by small amounts to more closely match the individual being investigated or suit the purpose to which they are put. These two advantages make them to be the most popular computational human model recently in electromagnetic applications.

However, there is no perfect computational human model without drawbacks. Voxel models also have several shortcomings as follows.

1) Firstly, the internal structures of the human body having dimensions less than the dimensions of the voxels cannot be accurately segmented. For example the skin thickness is defined by the side length of a pixel and this may result in a skin thickness and mass that are too large [30]. Also the “bone surface” (periosteum) is too thin to be represented by one voxel [31]. Some special methods must be used if those thin tissues have very large influence on the simulation results.

2) Being composed of voxels, the surface of an organ has a “stepped” nature rather than being a smooth surface. This will have the effect of overestimating the surface area of an organ.

3) Medical images from extensive CT and MRI scans are usually acquired from patients that are supine. Consequently the weight bearing surfaces are somewhat flattened

[32]. The abdominal cross section is influenced by the force of gravity acting towards the dorsal surface rather than towards the feet. The internal organs are shifted by the gravity to positions different from those that the organs would adopt if the subject had been standing [33]. While the supine position is required for the calculation, and the available voxel model was built from a standing person, the altered organ positions may need to be considered too.

4) Voxel models, being constructed from the images obtained from an individual, may differ significantly in their internal anatomy from that of another individual with similar size. Some limits to the uncertainty in organ sizes associated with individual variations can be considered if necessary.

5) At last, most medical images, which voxel models were constructed from, were from cadavers or patients. Those cadavers and individual subjects examined for diagnostic purpose may possess pathologies or significant changes from healthy anatomy.

2.3. Voxel-based Human Model: HUGO

Voxel-based human model datasets may come from four sources: existing images from an extensive clinical CT examination, whole body CT of cadavers, whole body MRI of volunteers and color photos from the Visible Human Project® [20] [34]. X-ray computed tomography (CT) measures the spatially varying X-ray attenuation coefficient [35], and shows internal structure. Magnetic resonance (MR) measures three physical properties [36]. One property is the distribution of “mobile” hydrogen nuclei, and the other two properties measure relaxation times of the nuclei. MR shows excellent contrast between varieties of soft tissues.

In reality, the large numbers of contiguous medical images which are necessary to construct a voxel model are not easy to obtain. An extensive CT scan of the human body results in the subject receiving a considerable exposure to ionizing radiation, hence it’s not ethical to recruit healthy volunteers. Usually, existing medical images of patients examined for clinical reasons are used. Even in this case, privacy and medical confidentiality issues restrict access to medical images. When clinical images are available, they may only include part of entire body, and they may not be ideal for image segmentation. Pixel size and slice interval may be greater than desired. MRI has been used to image volunteers for the express purpose of producing a whole body voxel model [22]. In this case, the pixel size and the slice interval may be selected as required. However, the time required to perform the MRI to scan the whole body is very long, around 8 hour in reference [22] and this allows subject movement and the heart beats to degrade the images.

Limitations on pixel resolution, field of view and slice separation imposed by clinical examinations of live patients, and the possibility of movement are not present when cadavers are imaged. When the cadavers are scanned, the concern about radiation exposure is also absent so slice interval can be reduced. For the purpose of producing high resolution tomographic images of male and female anatomy, in 1986 the US National Library of

Medicine began the Visible Human Project® (VHP). In 1994 MRI, CT images and photographic images of the frozen and sequentially sectioned cadaver were made available. One photographic image sample and one MR image sample from the VHP® are shown in Fig. 4 and Fig. 5. The photographic image production process results in the destruction of the cadaver, because the frozen cadaver must be cut into several thousand slices based on required intervals with one milling machine. When the cadavers are used it may be impossible to place the arms and legs as desired. The model from the VHP® has two arms crossed over the abdomen.

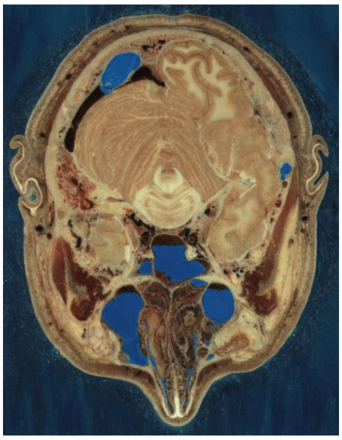

Fig. 4 Photographic image from VHP®

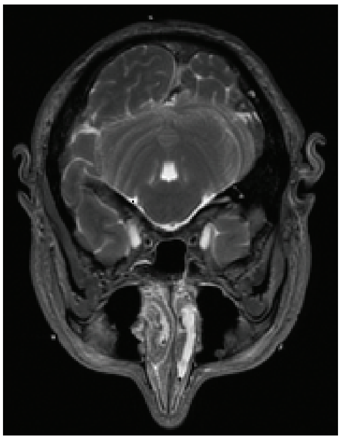

Fig. 5 MR image from VHP®

After medical images are available, the construction of voxel models requires the identification of the boundaries between all different organs and tissues that are displayed in a medical image. All pixels belonging to the same organ or tissue are assigned a tissue identification (ID) number that replaces their original gray scale value. In this way every pixel that belongs to an organ may be identified and distinguished from the pixels belonging to other organs. This process is known as image segmentation, as the image is literally divided into smaller segments. Image segmentation is generally very time-consuming. Six months to even three years have been reported by some researchers on this part of the work [22] [32]. Nowadays there are some algorithms which can use image processing techniques to find structures within the medical data or to filter the original data [37] [38] [39] [40]. Those algorithms can save the researcher some time, but in reality manual recognition and edition with the help of physicians are essential. An original MR image and its identified image from reference [22] are shown in Fig. 6 and Fig. 7 respectively. After all original medical images are segmented, all of these processed images will be combined into one dataset file which is just the so-called voxel-based human model dataset.

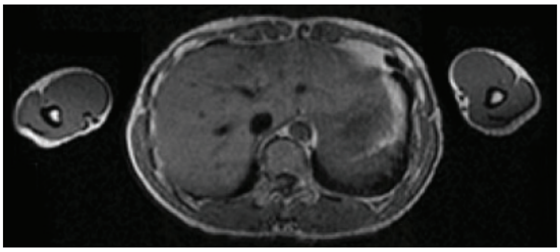

Fig. 6 Original MR image at abdomen level [22]

Fig. 7 Tissue and organ identified image [22]

The voxel-based human model used in this dissertation named “HUGO” [41] was built based on the human model from the VHP®. This model uses color medical images and digital images from CT and MRI to build up a digital anatomically realistic model of the human body, and has already been used for different kinds of applications especially in electromagnetic domains [42] [43] [44] [45] [46]. The human model used in this dissertation offers a variable voxel resolution ranging from 8 × 8 × 8 mm^3 to 1 × 1 × 1 mm^3. Each voxel is assigned to a unique tissue ID number, with totally 32 different tissue types. All tissue types and respective tissue ID numbers are listed in Table 1. In the finest resolution, the model consists of approximately 380 million voxels. It represents a 38 years old, male person of 187 cm height and an approximate weight of 113 kg. Its original posture is lying on an experimental table, similar like an upright standing one.

Table 1 Tissue types and corresponding identification number of HUGO model

Tissue	ID Nr.	Tissue	ID Nr.	Tissue	ID Nr.
Marrow	1	Fat	2	Bone	3
White substance	4	Gray substance	5	Skin	6
Eye	7	Muscle	8	Blood	9
Cerebellum	11	Lens	12	Nervus	13
Cartilage	14	Mucous membrane	15	Air	16
Lung	17	Large intestine	18	Kidney	19
Liver	20	Gland	22	Spleen	23
Stomach	24	Pancreas	25	Bladder	26
Gall bladder	27	Small intestine	28	Right ventricle	30
Left ventricle	31	Right atrium	32	Left atrium	33
Blood vessel	43	Blood aorta	44		

So in principle, the voxel model dataset itself consists of pure modified pixel data. With the help of computer graphics technique, the voxel dataset can be rendered as a three dimensional human model as Fig. 1 or Fig. 3 shows. The commercial image processing software Photoshop® can also open the voxel dataset file to show a sequence of segmented medical images as Fig. 8 shows. The commercial text editing software UltraEdit® can also open it to show tissue ID numbers of all voxels as Fig. 9 shows.

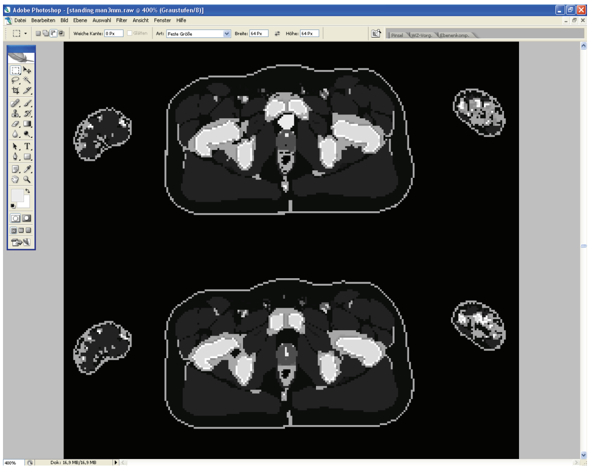

Fig. 8 HUGO data set opened in Photoshop®

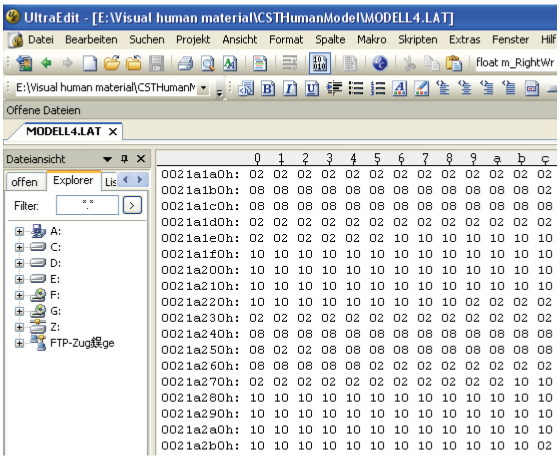

```
             0  1  2  3  4  5  6  7  8  9  a  b  c
0021a1a0h: 02 02 02 02 02 02 02 02 02 02 02 02 02
0021a1b0h: 08 08 08 08 08 08 08 08 08 08 08 08 02
0021a1c0h: 08 08 08 08 08 08 08 08 08 08 08 08 08
0021a1d0h: 02 02 02 02 02 02 02 02 02 02 02 02 02
0021a1e0h: 02 02 02 02 02 02 10 10 10 10 10 10 10
0021a1f0h: 10 10 10 10 10 10 10 10 10 10 10 10 10
0021a200h: 10 10 10 10 10 10 10 10 10 10 10 10 10
0021a210h: 10 10 10 10 10 10 10 10 10 10 10 10 10
0021a220h: 10 10 10 10 10 10 10 10 10 02 02 02 02
0021a230h: 02 02 02 02 02 02 02 02 02 02 02 02 02
0021a240h: 08 08 08 08 08 08 08 08 08 08 08 08 08
0021a250h: 08 02 02 08 08 08 08 08 08 08 08 08 08
0021a260h: 08 08 08 08 08 02 02 02 02 02 02 02 02
0021a270h: 02 02 02 02 02 02 02 02 02 02 02 10 10
0021a280h: 10 10 10 10 10 10 10 10 10 10 10 10 10
0021a290h: 10 10 10 10 10 10 10 10 10 10 10 10 10
0021a2a0h: 10 10 10 10 10 10 10 10 10 10 10 10 10
0021a2b0h: 10 10 10 10 10 10 10 10 10 10 10 10 02
```

Fig. 9 HUGO data set opened in UltraEdit®

2.4.Dielectric Properties of Biological Tissues

Voxel-based human models, in principle, only provide geometric information of whole human body and every tissue and organ. In order to perform electromagnetic simulations, the dielectric properties allocated to various tissues and organs in the frequency ranges concerned should be available. The dielectric properties of any material can be obtained from their complex relative permittivity, which can be expressed as

$$\underline{\varepsilon}(\omega) = \varepsilon'(\omega) - j\varepsilon''(\omega) = \varepsilon_r(\omega) - j\frac{\sigma(\omega)}{\varepsilon_0 \omega} \qquad (2\text{-}1)$$

where ε_r is the relative permittivity of the material, σ is the total conductivity of the material which may include a contribution from a frequency-independent static ionic conductivity σ_i, ε_0 is the permittivity of vacuum and ω is the angular frequency. Thus dielectric properties of any material are determined by its ε_r and σ values which are function of frequency for biological tissues.

To get detail dielectric information of human tissues and organs over ten frequency decades, Gabriel et al. performed an elaborate literature survey covering most contributions after 1950, and concluded the main features of the dielectric spectrum of a biological tissue as follows [47]:

1) The relative permittivity of a biological tissue can reach values of up to 10^6 or 10^7 at frequencies below 100 Hz.

2) The dielectric spectrum of a biological tissue is characterized by three main relaxation regions known as the α, β and γ dispersion regions at low, medium and high frequencies. Other minor dispersion regions are also reported such as the often mentioned δ dispersion region.

3) The γ dispersion, in the gigahertz region, is due to the polarization of water molecules.

4) The β dispersion, in the hundreds of kilohertz region, is due mainly to the polarization of cellular membranes which act as barriers to the flow of ions between the intra- and extra-cellular media.

5) The low frequency α dispersion is associated with ionic diffusion processes at the site of the cellular membrane.

6) Tissues have finite ionic conductivities commensurate with the nature and extent of their ionic content and ionic mobility.

In order to fill the gap exposed from the literature survey, Gabriel et al. measured the dielectric properties of a number of human and animal tissues based on automatic swept-frequency network and impedance analyzers. The measurements were performed at body temperature, across the frequency range from 10 Hz to 20 GHz both in vivo and in vitro [48]. Finally Gabriel et al. introduced a parametric model to describe the variation of the dielectric properties of biological tissues as a function of frequency based on the experimental data and the data surveyed from the literature [49] [50]. This parametric model was developed in order to make it very convenient to get access to the dielectric property data of different tissues and organs at all frequencies of interest.

For one kind of biological tissue or organ, each of its relaxation regions is characterized by one relaxation time constant τ. To a first order approximation, each relaxation region gives the following Debye expression for the complex relative permittivity as a function of angular frequency

$$\underline{\varepsilon} = \varepsilon_\infty + \frac{\varepsilon_s - \varepsilon_\infty}{1 + j\omega\tau} \tag{2-2}$$

where ε_∞ is the permittivity at field frequencies where $\omega\tau >> 1$, ε_s is the permittivity at $\omega\tau << 1$. The magnitude of the dispersion is described as

$$\Delta\varepsilon = \varepsilon_s - \varepsilon_\infty . \tag{2-3}$$

As an extension of the Debye equation, Gabriel et al. introduced an empirical distribution parameter α to include the influence that each dispersion region may be broadened by multiple contributions to it, and then gave an alternative to the Debye equation and known as the Cole-Cole equation

$$\underline{\varepsilon} = \varepsilon_\infty + \frac{\Delta\varepsilon}{1 + (j\omega\tau)^{(1-\alpha)}} . \tag{2-4}$$

Finally the dielectric spectrum of a biological tissue was modeled as the summation of multiple Cole-Cole dispersion equations in addition to a conductivity term:

$$\underline{\varepsilon} = \varepsilon_\infty + \sum_n \frac{\Delta\varepsilon_n}{1 + (j\omega\tau_n)^{(1-\alpha_n)}} + \frac{\sigma_i}{j\omega\varepsilon_0} \tag{2-5}$$

where σ_i is the static ionic conductivity. Equation (2-5) can be used to predict the dielectric behavior over the desired frequency range with a choice of parameters appropriate to the biological tissue concerned. All of these parameters were extracted from the experimental data and the previous data surveyed from the literature. In Gabriel's paper, the dielectric spectrum of a biological tissue extending from 10 Hz to 100 GHz was modeled as the summation of four dispersion regions. Although there are three main dispersion regions which are evident in the considered spectrum, a fourth order Cole-Cole model can provide more flexibility to achieve a better fit to the experimental data. The frequency dependence within each region was expressed as a Cole-Cole term.

Until now the Cole-Cole equation is the most popular material model used to predict dielectric properties of human tissues and organs. Several research institutions have developed online applications, which are used to check dielectric properties of biological tissues, based on the Cole-Cole equation. The first one can be found at following webpage http://www.fcc.gov/oet/rfsafety/dielectric.html (accessed on September 10, 2010), and it is provided by the Federal Communications Commission (FCC), USA. With the help of this application, the user can check the relative permittivity and conductivity of fortythree human tissues and organs in a frequency band ranging from 10 MHz to 6 GHz. The second one can be found at http://niremf.ifac.cnr.it/tissprop/ (accessed on September 10, 2010), and it is provided by the "Nello Carrara" Institute of Applied Physics (IFAC), Italy. With the help of this application, the user can check the relative permittivity and conductivity of fifty-seven human tissues or organs (including air and vacuum) ranging from 10 Hz and 100 GHz. Related loss tangents, wavelength and penetration depth corresponding to different tissues and frequencies are also calculated and displayed. There are three display modes available for convenience: all tissues at single frequency, single tissue at single frequency and single tissue at frequency range.

All application simulations in Chapter 5 and 6 of this dissertation were performed based on the Cole-Cole material model. Dielectric properties of HUGO model's tissues and organs at 50 Hz and 25 kHz frequency which will be used in Chapter 5 are listed in Table 2.

Table 2 Dielectric properties of HUGO model's tissues and organs at 50 Hz and 25 kHz

Tissue	50 Hz		25 kHz	
	Relative Permittivity	Conductivity S/m	Relative Permittivity	Conductivity S/m
Marrow	166,680	0.0016	311.27	0.0029
Fat	1,472,800	0.019	355.46	0.024
Bone	8,867.8	0.020	330	0.021
White substance	5,289,800	0.053	6,089.2	0.074
Gray substance	12,107,000	0.075	9,733.9	0.12
Skin	1,136	0.00020	1,130.8	0.00022
Eye	292,950	0.50	6,812.9	0.51
Muscle	17,719,000	0.23	13,669	0.35
Blood	5,259.9	0.70	5,230.5	0.70
Cerebellum	12,108,000	0.095	10,028	0.14
Lens	1,737,200	0.32	3,836.7	0.34
Nervus	1,608,800	0.027	17,912	0.057
Cartilage	1,637,700	0.17	3,066.1	0.18
Mucous membrane	51,274	0.00042	26,246	0.011
Lung	5,758,900	0.068	7,508.8	0.098
Large intestine	32,096,000	0.054	6,424.5	0.24
Kidney	10,115,000	0.089	18,485	0.15
Liver	1,831,700	0.036	16,055	0.063
Gland	1,637,700	0.52	5,333.8	0.53
Spleen	10,188,000	0.085	7,740.5	0.11
Stomach	1,637,200	0.52	4,849.3	0.53
Pancreas	1,637,700	0.52	5,333.8	0.53
Bladder	481,640	0.21	3,203	0.22
Gall bladder	1,449.4	0.90	126.86	0.90
Small intestine	2,031,500	0.52	23,920	0.57
Right / Left ventricle	8,664,600	0.083	30,695	0.18
Right / Left atrium	8,664,600	0.083	30,695	0.18
Blood vessel / aorta	8,095,800	0.26	3,039.5	0.32

3. Introduction to Main Algorithms

There are two important algorithms used in the poser program package, both stemming from the computer graphics domain: a three-dimensional rendering algorithm named marching cubes and a three-dimensional deformation technique named free form deformation. The combination of these two algorithms allows the user of the poser program to see postured human body models before they are exported as new voxel datasets, which can save user a lot of time.

Apart from that, this dissertation mainly discusses application of the postured human body models in electromagnetic domain. There will be three application examples simulated in Chapter 5 and 6 with the commercial software CST STUDIO SUITE® [51]. Here the time domain electromagnetic simulation algorithm Finite Integration Technique (FIT) developed by Weiland [2] is introduced. Similar as the finite difference time domain technique (FDTD) [52], stable time step of the FIT is constricted by the Courant limit for stability. Hence, simulation models with geometric details that are very small compared to signal wavelengths stress these two techniques, because very huge number of time steps ($>10^8$) will be possibly needed. The reduced *c* technique suggested by Holland [53] [54] can get a much longer stable time step than the value specified by the Courant limit for stability by mathematically decreasing the speed of light *c*, and then speedup simulation calculations several times. Its working principle will be also introduced here.

3.1. 3D Deformation Technique: Free Form Deformation

In 1986, Sederberg and Parry introduced the free form deformation technique (FFD) [55] [56]. It is a very powerful tool to deform three-dimensional solid geometric models. Through operating the FFD control lattice, the FFD technique can deform any kinds of complex geometric model in a free form style. At the same time continuity and topology of the original model can be conserved. The FFD technique has been proved to be a very intuitive and efficient modeling technique highly appreciated by designers [57].

The FFD technique is mainly used to deform flexible objects, which means that the original considered object has very good flexibility and can be deformed easily under external forces. Its general idea is as follows: the deformation operation is not imposed on the original object directly, but on a control lattice in which the original object is embedded. Designers can deform the control lattice directly by moving one or more control points of the control lattice, and deformations of the control lattice will be automatically passed to the object by some mathematical mapping relationship to realize deformation of the original object. The shape of the control lattice is generally a three-dimensional parallelepiped regularly subdivided. In 1990, Coquillart proposed an extended free form deformation technique (EFFD), in which the shape of the control lattice can be defined as any convenient shape which suits the original object [58]. Until now the FFD technique is the most convenient method in computer graphics domain to deform flexible objects.

3.1.1. Working Principle of the FFD Technique

A good physical analogy to the FFD technique is to consider a parallelepiped of transparent, flexible plastic, in which the original object is embedded. The original object is imagined to be also flexible, so that it deforms along with the plastic that surrounds it [56]. The FFD technique uses a special mathematical mapping to pass the deformation of the FFD control lattice on to the original object. Its working principle is as follows.

Step 1: Building the FFD control lattice.

The FFD control lattice can be defined as different shapes based on the structure of the geometry. For standard FFD technique, the most common shape for the control lattice is parallelepiped, which needs the simplest mathematical calculations comparing to the other shapes. A parallelepiped FFD control lattice, which is regularly subdivided, is shown in Fig. 10. All points of intersection in the control lattice are control points. Let *l*, *m* and *n* be the number of subdivisions along each of the three directions $\vec{S}$, $\vec{T}$ and $\vec{U}$ as Fig. 11 shows. These numbers can be chosen by the user depending on the deformation he or she wants to produce (in Fig. 11, $l = 1$, $m = 2$ and $n = 2$). The range of the FFD control lattice should surround the whole original model that has to be deformed.

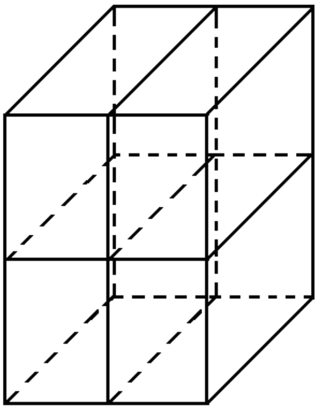

Fig. 10 A parallelepiped FFD control lattice

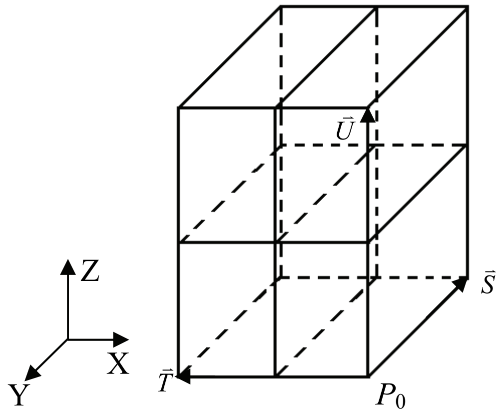

Fig. 11 Local coordinates P_0 - *STU*

Step 2: Embedding the original geometry model into the FFD control lattice.

This step is aim to calculate the coordinates of all points *P* (*x, y, z*) of the original object in the local coordinate system $P_0 - STU$ as P_L (*s, t, u*). In order to realize this step conveniently, first of all, a local coordinate system (LCS) $P_0 - STU$ must be built in the parallelepiped region as Fig. 11 shows. P_0 is position of the origin of the LCS in the global coordinate system (GCS). Then, the position vector of any point *P* in the original model, which has local coordinates P_L (*s, t, u*) in this LCS is

$$\vec{P}(x,y,z) = \vec{P}_0(x,y,z) + s\vec{S} + t\vec{T} + u\vec{U} = \vec{P}_0 + \vec{P}_L(s,t,u). \tag{3-1}$$

The local coordinates (*s, t, u*) of the point P_L can be easily found using linear algebra. A vector solution is

$$s=\frac{\vec{T}\times\vec{U}\cdot(\vec{P}-\vec{P}_0)}{\vec{T}\times\vec{U}\cdot\vec{S}},t=\frac{\vec{U}\times\vec{S}\cdot(\vec{P}-\vec{P}_0)}{\vec{U}\times\vec{S}\cdot\vec{T}},u=\frac{\vec{S}\times\vec{T}\cdot(\vec{P}-\vec{P}_0)}{\vec{S}\times\vec{T}\cdot\vec{U}}. \tag{3-2}$$

Note that for any point *P* interior to the parallelepiped, the conditions $0<s<1$, $0<t<1$ and $0<u<1$ exist. Apart from that, (*s, t, u*) should be calculated after the FFD control lattice is defined and before the FFD control lattice is deformed, and then cannot be changed any more unless the FFD control lattice is redefined. For simplicity, with the parallelepiped FFD control lattice, each axis of the LCS $P_0 - STU$ can be set to be parallel to the related axis of the GCS as Fig. 11 shows. Then, this step requires only the solution of three linear equations.

Step 3: Deform the FFD control lattice.

After the FFD control lattice is built, a grid of FFD control points P_{ijk} can be defined at all points of intersection of the FFD control lattice. These $(l+1)\times(m+1)\times(n+1)$ FFD control points will form $(l+1)$ planes in the $\vec{S}$ direction, $(m+1)$ planes in the $\vec{T}$ direction and $(n+1)$ planes in the $\vec{U}$ direction. Their locations in the GCS are

$$\begin{aligned}&\vec{P}_{ijk}(x,y,z)=\vec{P}_0(x,y,z)+\frac{i}{l}\vec{S}+\frac{j}{m}\vec{T}+\frac{k}{m}\vec{U}=\vec{P}_0+\vec{P}'_{ijk}(s,t,u)\\&(i=0,1,...l;j=0,1,...m;k=0,1,...n)\end{aligned} \tag{3-3}$$

In order to realize the required deformation shape, the user can deform the FFD control lattice now by moving the FFD control points P_{ijk} from their original positions, and impose tension, compression, bending, torsion or any other deformation effect on the initial control lattice. $\vec{P}'_{ijk}$ is a vector containing the local coordinates of the displaced FFD control points in the LCS. All of these deformations can be passed to the original object in the next step.

Step 4: Deform the original object.

After deforming the FFD control lattice, new local coordinates of the points P_L in the deformed object, denoted by P_{ffd}, can be computed. The deformation function of the FFD technique is defined by a trivariate tensor product as follows

$$\vec{P}_{\text{ffd}}=\sum_{i=0}^{l}\sum_{j=0}^{m}\sum_{k=0}^{n}H_i^l(s)H_j^m(t)H_k^n(u)\vec{P}'_{ijk} \tag{3-4}$$

where (*s, t, u*) are the original local coordinates of the original object point P_L in the LCS, $\vec{P}_{\text{ffd}}$ is a vector containing the local coordinates of the displaced point P_{ffd} in the deformed object, and *H* is the basis function. Different basis functions, such as B-Spline FFD [59], Rational Bernstein FFD [60] and NURBS (Non-Uniform Rational B-Spline) FFD [61], will result in FFD formulations with different properties.

Generally, the deformed position of any arbitrary point *P* in the original object is calculated by first computing its original local coordinates P_L (*s, t, u*) from equation (3-2), and then evaluating the deformed position P_{ffd} in the LCS according to equation (3-4), at last using equation (3-1) to calculate the coordinates of the deformed position in the GCS to get a deformed object. Equation (3-4) also shows that deformed positions of the original object points are completely determined by the deformed positions of the FFD control points. Different positions of the FFD control points, which indicate different kinds of deformation effects of the FFD control lattice, will result in different deformed objects.

In conclusion, the workflow of the FFD technique can be shown as Fig. 12.

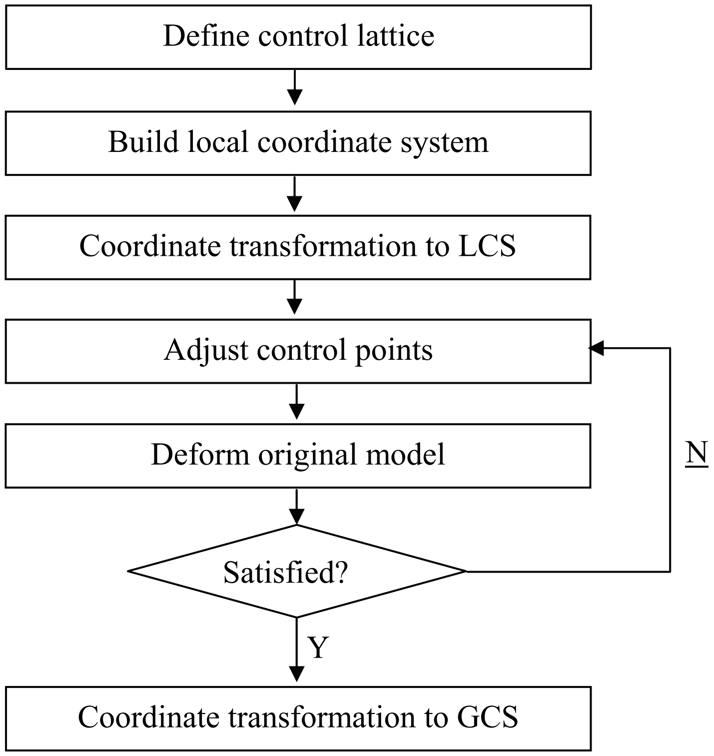

Fig. 12 Flow chart of the free form deformation technique

3.1.2. FFD Technique Based on Bernstein Basis Function

In this dissertation, the FFD technique based on the Bernstein basis functions is used to deform the voxel-based human model. The Bernstein basis function is commonly used in the Bezier curve and the Bezier surface patch, and are expressed by the following formula

$$B_i^n(t) = \frac{n!}{i!(n-i)!} t^i (1-t)^{n-i} = C_n^i t^i (1-t)^{n-i}. \tag{3-5}$$

The Bernstein basis function has several good mathematical properties, one of which is that the Bernstein basis polynomials of degree n can form a partition of unity, which can be proved as follows.

Firstly, the following equation can be deduced from equation (3-5)

$$\sum_{i=0}^{n} B_i^n(t) = \sum_{i=0}^{n} \frac{n!}{i!(n-i)!} t^i (1-t)^{n-i} = \sum_{i=0}^{n} C_n^i t^i (1-t)^{n-i}. \tag{3-6}$$

Because of the binomial theorem

$$\sum_{i=0}^{n} C_n^i a^i b^{n-i} = (a+b)^n, \tag{3-7}$$

Equation (3-5) can be rewritten as

$$\sum_{i=0}^{n} B_i^n(t) = \sum_{i=0}^{n} C_n^i t^i (1-t)^{n-i} = (t+(1-t))^n = 1. \tag{3-8}$$

This property will be used a little later to prove one important property of the Bernstein FFD technique.

Now using the Bernstein basis function instead of the basis function H in equation (3-4), the Bernstein FFD formulation is obtained

$$\vec{P}_{\text{ffd}} = \sum_{i=0}^{l}\sum_{j=0}^{m}\sum_{k=0}^{n} B_i^l(s) B_j^m(t) B_k^n(u) \vec{P}'_{ijk}. \tag{3-9}$$

By using the extension (3-5) of the Bernstein basis function, (3-9) becomes

$$\begin{gathered}\vec{P}_{\text{ffd}} = \sum_{i=0}^{l} C_l^i s^i (1-s)^{l-i} \sum_{j=0}^{m} C_m^j t^j (1-t)^{m-j} \sum_{k=0}^{n} C_n^k u^k (1-i)^{n-k} \vec{P}'_{ijk} \\ (i = 0,1,\ldots l; j = 0,1,\ldots m; k = 0,1,\ldots n)\end{gathered} \tag{3-10}$$

Fig. 11 and equation (3-3) both show that the control lattice of the FFD technique is regularly segmented into l, m and n parts along the S, T and U direction respectively at the very beginning. The number of l, m and n can be selected by user based on the requirements. Larger values of l, m and n can realize a finer adjustment on the original object, but the calculation cost will increase. It is also possible to refine the FFD control lattice locally if only a part of the original object needs very fine deformation.

Before the FFD control lattice is deformed, all the FFD control points are arranged at regular intervals. Now after process of equation (3-10), this kind of regular FFD control lattice does not deform the original object model, which can be proved as follows.

Let $P_{\text{ffd}} = P_{\text{ffd}}(s_{\text{d}}, t_{\text{d}}, u_{\text{d}})$ be the local coordinates of the deformed object points with local coordinates $P_{\text{L}}(s, t, u)$ in the original object. If the FFD control lattice isn't deformed, the local coordinates of all FFD control points can be obtained from equation (3-3) as follows

$$\vec{P}'_{ijk}(s,t,u) = \frac{i}{l}\vec{S} + \frac{j}{m}\vec{T} + \frac{k}{m}\vec{U}. \tag{3-11}$$

Then s_{d} can be calculated as follows based on equation (3-10):

$$s_{\text{d}} = \sum_{i=0}^{l} B_i^l(s) \frac{i}{l} \sum_{j=0}^{m} B_j^m(t) \sum_{k=0}^{n} B_k^n(u). \tag{3-12}$$

Because of the property (3-8), the equation above can be transformed to

$$s_{\text{d}} = \sum_{i=0}^{l} B_i^l(s) \frac{i}{l} = \sum_{i=0}^{l} C_l^i s^i (1-s)^{l-i} \frac{i}{l}. \tag{3-13}$$

While $i = 0$, the product term will turn to be 0, so the index i can start from 1. Then by expanding and simplifying the equation above, the following result is obtained

$$\begin{aligned} s_{\mathrm{d}} &= \sum_{i=1}^{l} C_l^i s^i (1-s)^{l-i} \frac{i}{l} \\ &= \sum_{i=1}^{l} \frac{l!}{i!(l-i)!} s^i (1-s)^{l-i} \frac{i}{l} \\ &= \sum_{i=1}^{l} \frac{(l-1)!}{(i-1)!(l-i)!} s^i (1-s)^{l-i} \\ &= \sum_{i=1}^{l} \frac{(l-1)!}{(i-1)![(l-1)-(i-1)]} s^{i-1} (1-s)^{[(l-1)-(i-1)]} \cdot s \\ &= \sum_{i=1}^{l-1} B_{i-1}^{l-1}(s) \cdot s \\ &= 1 \cdot s \\ &= s. \end{aligned} \tag{3-14}$$

Similarly, $t_{\mathrm{d}} = t$ and $u_{\mathrm{d}} = u$ can be also proven. Therefore, if the FFD control lattice isn't deformed, any object point in the "deformed" object model has exactly the same local coordinates as its local coordinates in the original object model, which means the original model will not deform either. This property can be used to test the program. After the FFD control lattice is defined, the user can perform one deformation calculation directly before moving the FFD control points. If this calculation results in a deformed object model, there must be some problems in the program, and then the related parts of the code should be modified until the original object model doesn't deform any more.

3.1.3. Two Exercise Examples of Bernstein FFD technique

In this section, two deformation examples are given to show the performance of the Bernstein FFD technique. The first one is a two-dimensional example which shows the deformation of a Bezier curve, while the second one is a three-dimensional example which shows the deformation of a Bezier surface. These two parameter objects have very close relationship with the FFD technique.

Although the FFD technique is mainly used to deform three-dimensional objects, it's also possible to use it to deform two-dimensional objects such as curves or pictures. In a two-dimensional situation, the deformation formulation of the Bernstein FFD technique reduces to:

$$\vec{P}_{\mathrm{ffd}} = \sum_{i=0}^{l} \sum_{j=0}^{m} B_i^l(s) B_j^m(t) \vec{P}'_{ij} \; . \tag{3-15}$$

Bezier curves are parametric curves often used in computer graphics and related research domains. They were widely publicized in 1962 by French engineer Pierre Bezier, who used them to design automobile bodies. Until now Bezier curves are still widely used to model smooth curves. The Bezier curve is completely controlled by its control vertexes, which can be graphically displayed and used to manipulate the curve intuitively. Many transformations such as translation or rotation can be applied on the curve by applying respective transformation on the control vertexes of the curve. In animation applications, Bezier curves are used to outline, for example, movement. Users can firstly outline the wanted path in Bezier curves, and then the application creates the needed frames for the object to move it along the path.

Quadratic and cubic Bezier curves are most common, because higher degree curves are more expensive to evaluate. When more complex shapes are needed, low order Bezier curves are patched together. To guarantee smoothness, the control vertexes at which two curves meet must be on the line between the two control vertexes on either side [62]. A cubic Bezier curve can be expressed by following formulation.

$$\begin{aligned} \vec{P}(t) &= \sum_{i=0}^{3} \vec{P}_i B_i^3(t) \qquad (0 < t < 1) \\ B_i^3(t) &= C_3^i t^i (1-t)^{3-i} \end{aligned} \tag{3-16}$$

Equation (3-16) shows that the Bezier curve is defined by its control vertexes P_i and the Bernstein basis function. Different positions of the control vertexes P_i will result in different Bezier curves. In the following example, the user of the program can move the green FFD control points directly but not the red control vertexes of the Bezier curve, positions of the four red control vertexes of the Bezier curve are determined by positions of the sixteen green FFD control points.

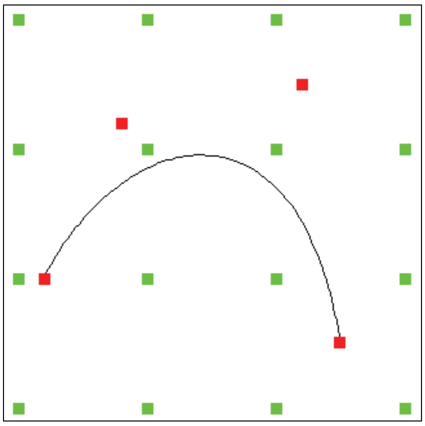

Fig. 13 Initial Bezier curve and FFD control points

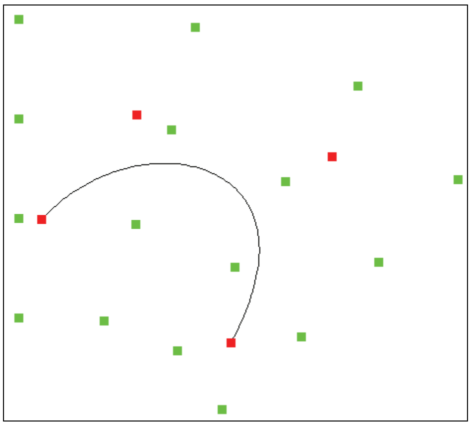

Fig. 14 Deformed Bezier curve and moved FFD control points

This example was realized by Microsoft Visual Studio® and C++ language, by means of a simple graphical user interface (GUI). There are sixteen FFD control points totally which the user can select and move directly by mouse as the sixteen green points shown in Fig. 13 and Fig. 14. Four red points, which user cannot move directly, are control vertexes of the considered Bezier curve. At the very beginning, all FFD control points are arranged at regular intervals as Fig. 13 shows, and the Bezier curve has one initial shape. The user can move all or part of the FFD control points as Fig. 14 shows, after the FFD calculation is finished, the four red control vertexes will move to their new positions based on the deformed FFD control lattice, and then the Bezier curve will be changed into another shape. The Bernstein FFD calculation itself is very fast, the user of the program can deform this Bezier curve on a real-time basis without any delay.

As generalizations of the Bezier curves to higher order, Bezier surfaces are species of mathematical spline often used in computer graphics, computer-aided design and finite element modeling. Like the Bezier curves, a Bezier surface is also defined by a set of control vertexes. They are visually intuitive, easy to manipulate, and for many applications, mathematically convenient. In addition, other common parametric surfaces such as spheres and cylinders can be well approximated by a small numbers of cubic Bezier patches. Bezier surfaces can be of any degree, but bi-cubic Bezier surfaces generally provide enough degrees of freedom for most applications [63] [64]. One bi-cubic Bezier surface can be expressed by following formulation.

$$\begin{gathered}\vec{P}(s,t)=\sum_{i=0}^{3}\sum_{j=0}^{3}\vec{P}_{i,j}B_i^3(s)B_j^3(t)\qquad(0<s,t<1)\\ B_i^3(s)=C_3^i s^i(1-s)^{3-i},B_j^3(t)=C_3^j t^j(1-t)^{3-j}.\end{gathered}\tag{3-17}$$

In following three-dimensional Bernstein FFD example, the user can move the FFD control points directly but not the control vertexes of the Bezier surface. The positions of the sixteen red control vertexes of the Bezier curve are determined by the positions of the sixty-four green FFD control points.

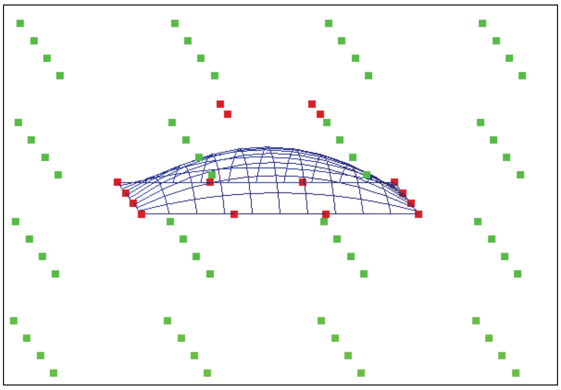

Fig. 15 Initial Bezier surface and FFD control points

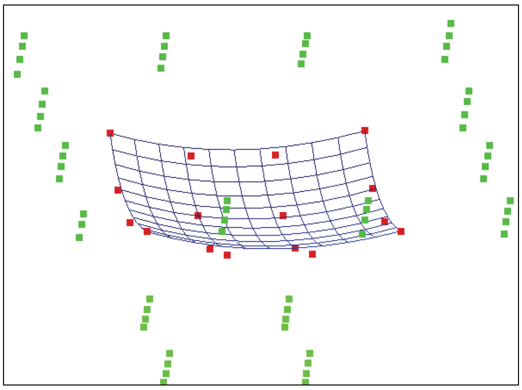

Fig. 16 Deformed Bezier surface and moved FFD control points

In this example, there are sixty-four FFD control points which the user can select and move with a dialog box in order to realize precise movement along three directions as the green points shown in Fig. 15 and Fig. 16. Sixteen red points, which the user cannot move directly, are control vertexes of the considered Bezier surface. The user can move all or part of the FFD control points as Fig. 16 shows, after the FFD calculation is finished, sixteen red control vertexes will move to their new positions based on the deformed FFD control lattice, and then the Bezier surface will be changed into another shape.

3.1.4. Applying FFD Technique to Deform Voxel-based Human Model

In this dissertation, the FFD technique is used to deform the voxel-based human model HUGO. Detail information about this part work will be introduced in the next chapter. Here, a simple example including a HUGO leg model is used to explain how to apply the Bernstein FFD technique to deform a voxel-based human model as Fig. 17 shows.

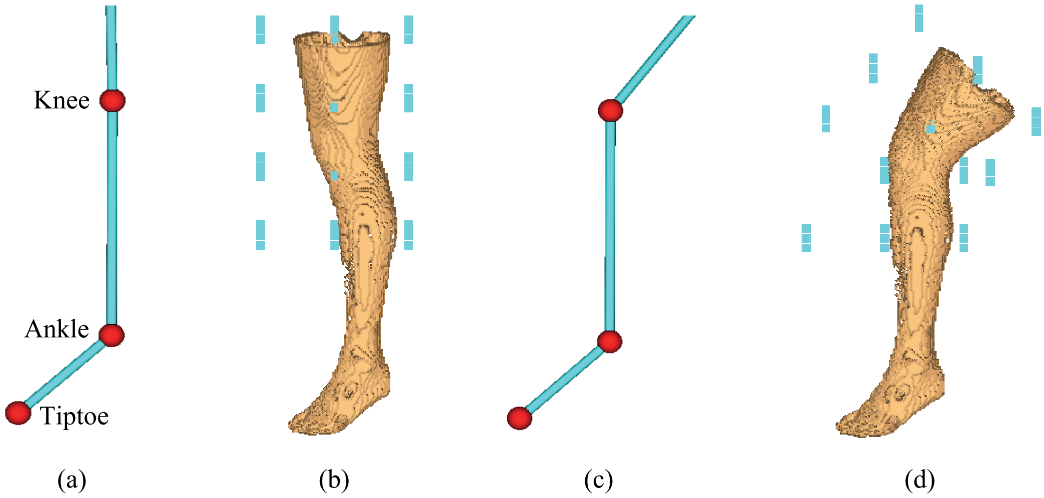

Fig. 17 Application of the FFD technique to deform a voxel-based human leg model (a) Skeleton model of the original leg model indicating positions of all joints (b) Original 3D fat tissue leg model and related FFD control points around the knee joint (c) Skeleton model of the deformed leg model (d) Deformed 3D fat tissue leg model and related deformed FFD control lattice

In any voxel-based human model, every voxel has its own position coordinates based on the voxel size and intervals along *z*-direction. For example, the position of one voxel in this leg model can be defined by its coordinates (x, y, z) in the GCS. After the whole leg model is rendered and checked, the positions of some important joints in this leg model such as knee and ankle should be determined as the skeleton model in Fig. 17 – (a) shows. Then by reference to the positions of these joints, three vectors $\vec{S}$, $\vec{T}$, $\vec{U}$ are defined to surround that part of the leg model which will be deformed. These three vectors can compose a LCS. If the origin of this LCS is P_0, the positions of each voxel in the GCS can be written as sum of $\vec{P}_0$ and the vector $\vec{P}_L$ (s, t, u). Here, small s, t and u are coordinates of a voxel in the LCS.

After that, sixty-four control points P_{ijk} can be defined around the part of the considered leg model as Fig. 17 - (b) shows. At the very beginning, they are defined along the three vectors $\vec{S}$, $\vec{T}$, $\vec{U}$ at regular intervals. Now after process of the formulation (3-10), any voxel with local coordinates (s, t, u) will get its original local coordinates. Then all voxels will not move at all, which means original leg model will not deform.

Afterwards, the rotation angles of the joints can be adjusted by the user such as the knee joint in Fig. 17 - (c). At the same time, all control points P_{ijk} defined around the knee joint will be moved and rotated. As a result, their local coordinates will be changed too. After applying the formula (3-10), any voxel with original local coordinates (s, t, u) will change to its new position P_{ffd}, whose local coordinates are determined by new positions of the FFD control points. This operation will result in a deformed leg model as Fig. 17 - (d) shows. It means that if the user changes the positions of these FFD control points, all voxels in the FFD control lattice will move based on the deformation of the FFD control lattice and the human leg model will deform accordingly.

3.2. 3D Rendering Algorithm: Marching Cubes

Three-dimensional surfaces of the human anatomy offer a valuable medical tool. Images of these surfaces, constructed from multiple two-dimensional slices of computer tomography (CT), magnetic resonance imaging (MRI), and single-photon emission computed tomography (SPECT), help physicians to understand the complex human anatomy present in the slices [65] [66] [67].

There are several approaches available for the three-dimensional surface generation problem. The very first one is called contour connection, which starts with building contour curves on every slice medical image, and then connects the contours on consecutive slices together with triangles [68]. In this method, if too many contour curves exist on two slices, ambiguities arise when determining which contours should be connected [69] [70]. The second approach, named cuberille method, was developed by Herman [71]. It dissects the considered space including the human model with equal cubes by three orthogonal sets of parallel planes, and each cube is called a cuberille [72]. The cuberille method creates one cuberille for every voxel of the medical dataset, and uses the outer surfaces of all cuberilles to create surfaces of different organs and tissues. Meagher used an octree representation data structure to compress the storage of the data, allowing rapid manipulation and display of voxels [73]. This method is very easy to realize using modern computer, memory requirement is low, and rendering process is very fast. Its main drawback is that the outer surface of the human model is not smooth but staircase shape. One example of the cuberille method is shown in Fig. 3.

The marching cubes algorithm used in this dissertation can extract a polygonal representation of constant density surface from a three-dimensional array of data. The resulting triangle surface model can be displayed on conventional graphics display systems using standard rendering algorithms [66]. The marching cubes algorithm has much better rendering quality than the contour connection and cuberille method, and much faster rendering speed than the volume ray casting method.

3.2.1. Working Principle of the Marching Cubes Algorithm

The marching cubes (MC) algorithm is mainly used for extracting a polygonal surface representation of an iso-surface from a three-dimensional scalar field [66]. It’s a well-known surface rendering algorithm used for building three-dimensional human body models based on the voxel dataset for different tissues and organs. Because it works on the look-up tables, it is very convenient to be realized in computer and its rendering speed is fast. The general idea of this algorithm is as follows: firstly importing part or whole of the scalar field, taking eight neighboring points and forming an imaginary cube, then extracting the polygons to represent the part of the iso-surface in this imaginary cube. All of these neighboring points (imaginary cubes) will be processed one by one, at last all of the extracted polygons can be combined together to represent the whole iso-surface.

It can be seen that the most important step of the MC algorithm is to extract the polygons from the imaginary cube. Because the imaginary cube is defined by eight neighboring points of the scalar field and the scalar values at each point, the iso-surface may pass through this cube, or may not pass through this cube. When it passes through the cube, it may cut one edge of the cube, or cut many edges. All of these possibilities can be determined by comparing the scalar values at the eight points of the cube and the scalar values of the iso-surface. If the scalar value of one point is larger than the value of the iso-surface and the value of its adjacent point is smaller than the iso-surface value, the iso-surface cuts the edge between these two points. The position where it cuts the edge can be linearly interpolated. The ratio of the length between the cutting point and the two points is the same as the ratio of the iso-surface value to the scalar values at these two points.

An example is given here to explain how to realize the idea mentioned above in computer. There is an imaginary cube in Fig. 18, which has eight vertexes and twelve edges. Because the imaginary cube is part of a scalar field, the scalar field has different scalar values at different vertexes. For convenience, each edge and vertex were numbered with an index. The edge index and the vertex index used in the algorithm are shown in Fig. 18. If the scalar value at vertex 3 is smaller than the iso-surface value, and all the scalar values at other vertexes are larger than the iso-surface value, a triangular facet which cuts through edges 2, 3 and 11 can be created as the blue iso-surface facet 1 shows. The exact positions of the vertexes of the extracted triangular facet depend on the ratio of the iso-surface value to the scalar values at the vertexes 3-2, 3-0 and 3-7 respectively. If vertex 0 and 3 are both smaller than the iso-surface value, a quadrangle facet which cuts through edges 0, 8, 11 and 2 can be created as the pink iso-surface facet 2 shows.

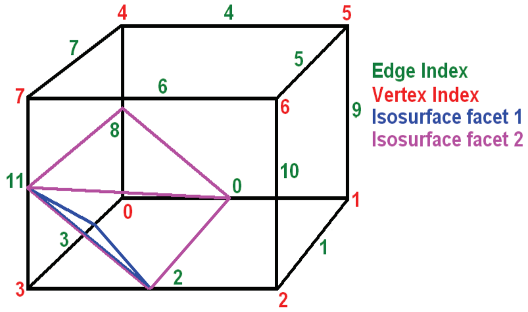

Fig. 18 Edge index, vertex index and two facets in an imaginary cube

In the MC algorithm, there are two look-up tables. This first one is the edge table, which relates the indexes of the vertexes, whose scalar values are smaller than the iso-surface value, to the indexes of the intersecting edges. The second one is the triangular table, which includes the sequence of the vertex to be obeyed to build the facets in the considered imaginary cube. Building these two look-up tables is error-prone, because every vertex has two possible statuses (smaller or larger than the iso-surface value), and then there are $2^8 = 256$ possibilities in total. Fortunately, the MC algorithm has already developed around twenty years, and there are already several mature look-up tables available in public domain, which were provided by some kind researchers for research reference.

This dissertation uses the look-up tables from Paul Bourke [74], which are both listed in Appendix A.

These two look-up tables can be used as follows: firstly, an eight bit index variable ($V_8V_7V_6V_5$ $V_4V_3V_2V_1$) is created for the imaginary cube, and each bit corresponds to the status of a vertex. In Fig. 18, if only the scalar value at vertex 3 is smaller than the iso-surface value, the index variable is set to be 0000 1000 or 8 in decimal system. Then it is time to check the edge table, it can be found that the 8th item of edge table is Edge table [8] = 0x80c = 1000 0000 1100, which means that the edges 2, 3 and 11 are intersected by the iso-surface. The concrete coordinates of the intersecting points between the iso-surface and the edges of the imaginary cube can be calculated by linear interpolation. If P_1 and P_2 are the two vertexes of the intersecting edge, and V_1 and V_2 are the scalar values at each vertex, the position vector of the intersecting point P can be calculated as

$$\vec{P} = \vec{P}_1 + (isovalue - V_1)\frac{\vec{P}_2 - \vec{P}_1}{V_2 - V_1}. \tag{3-18}$$

At last, the triangle table should be checked. The triangle table uses the same index variable, and it can be found that its 8th item is Triangle table [8] = {3, 11, 2, -1, -1, -1, -1, -1, -1, -1, -1, -1, -1, -1, -1, -1} which means three vertexes of the extracted triangular facet are located in edges 3, 11 and 2 respectively. If the scalar values at vertex 3 and 0 are both smaller than the iso-surface value, the index variable is changed to be 0000 1001 or 9 in decimal system. The 9th item of the edge table can be checked as Edge table [9] = 0x905 = 1001 0000 0101, which means the edges 0, 2, 8 and 11 are intersected by the iso-surface. The 9th item of the triangular table is Triangular table [9] = {0, 11, 2, 8, 11, 0, -1, -1, -1, -1, -1, -1, -1, -1, -1, -1}, which means three vertexes of the first extracted triangular facet are located in edges 0, 11 and 2, and three vertexes of the second extracted triangular facet are located in edges 8, 11 and 0 respectively.

3.2.2. Applying the MC Algorithm to Render the Voxel Model

Voxel-based human body model dataset, in principle, is a three-dimensional scalar field. In the dataset, each organ or tissue has its own tissue ID number which is different from others'. With these tissue ID numbers, the MC algorithm can draw three-dimensional outer surface for every tissue or organ. The whole work flow can be expressed as follows.

Step 1: Import four slices of the dataset into memory. In this dissertation, because the coordinates of all voxels must be calculated during the FFD calculation, the whole dataset is imported into memory in the first step.

Step 2: Create an imaginary cube from four neighboring voxels on one slice and the other four neighboring voxels on the next slice. For example, Fig. 19 shows two slices voxel data from the original dataset. All voxel tissue ID numbers of these two slices are defined in the intersecting points.

Step 3: Define the index variable for the imaginary cube by comparing the eight voxel values at the cube vertexes with the user specified organ or tissue ID number. And then use the index variable to loop up which edges are cut by the iso-surface (outer surface of the specified organ or tissue) from the edge table.

Step 4: Use the two voxel values at vertexes of the cut edges, calculate the coordinates of the intersecting points between the iso-surface and the intersecting edges by linear interpolation. And then use the triangular table to construct all triangular facets through this imaginary cube.

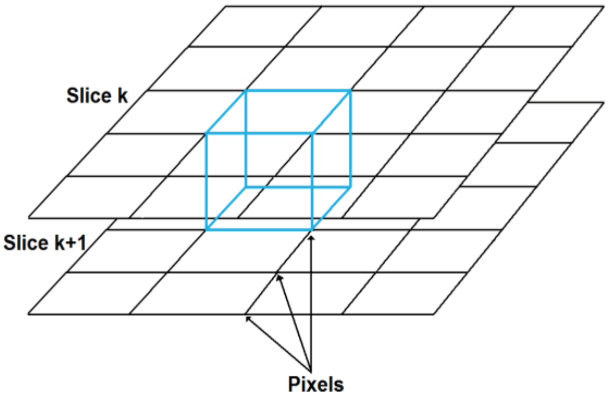

Fig. 19 An imaginary cube in the voxel dataset [66]

Step 5: Based on the principle mentioned above, all of these imaginary cubes can be checked one by one and facets representation can be created at the same time for all of them. At last, all of these small facets will combine a polygonal surface representation of the iso-surface which is just the outer surface of the specified tissue or organ.

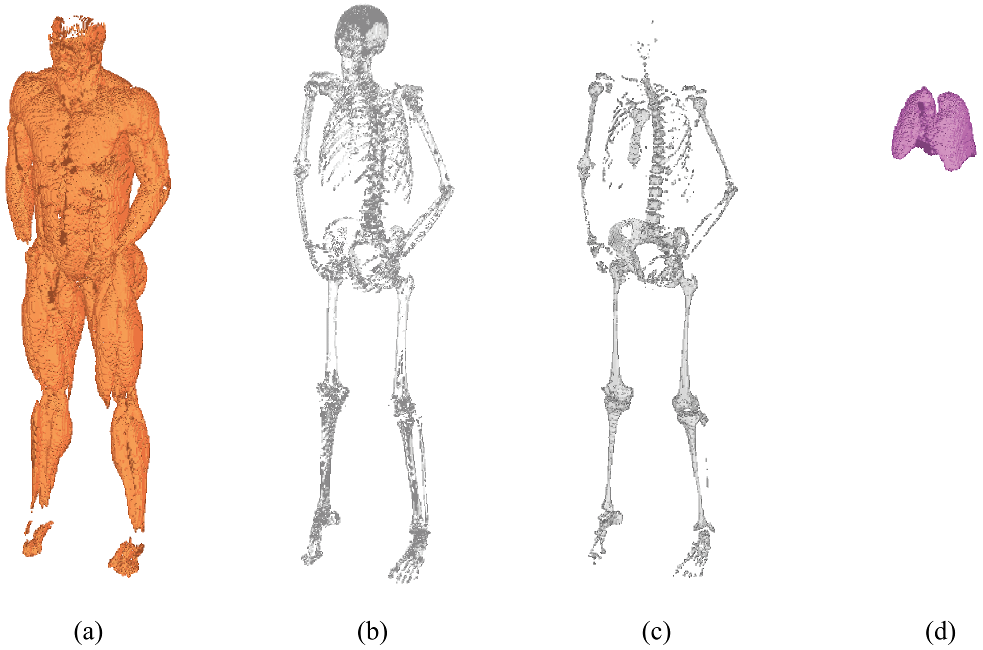

Fig. 20 Three-dimensional human models rendered by the marching cubes algorithm based on 4 mm HUGO model (a) Muscle (b) Skeleton (c) Marrow (d) Lung

A three-dimensional fat tissue model rendered by the marching cubes algorithm is shown in Fig. 1. Fig. 20 shows three-dimensional model examples of other four organs or tissues including muscle, bone, marrow and lung based on the 4 mm resolution HUGO model.

3.3. Combination of Marching Cubes Algorithm and FFD Technique

Apart from good rendering quality and fast rendering speed, the main advantage of the marching cubes algorithm used in the poser program package is to maintain the continuity of the human body model after deformation. If the most common rendering algorithm, the Cuberille method, is used to draw a small cube for every voxel in order to show the whole human body model with the outer surface of all voxels, originally all voxels should be arranged side by side, which results in a continuous geometry model such as the simple voxel model including nine voxels shown in Fig. 21. This model has a unique advantage in numerical simulation, because the geometry model in itself is just a hexahedral mesh model, and most of the electromagnetic simulation algorithms can be performed based on it directly. If the original voxel model is deformed, the positions of most voxels will change and they cannot be arranged side by side any more. Instead, they will be separated from each other and result in a non-continuous voxel model as Fig. 22 shows. This kind of model cannot be used directly, because the space among these voxels will lead to a serious problem during simulation.

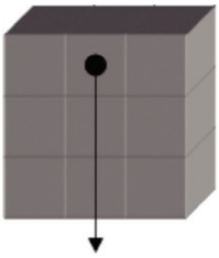

Fig. 21 Voxel model rendered by cuberille method before deformation [10]

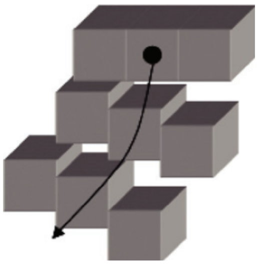

Fig. 22 Voxel model rendered by cuberille method after deformation [10]

Some researchers firstly transformed the cuberille voxel model into a polygon mesh model and then transformed it back to the cuberille voxel model after deformation to tackle this problem [10]. In fact, a combination of the marching cubes algorithm and the FFD technique can avoid this problem directly.

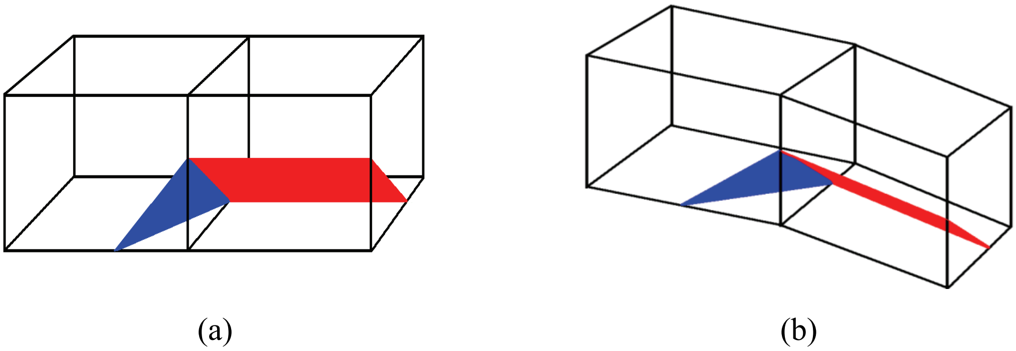

(a) (b)

Fig. 23 Two marching cubes side by side (a) Before model deformation (b) After model deformation

For example, there are two imaginary cubes of the marching cubes algorithm arranged side by side in Fig. 23 - (a). In the left one there is a small blue triangular facet and in the right one there is a small red rectangular facet which is composed of two triangular facets. These two facets should be part of the outer surface of some specific tissue or organ, so they must be connected to each other initially as Fig. 23 - (a) shows. After deformation of the model, the positions of the voxels might change as shown in Fig. 23 - (b). However, because these two imaginary cubes share one surface, it means that the blue triangular facet and the red rectangular facet will always share one edge. As a result, even after the deformation, these two facets are still connected to each other. Therefore, the poser program can still get a continuous human model after the deformation but before exporting the deformed human model as a new dataset file.

This property can save the user of the poser program a lot of time because exporting a new dataset file is always the most time-consuming step. With the help of this combination, the user can check the validity of the deformed human body model very early, and adjust related deformation parameters if some unsatisfactory deformations are found. After the user is completely satisfied with the deformed human model, the last postured human model can be exported as a new and satisfactory dataset file. Otherwise, if the user can only see a continuous human model based on the exported new dataset file, it's inevitable to export the new dataset file several times before a satisfactory one is found. Fig. 24 shows several deformed human models with different common postures rendered by the marching cubes algorithm after the FFD calculation is finished but before new dataset file is exported.

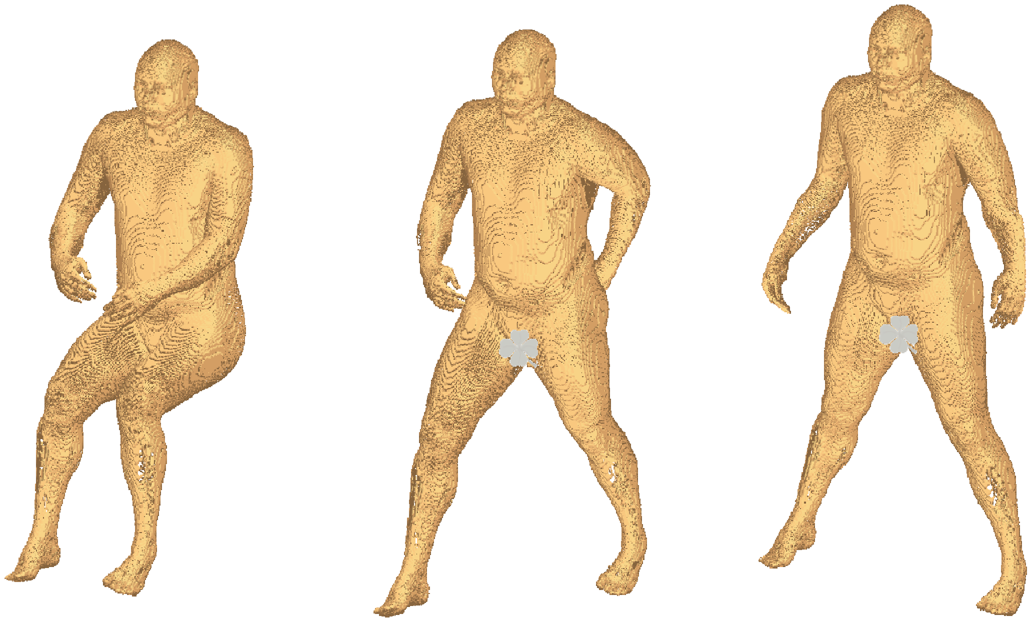

(a) (b) (c)

Fig. 24 Deformed three-dimensional fat human models with different postures rendered by the marching cubes algorithm (a) Sitting (b) Walking (c) Standing

3.4. Electromagnetic Field Simulation Algorithm

This dissertation mainly discusses applications of the postured voxel-based human body models used in the electromagnetic domain. Electromagnetic fields that vary with time are governed by physical laws described by a set of equations known collectively as Maxwell's equations. They are the fundamental equations to describe macroscopic electromagnetic phenomena in continuous space. Their integral forms will be firstly explained in this section.

In order to perform the electromagnetic simulation numerically, the time domain electromagnetic simulation algorithm Finite Integration Technique (FIT) developed by Weiland [2] will be shortly introduced. Similar to the finite difference time domain technique (FDTD) [52], the stable time step of the FIT is constricted by the Courant limit for stability. Hence, if the simulation models have geometric details which are very small compared to signal wavelengths, a huge number of time steps ($>10^8$) will be possibly needed. The reduced c technique suggested by Holland [53] [54] can get a much longer stable time step than the value specified by the Courant limit for stability by mathematically decreasing the speed of light c, and then speed up simulations several times. Its working principle will be also introduced here.

3.4.1. Maxwell's equations

The set of Maxwell's equations are the fundamental equations to describe macroscopic electromagnetic phenomena in continuous space. Their integral forms can be expressed as follows

$$\int_{\partial A} \vec{E}(\vec{r},t) \cdot d\vec{s} = -\iint_A \frac{\partial}{\partial t} \vec{B}(\vec{r},t) \cdot d\vec{A}, \tag{3-19}$$

$$\int_{\partial A} \vec{H}(\vec{r},t) \cdot d\vec{s} = \iint_A (\frac{\partial}{\partial t} \vec{D}(\vec{r},t) + \vec{J}(\vec{r},t)) \cdot d\vec{A}, \tag{3-20}$$

$$\iint_{\partial V} \vec{B}(\vec{r},t) \cdot d\vec{A} = 0, \tag{3-21}$$

$$\iint_{\partial V} \vec{D}(\vec{r},t) \cdot d\vec{A} = \iiint_v \rho(\vec{r},t) dV, \tag{3-22}$$

for any area A, volume V and their respective boundaries ∂A and ∂V. The spatial variable is denoted by vector $\vec{r}$ and the temporal variable by t. The vector quantities $\vec{E}$ ($\vec{H}$) refer to the electric (magnetic) field intensity, $\vec{D}$ ($\vec{B}$) is the electric (magnetic) flux density, $\vec{J}$ denotes the electric current density and ρ is the electric charge density. The current density $\vec{J}$ can be decomposed into three parts: conduction current density $\vec{J}_k$, externally imposed current density $\vec{J}_i$ and convection current density $\vec{J}_c$.

Equation (3-19) is sometimes called Faraday's law and equation (3-20) is called Ampere's law. The third equation (3-21) states the absence of magnetic charges and the fourth equation (3-22) is called Gauss's law. Maxwell's equations can be also written in differential form which can be derived by applying the theorems of Gauss and Stokes to the integral form.

The relationship between field intensity and flux is described by constitutive equations. In the general case, the constitutive equations can be expressed as:

$$\vec{D}(\vec{r},t) = \varepsilon_0 \vec{E}(\vec{r},t) + \vec{P}(\vec{r},t), \tag{3-23}$$

$$\vec{B}(\vec{r},t) = \mu_0 \vec{H}(\vec{r},t) + \mu_0 \vec{M}(\vec{r},t), \tag{3-24}$$

$$J_k(\vec{r},t) = \sigma(\vec{r}) \vec{E}(\vec{r},t). \tag{3-25}$$

Equation (3-25) is called Ohm's law. Here ε_0 denotes the electric permittivity of vacuum, μ_0 is the magnetic permeability of vacuum, and σ is the conductivity of the medium. The vector $\vec{P}$ is the electric dipole moment density and $\vec{M}$ is the magnetic dipole moment density. The permittivity and permeability of a material are commonly given relative to the respective values in vacuum ε_0 and μ_0 as

$$\mu(\vec{r}) = \mu_0 \mu_r(\vec{r}) \quad \text{with} \quad \mu_0 = 4\pi \times 10^{-7}\,\text{Vs/Am} \tag{3-26}$$

$$\varepsilon(\vec{r}) = \varepsilon_0 \varepsilon_r(\vec{r}) \quad \text{with} \quad \varepsilon_0 = \frac{1}{\mu_0 c_0^2} \approx 8.854 \times 10^{-12}\,\text{As/Vm} \tag{3-27}$$

where $c_0 \approx 2.998\times10^8$ m/s is the speed of the light in vacuum.

The material properties of almost all human tissues and organs change with frequency. In frequency domain computation, which is based on the analysis of electromagnetic fields at one specific frequency assuming harmonic time dependence, for such linear, homogeneous, isotropic, dispersive materials, the constitutive equations can be expressed as:

$$\vec{D}(\vec{r},\omega) = \varepsilon(\vec{r},\omega) \vec{E}(\vec{r},\omega), \tag{3-28}$$

$$\vec{B}(\vec{r},\omega) = \mu(\vec{r},\omega) \vec{H}(\vec{r},\omega), \tag{3-29}$$

$$J_k(\vec{r},\omega) = \sigma(\vec{r},\omega) \vec{E}(\vec{r},\omega) \tag{3-30}$$

where ε and μ are complex quantities described as

$$\varepsilon(\vec{r},\omega) = \varepsilon_0 (\varepsilon'(\vec{r},\omega) - j\varepsilon''(\vec{r},\omega)), \tag{3-31}$$

$$\mu(\vec{r},\omega) = \mu_0 (\mu'(\vec{r},\omega) - j\mu''(\vec{r},\omega)). \tag{3-32}$$

3.4.2. Foundation of Finite Integration Technique

Solving Maxwell's equations analytically can be only realized in very few electromagnetic problems containing simple geometric models. In modern electromagnetic simulations with very complicated equipments, using numerical methods to solve Maxwell's equations is the only choice. As one of the most popular electromagnetic simulation algorithm, the Finite Integration Technique (FIT) was introduced by Weiland in 1977 [2] . In following decades, it was extended and completed into a generalized scheme for the solution of electromagnetic problems in a discrete space.

In FIT, the calculation domain, which contains the space of interest, must be defined as a bounded three dimensional volume $\Omega \in \mathbf{R}^3$ with boundary $\partial\Omega$. A spatial discretization process is performed to decompose the calculation domain into a finite number of volume cells V_i such as hexahedra or tetrahedra, and the volume cells have to fit exactly to each other. This decomposition yields the finite grid cell complex G, which is the first set computational grid. Because the voxel-based human models can be transformed into hexahedral mesh models conveniently, all simulations in this dissertation use three-dimensional Cartesian coordinate grid. The FIT allows considering all types of coordinate meshes, orthogonal and non-orthogonal meshes [75] [76]. Even consistent sub-gridding schemes have been developed [77].

In Cartesian coordinates, the grid cell complex G is composed of hexahedral elementary volumes $V(i, j, k)$. The grid facets, which is the intersection of two neighboring grid cells, are associated with three different directions along the u-, v- and w-axis and denoted by $A_u(i, j, k)$, $A_v(i, j, k)$ and $A_w(i, j, k)$. The intersection of two grid facets, called grid edge, is denoted by $L_u(i, j, k)$, $L_v(i, j, k)$ and $L_w(i, j, k)$. Each edge of the volume cells includes an initial orientation, pointing into the direction of the respective grid coordinates towards higher indices. Analogously every grid facet is also associated with a similarly defined direction.

In order to transfer Faraday's law in integral form (3-19) into the grid space, two integral state variables referred to as electric edge voltage and magnetic facet flux should be defined. Integrating the continuous electric field intensity along the edge $L_u(i, j, k)$ yields the electric edge voltage as

$$\widehat{\mathrm{e}}_u(i,j,k) = \int_{L_u(i,j,k)} \vec{E} \cdot d\vec{s}. \tag{3-33}$$

Integrating the continuous magnetic flux density over the facet $A_w(i, j, k)$ yields the magnetic facet flux as

$$\widehat{\widehat{\mathrm{b}}}_w(i,j,k) = \int_{A_w(i,j,k)} \vec{B} \cdot d\vec{A}. \tag{3-34}$$

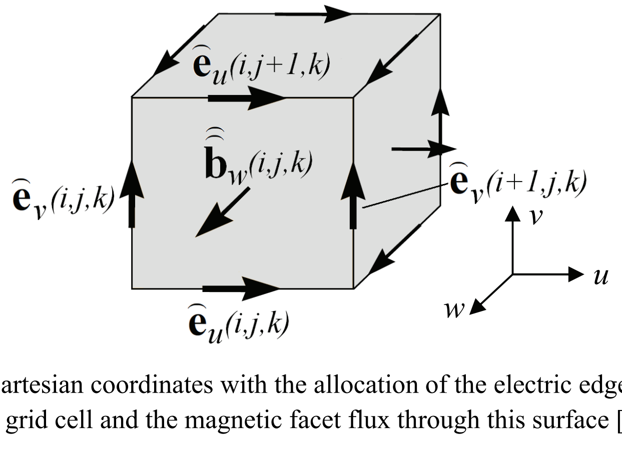

Fig. 25 A grid cell G in Cartesian coordinates with the allocation of the electric edge voltages on the edges of the front surface of the grid cell and the magnetic facet flux through this surface [78]

Now applying Faraday's law on the front facet $A_w(i, j, k)$ of the volume cell $V(i, j, k)$ as Fig. 25 shows will derive following ordinary differential equation:

$$\hat{\mathrm{e}}_u(i,j,k)+\hat{\mathrm{e}}_v(i+1,j,k)-\hat{\mathrm{e}}_u(i,j+1,k)-\hat{\mathrm{e}}_v(i,j,k)=-\frac{d}{dt}\hat{\hat{\mathrm{b}}}_w(i,j,k) \tag{3-35}$$

Orientation of the cell edges and facets decides the signs of the items in equation (3-35).

Faraday's law can be applied for each facet of the grid cell complex *G* and results in similar equations as (3-35). All electric edge voltages and magnetic facet fluxes over the whole grid cell complex *G* can be arranged in vectors as:

$$\hat{\mathrm{e}}:=(\hat{\mathrm{e}}_{u,n}\,|\,\hat{\mathrm{e}}_{v,n}\,|\,\hat{\mathrm{e}}_{w,n})^T \qquad n=1,\dots,N_p\,, \tag{3-36}$$

$$\hat{\hat{\mathrm{b}}}:=(\hat{\hat{\mathrm{b}}}_{u,n}\,|\,\hat{\hat{\mathrm{b}}}_{v,n}\,|\,\hat{\hat{\mathrm{b}}}_{w,n})^T \qquad n=1,\dots,N_p\,. \tag{3-37}$$

Then equations (3-35) of all grid cell facets of the grid cell complex *G* can be collected in a matrix form

$$\mathrm{C}\hat{\mathrm{e}}=-\frac{d}{dt}\hat{\hat{\mathrm{b}}}. \tag{3-38}$$

The matrix **C** contains only topological information on the incident relation of the cell edges and their orientation. Then it includes all signs appearing in equations (3-35) and represents a discrete curl operator on the grid cell complex *G*.

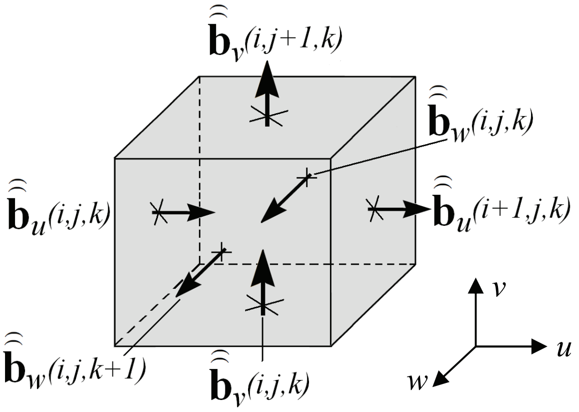

Fig. 26 A grid cell *G* in Cartesian coordinates with the allocation of the magnetic facet fluxes through the facets of the grid cell [78]

The second discrete operator in the FIT is the divergence operator. It can be derived by applying Maxwell equation (3-21) on the grid cell complex *G* for the volume cell as Fig. 26 shows. The evaluation of the surface integral over the six facets of the volume cell leads to

$$\begin{aligned}&\hat{\hat{\mathrm{b}}}_u(i+1,j,k)+\hat{\hat{\mathrm{b}}}_v(i,j+1,k)+\hat{\hat{\mathrm{b}}}_w(i,j,k+1)\\&\qquad-\hat{\hat{\mathrm{b}}}_u(i,j,k)-\hat{\hat{\mathrm{b}}}_v(i,j,k)-\hat{\hat{\mathrm{b}}}_w(i,j,k)=0.\end{aligned} \tag{3-39}$$

Similarly, the relation expressed by equation (3-39) can be also applied on other grid cells of *G*, and then Maxwell equation (3-21) can be transformed into its discrete form:

$$\mathrm{S}\hat{\hat{\mathrm{b}}}=0 \tag{3-40}$$

The discrete divergence operator **S** with the dimension $N_p \times 3\, N_P$, which is related to the zero flux balance of each grid cell of *G*, also only depends on the grid topology as the discrete curl operator **C**.

Now there are two Maxwell equations (3-20) and (3-22) left. Discretization of these two equations with the FIT needs introduction of the dual grid cell complex $\tilde{G}$ of the primary grid cell complex *G*. In Cartesian coordinates, the dual grid cell complex $\tilde{G}$ is defined by taking the focal points of the grid cell complex *G* as grid nodes of the mesh cells of $\tilde{G}$. Thus there is a one-to-one relationship between the cell edges of *G* cutting through the facets of $\tilde{G}$ and vice versa.

In the dual grid cell complex $\tilde{G}$, integrating the magnetic field intensity along the dual grid edge $\tilde{L}_u$ can get the magnetic edge voltage as:

$$\overset{\frown}{\mathrm{h}}_u(i,j,k)=\int_{\tilde{L}_u(i,j,k)}\vec{H}\cdot d\vec{s}, \tag{3-41}$$

and integrating the electric flux density and current density along the dual grid facet $\tilde{A}_w$ can result in the electric facet flux and electric facet current as:

$$\overset{\frown}{\overset{\frown}{\mathrm{d}}}_w(i,j,k)=\int_{\tilde{A}_w(i,j,k)}\vec{D}\cdot d\vec{A}, \tag{3-42}$$

$$\overset{\frown}{\overset{\frown}{\mathrm{j}}}_w(i,j,k)=\int_{\tilde{A}_w(i,j,k)}\vec{J}\cdot d\vec{A}. \tag{3-43}$$

In analogy to Faraday’s law (3-19), discretization of Ampere’s law (3-20) can be performed on a facet of a dual grid cell, which shows that summation of four magnetic edge voltages equals the displacement current and conductive current through the cell facet that the four edges surround. At last Gauss’s law (3-22) can be discretized for the dual grid cell complex $\tilde{G}$ similarly as the discretization of equation (3-21) on the primary gird cell complex *G*. The volume integral of the charge intensity in a dual grid cell can be related to a discrete charge on the single grid node of the primary grid cell complex *G* which is in the considered dual grid cell. These two discretization processes will also result in matrix equations which are similar as equations (3-38) and (3-40). Now an exact representation of Maxwell’s equations for the grid cell complex pair {*G*, $\tilde{G}$ }, named Maxwell-Grid-Equations (MGE), can be given by:

$$\mathrm{C}\overset{\frown}{\mathrm{e}}=-\frac{d}{dt}\overset{\frown}{\overset{\frown}{\mathrm{b}}}, \tag{3-44}$$

$$\tilde{\mathrm{C}}\overset{\frown}{\mathrm{h}}=\frac{d}{dt}\overset{\frown}{\overset{\frown}{\mathrm{d}}}+\overset{\frown}{\overset{\frown}{\mathrm{j}}}, \tag{3-45}$$

$$\mathrm{S}\overset{\frown}{\overset{\frown}{\mathrm{b}}}=0, \tag{3-46}$$

$$\tilde{\mathrm{S}}\overset{\frown}{\overset{\frown}{\mathrm{d}}}=\mathrm{q} \tag{3-47}$$

where $\tilde{\mathrm{C}}$ and $\tilde{\mathrm{S}}$ are dual discrete curl operator and dual discrete divergence operator.

Several basic properties of the discrete operators of the FIT, which were proved and stated in [78] [79] [80] [81] in detail, are introduced briefly here. The relation between the primary grid curl operator **C** and the dual gird curl operator **C** is proved as:

$$\mathrm{C} = \tilde{\mathrm{C}}^T. \tag{3-48}$$

And another one essential property lies in the analogy to the vector analytical identities

$$\nabla \cdot \nabla \times \vec{A} = 0 \quad \text{and } \nabla \times \nabla \Phi = 0 \tag{3-49}$$

given with the matrix equations

$$\mathrm{SC} = 0 \text{ and } \tilde{\mathrm{S}}\tilde{\mathrm{C}} = 0, \tag{3-50}$$

$$\mathrm{C}\tilde{\mathrm{S}}^T = 0 \text{ and } \tilde{\mathrm{C}}\mathrm{S}^T = 0 \tag{3-51}$$

for the grid cell complex pair $\{G, \tilde{G}\}$.

3.4.3. Courant Limit for Stability and Reduced *c* Technique

In the explicit leapfrog algorithm used for the FIT or the Finite Difference Time Domain method (FDTD) [52], for computational stability, it is necessary to satisfy a relation between the space increment and the time increment. For constant ε and μ, computational stability requires approximately that

$$\Delta t \le \frac{1}{c} \cdot \frac{1}{\sqrt{\left(\frac{1}{\Delta x}\right)^2 + \left(\frac{1}{\Delta y}\right)^2 + \left(\frac{1}{\Delta z}\right)^2}}, \text{ with } c = \frac{1}{\sqrt{\varepsilon\mu}} = \frac{1}{\sqrt{\varepsilon_r \varepsilon_0 \mu_r \mu_0}} \tag{3-52}$$

where c is the speed of light [82]. If the speed of light has different values in the different materials of the computational region concerned, the maximum value should be selected. This requirement, which is called Courant limit for stability or Courant-Friedrich-Levy criterion (CFL-Criterion), puts a restriction on time step Δt for the chosen space step Δx Δy and Δz. The physical explanation of this condition can be expressed as follows: when an electromagnetic wave propagates in a discrete grid, the time step must be less than the time for the electromagnetic wave to travel adjacent grid points.

The Courant limit for stability makes it difficult to use the leapfrog algorithm to solve application simulation problems where slowly-varying electromagnetic excitations are present (so called quasistatic electromagnetic simulation) or illuminated geometric details are very small electrically which means very small compared to the shortest signal wave length. This occurs because in such problems the Courant limited time step can become small enough to require the usage of several billion time steps to finish the whole simulation, which needs very long calculation time. In order to solve this problem, Holland demonstrated a procedure to elude the Courant stability condition by decreasing the speed of the light mathematically in 1995 [53] [54]. This so called "reduced *c*" technique can be used for any electromagnetic simulation problem where stable time step is limited by the smallness of the geometry, not by a physical requirement for extremely fine temporal electromagnetic resolution. For this kind of problem, an alternative solution is to use implicit method which remains stable for any time step. But even for a normal scale simulation, implicit three-dimensional FIT or FDTD codes involve manipulation of huge matrixes which are not necessarily banded or diagonally dominant and then very difficult to process.

In most of the quasistatic electromagnetic problems, there is no electromagnetic wave transmitting to the outside and then this sort of problem has a solution which seldomly depends on the speed of the light c. This means that if an artificially reduced c can be used in the simulation, which can be realized by increasing permeability μ or permittivity ε mathematically but not both, the leapfrog algorithm can accept a significantly relaxed and unacceptably large stable time step. But the speed of light c cannot be slowed without limitation. In order to ensure validity of the results, the speed of light cannot be slowed over the point where the geometry is no longer small compared to the shortest wavelength of interest.

Calculations made in this manner will have one other scaling aspect to be aware of. If ε is scaled by ε_s, μ is not scaled, and the input drive is magnetic field, the reduced c technique will output electric fields that are too low by the factor $(\varepsilon_s)^{1/2}$. Otherwise if the incident field is specified by an electric field, the magnetic field will be scaled too high by the same factor. This phenomenon occurs because the computed mathematical model of impedance will now be related by $(\mu / \varepsilon\varepsilon_s)^{1/2}$, not by $(\mu / \varepsilon)^{1/2}$. Scaling μ will lead to similarly scaled field results by the factor $(\mu_s)^{1/2}$.

Increasing permeability μ or permittivity ε depends on the content of the simulation case. In Holland's simulation which evaluated the magnetic fields diffusing into an aluminum or steel enclosure and is a magneto-quasistatic problem in principle, permittivity ε is increased because the simulation includes magnetically nonlinear material such as steel and manipulation of permeability μ will lead to troubles.

In this dissertation, the reduced c technique is studied to be applied to speedup electro-quasistatic simulations. Because of biological tissues' dispersive nature, their permittivity changes with frequency, and then cannot be scaled as easily as Holland did. Instead, all materials' permeability is tried to be scaled to realize the effect of "reduced c", and then speedup original simulations. All of these contents including a detail error analysis of the reduced c technique will be explained in Chapter 5.

4. Generation of Postured Human Models

In the present chapter, the developed software tool used to generate deformed human body models with different common postures is introduced in detail. In order to realize all required functions conveniently, a Graphical User Interface (GUI) was developed for this poser program. The marching cubes algorithm and the FFD technique introduced in former chapter are both used in this platform. Except for the basic functions such as importing original dataset file, rendering the voxel-based human body models, deforming original human model to make it have different postures and exporting the deformed human model as a new dataset file, several other necessary functions including separating arm voxels away from the trunk to deform two arms of the original human model, rotating patella of the leg model while the knee joint is bent, mass calculation and comparison for all tissues and organs between the original human model and the deformed human model, are also explained here and realized in the poser program. To get a satisfactory outer deformation shape of the postured human body model and better mass conservation result, the strategy used to define and operate the FFD control lattice is the most critical point in the whole FFD technique. A matrix manipulation method was applied in the poser program to define initial positions and adjust rotation angles of the FFD control points, its working principle and related knowledge are also introduced here.

This poser program was developed based on Microsoft Visual Studio 2008®, C++ language and OpenGL® programming environment, on the Microsoft Windows XP® professional version operating system. The GUI was developed with the MFC (Microsoft Foundation Class). Until now it has two versions which are used for 32 bit (x86) and 64 bit (x64) computer respectively. They have been also tested and can run successfully on the operating systems Microsoft Windows Vista® and Microsoft Window 7®.

This chapter is organized as follows: the first section will make a general introduction to the whole poser program including all function modules, work flow and main interfaces of the poser program, and then all contents left are arranged based on the working flow of the poser program. The way of importing and storing original dataset file in the program is explained in the second section. The third section explains how to determine locations of all joint points in the original human body model, the definition of the FFD control lattice based on different parts of the original human body model, and operate the FFD control lattice based on rotation angles of different joint points. Several special techniques including segmenting arm voxels away from the trunk, swelling muscles of the arm with the bent elbow joints, rotating patella with the bent knee joints, are explained in the fourth section. Exporting the deformed human body models as new dataset files, and mass calculation and comparison between the deformed human body models and the original human model are presented in the last section.

4.1. Introduction to the Poser Program

4.1.1. Program Function Module Design

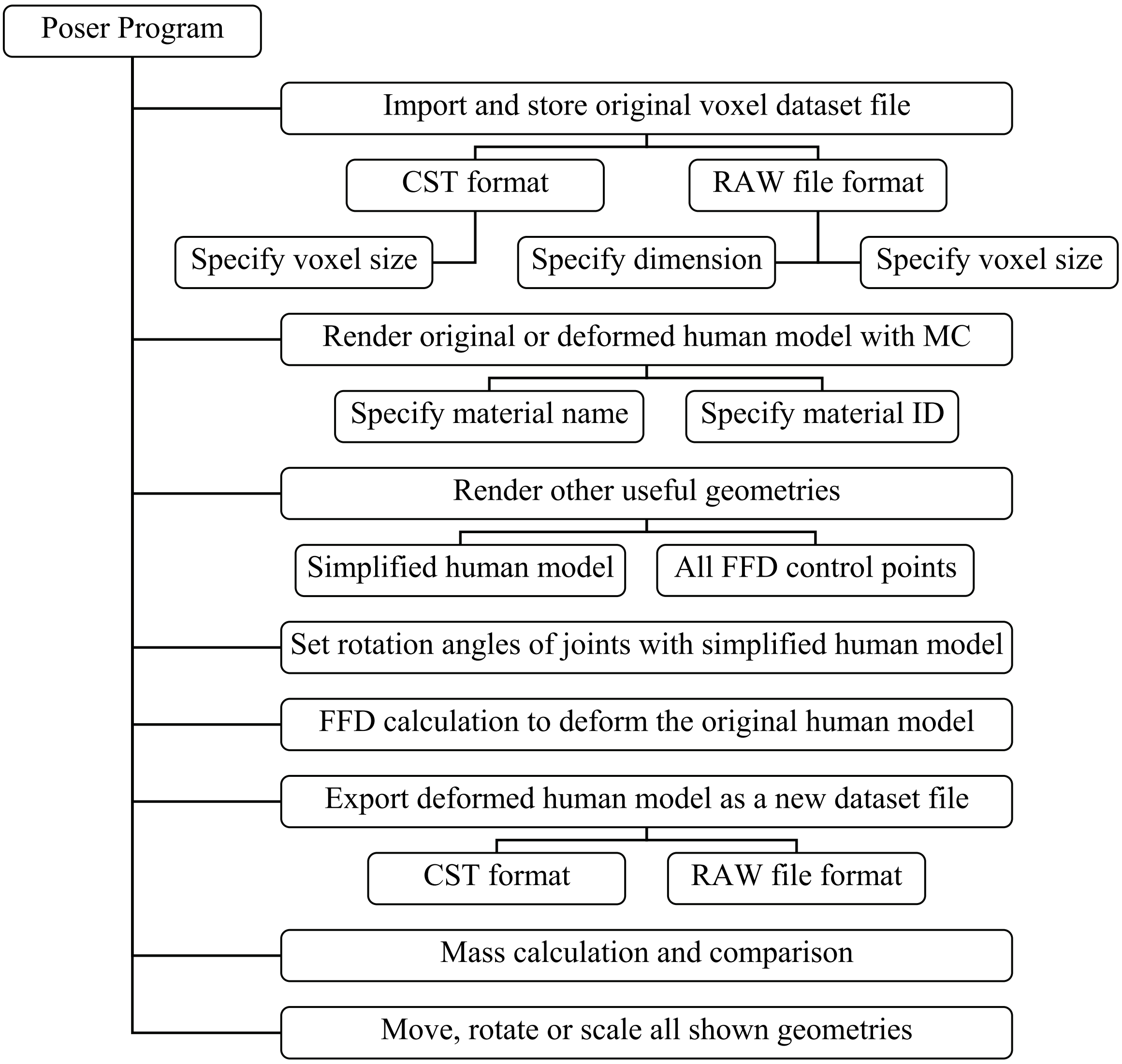

Fig. 27 Function modules of the poser program

All functional modules of the poser program are shown in Fig. 27, and their detail functions are as follows:

1) Import and store original voxel dataset file.

The very first step of the poser program is to import the original voxel dataset file. This poser program can import not only the HUGO model with CST® voxel file format, but also other voxel dataset files with general pure voxel data file format ∗.raw. In CST® voxel file format, there are 148 bytes header information including dimension information of the dataset, and the poser program can read them automatically, so the user only needs to choose which voxel size he or she wants to use. However, since ∗.raw file has no header information, the user much specify both voxel size and dimension information of the voxel dataset before the original voxel dataset file is imported into the program.

2) Render original or deformed human model with MC.

After the original voxel dataset is imported into the program, different tissues or organs of the original model, or the deformed human model after the FFD calculation is finished, can be rendered with the MC algorithm. For the HUGO model, the user can select any tissues or organs conveniently based on their names, and for other voxel models, the user can select any other tissues or organs by specifying concrete tissue ID numbers directly.

3) Render other useful geometries.

Except for the voxel based human body models imported from external files, in the program there is one simplified human model, which consists of spheres, cylinders and elliptic cylinders, and has similar body dimension as the HUGO model. Apart from that, the user can also observe the whole FFD control lattice including all FFD control points before and after the deformation calculation to adjust deformation style of the FFD control lattice if the deformed human body model is not satisfactory.

4) Set rotation angles of joints with simplified human model.

With the help of the simplified human model mentioned above, the user can set rotation angles of different joints by selecting the concerned body part and moving sliding controls of a dialog box. The simplified human model will be deformed based on these rotation angles and the user can see the deformation effect of the simplified human model in real time. Rotation angles of the joints user sets will be remembered by the program, and then the FFD control lattice will be deformed accordingly based on these values.

5) FFD calculation to deform the original human model.

This module will deform the original HUGO model according to the deformation of the FFD control lattice. After the FFD calculation is finished, the user can see the deformed human body model directly with the rendering function of the poser program.

6) Export the deformed human model as a new dataset file.

This function can export the deformed (or original if needed) voxel-based human body model as a new voxel dataset file with CST® voxel file format or ∗.raw file format. The poser program has two versions for export function: the first one occupies low memory, while the second one has faster calculation speed. The user can choose any one of them based on his or her computer configuration.

7) Mass calculation and comparison.

This function can calculate and show the mass of every tissue and organ of the original HUGO model and of the deformed human model, and calculate relative errors referring to the original model. The mass of whole body and related relative error will be also calculated.

8) Move, rotate or scale all shown geometries.

For voxel-based human body models, simplified human model and the FFD control lattice, user can move, rotate or scale them to observe from different directions.

4.1.2. Workflow of the Poser Program

The workflow of the developed poser program which is designed to posture the voxel-based human body model is shown in Fig. 28.

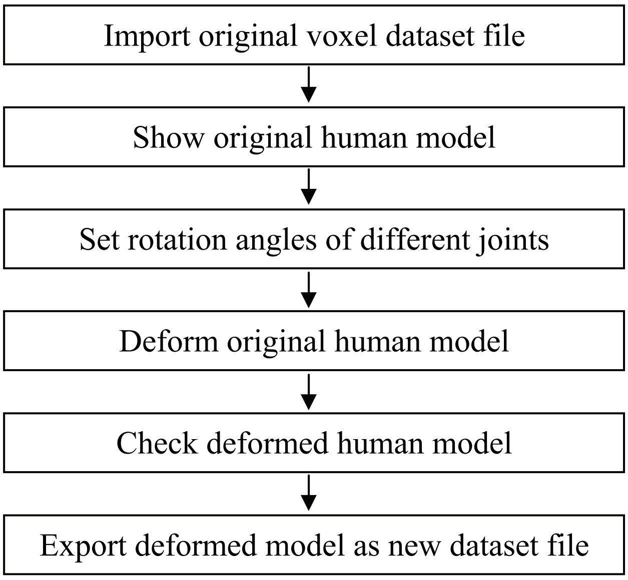

Fig. 28 Workflow of the developed poser program

The very first step is to import the original voxel dataset file into a three dimensional array. Each element of this array stands for a voxel class which includes voxel value (tissue ID number), voxel position information and body parts information, which indicates which body part this voxel belongs to e.g. arm, leg, head, trunk, etc. Then, three-dimensional human body models can be built with the help of the MC algorithm based on different tissues or organs such as the three-dimensional fat tissue model shown in Fig. 1.

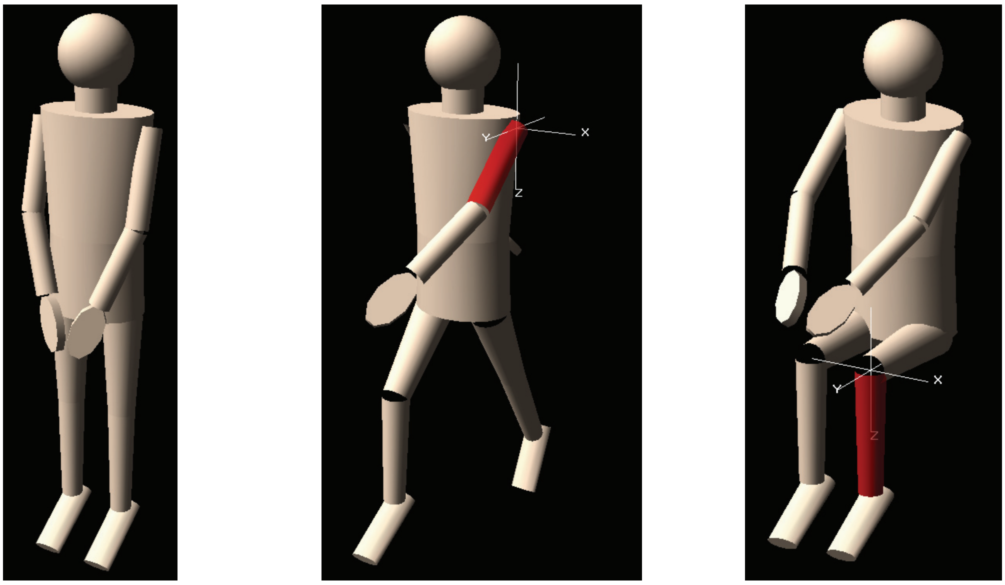

(a) (b) (c)

Fig. 29 Simplified human models used to define rotation angles of different joints (a) Original posture (b) Walking posture (c) Sitting posture

After checking the original voxel-based human body model, the user of the program will switch to the simplified human model shown in Fig. 29 - (a) to define rotation angles of different joints along *x*-, *y*- and *z*-direction, at the same time getting a very rough impression about the deformation effects of the postured human body models as Fig. 29 - (b) and (c) show.

After the rotation angles of all concerned joints are defined satisfactorily, the FFD calculation can be performed to deform the original voxel-based human body model. After the FFD calculation is finished, positions of all voxels of the original human body model will be changed, and then the resulting postured human body model is displayed directly as Fig. 30 - (a) shows. The FFD calculation itself is very fast. The deformed human body model shown in Fig. 30 - (a) has 4 mm resolution, and the FFD calculation used to generate this posture only takes around 20 sec. It should be noticed again that with the help of combination of the MC algorithm and the FFD technique, the user of the poser program can check the deformed human body model before exporting it as a new dataset file. If the deformed human body model is not satisfactory, the user can go back to the simplified human model mentioned above to adjust rotation angles of some joints and then perform the FFD calculation again until a satisfactory result is available.


(a) (b) (c)

Fig. 30 Deformed human body models (a) Walking posture shown in the poser program (b) Walking posture shown in CST® (c) Sitting posture shown in CST®

After the posture of the deformed human body model is satisfactory, it can be re-voxelized and exported as a new voxel dataset file. More detail information about export algorithm will be explained in following sections. The new dataset file of the deformed human body model can be imported into other commercial software packages such as CST MICROWAVE STUDIO® as shown in Fig. 30 - (b) and (c). The time that export process takes depends on the complexity of the new posture and on the resolution of the voxel dataset. Exporting the deformed human models in Fig. 30 with 4 mm resolution takes around 1 min. Until now the export process with voxel size bigger than 3 mm can be finished in 3 min. Exporting 2 mm and 1 mm resolution dataset needs more time and memory. The computer configuration used in this section is Intel® Xeon CPU 3.06GHz, Dell workstation, 2.00G RAM.

As mentioned before, the HUGO model has variable voxel resolutions ranging from 8 × 8 × 8 mm^3 to 1 × 1 × 1 mm^3, and the poser program can deal with all these models with different resolutions. This is because although the resolution is different, all HUGO models have the same body size and joint positions, then all models can be deformed using only one set FFD control lattice, which is also a great advantage of the FFD technique.

4.1.3. Main Program Interfaces

Some graphical interfaces of the poser program in several important steps are shown in Fig. 31. Except for the dialog boxes in the following interfaces, there are several more dialog boxes designed to show important information such as informing the user that the import or export process is finished, setting tissues ID numbers or selecting tissues or organs directly, informing the user that the FFD calculation is finished, showing consumed time of the FFD calculation or export process, showing dimension information of the new dataset file.

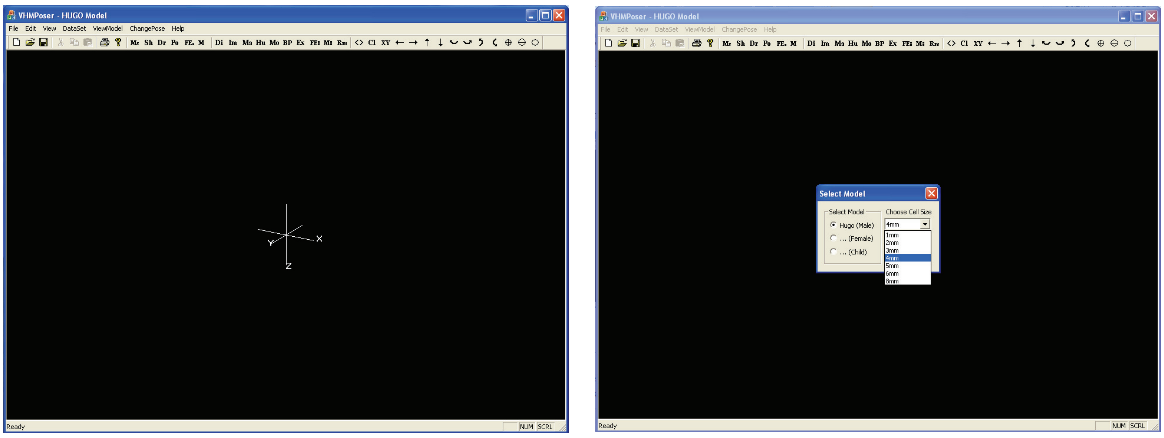

Select Model
● Hugo (Male)
○ … (Female)
○ … (Child)

Choose Cell Size: 4mm

(a) Start-up interface

(b) Select original dataset and voxel size

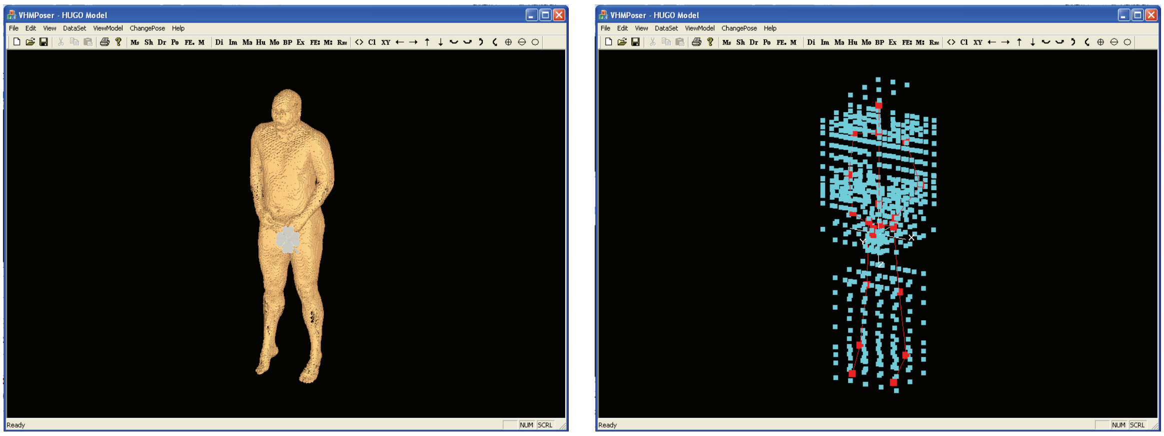

(c) Render original voxel model

(d) All FFD control points (blue) and joints (red)

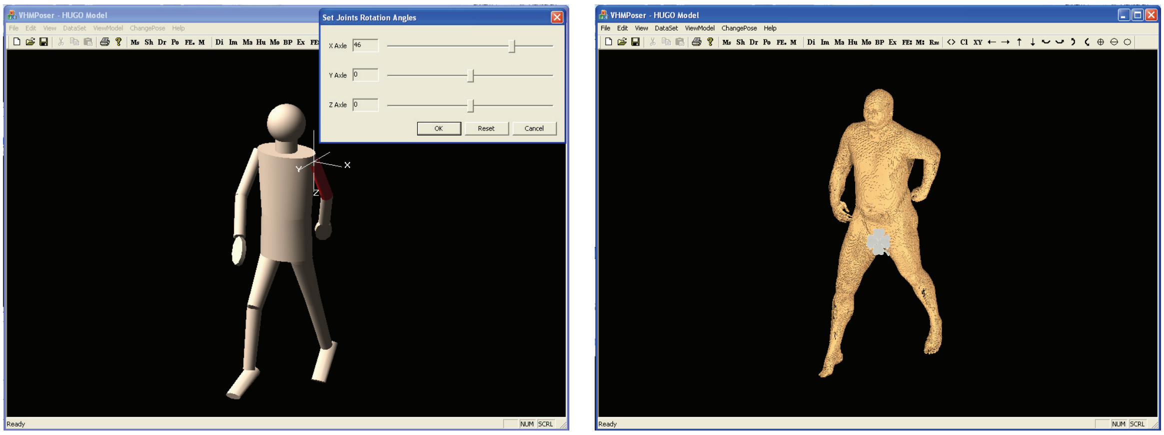

X Axle 46
Y Axle 0
Z Axle 0

(e) Set rotation angles of concerned joints (f) Get deformed human body model with FFD

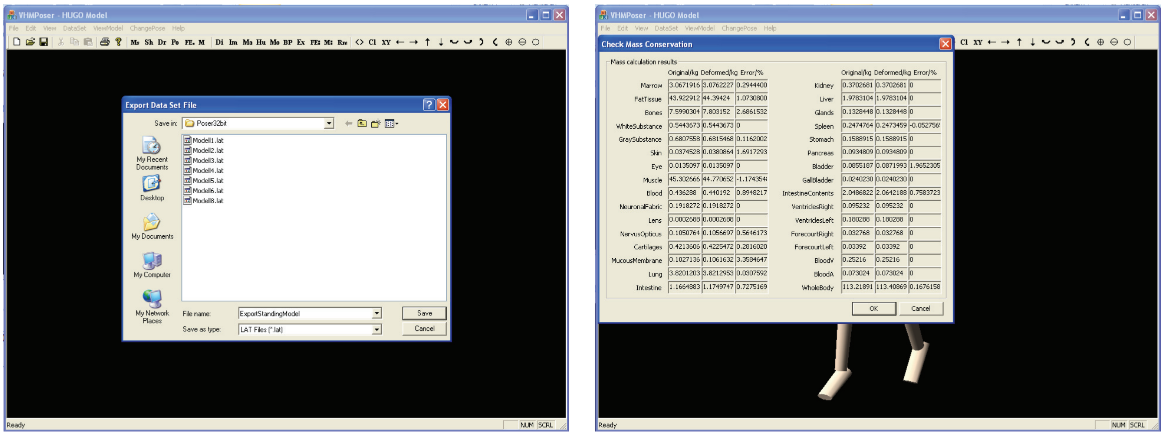

Save in: Poser32bit

Modell1.lat
Modell2.lat
Modell3.lat
Modell4.lat
Modell5.lat
Modell6.lat
Modell8.lat

File name: ExportStandingModel
Save as type: LAT Files (*.lat)

Mass calculation results

	Original/kg	Deformed/kg	Error/%		Original/kg	Deformed/kg	Error/%
Marrow	3.0671916	3.0762227	0.2944400	Kidney	0.3702681	0.3702681	0
FatTissue	43.922912	44.39424	1.0730800	Liver	1.9783104	1.9783104	0
Bones	7.5990304	7.803152	2.6861532	Glands	0.1328448	0.1328448	0
WhiteSubstance	0.5443673	0.5443673	0	Spleen	0.2474764	0.2473459	-0.052756
GraySubstance	0.6807558	0.6815468	0.1162002	Stomach	0.1588915	0.1588915	0
Skin	0.0374528	0.0380864	1.6917293	Pancreas	0.0934809	0.0934809	0
Eye	0.0135097	0.0135097	0	Bladder	0.0855187	0.0871993	1.9652305
Muscle	45.302666	44.770652	-1.174354	GallBladder	0.0240230	0.0240230	0
Blood	0.436288	0.440192	0.8948217	IntestineContents	2.0486822	2.0642188	0.7583723
NeuronalFabric	0.1918272	0.1918272	0	VentriclesRight	0.095232	0.095232	0
Lens	0.0002688	0.0002688	0	VentriclesLeft	0.180288	0.180288	0
NervusOpticus	0.1050764	0.1056697	0.5646173	ForecourtRight	0.032768	0.032768	0
Cartilages	0.4213606	0.4225472	0.2816020	ForecourtLeft	0.03392	0.03392	0
MucousMembrane	0.1027136	0.1061632	3.3584647	BloodV	0.25216	0.25216	0
Lung	3.8201203	3.8212953	0.0307592	BloodA	0.073024	0.073024	0
Intestine	1.1664883	1.1749747	0.7275169	WholeBody	113.21891	113.40869	0.1676158

(g) Export the deformed human body model as a new dataset file (h) Mass calculation and comparison

Fig. 31 Main graphical interfaces of the poser program

4.2.Import and Storage of Original Voxel Dataset

Dataset file of the voxel-based human body model consists of Z pieces of contiguous medical images, while each of these images has X pixels and Y pixels in length and width respectively as Fig. 32 shows.

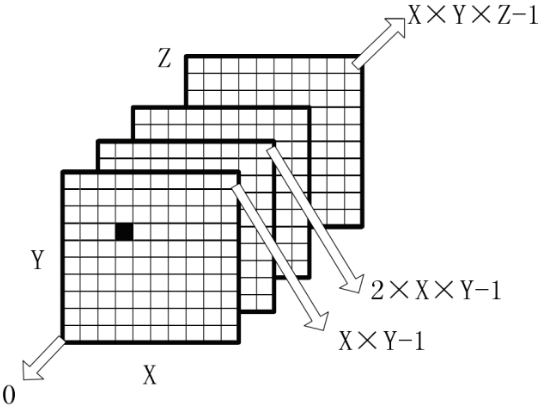

Fig. 32 Structure of dataset file of the voxel-based human body model

Thus, the dimension of the dataset can be defined by using these integer numbers X, Y and Z. In the poser program the whole dataset is imported and stored in a one dimensional array which has X × Y × Z elements and all voxel values are stored in this array one by one. In this array, the first line pixels of the first medical image are stored from element 0 to element X – 1; the second line pixels of the first image are stored from element X to element 2 × X – 1 and so on. All pixels of the first image are stored from element 0 to element X × Y – 1, and all pixels of the second image are stored from element X × Y to element 2 × X × Y – 1 and so on. In this format, the sequence number of all voxels will be between 0 and X × Y × Z - 1 as Fig. 32 shows.

The other storage method available is just to use a three dimensional array to store all voxel data by the same way as which it is stored in Fig. 32. If it's assumed that the *n*th element in the one dimensional array is the same as the element [*i*][*j*][*k*] in the three dimensional array, the value of array indexes *i*, *j*, and *k* can be calculated from the value of *n* based on following three formulas

$$i = [n\%(X \times Y)]\%X, \tag{4-1}$$

$$j = (\mathrm{int})[n\%(X \times Y)] / X, \tag{4-2}$$

$$k = (\mathrm{int})n / (X \times Y). \tag{4-3}$$

The value of *n* can be also calculated from the value of *i*, *j*, and *k* based on following formula

$$n = k \times Y \times X + j \times X + i\ . \tag{4-4}$$

Here (int) means rounding the number to the nearest integer, and % is to calculate the remainder of the number. These two storage methods can be used in different kinds of situations based on different requirements.

Actually in order to perform the FFD calculation and export new dataset files, the poser program needs not only voxel values, but also position coordinates of each voxel and, for some special voxels e.g. arm voxels, body parts information that means which body part this voxel belongs to. Detail information about dividing all voxels of the human body model into different body parts will be explained in following section. In the poser program, one C++ class is defined for the voxel and it includes the voxel's three kinds of necessary information explained above. Each element of the one-dimensional or three-dimensional array mentioned above is the example of this voxel class. The storage format of the one-dimensional array is shown in Fig. 33.

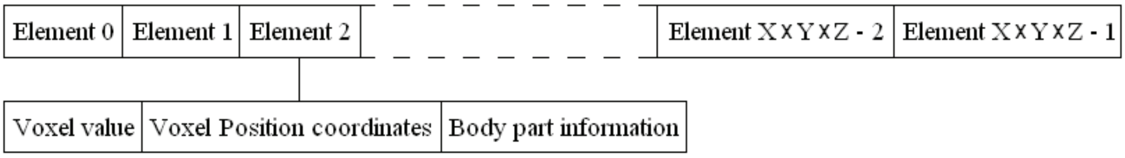

Fig. 33 Storage of the original voxel dataset in a one-dimensional array

4.3. Definition and Operation of FFD Control Lattices

After the original voxel-based human body model is imported and stored in the poser program, it can be rendered directly based on different tissues or organs with the MC algorithm such as the rendered human body models shown in Section 3.2 of Chapter 3. After showing and checking the original voxel model, the next task, which is also the most important function of the poser program, is to deform it to a different posture. The deformation function of the poser program is realized by the FFD technique introduced in Section 3.1 of Chapter 3. In all features of the FFD technique, the one which can influence the last deformation effects and the results of mass conservation of every tissue and organ significantly is how to define and operate the FFD control lattices. The FFD control lattices of the poser program and its operation approach have been checked, tested and modified lots of times until now, and then it can generate a postured human body model with satisfactory deformation effects and very low mass error between the original model and the deformed model. This section mainly discusses how to define and operate FFD control lattices in the poser program.

4.3.1. Location of All Joint Points

In reality a human moves different parts of the body, e.g. arms or legs, based on corresponding joints, i.e. elbows or knees. In order to deform the voxel-based human model in the same manner as that of an actual person, a single joint point is defined at each joint of the original voxel model. Each defined joint point is responsible for the deformation of the body part which is near and around it, and the joint point itself is assumed to be the center of movement of the body part. In the poser program, these joint points work similarly as a ball-and-socket joint to realize a variety of movements of human's joints such as flexion, extension, rotation, abduction, adduction, circumduction, etc. The positions of these joint points were determined by observing, checking and measuring the finest 1 mm resolution HUGO model. Their coordinates were defined as global variables in the poser program, and they can be modified very conveniently if necessary in the future. The coordinates of all joint points defined in the original HUGO model are listed in Table 3 (the origin of the coordinate system is in the middle of the HUGO model below the bladder as Fig. 34 – (a) shows). The detail joint point positions are shown in Fig. 34.

Table 3 Coordinates of all joint points defined in original HUGO model in CST®

Joint point	Coordinates / mm	Joint point	Coordinates / mm
Waist	(4, 2, 198)	Right hip joint	(-78, 18, 60)
Neck	(4, 2, 658)	Rotation center of right patella	(-110, 19, -370)
Right shoulder	(-182, 16, 620)	Right knee joint	(-110, 45, -394)
Right elbow	(-250, 68, 320)	Right ankle joint	(-164, 58, -782)
Right wrist	(-124, -100, 150)	Right foot tiptoe	(-136, -86, -920)
Right fingertip	(25, -100, 70)	Left hip joint	(96, 25, 56)
Left shoulder	(186, 16, 633)	Rotation center of left patella	(120, 50, -350)
Left elbow	(255, 80, 340)	Left knee joint	(130, 45, -394)
Left wrist	(175, -90, 165)	Left ankle joint	(170, 52, -785)
Left fingertip	(30, -120, 40)	Left foot tiptoe	(160, -86, -920)

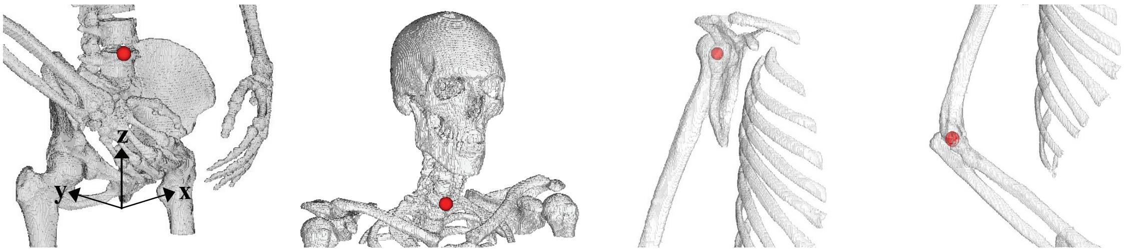

(a) Waist (b) Neck (c) Right shoulder (d) Right elbow

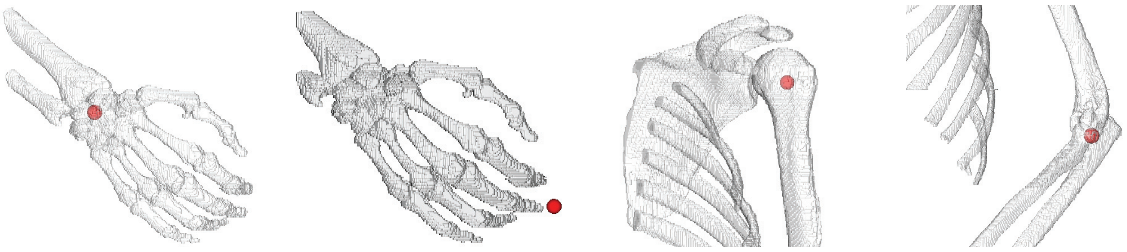

(e) Right wrist (f) Right fingertip (g) Left shoulder (h) Left elbow

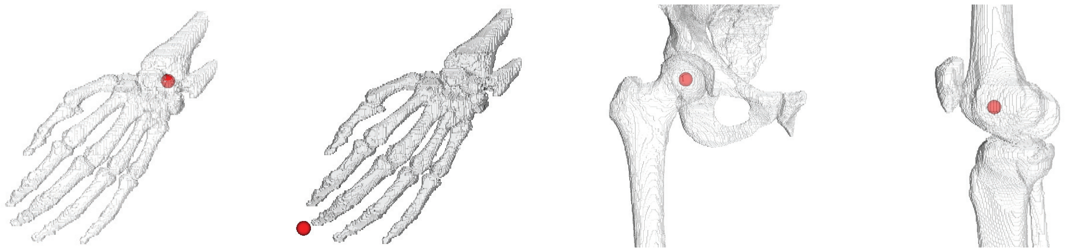

(i) Left wrist (j) Left fingertip (k) Right hip joint (l) Rotation center of right patella

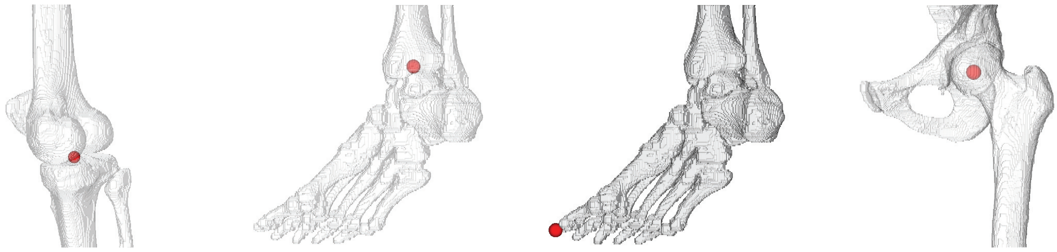

(m) Right knee joint (n) Right ankle joint (o) Right foot tiptoe (p) Left hip joint

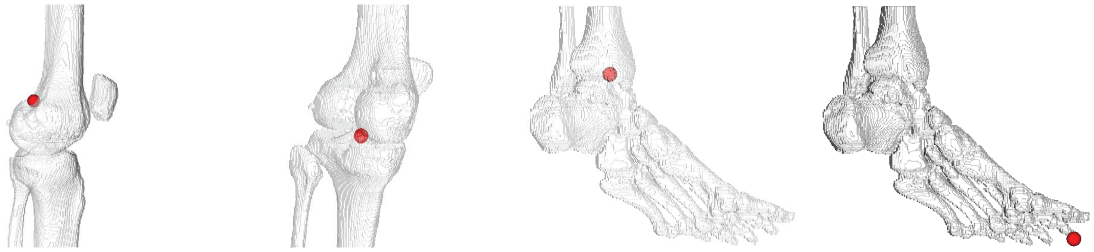

(q) Rotation center of left patella (r) Left knee joint (s) Left ankle joint (t) Left foot tiptoe

Fig. 34 Positions of all joint points defined in the original HUGO model

The simplified human body model in the poser program as Fig. 29 shows was just built by connecting cylinders, spheres and elliptic cylinders together based on the joint points' coordinate information in Table 3. In detail, one arm model can be built by connecting the shoulder joint and the elbow joint with one cylinder, and then using another cylinder to connect the elbow joint and the wrist joint, at last using one elliptic cylinder to connect the wrist joint and the fingertip of the hand; one leg model can be built by connecting the hip joint and the knee joint with one cylinder, and then using another cylinder to connect the knee joint and the ankle joint, at last using one elliptic cylinder to connect the ankle joint and the foot tiptoe of the foot; the trunk model can be built by connecting one hip joint and the waist joint with one elliptic cylinder to symbolize the abdomen, then using another elliptic cylinder to connect the waist joint and the neck joint to symbolize the chest, at last using a small cylinder to symbolize the neck and using a sphere to symbolize the head. Thus the simplified human body model can have similar body dimension and initial posture as the original HUGO model.

4.3.2. Procedure of Defining FFD Control Lattice System

To posture the simplified human body model or the voxel-based human body model, the related body parts should be able to rotate around corresponding joints. The coordinates in Table 3 have defined initial positions of all joint points. Three variables, which indicate rotation angles of the considered joint, were defined for each joint: the rotation angles along x-direction α, y-direction β, and z-direction γ. These rotation angles are parameters that the user of the poser program can adjust directly.

Before starting to deform the voxel-based human body model or just the simplified human body model, there is still one important point which should be considered: the joints of the human body do not move independently, and rotating one joint can maybe influence positions of some other joints. For example, if the human bends his or her waist, the whole trunk will be bent, and the positions of some joints such as neck, shoulder, elbow wrist, etc. will be changed at the same time. Similarly if the hip joint is rotated, the knee joint and the ankle joint will also change their positions. As a result, the whole human body must be divided into three joint groups: trunk, right leg and left leg. The abdomen is the only body part which does not need to be deformed, and the waist and hip joints are basis joints. All other joint points' positions can be calculated from the coordinates of the basis joints by graph transformation.

Here an example is given to explain the steps of defining positions of the knee joint point, ankle joint point, foot tiptoe point of the right leg, and related FFD control lattices based on the coordinates of the right hip joint point, which can be called hip – knee – ankle – foot tiptoe system. The initial position of the origin and coordinate axis' directions of the local coordinate system (LCS) used in following steps are the same as that of the global coordinate system (GCS) as shown in Fig. 34 - (a).

Step 1: Move the LCS from the origin of the GCS to the right hip joint point's position (-78, 18, 60), while the directions of all LCS's coordinate axes do not change. Now the FFD control lattice around the right hip joint can be defined based on the present LCS. The method to define and operate the FFD control lattice will be explained in following sub-section.

Step 2: Because initial coordinates of the right knee joint point in the original HUGO model are (-110, 45, -394), in order to move the LCS from the right hip joint point's position to this position and consider the influence of rotation angles of the right hip joint point α_{hip}, β_{hip} and γ_{hip} which all have zero initial value but can be adjusted by user of the poser program in the future, firstly rotate the LCS along its *x*-axis anticlockwise

$$\alpha_{\text{LCS,hip}} = \arctan(\frac{|45-18|}{|-394-60|}) + \alpha_{\text{hip}} = \arctan(\frac{27}{454}) + \alpha_{\text{hip}} \text{ (rad).} \tag{4-5}$$

Then rotate the LCS along its *y*-axis anticlockwise

$$\begin{aligned}\beta_{\text{LCS,hip}} &= \arctan(\frac{|-110-(-78)|}{\sqrt{(45-18)^2+(-394-60)^2}}) + \beta_{\text{hip}} \\ &= \arctan(\frac{32}{\sqrt{206845}}) + \beta_{\text{hip}} \text{ (rad).}\end{aligned} \tag{4-6}$$

At last, rotate the LCS along its *z*-axis γ_{hip} rad and translate it along its *z*-axis

$$z_{\text{LCS,hip}} = -\sqrt{(-110+78)^2+(45-18)^2+(-394-60)^2} = -\sqrt{267869} \text{ (mm).} \tag{4-7}$$

The minus sign used here is because the knee joint is below the hip joint and the direction of *z*-axis of the LCS is from foot to head. Now the LCS has been moved to the right knee joint point's position, and if the rotation angles of the right hip joint point are adjusted, the LCS can also be moved to its correct positions in accordance.

Step 3: Rotate the LCS along its *y*-axis anticlockwise $-\beta_{\text{LCS,hip}}$ rad, and then along its *x*-axis anticlockwise $-\alpha_{\text{LCS,hip}}$ rad respectively to recover directions of its coordinate axes. Now the FFD control lattice around the right knee joint point can be defined based on the present LCS.

Step 4: Move the LCS from the right knee joint point's position to the right ankle joint point's position (-164, 58, -782). Similarly the influence of rotation angles of the right knee joint point α_{knee}, β_{knee} and γ_{knee} should be considered. Firstly rotate the LCS along its *x*-axis anticlockwise

$$\alpha_{\text{LCS,knee}} = \arctan(\frac{|58-45|}{|-782-(-394)|}) + \alpha_{\text{knee}} = \arctan(\frac{13}{388}) + \alpha_{\text{knee}} \text{ (rad).} \tag{4-8}$$

And then rotate the LCS along its *y*-axis anticlockwise

$$\begin{aligned}\beta_{\text{LCS,knee}} &= \arctan(\frac{|-164-(-110)|}{\sqrt{(58-45)^2+(-782+394)^2}}) + \beta_{\text{knee}} \\ &= \arctan(\frac{54}{\sqrt{150713}}) + \beta_{\text{knee}} \text{ (rad).}\end{aligned} \tag{4-9}$$

At last rotate the LCS along its *z*-axis γ_{knee} rad and then translate it along its *z*-axis

$$z_{\text{LCS,knee}} = -\sqrt{(-164+110)^2+(58-45)^2+(-782+394)^2} = -\sqrt{153629} \text{ (mm).} \tag{4-10}$$

Now the LCS has been moved to the right ankle joint point's position, and if the rotation angles of the right knee joint point are adjusted, the LCS can also be moved to its correct positions in accordance.

Step 5: Rotate the LCS along its y-axis anticlockwise $-\beta_{\mathrm{LCS,knee}}$ rad, and then along its x-axis anticlockwise $-\alpha_{\mathrm{LCS,knee}}$ rad respectively to recover directions of its coordinate axes. Now the FFD control lattice around the right ankle joint point can be defined based on the present LCS.

Step 6: The last step is to move the LCS from the right ankle joint point's position to the right foot tiptoe point's position (-136, -86, -920) and consider the influence of rotation angles of the right ankle joint point α_{ankle}, β_{ankle} and γ_{ankle}. Firstly rotate the LCS along its x-axis clockwise

$$\alpha_{\mathrm{LCS,ankle}} = \arctan(\frac{|-86-58|}{|-920-(-782)|}) + \alpha_{\mathrm{ankle}} = \arctan(\frac{144}{138}) + \alpha_{\mathrm{ankle}} \text{ (rad).} \tag{4-11}$$

And then rotate the LCS along its y-axis clockwise

$$\begin{aligned} \beta_{\mathrm{LCS,ankle}} &= \arctan(\frac{|-136-(-164)|}{\sqrt{(-86-58)^2+(-920+782)^2}}) + \beta_{\mathrm{ankle}} \\ &= \arctan(\frac{28}{\sqrt{39780}}) + \beta_{\mathrm{ankle}} \text{ (rad).} \end{aligned} \tag{4-12}$$

At last rotate the LCS along its z-axis γ_{ankle} rad and then translate it along its z-axis

$$z_{\mathrm{LCS,ankle}} = -\sqrt{(-136+164)^2+(-86-58)^2+(-920+782)^2} = -\sqrt{40564} \text{ (mm).} \tag{4-13}$$

Now the LCS has been moved to the right foot tiptoe point's position, and if rotation angles of the right ankle joint point are adjusted, the LCS can also be moved to its correct positions in accordance. The foot tiptoe point is only used to define dimension of the foot in the simplified human body model, in this section of the program, there is no FFD control lattice around it. The FFD control lattice around the foot was defined together with the FFD control lattice around the ankle joint point.

Until now, the LCS has passed all joint points of the right leg and all FFD control lattices around the right leg have been also defined during this process. While the user of the poser program adjusts rotation angles of the right hip joint point, the FFD control lattice around the right hip joint will be deformed based on some rules, which will be explained in next sub-section, to deform the body part of the original HUGO model around the right hip joint. At the same time, the right knee joint point, right ankle joint point and right food tiptoe point will be rotated in accordance based on rotation angles of the right hip joint point, the FFD control lattices around them will be also rotated as a whole but not deformed. As a result, the whole right leg will be rotated as a whole indicating the real movement of an actual person. After the FFD calculation is finished, a deformed human body model is obtained with a rotated right leg and smoothly deformed right hip.

Similarly, if the user of the poser program only adjusts rotation angles of the right knee joint point, the FFD control lattice defined around the right knee joint will be moved to deform the body part around the right knee joint. At the same time, the right ankle joint point and the right foot tiptoe point will be rotated in accordance and the FFD control lattices around them will be rotated as a whole but not deformed. After the FFD calculation is finished, user can get a deformed human body model with a bent right shank, rotated but undeformed right ankle and foot, and smoothly deformed right knee.

The method used above can be applied to the left leg model directly without any modification, so will not be repeated here. The rotation angles along *x*- and *y*-axis and the translation distances along *z*-axis of the LCS, while it is moved from one joint point to the next one, are listed in Table 4.

Table 4 Rotation angles and translation distance of the LCS (left leg model)

From	To	Rotation (*x*-axis) / rad	Rotation (*y*-axis) / rad	Translation (*z*-axis)
Left hip	Left knee	$\arctan(\frac{20}{450})+\alpha_{\text{hip}}$	$\arctan(\frac{34}{\sqrt{202900}})+\beta_{\text{hip}}$ *	$-\sqrt{204056}$ mm
Left knee	Left ankle	$\arctan(\frac{7}{391})+\alpha_{\text{knee}}$	$\arctan(\frac{40}{\sqrt{152930}})+\beta_{\text{knee}}$ *	$-\sqrt{154530}$ mm
Left ankle	Left tiptoe	$\arctan(\frac{138}{135})+\alpha_{\text{ankle}}$ *	$\arctan(\frac{10}{\sqrt{37269}})+\beta_{\text{ankle}}$	$-\sqrt{37369}$ mm

* This symbol means clockwise direction. If there is no this symbol, the rotation direction is anticlockwise.

Because of similar internal structure configuration, this method can be also applied to the arm models: shoulder – elbow – wrist – fingertip system directly, and the related rotation angles and translation distances of the LCS are listed in Table 5 and Table 6.

Table 5 Rotation angles and translation distance of the LCS (right arm model)

From	To	Rotation (*x*-axis) / rad	Rotation (*y*-axis) / rad	Translation (*z*-axis)
Right shoulder	Right elbow	$\arctan(\frac{52}{300})+\alpha_{\text{shoulder}}$	$\arctan(\frac{68}{\sqrt{92704}})+\beta_{\text{shoulder}}$	$-\sqrt{97328}$ mm
Right elbow	Right wrist	$\arctan(\frac{168}{170})+\alpha_{\text{elbow}}$ *	$\arctan(\frac{126}{\sqrt{57124}})+\beta_{\text{elbow}}$ *	$-\sqrt{73000}$ mm
Right wrist	Right fingertip	$\frac{\pi}{2}+\alpha_{\text{wrist}}$ *	$\arctan(\frac{149}{80})+\beta_{\text{wrist}}$ *	$-\sqrt{28601}$ mm

Table 6 Rotation angles and translation distance of the LCS (left arm model)

From	To	Rotation (*x*-axis) / rad	Rotation (*y*-axis) / rad	Translation (*z*-axis)
Left shoulder	Left elbow	$\arctan(\frac{64}{293})+\alpha_{\text{shoulder}}$	$\arctan(\frac{69}{\sqrt{89945}})+\beta_{\text{shoulder}}$ *	$-\sqrt{94706}$ mm
Left elbow	Left wrist	$\arctan(\frac{170}{175})+\alpha_{\text{elbow}}$ *	$\arctan(\frac{80}{\sqrt{59525}})+\beta_{\text{elbow}}$	$-\sqrt{65925}$ mm
Left wrist	Left fingertip	$\arctan(\frac{30}{125})+\alpha_{\text{wrist}}$ *	$\arctan(\frac{145}{\sqrt{16525}})+\beta_{\text{wrist}}$	$-\sqrt{37550}$ mm

Now, the positions of all joint points and related FFD control lattices of four limbs have already been defined. It should be still noticed that positions of all joint points of the arm models are influenced by rotation angles of the waist joint point. So the last step is to define positions of the shoulder joint point, neck joint point and related FFD control lattices based on position of the waist joint point, which can be called waist – neck – right shoulder / left shoulder system.

The method used for this trunk model is also similar to the method used for the right leg model. However, there are three differences which should be pointed out here clearly. Firstly, because the coordinates of the waist joint point and the neck joint point are (4, 2, 198) and (4, 2, 658) respectively with the same x and y coordinate, the LCS can be translated from the waist joint point to the neck joint point simply by translation transformation along z-axis, the rotation transformation is not necessary anymore. Apart from that, because the neck joint is above the waist joint, the translation distance should be positive, which is different from other joint points. Secondly, because rotating the neck joint does not influence the position of the shoulder joint point, while the LCS is moved from the neck joint point to the right / left shoulder joint point, rotation angles of the neck joint point cannot be added. Thirdly, because of the special relative positions between the neck joint point and the right / left shoulder joint point, while the LCS is moved from the neck joint point to the shoulder joint point, the rotation axes are changed to y- and z-axis, and the translation axis is switched to x-axis. Apart from that, because the initial direction of the x-axis of the LCS is from right side to the left side, and left shoulder joint is located in the left side of the neck joint, the translation distance from the neck joint point to the left shoulder joint point is also positive. Finally, the rotation angles, rotation axes, translation distances and translation axes of the LCS used for this trunk model are listed in Table 7.

Table 7 Rotation angles and translation distance of the LCS (trunk model)

From	To	Rotation / rad	Rotation / rad	Translation
Waist	Neck	α_{waist} / x-axis	β_{waist} / y-axis	460 mm / z-axis
Neck	Right shoulder	$\arctan(\frac{38}{186})$ * / y-axis	$\arctan(\frac{14}{\sqrt{36040}})$ * / z-axis	$-\sqrt{36236}$ mm / x-axis
Neck	Left shoulder	$\arctan(\frac{25}{182})$ / y-axis	$\arctan(\frac{14}{\sqrt{33749}})$ / z-axis	$\sqrt{33945}$ mm / x-axis

By now, the whole procedure used to define a consistent FFD control lattice system, which can be deformed in the same manner as an actual person, for the whole voxel-based human body model has been finished.

4.3.3. Defining and Operating FFD Control Lattices

The section above has explained when to define the FFD control lattices for different body parts around specific joints. The approach about how to define and operate them will be introduced and discussed in this section. First of all, as discussed above, the whole original HUGO model should be segmented into several body parts on the basis of the joint points as Fig. 35 shows.

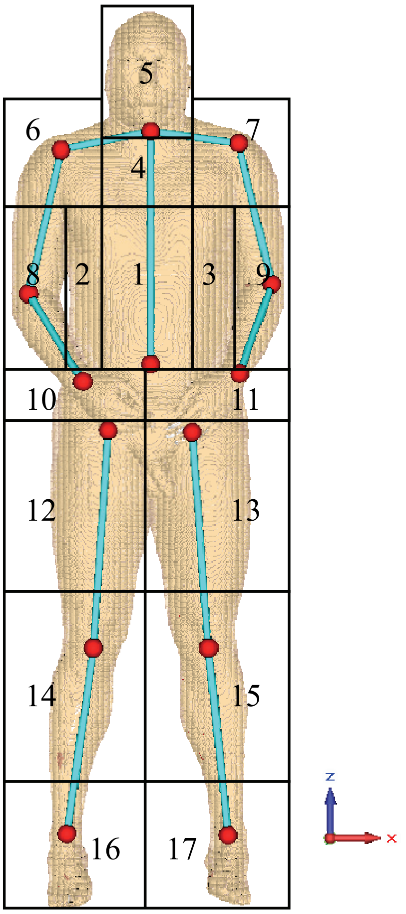

Fig. 35 Segmentation of the original HUGO model on the basis of the joint points

For convenience of comprehension, Fig. 35 also shows the initial positions of all studied joint points in the whole original HUGO model, which was segmented into 17 body parts. Each body part includes one specific joint point, and all voxels in this body part will move or rotate based on this joint point during the FFD calculation. In order to build a consistent FFD control lattice system, the trunk was divided into 4 body parts. Body parts 2, 3 and 4 will all deform based on the waist joint which is located at bottom of body part 1. Apart from that, because the arms of the original HUGO model both touch the trunk, the right side of body part 8 overlaps with the left side of body part 2 to some extent. Similar situation also happens between body part 10 and 12, body part 3 and 9, and body part 11 and 13. The algorithm used to separate the arms away from the trunk will be explained in the next section. In Fig. 35, body parts 8, 9, 10 and 11 are responsible for arm and hand models, body parts 1, 2, 3 and 4 are for trunk model, and body parts 12 and 13 are for abdomen and thigh models.

Based on different operation rules of the FFD control lattices, all joint points of the whole human body model can be divided into four types: waist and neck joint; knee, ankle, elbow and wrist joint; left and right hip joint; left and right shoulder joint. The strategies of defining and operating FFD control lattices around different types of joint points are a little different from each other.

FFD Control Lattice around the Waist Joint

The first kind of joint point includes the waist joint and the neck joint, which together are responsible for the deformation of body parts 1, 2, 3, 4, and 5 in Fig. 35. The FFD control lattices around the waist joint control the first four body parts, while the FFD control lattice around the neck joint only controls the body part 5. Here an example is given to explain the detail procedure of using the FFD technique to deform the body parts 1 and 4 of the HUGO model based on rotation angles of the waist joint point α_{waist} which can be adjusted by user of the poser program. The deformation of the body parts 2 and 3 was realized in an identical manner to the body part 1, and deformation of the body part 5 can be realized in a similar way around the neck joint point.

Step 1: After the LCS used in the last section was moved from the origin of the GCS to the waist joint point's position, firstly the voxel index ranges of the body part 1 and 4 along *x*-, *y*- and *z*-direction must be determined. The whole HUGO model has totally (594 / *resolution*) × (341 / *resolution*) × (1873 / *resolution*) voxels in the three space directions. The voxel index ranges of the body part 1 are $x \in [200, 400] / resolution$, $y \in [0, 341] / resolution$ and $z \in [420, 740] / resolution$, which were determined by observing detail internal body structure of the finest 1 mm resolution HUGO model around the waist joint. The body part 4 has the same index ranges along *x*- and *y*- direction, and the index range along the *z*-direction is $z \in [280, 420] / resolution$. The separated body part 1 and 4 are shown in Fig. 36 – (a) with 4 mm resolution.

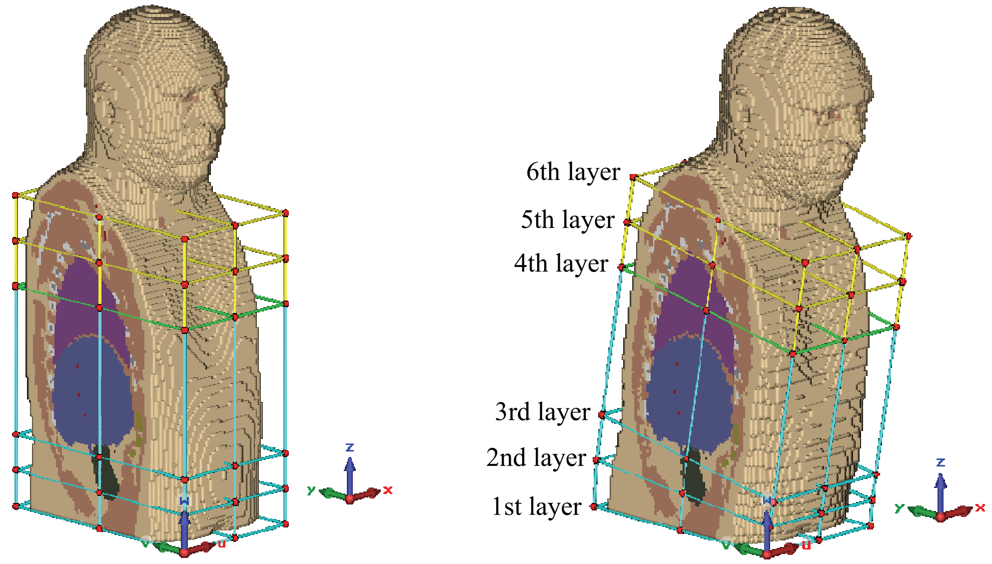

(a) Initial body part 1, 4 and FFD control lattices (b) Deformed body part 1, 4 and FFD control lattices

Fig. 36 Using the FFD technique to deform trunk of the HUGO model

Step 2: Define initial positions of all FFD control points as Fig. 36 – (a) shows. For body parts 1 and 4, there are in total 6 layers of FFD control points defined as Fig. 36 – (b) shows, and all of them will compose two sets FFD control lattices, which look like two cuboids and surround the whole body part 1 and 4 respectively. In Fig. 36, the blue FFD control lattice, which includes 4 layers × 3 × 3 = 36 control points, is defined for the body part 1, while the yellow FFD control lattice, which includes 3 layers × 3 × 3 = 27 control points, is used for the body part 4. The green interface layer is shared by these two set control lattices.

The approach of defining and distributing the FFD control points for different body parts must consider the internal body structure and related deformation rules of the concerned body parts. Here the deformation rules used for the body part 1 and 4 are as follows: while the human bends his or her waist, the body part between the 1st layer and the 3rd layer control points will be deformed flexibly; at the same time, the body part above the 3rd layer control points will be rotated as a whole based on rotation angles of the waist joint point. The concrete positions of different layers along *z*-direction were determined by internal body structure of the trunk.

Step 3: Build local coordinate system of the FFD technique $\mathrm{LCS}_{\mathrm{FFD}}$, and transform the global position coordinates of all voxels in the body part 1 and 4 into their local coordinates in $\mathrm{LCS}_{\mathrm{FFD}}$. At the same time, the global position coordinates of all FFD control points defined in Step 2 should be also transformed into their local coordinates in $\mathrm{LCS}_{\mathrm{FFD}}$. It should be paid attention that this local coordinate system $\mathrm{LCS}_{\mathrm{FFD}}$ used for FFD calculation is not the same as the LCS used above. Apart from that, it is defined based on different body parts, and it must be redefined while deforming the other body parts.

For calculation convenience, the origin of the $\mathrm{LCS}_{\mathrm{FFD}}$ (u_0, v_0, w_0) can be located at the position of the FFD control point which has the minimum *x*, *y* and *z* global coordinates, and the directions of coordinate axles are the same as those of the GCS. The local coordinate system *u*-*v*-*w* shown in Fig. 36 – (a) is just the $\mathrm{LCS}_{\mathrm{FFD}}$ used for the body parts 1 and 4. Besides, the FFD technique also requires that all local coordinates of the deformed objects be normalized into the range [0, 1], which can be realized by dividing the local coordinates by the full length of the FFD control lattices along *u*-, *v*- and *w*-directions: l_u, l_v, and l_w. Finally, the coordinate transformation from the GCS to the $\mathrm{LCS}_{\mathrm{FFD}}$ can be expressed by

$$u=(x-x_0)/l_\mathrm{u},\ v=(y-y_0)/l_\mathrm{v},\ w=(z-z_0)/l_\mathrm{w}. \tag{4-14}$$

Here (u, v, w) are normalized local coordinates of the voxels or the FFD control points of the body part 1 and 4, and (x, y, z) are their original global coordinates.

Step 4: Set rotation angles of the waist joint point to deform the FFD control lattices, and then perform the FFD calculation to deform the body parts 1 and 4. Rotation angles of the joint points can be adjusted by the user of the poser program directly, and the program will deform the FFD control lattices based on these values. Fig. 36 – (b) shows the deformed FFD control lattices of the body parts 1 and 4 after the trunk is bent 10° degree forward, which means $\alpha_{\mathrm{waist}} = 10°$, around *u*-axis of the LCS located at the waist joint point's position. Detail deformation rules are as follows: because the waist joint point is located on the same plane as the 1st layer control points, all control points of the 1st layer do not move at all; the 2nd layer control points rotate around the waist joint point $\alpha_{\mathrm{waist}} / 2 = 5°$; and the 3rd, 4th, 5th, and 6th layer control points rotate around the waist joint point

$\alpha_{\text{waist}} = 10°$. According to these rules, the body part between the 1st layer and the 3rd layer control points will be deformed smoothly, and the body part above the 3rd layer control points will be rotated as a whole.

After the FFD control lattices are deformed, the FFD calculation can be performed based on equation (3-10) to deform the body parts 1 and 4. The final deformation effect of the body parts 1 and 4 with a bent waist is shown in Fig. 36 – (b).

Step 5: Transform local coordinates of all voxels of the deformed body part 1 and 4 in the LCS_{FFD} back to their new global coordinates in the GCS, and then get the final deformed whole body human model with a bent waist. The formulas of the coordinate transformation from the LCS_{FFD} to the GCS are given by

$$x' = x_0 + l_u \times u',\ y' = y_0 + l_v \times v',\ z' = z_0 + l_w \times w'. \tag{4-15}$$

Here (u', v', w') are local coordinates of the voxels in the deformed body part 1 and 4, and (x', y', z') are their global coordinates in the GCS.

FFD Control Lattice around the Knee Joint

The second kind of joint point includes four members: knee, ankle, elbow and wrist. Anatomically, they are all used to connect two rod-like bones and therefore are moved in similar ways. Here an example is give to explain how to use the FFD technique to bend the right knee joint.

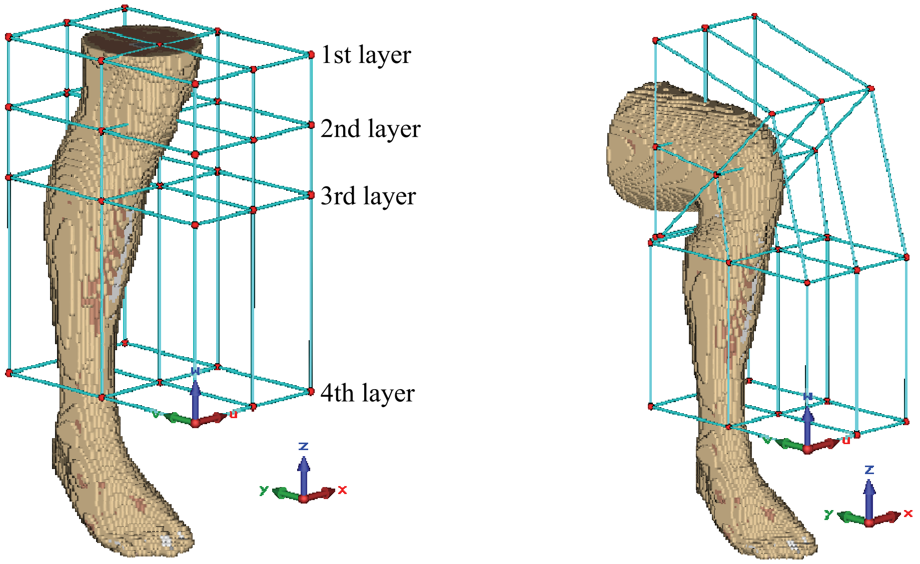

(a) Initial body part 14 and FFD control lattice (b) Deformed body part 14 and FFD control lattice

Fig. 37 Using the FFD technique to deform right knee of the HUGO model

The general calculation procedure for deforming the right knee and right shank model is the same as that used for the trunk model, and will not be repeated here anymore. The main difference lies in the definition and operation rules of the FFD control lattices. The FFD control lattice around the right knee joint point is composed of 4 layers × 3 × 3 = 36 control points as Fig. 37 – (a) shows. During the FFD calculation, the body part between the 1st layer and the 3rd layer control points will be deformed flexibly, and the body part between the 3rd layer and the 4th layer control points will be rotated as a whole based on rotation angles of the right knee joint point.

Fig. 37 – (b) shows the deformed FFD control lattice of the body part 14 after the right knee is bent 90° degree, which means $\alpha_{\text{knee}} = 90°$, around the u-axis of the LCS located at right knee joint point's position. Detail deformation rules are as follows: the 1st layer control points are kept to be perpendicular to the thigh; the 2nd layer control points rotate around right knee joint point $\alpha_{\text{knee}} / 2 = 45°$; the 3rd layer control points are kept perpendicular to the shank; the 4th layer control points rotate around the right knee joint point $\alpha_{\text{knee}} = 90°$. The final deformation effect of the body part 14 with a bent right knee is shown in Fig. 37 – (b).

Here, there is a small problem that should be discussed now. In real life, people can only bend his or her knee joint backwards. Bending right or left knee joint forwards, although possible in the FFD technique, is impossible for normal situations. Similar limitations on the rotation angles also appear in several other joints. In order to prevent the user of the poser program from generating some unreasonable postured human models, rotation angles of all studied joint points can be only adjusted in an appropriate range, not the full range [-180°, 180°]. Apart from that, the user of the poser program should check the postured simplified human model before starting to deform the HUGO model to ensure that the deformed human model has a reasonable new posture.

FFD Control Lattice around the Hip Joint

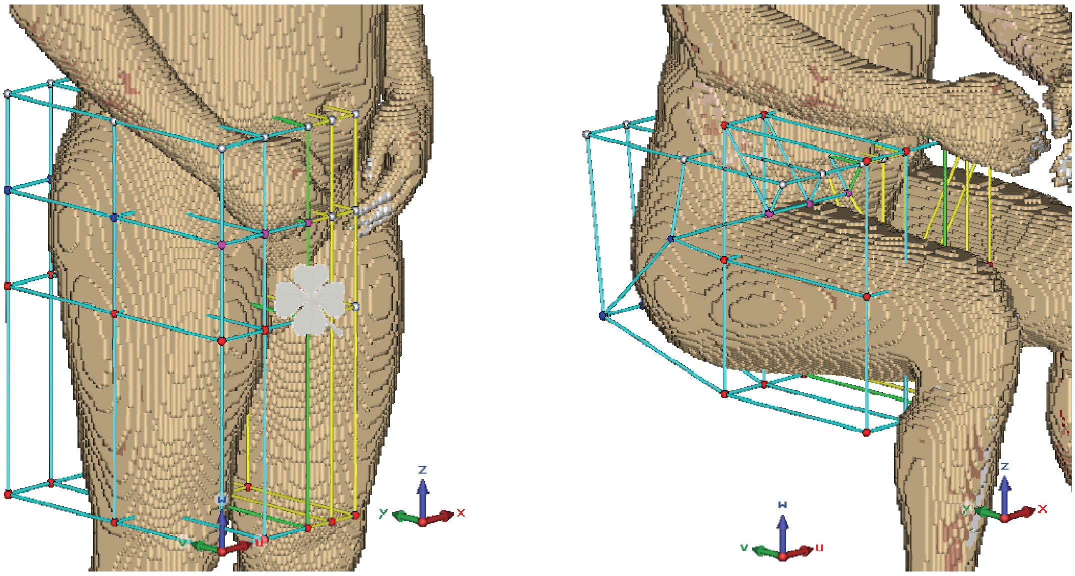

(a) Initial body part 12 and FFD control lattice (b) Deformed body part 12 and FFD control lattice

Fig. 38 Using the FFD technique to deform right hip joint of the HUGO model

The third kind of joint point is the hip joint, which connects pelvis and femur together. The initial body part 12, which includes right half part of the abdomen and right thigh, and the defined FFD control lattice around the right hip joint are shown in Fig. 38 – (a).

Because the operation rules of the hip joint are a little complicated, the FFD control lattice is also shown separately in Fig. 39.

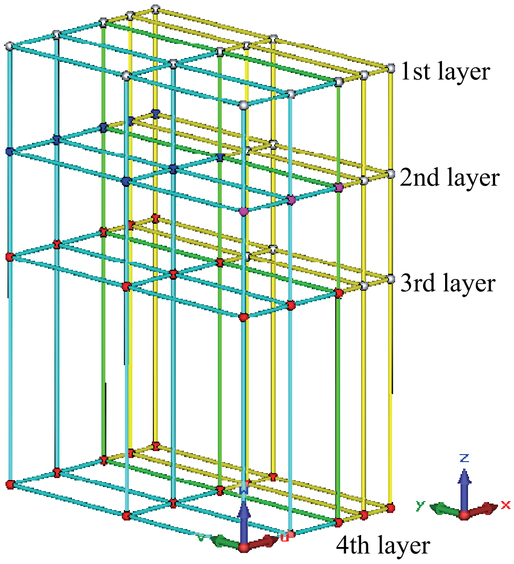

Fig. 39 FFD control lattice of right hip joint

While a human rotates his or her hip joint, the whole leg will be rotated in accordance, but the pelvis and all tissues in it do not move or deform. Because of this special anatomical structure, the FFD control lattice defined around the right hip joint includes two sets. The first set with blue color, which includes 4 layers × 3 ×3 = 36 FFD control points, is used for the right thigh model, and the yellow one, which also includes 4 layers × 3 ×3 = 36 FFD control points, is mainly designed for the undeformed tissues in the pelvis. The green interface layer is shared by these two set control lattices.

In order to explain the operation rules of these two sets of FFD control lattices more clearly, all FFD control points in Fig. 39 are rendered with four different colors. It should be noted that the right hip joint is approximately located in the center of the 2^{nd} layer control points. Fig. 38 – (b) shows the deformed FFD control lattices of the body part 12 after the right hip joint is bent 90° degree, which means $\alpha_{\text{hip}} = 90°$, around the *u*-axis of the LCS located at right hip joint point's position. Detail deformation rules are as follows: all grey FFD control points are fixed points, and they do not move while rotation angles of the right hip joint are adjusted. As a result, all voxels near these grey control points do not move either, and then the pelvis and all tissues in it will not be deformed. Three purple control points in the 2^{nd} layer rotate around the right hip joint point $\alpha_{\text{hip}} / 3 = 30°$, all blue control points rotate $\alpha_{\text{hip}} / 2 = 45°$, and all red control points rotate $\alpha_{\text{hip}} = 90°$. According to these rules, except the pelvis and all tissues in it, the body part between the 1^{st} layer and the 3^{rd} layer control points will be deformed smoothly, and the body part below the 3^{rd} layer control points will be rotated as a whole. The final deformation effect of the body part 12 with a bent hip joint is shown in Fig. 38 – (b).

FFD Control Lattice around the Shoulder

The fourth kind of joint point is the shoulder joint, which connects chest and upper arm together. The initial body part 6, which includes a little part of the chest, right shoulder and right upper arm, and the defined FFD control lattices around the right shoulder joint are shown in Fig. 40 – (a).

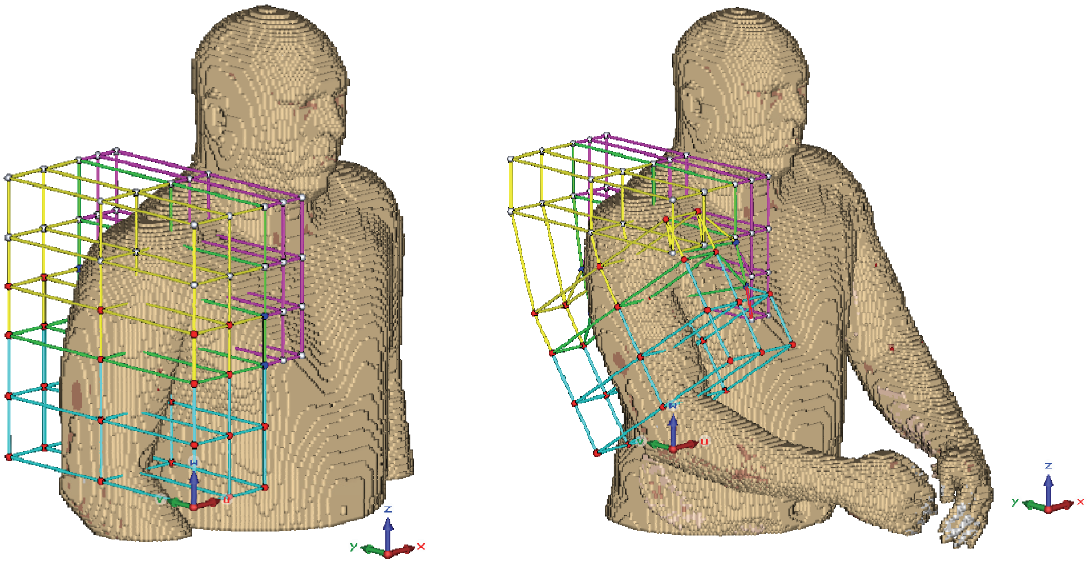

(a) Initial body part 6 and FFD control lattice (b) Deformed body part 6 and FFD control lattice

Fig. 40 Using the FFD technique to deform right shoulder of the HUGO model

The FFD control lattices are also shown separately in Fig. 41.

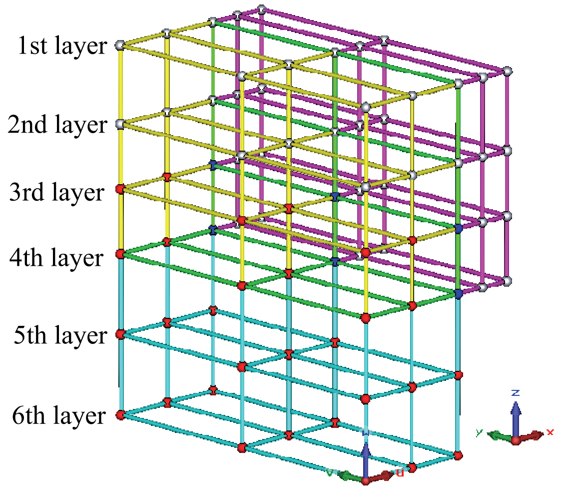

Fig. 41 FFD control lattice of right shoulder joint

While human rotates the shoulder joint, the whole arm will be rotated in accordance, the connection area between the shoulder and the chest is deformed smoothly, and the chest itself and top part of the shoulder do not deform. In order to realize this special anatomical structure, the FFD control lattices defined around the right shoulder joint include three sets. The first set with blue color, which includes 3 layers × 3 ×3 = 27 FFD control points, is used to rotate the right upper arm; the yellow one, which includes 4 layers × 3 ×3 = 36

FFD control points, is used to deform the right shoulder; and the purple one, which also includes 4 layers × 3 ×3 = 36 FFD control points, is mainly designed for the undeformed chest. The two green interface layers are shared by these three sets control lattices.

All FFD control points in Fig. 41 are rendered with three different colors. It should be also noted that the right shoulder joint is approximately located in the center of the 2nd layer control points. Fig. 40 – (b) shows the deformed FFD control lattices of the body part 6 after the right shoulder joint is bent 30° degree, which means $\alpha_{\text{shoulder}} = 30°$, around u-axis of the LCS located at right shoulder joint point's position. Detail deformation rules are as follows: all grey FFD control points are fixed points, and they do not move while rotation angles of the right shoulder joint are adjusted. As a result, the chest and top part of the right shoulder will not be deformed. The six blue control points in the 3rd and 4th layers rotate around the right shoulder joint point $\alpha_{\text{shoulder}} / 2 = 15°$, and all red control points rotate $\alpha_{\text{shoulder}} = 30°$. According to these rules, except the undeformed parts, the body part between the 2nd layer and the 4th layer control points, including the connection area between the right shoulder and the chest, will be deformed smoothly. And the body part below the 4th layer control points will be rotated as a whole. The final deformation effect of the body part 6 with a rotated shoulder joint is shown in Fig. 40 – (b).

4.3.4. Graph Transformation Realized by Matrix Manipulation

Until now, the calculation procedure of using the FFD technique to deform the voxel-based human body model has been introduced completely. It can be seen that during the whole calculation, there are lots of translation and rotation transformations that should be performed. Firstly they are used to move the LCS from one joint point to the next one, secondly they are also needed to define and operate FFD control lattices based on positions and rotation angles of specific joint points. In order to realize these two graph transformations in a unified way, the so called three-dimensional coordinate transformation matrix, which is often used in computer graphics domain, was used in the poser program. With the help of this matrix, all graph transformations including translation, rotation, scale, mirror, shear, etc. can be realized conveniently by matrix multiplication. This matrix can be expressed by

$$T_{3D} = \begin{pmatrix} a & b & c & p \\ d & e & f & q \\ g & h & i & r \\ l & m & n & s \end{pmatrix}. \tag{4-16}$$

Here, the matrix elements a, b, c, d, e, f, g, h and i can be used for the rotation transformation, elements p, q and r are used for the translation transformation, and the remaining four elements l, m, n and s are set to be 0, 0, 0 and 1 respectively during all calculations.

If the original coordinates of one object point are $P\ (x, y, z)$, and after transformation they are changed to be $P'\ (x', y', z')$, this transformation process can be expressed mathematically by the following formula

$$P' = \begin{pmatrix} x' & y' & z' & 1 \end{pmatrix} = T_{3D} \cdot P = \begin{pmatrix} a & b & c & p \\ d & e & f & q \\ g & h & i & r \\ 0 & 0 & 0 & 1 \end{pmatrix} \cdot \begin{pmatrix} x \\ y \\ z \\ 1 \end{pmatrix}. \tag{4-17}$$

Translating the point P (x, y, z) to another position P' (x', y', z') can be calculated by

$$\begin{aligned} x' &= x + t_x, \\ y' &= y + t_y, \\ z' &= z + t_z. \end{aligned} \tag{4-18}$$

Here t_x, t_y and t_z are translation distances along x-, y- and z-directions. With the matrix T_{3D}, these three formulas can be integrated into one matrix formula:

$$P' = \begin{pmatrix} x' & y' & z' & 1 \end{pmatrix} = T_{3D} \cdot P = T(t_x, t_y, t_z) \cdot P = \begin{pmatrix} 1 & 0 & 0 & t_x \\ 0 & 1 & 0 & t_y \\ 0 & 0 & 1 & t_z \\ 0 & 0 & 0 & 1 \end{pmatrix} \cdot \begin{pmatrix} x \\ y \\ z \\ 1 \end{pmatrix}. \tag{4-19}$$

The new position of the original point P (x, y, z) after rotating it $\theta°$ degree anticlockwise along z-axis can be calculated by

$$\begin{aligned} x' &= x\cos(\theta) - y\sin(\theta), \\ y' &= x\sin(\theta) + y\cos(\theta), \\ z' &= z. \end{aligned} \tag{4-20}$$

With the matrix T_{3D}, this process can be expressed by

$$P' = \begin{pmatrix} x' & y' & z' & 1 \end{pmatrix} = T_{3D} \cdot P = R_z(\theta) \cdot P = \begin{pmatrix} \cos(\theta) & -\sin(\theta) & 0 & 0 \\ \sin(\theta) & \cos(\theta) & 0 & 0 \\ 0 & 0 & 1 & 0 \\ 0 & 0 & 0 & 1 \end{pmatrix} \cdot \begin{pmatrix} x \\ y \\ z \\ 1 \end{pmatrix}. \tag{4-21}$$

Similarly, the rotation transformation matrix around x- and y-axis can be calculated as

$$\begin{aligned} R_x(\theta) &= \begin{pmatrix} 1 & 0 & 0 & 0 \\ 0 & \cos(\theta) & -\sin(\theta) & 0 \\ 0 & \sin(\theta) & \cos(\theta) & 0 \\ 0 & 0 & 0 & 1 \end{pmatrix}, \text{ and} \\ R_y(\theta) &= \begin{pmatrix} \cos(\theta) & 0 & \sin(\theta) & 0 \\ 0 & 1 & 0 & 0 \\ -\sin(\theta) & 0 & \cos(\theta) & 0 \\ 0 & 0 & 0 & 1 \end{pmatrix}. \end{aligned} \tag{4-22}$$

If the original point P (x, y, z) is firstly rotated 30° degree anticlockwise around the x-axis, secondly rotated 45° degree clockwise around the y-axis, at last translated 10 mm along the z-axis, its final new coordinates can be calculated as a compound transformation by following formula

$$P' = T_{3D}\cdot P = T(0,0,10)\cdot R_y(-45)\cdot R_x(30)\cdot P. \tag{4-23}$$

With the help of this method, all FFD control lattices can be defined and operated very conveniently. Here an example is given to explain how to use this method to define and operate a typical FFD control lattice as Fig. 42 shows, which has a total of 3 layers × 3 × 3 = 27 FFD control points.

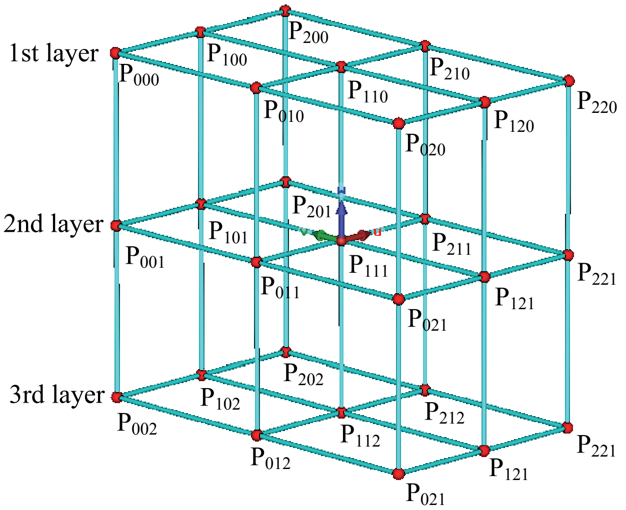

Fig. 42 Using the coordinate transformation matrix to define a typical FFD control lattice

In this FFD control lattice, the position of the joint point (x_0, y_0, z_0), where the origin of the LCS (local coordinate system u-v-w in Fig. 42) is located, is in the center of the FFD control lattice for simplicity. It should be noted that this situation is not always true for all joint points, and it is possible that the origin of the LCS does not superpose with any FFD control point. All FFD control points of the FFD control lattice in Fig. 42 are numbered based on the row, line and layer they are in, and length, width and height of the whole FFD control lattice are assumed to be l_u, l_v, l_w respectively. Detail deformation rules of this FFD control lattice are as follows: while rotation angles of the joint point are adjusted, e.g. rotation angle along u-axis α_{joint} is adjusted from 0° to θ°, the 1st layer control points will be rotated around the joint point $(\theta / 2)$ ° anticlockwise; the 3rd layer control points will be rotated $(\theta / 2)$ ° clockwise; and the 2nd layer control points do not move.

Let's first consider the second layer FFD control points because they are comparatively simpler. From Fig. 42 it can be seen that translating one point, which is located at the origin of the LCS, $-\ l_v / 2$ along u-axis and then $l_u / 2$ along v-axis can transform the origin into the point P_{001}. Then the FFD control point P_{001} can be defined as

$$P_{001} = T(-l_v/2, l_u/2, 0)\cdot(x_0 \quad y_0 \quad z_0 \quad 1)^{-1} . \tag{4-24}$$

Similarly the other 2 FFD control points in the first row of the 2nd layer can be defined as

$$P_{101} = T(0, l_u/2, 0)\cdot(x_0 \quad y_0 \quad z_0 \quad 1)^{-1}, \text{ and} \tag{4-25}$$

$$P_{201} = T(l_{\mathrm{v}}/2, l_{\mathrm{u}}/2, 0)\cdot(x_0 \quad y_0 \quad z_0 \quad 1)^{-1}. \tag{4-26}$$

The remaining 6 FFD control points in the 2nd layer can be defined in the same way and will not be repeated here anymore.

To define the 1st layer FFD control points, the point, which is located at the origin of the LCS, should be firstly translated l_{w} / 2 along *w*-axis, and then translated in the same way as that the 2nd layer FFD control points use. In order to consider rotation angles of the joint point along three different axes: α_{joint}, β_{joint} and γ_{joint}, three rotation transformations must be added after the translation transformation along *w*-axis. Then the FFD control point P_{000} can be defined as

$$\begin{aligned} P_{000} = {} & T(-l_{\mathrm{v}}/2, l_{\mathrm{u}}/2, 0)\cdot R_{\mathrm{w}}(\gamma_{\mathrm{joint}}/2)\cdot R_{\mathrm{v}}(\beta_{\mathrm{joint}}/2)\cdot R_{\mathrm{u}}(\alpha_{\mathrm{joint}}/2) \\ & \cdot T(0,0,l_{\mathrm{w}}/2)\cdot(x_0 \quad y_0 \quad z_0 \quad 1)^{-1}. \end{aligned} \tag{4-27}$$

The remaining eight FFD control points in the 1st layer can be defined similarly.

The 3rd layer FFD control points can be defined and operated in an analogous way. The main difference lies in the reversed directions of the translation transformation along *w*-axis and rotation transformation along three axes. As a result, the FFD control point P_{002} can be defined as

$$\begin{aligned} P_{002} = {} & T(-l_{\mathrm{v}}/2, l_{\mathrm{u}}/2, 0)\cdot R_{\mathrm{w}}(-\gamma_{\mathrm{joint}}/2)\cdot R_{\mathrm{v}}(-\beta_{\mathrm{joint}}/2)\cdot R_{\mathrm{u}}(-\alpha_{\mathrm{joint}}/2) \\ & \cdot T(0,0,-l_{\mathrm{w}}/2)\cdot(x_0 \quad y_0 \quad z_0 \quad 1)^{-1}. \end{aligned} \tag{4-28}$$

The remaining eight FFD control points in the 3rd layer can be defined similarly.

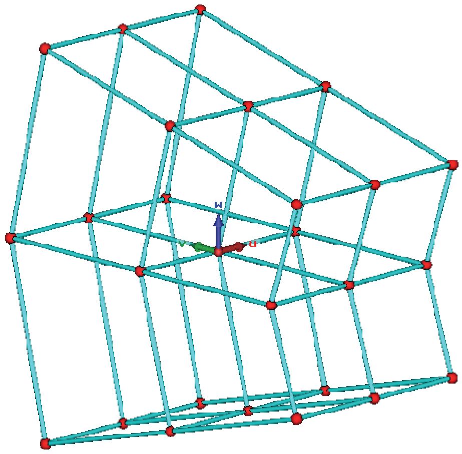

Fig. 43 Using the coordinate transformation matrix to operate a typical FFD control lattice

The initial values of the rotation angles α_{joint}, β_{joint} and γ_{joint} are all zero. As a result, the initial configuration of the FFD control lattices is a regular cuboid like Fig. 42 shows, and the studied object must be embedded in this cuboid. If these three angles are adjusted by the user of the poser program, e.g. α_{joint} is adjusted from 0° to 30°, position coordinates of all FFD control points will be recalculated, and then the FFD control lattice will be deformed as Fig. 43 shows. After that, the FFD calculation can be performed to deform the original human body model based on the deformed FFD control lattices.

4.4.Deformation of Original Voxel-based Human Body Model

The internal structure of the human body is very complicated. To deform the human body model as reasonably as possible, several specific problems must be considered, including dividing all voxels of the human body model into different parts, swelling arm muscles when the elbow joint is bent, rotating patella when the knee joint is bent, and preventing unreasonable deformation of bone and marrow. This section will discuss these problems which are essential for generating a reasonably deformed human body model.

4.4.1. Dividing Voxels into Different Body Parts

To perform the FFD calculation as conveniently as possible, dividing the whole human body model into several different parts and set FFD control lattice for each of them individually is a good strategy. Sometimes this process is inevitable if some special parts of the human body need to be deformed, e.g. two arms. Most voxel-based human body models have their two arms separated away from the trunk initially. Even for this situation a simple cutting procedure must be performed to separate arm voxels away from the chest neat the armpit [10], which may introduce errors. The configuration of the voxel-based human model studied in this dissertation, which was built based on the human model from the VHP®, is even more complicated. As Fig. 44 shows, originally, its two arms are bent in front of the abdomen and touch the trunk, which makes it difficult to deform the whole body model. The problem is: when the arm is moved or bent, all voxels which are near the arm, in the control lattice of the arm, but belong to the trunk cannot be moved. It means that all voxels which belong to the arm must be separated away from the trunk.

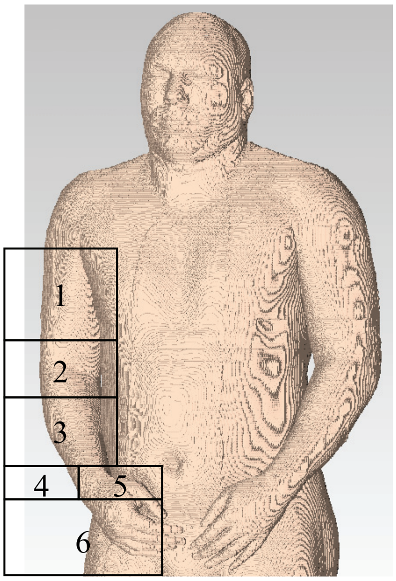

Fig. 44 Original human body model and six parts of the arm model

The approach to solve this problem is to use the skin voxels to separate all arm voxels away from the trunk. In the finest 1 mm resolution dataset, a continuous layer of skin voxels exists on the outer surface of the whole model, which can be used for arm segmentation. This method can avoid the possible errors caused by the simple cutting procedure. However, because the configuration of the original human body model is complicated near the arm, the part of whole body model near the arm must be divided into six parts, which are treated separately, to get an accurate enough result as Fig. 44 and Fig. 45 show.

(a) Part I (b) Part II

(c) Part III (d) Part IV

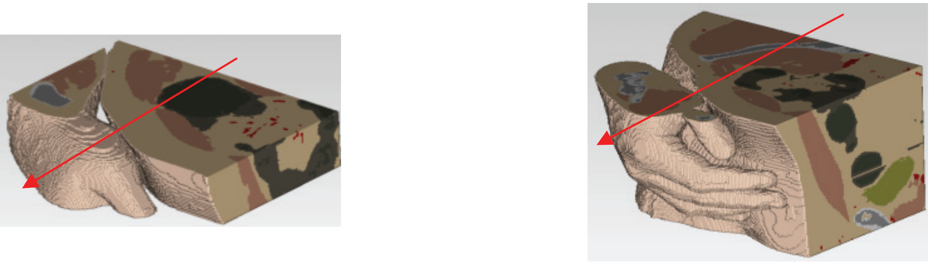

(e) Part V (f) Part VI

Fig. 45 Six parts of the whole human body model near right arm and their checking directions

In the following, an example is given to explain how to separate right arm away from the trunk. The left arm can be dealt with similarly. The whole right arm model can be divided into a total of six parts as Fig. 44 shows. The first part is below the shoulder as Fig. 45 - (a) shows. After the original dataset file is imported and stored in the program, this part of the model will be scanned and checked from the center to its right side, as the red arrow in Fig. 45 - (a) shows, and all voxels after the first skin voxel will be set as arm voxels. As Fig. 45 - (b) shows, the second part is near the elbow, and it can be also checked from the center to the right side. In this part the arm model doesn't touch the trunk, so all voxels found after the air voxel which is after the skin voxel can be set as arm voxels. The third part as Fig. 45 - (c) shows can be separated using the same method as for the first part.

The fourth part is shown in Fig. 45 - (d). This small part of the arm model is very far away from the trunk model. The air voxels between it and the trunk can be used to separate them away from each other easily. The fifth part is near the wrist as Fig. 45 - (e) shows. This part is in front of the trunk and touches the trunk. It can be checked from the back side to the front side of human body model and all voxels after the skin voxel can be set as arm voxels. The last part is the hand as Fig. 45 - (f) shows, the hand model is in front of the trunk model too, but it doesn't touch the trunk. Then this part of the model can be also checked from back side to front side and all voxels after the air voxel which is after the skin voxel can be set as arm voxels. In this way, all voxels belonging to the right arm can be separated away from the trunk.

Apart from the two arms, there are several other body parts which must be separated away from other parts of the whole human body model. This requires that the deformation of these body parts can be performed individually and will not influence other body parts which are around or near them. Separating these body parts can be realized by using the finest 1 mm resolution HUGO model in CST® and finding the corresponding voxel index range they occupy. For example, in order to rotate the patella as a rigid body while the knee joint is bent, the right and left patella must be separated and dealt with individually. The initial position of the right patella is shown in the left figure of Fig. 46.

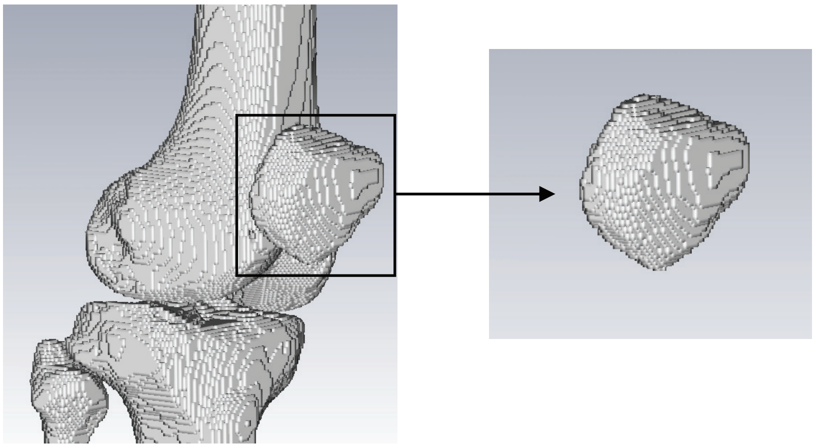

Fig. 46 Figure of right knee and individual right patella

CST® allows the partial import of the whole voxel model by specifying a voxel index range, for instance, the part of whole voxel model occupied by the right patella, such as the right figure of Fig. 46 shows. The voxel index range of right patella in the 1 mm resolution HUGO model is from (144, 173, 1257) to (198, 200, 1313), thus all bone voxels and marrow voxels in this index range can be recognized as right patella voxels, allowing the clear identification of the right patella by the poser program. For other resolutions, the voxel index range can be calculated by dividing the index range calculated from 1 mm resolution HUGO model by the concerned voxel size. For example, if the voxel size is 4 mm, the index range can be calculated as ranging from (144 / 4 = 36, 173 / 4 ≈ 43, 1257 / 4 ≈ 314) to (198 / 4 ≈ 50, 200 / 4 = 50, 1313 / 4 ≈ 328). Other body parts can be separated by a similar approach. All separated individual body parts and the corresponding body part numbers in the poser program are listed in Table 8.

Table 8 Separated body parts and body part numbers in poser program

Body part name	Number	Body part name	Number	Body part name	Number
Right leg	1	Penis	5	Right tibia head	9
Left leg	2	Right patella	6	Left femur head	10
Right arm	3	Left patella	7	Left tibia head	11
Left arm	4	Right femur head	8	Others	0

4.4.2. Swelling Arm Muscles

In real life, when a human bends his or her elbow, the muscles of the upper arm will swell to some extent based on how much force he or she uses. This sub-section explains how to realize this phenomenon by operating the FFD control lattice around the arm model.

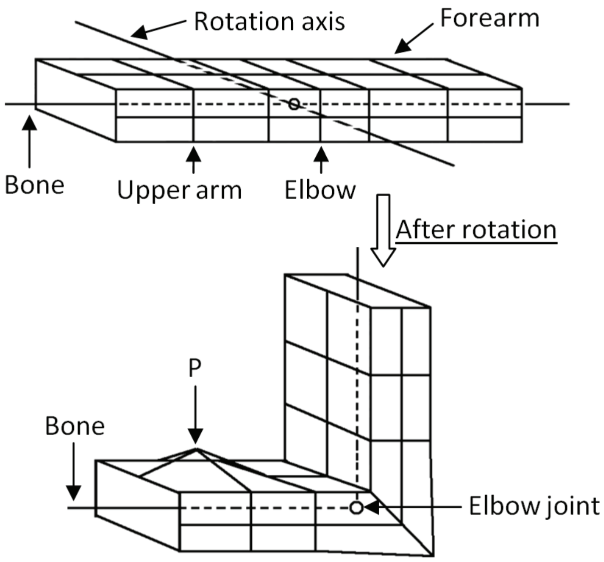

Fig. 47 The FFD control lattice defined around arm

The FFD control lattice of the arm model, including upper arm, elbow joint and forearm, is defined around the outer surface of the arm model as the first figure of Fig. 47 shows. When the elbow joint is bent by 90°, the positions of the FFD control points are moved based on following rules: in the forearm part, the control points are rotated by 90° directly around a rotation axis through the elbow joint as Fig. 47 shows. In the upper arm part, most of the control points don't move and stay at their original locations. The upper central control point P as indicated in Fig. 47 has an independent position which can be adjusted by the poser program. Therefore, the swelling of the arm muscles can be simulated by changing its position according to the angle of bending motion of the elbow joint. Even for the same bending angle of the elbow joint, the degree to which arm muscles swell to can be adjusted by setting different values for an parameter in the poser program, with the purpose of simulating the situation in which human uses different forces. In the elbow part, the positions of the control points are all determined by the condition of smooth outer surfaces of the elbow joint, and by the fact that the positions of the control points on the rotation axis do not change. At any other bending angles of the elbow joint, the positions of the control points are determined by interpolation of the bending angles using arrangements of the control points at 0° and 90° degrees of the elbow joint, while maintaining the smooth outer surfaces of the joint. The deformation effect of this strategy is shown in Fig. 48.

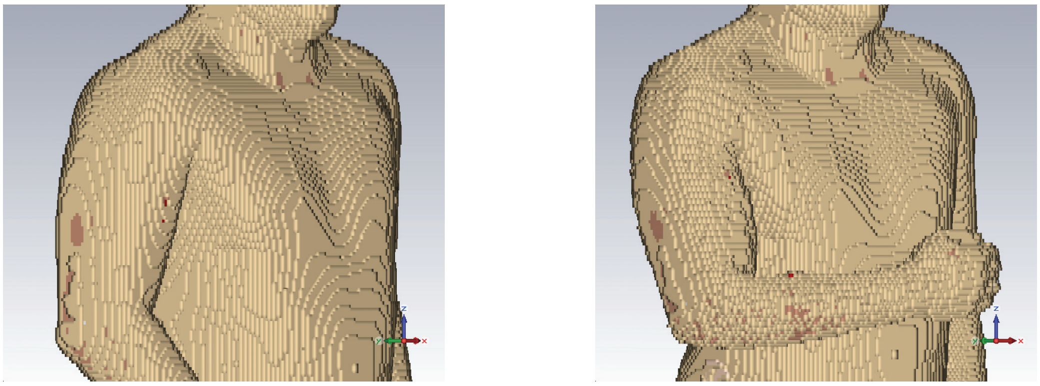
(a) Original configuration (b) Swelled upper arm with bent elbow joint

Fig. 48 Swelling arm muscles while elbow joint is bent

4.4.3. Deforming the Knee Joint

The main advantage of the FFD technique in deforming the voxel-based human body model is that it can keep continuity of internal tissues and organs, and result in a continuous deformed human body model. However, the movement of the human body is very complicated in some special joints such as the knee. The deformation of the knee joint includes not only flexible deformation of the fat, muscle, etc., but also rigid body movement and rotation of the skeleton. Fig. 49 shows detail information of the knee joint movement with two CT images [83].

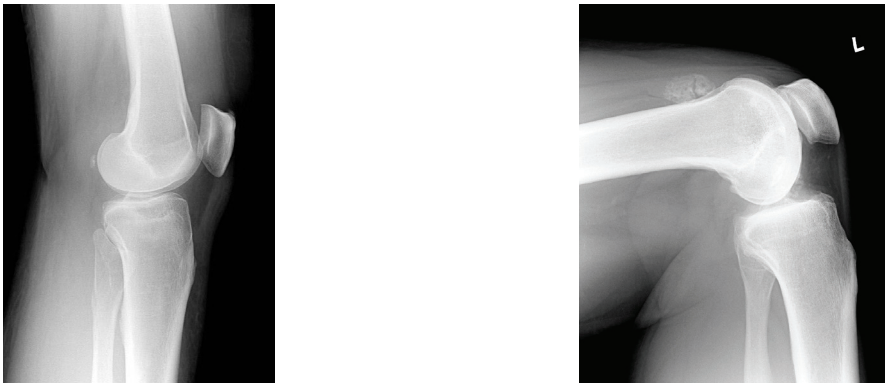

(a) Original internal configuration (b) After the knee is bent

Fig. 49 Deformation of the knee joint

When the knee joint is bent, the tibia head will rotate around the outer surface of femur head, and at the same time, the patella will also rotate around the other part of the same surface. Because the standard FFD is a kind of flexible deformation technique, while it is used to deform the knee joint as a whole, it will deform the bones to some extent and the patella cannot be rotated at all. Fig. 50 shows the deformation effects of this problem in detail: figure (a) was realized by author's testing program and figure (b) is from reference

[10]. In these deformations, the femur head and the tibia head are both deformed and the patella remains at its original position. Compared to the real anatomic structure shown in Fig. 49, these deformations are obviously anatomically incorrect.

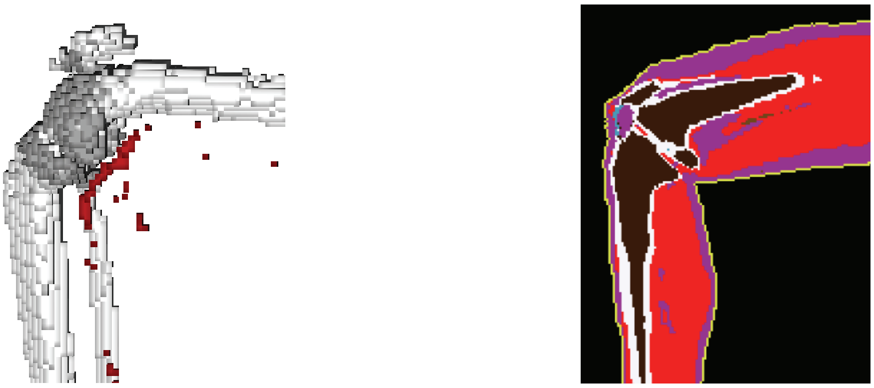

(a) From author's testing program

(b) From other researcher's paper [10]

Fig. 50 Bone deformation and wrong position of patella while using standard FFD to deform the knee joint

Some special measures must be taken to solve the problem mentioned above and obtain a deformed human body model with correct internal anatomic structure. It should be noticed that although the FFD is a flexible deformation technique, if the FFD control lattice doesn't deform, FFD can also realize rigid body movement and rotation by moving and rotating the concerned FFD control lattice as a whole rigid body. In order to realize all movements mentioned above while the knee joint is bent, three sets of FFD control lattices must be defined around the knee joint as Fig. 51 shows, and each of them is responsible for only one part of the knee voxels.

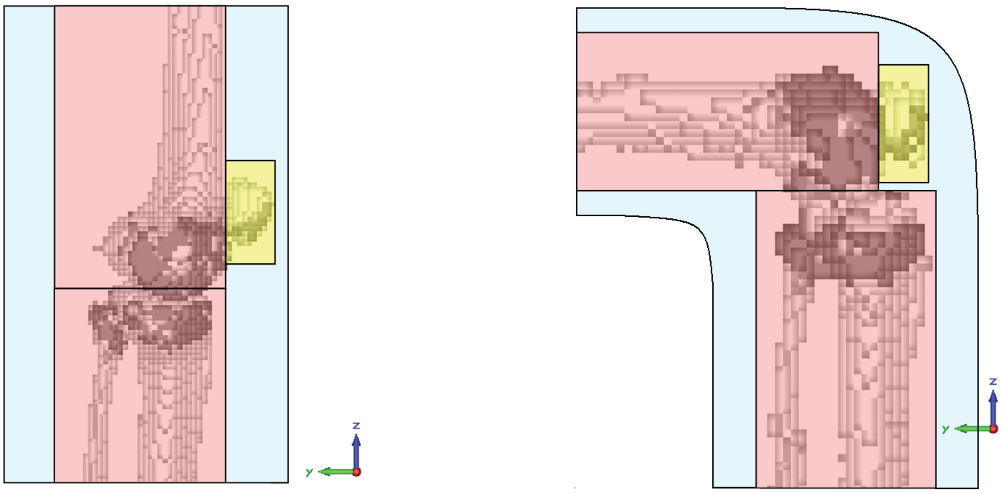

(a) Three sets FFD control lattice around the knee joint before deformation

(b) Configuration of the three sets of FFD control lattices after deformation

Fig. 51 Three sets FFD control lattice around knee joint before and after deformation

The first FFD control lattice indicated with blue color is defined to deform the flexible materials such as the fat, muscle, skin, etc.; the second set with light pink color is used to rotate the femur head and tibia head, and the third set with yellow color is used to rotate the patella based on the bending angles of the knee joint. While the knee joint is bent, the first set FFD control lattice with blue color will be deformed flexibly as Fig. 51 – (b) shows. At the same time the second and third set will be rotated as rigid, non-deformed bodies, so that all voxels they control, such as femur head, tibia head, patella, etc. will be rotated to their right positions in accordance and not deformed.

Because all voxels of the knee joint are divided into three parts and deformed by three sets FFD control lattices separately, after the deformation calculation is finished, there will be possibly some small leaks between the rigid and flexible materials. Since the internal part of the knee joint consists of only three tissues: bone, marrow and fat, these small leaks can be filled with the fat tissue directly. At last, the modified deformed model of two knee joints is shown in Fig. 52. In this figure the femur head and tibia head are not deformed, the tibia head has been rotated around outer surface of the femur head, and the patella has also been rotated around the other surface of the femur head. The whole deformation effect looks very similar to the real internal anatomic structure shown in Fig. 49 – (b).

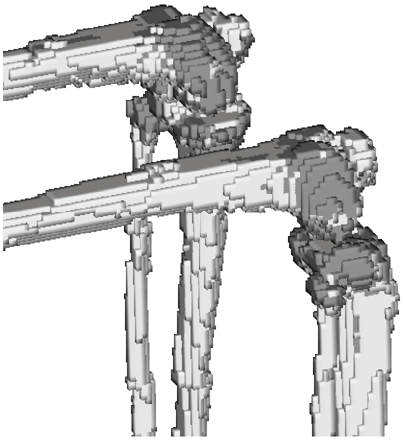

Fig. 52 Modified deformation effect of the knee joint

4.4.4. Deforming the Whole Human Body Model

Until now, original voxel-based human body model HUGO can be deformed with an anatomic correctly way by setting rotation angles of different joints directly. In this dissertation, three deformed human body models generated by the poser program were used in electromagnetic applications: one walking human body model and one standing human body model with separated legs used in a step voltage application example, and one sitting human body model used in an SAR application example. These application examples will be described in Chapters 5 and 6.

The outer surfaces of these three postured human body models are shown in Fig. 53. These three postures mainly include rotation and deformation of the knee joint, hip joint and shoulder joint. Fig. 53 also shows a cut plane drawing for every deformed human body model, and it can be seen that all internal tissues and organs are deformed continuously and smoothly. Because of the special methods explained above around the knee joint, the femur, tibia and patella are all moved into anatomically correct positions and their original shapes are maintained.

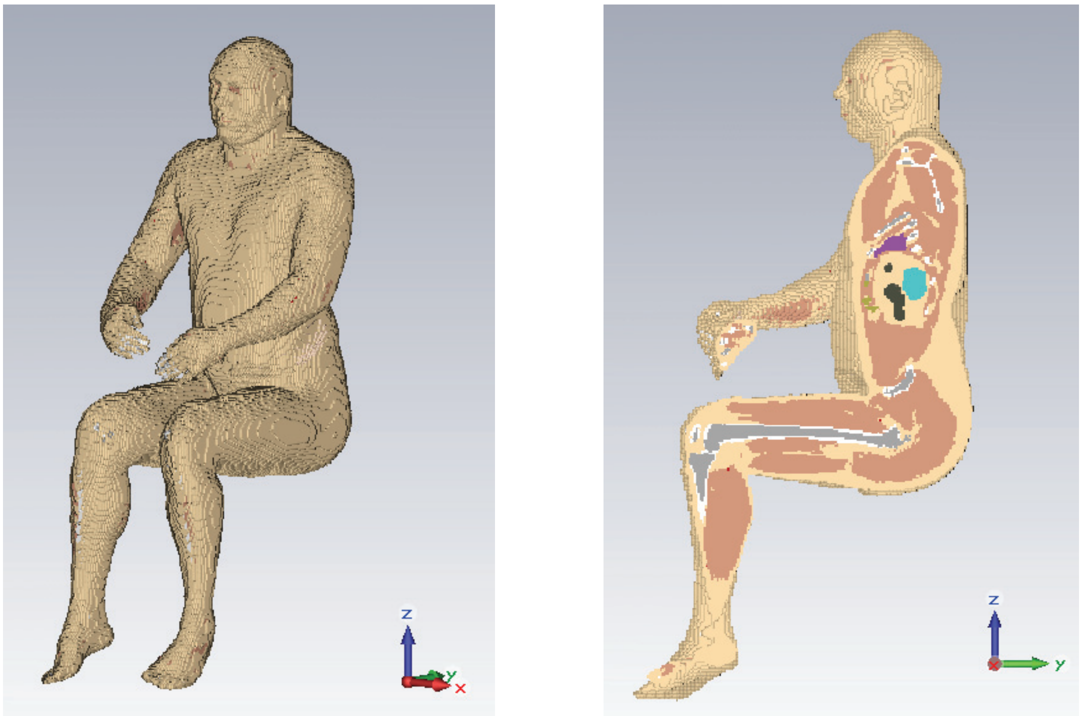

(a) Sitting human body model

(b) Cut plane drawing of sitting human model

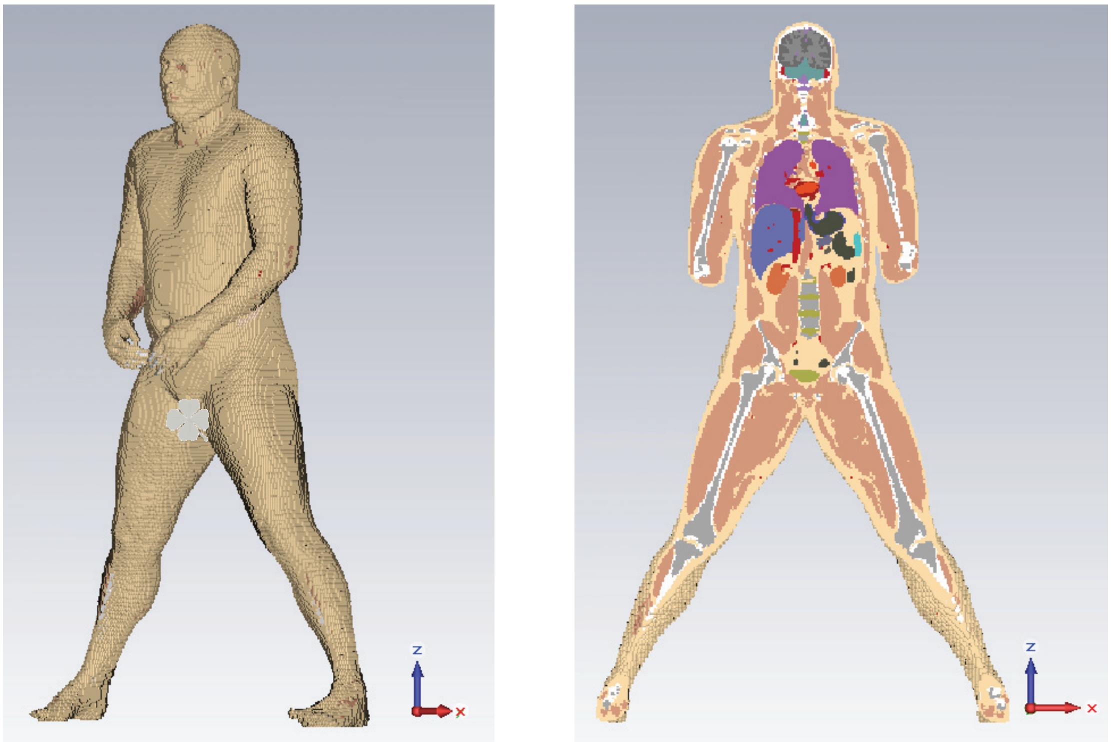

(c) Standing human body model

(d) Cut plane drawing of standing human model

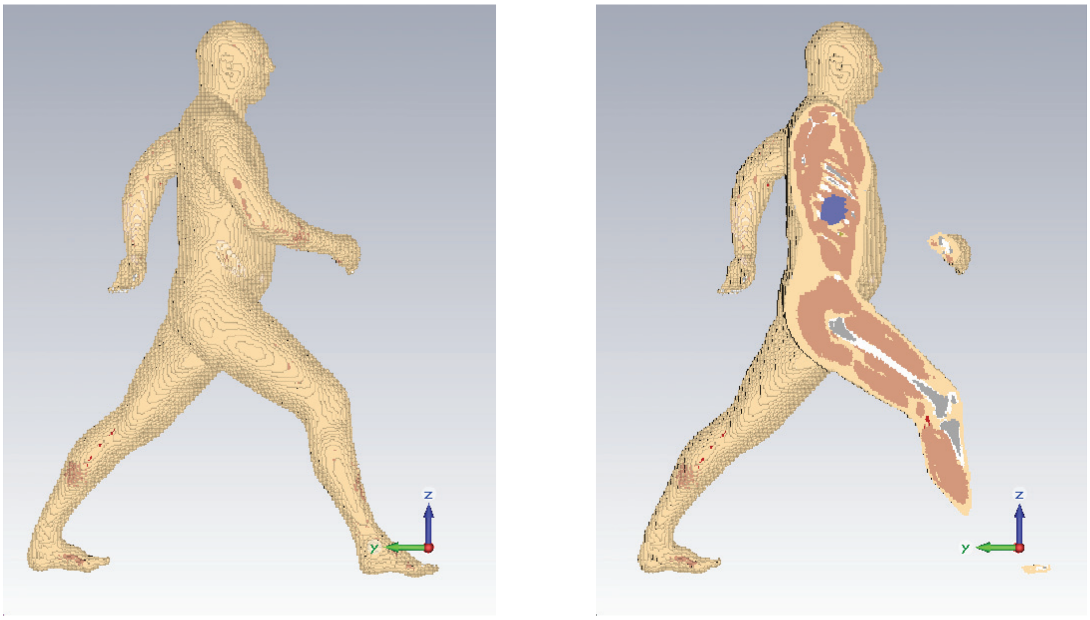

(e) Walking human body model (f) Cut plane drawing of walking human model

Fig. 53 Postured human body models generated with the poser program

4.5. Export of the Postured Human Models

After the posture transformation, the human body models need to be exported as new voxel dataset files, such that other software tools can import and use them for further research work. At the very beginning, the entire domain of the original voxel space must be extended, because any stretched arm or leg will protrude outside the voxel space of the initial posture. The position coordinates of each voxel of the original human body model modified by movements of the FFD control lattices are known, therefore their minimum and maximum values can be found. The dimension of the new dataset along the *x*-direction, which means the number of new voxels in the *x*-direction, can be calculated by

$$X = \left[\frac{|x_{\max} - x_{\min}|}{\text{resolution}} \right] + 2. \tag{4-29}$$

Here [ ] means rounding the number to the nearest integer, and the purpose of adding 2 in the end is to ensure that the calculated dimension value is large enough for two sides of the postured human body models. The dimension of the new dataset file along *y*- and *z*-direction can be determined similarly.

And then exporting a new dataset needs to voxelize the whole space, which the deformed human body model occupies, based on the calculated new dimension values and required resolution. The export of the new dataset works similarly to the meshing of the whole deformed human body model and the space around it, using a regular mesh of identical cubes. After that different tissue identification numbers (IDs) should be assigned to each new voxel in the extended voxel space. In order to realize this function, one voxel point was defined in the center of each original voxel of the deformed human body model as Fig. 54 – (a) shows, having the same tissue ID information as the voxel it is in. To get higher calculation accuracy, each original voxel can be subdivided into 2 × 2 × 2 = 8, 4 × 4 × 4 = 64 or even more sub-voxels, each containing one voxel point as Fig. 54 – (b) and (c) shows. It should be paid attention that finer sub-division can improve not only voxelization accuracy, but also increase memory requirement. All of these voxel points will be then allocated into different new voxels based on their own coordinates and the space each new voxel occupies. As a result every new voxel will include several kinds of voxel points with different tissue IDs. Therefore, the number of the voxel points with different tissue IDs in each new voxel can be calculated, and the tissue ID of the new voxel is determined by the tissue ID with the largest numbers of voxel points.

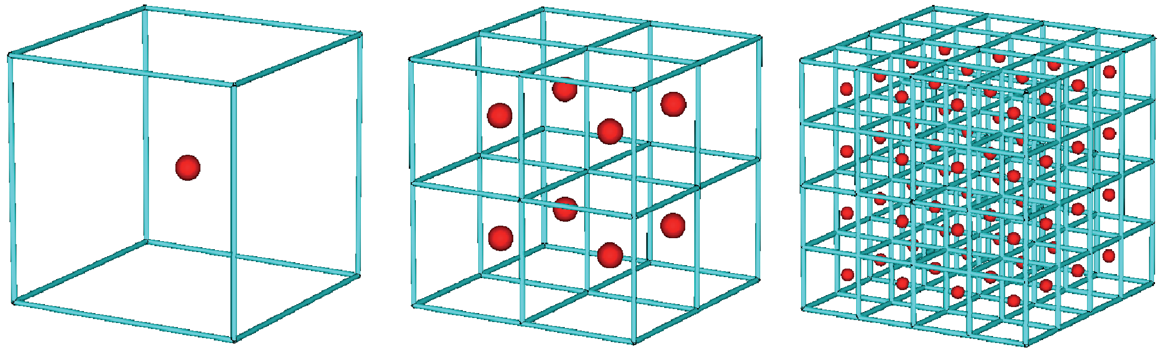

(a) 1 × 1 × 1 (b) 2 × 2 × 2 (c) 4 × 4 × 4

Fig. 54 Voxel points defined in one original voxel or sub-voxels

When the original human body model is deformed with the FFD technique, the position coordinates of every voxels will change; during this process some voxels will move nearer, and some voxels will be separated away from each other. If each original voxel only has one voxel points in it, and a new voxel is just located in the space between two separated voxel points, it will not be allocated with any voxel points and result in 0 tissue ID. Actually, because of deformation characteristics of the human body, the voxels cannot be separated too far away from each other. This problem can be avoided by sub-dividing the original voxels to make them have more voxel points.

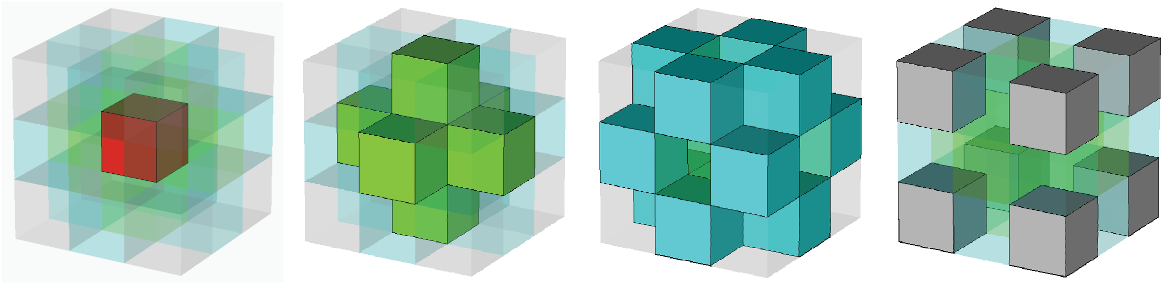

(a) New voxel with 0 ID (b) Surface contact (c) Edge contact (d) Vertex contact

Fig. 55 Compensation algorithm used to fill up new voxels with 0 ID number

Sub-dividing the original voxels needs more memory and longer calculation time. In order to decrease the memory requirement, one compensation algorithm was developed to automatically and reasonably fill in all 0 tissue ID voxels with appropriate tissue ID numbers. With the help of this compensation algorithm, each original voxel only needs one voxel point in it, and the exported deformed human body model will have a continuous internal structure without 0 tissue ID voxels.

The concept of the compensation algorithm refers to the idea of the tri-linear interpolation algorithm [40] which is often used when the original voxel model is generated from the CT or MRI medical images. The tri-linear interpolation algorithm is mainly used to generate additional medial image slices between two existing medical images, because sometimes the interval between two medical image slices is much larger than the size of the voxel. The general idea of the compensation algorithm is to specify the tissue ID of the considered voxel based on the tissue IDs of the other voxels around it. For example, there is one 0 tissue ID voxel shown in Fig. 55 – (a), and the six voxels, which have surface contact with the considered voxel as Fig. 55 – (b) shows, may have different tissue IDs. Because the human internal anatomical structure should be continuous, the number of voxels with different tissue IDs around the considered voxel can be calculated, and the tissue ID of the considered 0 tissue ID voxel can be specified as the tissue ID with the most number of the voxels around it. If two or more different tissue IDs have the same number of voxels, the algorithm will go on considering the twelve voxels with edge contact with the considered voxel or even the eight voxels with vertex contact condition, as Fig. 55 – (c) and (d) shows.

The poser program can export the new datasets in two kinds of file formats: $*$.lat file that CST$^{®}$ uses, and $*$.raw file that includes only voxel tissue ID data without any header information. The $*$.lat file has some header information which contains dimension values of the dataset along three directions, total number of the voxels, etc., and occupies 148 bytes. While the poser program is required to export the $*$.lat file, it will write the header information firstly in the dataset file and then append all voxel tissue ID data after them.

4.6.Mass Calculation and Comparison

An important issue for the deformation of biological models is the conservation of their mass. This is especially important for simulations involving the calculation of the specific absorption rate, whose accuracy depends in an essential way on the tissue mass. In reality, when human being moves his own arms or legs, the mass of each tissue or organ should not change. To date, it’s almost impossible to conserve the mass of each tissue and organ completely after the original voxel-based human body model is deformed. In the developed poser program, the closer the FFD control lattice is moved to reality, the better will be the deformation effects and mass conservation results. Deformation strategy of the FFD control lattice used in the poser program has been tested and modified lots of times in detail. Its deformation effects are satisfactory and mass conservation level is usually controlled below 5% for common human postures. In the poser program, the mass of each tissue or organ is calculated by multiplying the number of specific tissue voxels by the volume of one voxel and by the mass density of the specific tissue or organ.

Mass calculation results of the sitting human body model shown in Fig. 53 compared with the original HUGO model are shown in Fig. 56 and Table 9. The very last item of the Table 9 is the mass of the whole human body which is calculated as the sum of all tissues and organs. The mass comparison results show that mass errors of most tissues and organs including the whole body are very low, and all tissues and organs have a mass error below 4.3% which is a reasonable level for usual simulations involving human body. The mass error of the whole human body is only around 0.24%.

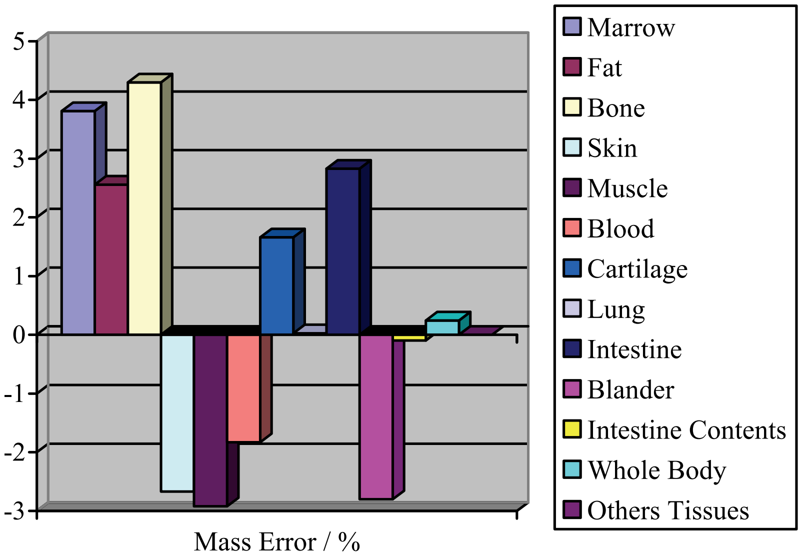

Fig. 56 Mass errors between original model and sitting human body model

The concrete values of the mass errors shown in Fig. 56 and the corresponding masses of every tissue and organ of the original and the deformed sitting human body model are listed in Table 9.

Table 9 Mass calculation and comparison between original model and sitting human body model

Material	Original Mass/kg	Deformed Mass/kg	Mass Error/%
Marrow	3.067	3.184	3.81
Fat	43.923	45.048	2.56
Bone	7.599	7.926	4.30
Skin	0.0375	0.0365	-2.67
Muscle	45.303	43.979	-2.92
Blood	0.436	0.428	-1.83
Cartilages	0.421	0.428	1.66
Lung	3.820	3.821	0.026
Intestine	1.166	1.199	2.83
Blander	0.0855	0.0831	-2.80
Intestine Contents	2.049	2.047	-0.097
Other tissues	--	--	0
Whole body	113.219	113.495	0.24

In the poser program, because the human body model with smaller voxel size has a better approximation of the outer shapes of different internal tissues and organs, the mass error decreases with decreasing voxel size Δx of the human body model, as shown in Fig. 57. For the sitting human body model with 1 mm resolution, the relative error of the mass of any tissue or organ is below 3.5% as compared to the original model. The numerical experiments indicate that the convergence of the whole body mass is of the order $O(\Delta x^{1/2})$ as shown in Fig. 57.

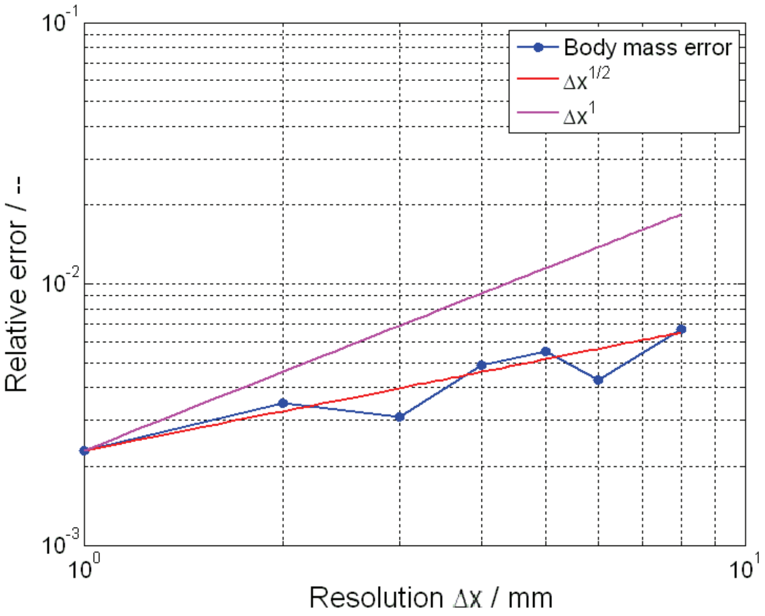

Fig. 57 Relative error of the total body mass, after the movement of the human model to a sitting position; the curves Δx^1 and $\Delta x^{1/2}$ are also displayed for reference.

5. Study on Step Voltage with Postured Human Models

Postured voxel-based human body models generated by the developed poser program have very broad application prospect in electrical engineering, mechanical engineering, aerospace engineering, etc. This dissertation discusses their applications in Bioelectromagnetics which mainly studies interaction between electromagnetic fields and biological tissues. There are three application examples discussed in this dissertation covering static field analysis, quasi-static field analysis and high frequency field analysis, which were all simulated with the commercial software CST MICROWAVE STUDIO®, CST EM STUDIO®, in part using also the reduced *c* technique introduced in Chapter 3.

In this chapter, two simulation application examples were performed to study distribution situation of the internal electric field and current density field in the human body models excited by the step voltage, and their influences on human's health. In order to consider the effects of human's posture on the simulation results, two postured human body models, one standing and one walking model, were used.

The first example studies the step voltage caused by a broken and downed high voltage power line, whose electric potential has a fixed effective value. It can be simulated by the stationary current solver of CST EM STUDIO®. The step voltage in the second example is caused by a lightning current, which is a low frequency long-duration time-domain current signal, and can be simulated by the transient solver of CST MICROWAVE STUDIO®. To speed up the simulation, the above mentioned reduced *c* technique was used. In the first stage, the electric potential distribution on the ground surface due to the lightning strike was calculated to obtain the step voltage between feet of the human being. This step voltage was used in the second stage to excite two perfect electric conductive patches placed below the human body models' feet. Because of the very low frequency spectrum of the excitation signal, the simulation studied here is an electro-quasistatic problem. However, the dispersive nature of the biological materials required the use of a full-wave transient simulator, which can deal with such materials. Due to the Courant time step limitation and long duration of the excitation signal, the lightning signal would require a huge number of time steps to be simulated, which needs very long calculation time. In order to alleviate this problem and speedup simulations, the reduced *c* technique, which was introduced by Holland in 1995 and always applied by several authors for solving magneto-quasistatic problems, was firstly studied to be used in this electro-quasistatic simulation to get a much larger stable time step and accurate enough simulation results after an error analysis. The simulation results here are very useful references for design, manufacturing and optimization of lightning protection equipment and grounding equipment.

5.1.Step Voltage Caused by Downed Power Lines

5.1.1. Introduction to Step Voltage

In electrical power systems, a broken and downed power line is an obvious dangerous source of electric shock, because the voltage between the power line and the earth ground can reach several hundred kV. Direct contact with the downed power line will almost certainly cause death, but other unobvious hazards such as step voltage also exist.

Step voltage is a very common phenomenon in electrical engineering. If a broken power line touches the ground as Fig. 58 shows, the current will be discharged in the earth and travel between the downed conductor and the nearest grounding point of the power system, which will be some kind of conductor buried in the ground for good contact, to establish a closed circuit. Although the earth in principle is a conductor, its conductivity is much smaller than that of the metal cables of the power lines. Thus there will be substantial voltage drop between the touching point of the broken power line and the grounding point of the power system, and very little voltage drop along the rest power lines.

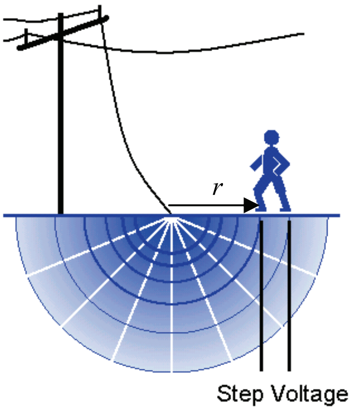

Fig. 58 Step voltage caused by downed power line [84]

Because the discharged current from the broken power line will cause strong electric field in the ground near the touching point of the broken power line, humans or animals walking or standing on the ground near this region will be in danger of receiving an electric shock by the electric potential difference between their feet which is called step voltage. It will be very dangerous if the voltage of the power line is very high and the human or animal is very near to the broken power line because of very high step voltage. It means that a person or animal can become a victim of electric shock from a downed power line without even coming into contact with that line.

If anybody sees a power line about to hit the ground, the action he or she should take is to contact the ground at one point to prevent the deadly step voltage to be applied across the body through two legs. Specifically, he or she can stand on one foot or just run away as soon as possible because when human runs, there is always only one foot contacting the ground at any given time. Obviously, if there is somewhere safer nearby, running away is the best choice [85].

5.1.2. Analytical Analysis of Step Voltage

Before starting to calculate the internal current density distribution excited by the step voltage in the human body model, an analytical model of the step voltage was built here to deduce the relation between the value of the step voltage and the distance between the victim shocked by the step voltage and the touching point of the broken power line.

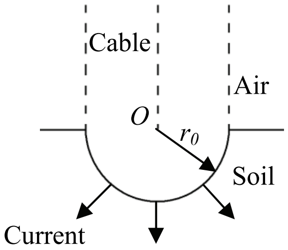

Fig. 59 Analytical model of step voltage

Fig. 59 shows the analytical model of the step voltage indicating cable head of the broken power line which is represented by a half sphere electrode and buried in the ground. The radius of the cable head is r_0 and the position where the cable head touches the ground is the point O. It's assumed that the current is discharged homogeneously along all directions into the earth, and conductivity of the soil is σ everywhere. Based on the geometric information of Fig. 59 and electric resistance formula $R = l/\sigma S$, the grounded resistance of this cable can be calculated as:

$$R = \int dR = \int_{r_0}^{\infty} \frac{dR}{2\pi r^2 \sigma} = \frac{1}{2\pi r_0 \sigma}. \tag{5-1}$$

If the electric potential of the cable is U_0, the total grounded current is

$$I = \frac{U_0}{R} = 2\pi r_0 \sigma U_0 \tag{5-2}$$

and the current density in the ground can be calculated as:

$$J = \frac{I}{2\pi r^2} = \frac{U_0 r_0 \sigma}{r^2}, \tag{5-3}$$

where r is the distance away from the touching point O. The electric potential then can be calculated as:

$$U(r) = \int_r^{\infty} \vec{E} \cdot d\vec{r} = \int_r^{\infty} \frac{\vec{J}}{\sigma} \cdot d\vec{r} = \int_r^{\infty} \frac{U_0 r_0}{r^2} dr = \frac{U_0 r_0}{r}. \tag{5-4}$$

It means the iso-potential surfaces in the ground are hemisphere surfaces whose centers are the touching point O. On the ground surface, the iso-potential lines are concentric circles around the touching point O. The electric potential difference between two points, whose distances away from the touching point O are r_1 and r_2 respectively, can be calculated as:

$$U_{12} = U_{r_1} - U_{r_2} = U_0 r_0 (\frac{1}{r_1} - \frac{1}{r_2}) = U_0 r_0 \frac{r_1 - r_2}{r_1 r_2}. \tag{5-5}$$

Equation (5-5) shows that the distance difference r_1 - r_2 and the concrete values of the distances r_1 and r_2 can influence the value of the electric potential difference U_{12}. Shorter distance away from the touching point O can lead to higher potential difference even with fixed distance difference r_1 - r_2.

If it's assumed that normal human's step distance is 1 m, when one human stands r meters away from the touching point of the broken power line along radial direction, the electric potential difference applied across his or her body through two feet can be calculated as:

$$U_r = \frac{U_0 r_0}{r(r+1)} \tag{5-6}$$

The quantity U_r in equation (5-6) is just the step voltage. If it's assumed that the electric potential of the broken power line U_0 is 220 kV and the radius of the cable head r_0 is 20 mm, which are both common values of high-voltage power lines, the variation U_r of equation (5-6) has the plot of Fig. 60.

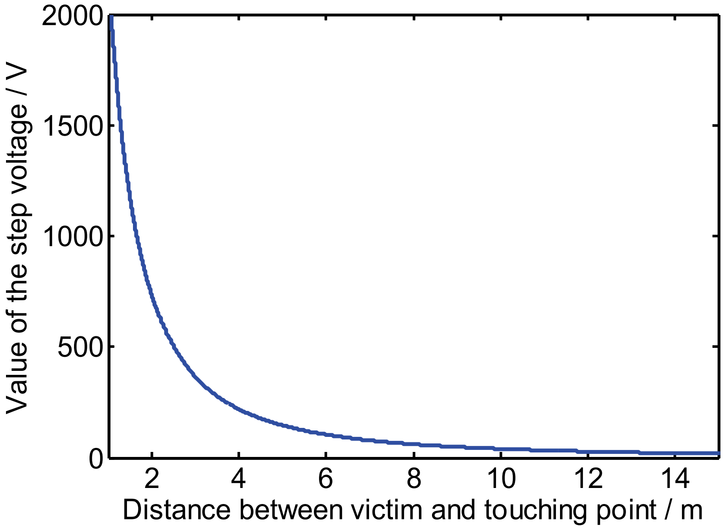

Fig. 60 Relationship between step voltage and distance between victim and touching point of the broken power line

It can be seen that the value of the step voltage will increase dramatically when the victim is very near to the touching point of the broken power line. The shortest safe distance away from the touching point under the assumption above is further than 11 m, where the step voltage is smaller than 30 V which is a safe voltage for most situations.

5.1.3. Physiological Effects of Electricity

To evaluate the dangerous level of the step voltage at different distances away from the touching point of the broken power line, some foundational knowledge about physiological effects of electricity and some safe current or current density criterions should be available for comparison.

Similar to the phenomenon that a metal conductor, loaded with current, will be warmed up, any lossy human tissue or organ will be heated up while there is current passing it. If the current has very high level and lasts for a long enough time, the internal tissues or organs of the victim may be even burnt. However, there is another effect of the electric current on the human body, which is in fact much more dangerous than the heat effect. It is that the electricity can disorder the whole nervous system. A simple survey on the related knowledge about electrical safety shows that the external electric current of sufficient magnitude conducting through the living tissue will override the tiny electrical signals generated by the neurons. As a result, the whole nervous system cannot work normally and then all signals originally used to actuate muscles will be prevented [85].

Many researches and experiences show that muscles triggered by the external current will involuntarily contract. If a victim contacts an energized conductor with his or her palms, because of the internal muscle structure of the human hands, the victim's hands will be clenched into a fist to make the victim grasp the wire more firmly. Thus the victim will be frozen on the wire and unable to leave any more. Even after the power is stopped, the victim still needs a not short time to recover completely.

Because the heart is composed of muscles, the external electric current can also make the heart contract involuntarily. What makes the things even worse is that very weak alternative current (AC), which cannot make the heart contract though, can still make the heart not to beat properly. Medically, this condition of the heart is called fibrillation. A fibrillating heart flutters rather than beats and then cannot pump blood to other organs. It should be noticed that the alternative current of industry frequency (60 Hz in the USA and 50 Hz in European) has greater risk to send the heart into a fibrillation condition than the direct current (DC) which tends to make the heart stand still. Because the heart can recover easier from a standing condition than the fibrillation condition, low frequency AC is much more dangerous than the DC of the same voltage and amperage [85].

Concrete human body effects corresponding to different current levels and possible safe current criterions differ from person to person. Gender, age, sickness, etc. are all influential factors. Despite these uncertainties, an approximate guideline had been developed by Kuphaldt through tests and literature survey as Table 10 shows.

Table 10 Body effect influenced by electrical current (in mA) [85]

Body effect	Direct current (DC)	60 Hz AC	10 kHz AC
Slight sensation felt at hands	Men = 1.0	0.4	7
	Women = 0.6	0.3	5
Threshold of perception	Men = 5.2	1.1	12
	Women = 3.5	0.7	8
Painful, but voluntary muscle control maintained	Men = 62	9	55
	Women = 41	6	37
Painful, unable to let go of wires	Men = 76	16	75
	Women = 51	10.5	50
Severe pain, difficulty breathing	Men = 90	23	94
	Women = 60	15	63
Possible heart fibrillation after 3 seconds	Men = 500	100	
	Women = 500	100	

The other valuable literature studying the body effect of electricity comes from the ICNIRP guidelines for limiting exposure to time-varying electric, magnetic, and electromagnetic fields (up to 300 GHz) [11]. It also provides a table to show threshold currents for various body effects of electricity as Table 11 shows.

Table 11 The threshold currents for various body effects of contact currents that result when the human body comes into contact with an object at a different electric potential, including children, women and men (in mA) [11]

Body effect	50 / 60 Hz	1 kHz	100 kHz	1 MHz
Slight touch perception	0.2 ~ 0.4	0.4 ~ 0.8	25 ~ 40	25 ~ 40
Pain on finger contact	0.9 ~ 1.8	1.6 ~ 3.3	33 ~ 55	28 ~ 50
Painful shock / let-go threshold	8 ~ 16	12 ~ 24	112 ~ 224	--
Severe shock / breathing difficulty	12 ~ 23	21 ~ 41	160 ~ 320	--

The data of Table 11 almost agrees with that of Table 10 especially the let-go and breathing difficulty threshold current values at industry frequency.

As a limitation guideline, reference [11] also sets restriction values of the current density and touching current at different frequency ranges for occupational and general public safety as Table 12 and Table 13 show. Safety factors used for occupational and general public case are 10 and 50 respectively to consider the possible uncertainties from insufficient information, severe environments, individual differences, etc.

Table 12 Restrictions for current density in head and trunk (in mA/m^2) (rms value)

Frequency range	Occupational case	General public case
Up to 1 Hz	40	8
1 – 4 Hz	40 / f	8 / f
4 Hz – 1 kHz	10	2
1 kHz – 10 MHz	f / 100	f / 500

The f in Table 12 means the frequency in Hz.

Table 13 Reference level for contact current from conductive objects (in mA)

Frequency range	Occupational case	General public case
Up to 2.5 kHz	1.0	0.5
2.5 – 100 kHz	0.4 f	0.2 f
100 kHz – 110 MHz	40	20

The f in Table 13 means the frequency in kHz.

5.1.4. Stationary Current Calculation

In order to determine the relation between the level of current excited by the step voltage through human body and the distance between the victim and the touching point of the downed power line based on a human model with real anatomic structure, and analyze internal current density distribution in the human body, two models including voxel-based human body models with different postures were developed as Fig. 61 and Fig. 62 show.

Fig. 61 depicts a standing human body model with a distance between two separated feet of one meter. The standing human body model was generated with the poser program. Its two ankle joints were bent to make both foot bottoms parallel with the ground surface and two feet to be located on the same plane. Apart from that, two arms were raised a little to place the hands a little away from the trunk for comparison convenience, since in the walking human body model, its two hands don’t touch the trunk and the resistance of the human body may be changed if the hand touches the trunk.

With the help of equation (5-6), the step voltages between two feet of the human body model corresponding to different distances between the victim and the touching point can be calculated. In the simulation models, below each foot a perfect electrical conductor (PEC) patch was built. The one below the right foot was loaded the electric potential which equals the step voltage value calculated above as excitation source, while the one below the left foot had zero potential to realize an electric potential difference between two feet the same as the value of the step voltage. The distance between the victim and the touching point of the power line (to be precise, between the right foot and the touching point as Fig. 58 shows) was set as a parameter in CST EM STUDIO® and the step voltage values could be set as a function of the distance parameter based on equation (5-6). In this model, the electric potential of the power line was assumed to be 220 kV and the radius of the cable was set to 20 mm, which are both common values of high voltage power line. Fig. 61 shows the potential values on two PEC patches when the distance parameter was 1 m.

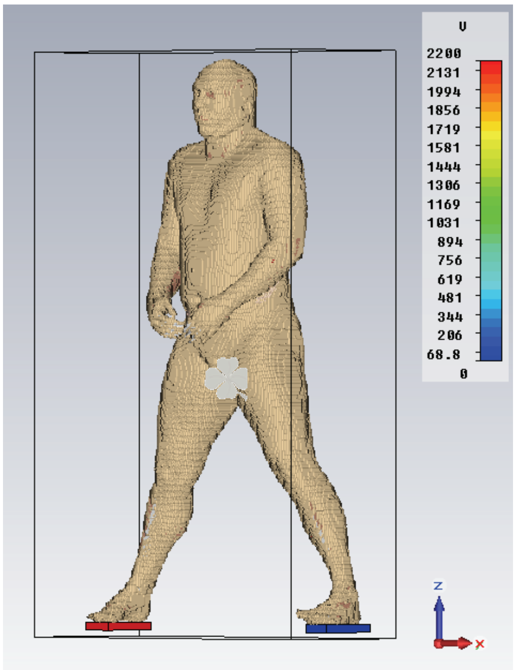

Fig. 61 Step voltage model including human model with standing posture

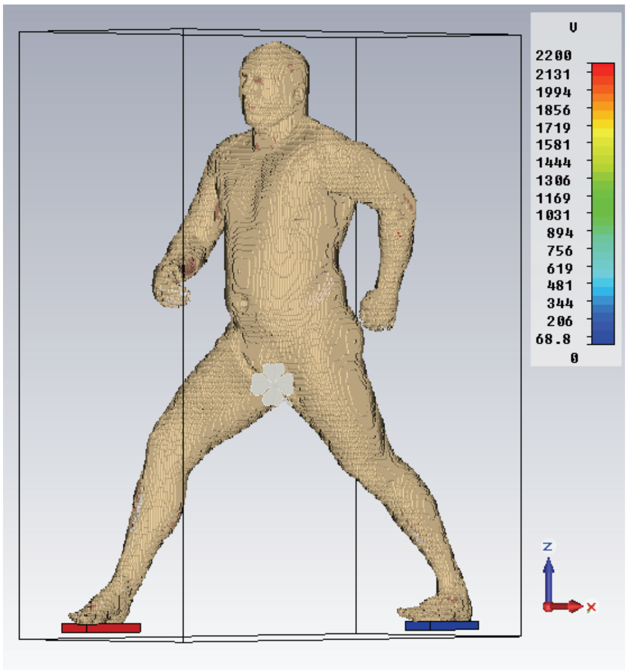

Fig. 62 Step voltage model including human model with walking posture

With the purpose of considering possible influence of the human posture on human resistance on the calculated results, a second step voltage model including a walking human model was built as Fig. 62 shows. All settings of this model are the same as those of the standing model. Only one point which should be paid attention in this model is that two ankle joints of the walking human model were also bent to make both foot bottoms parallel with the ground surface and two feet to be located on the same plane, although actually in most of time, when human walks, the rear foot only touches the ground with forefoot.

This modification was aimed to decrease the influence of touching areas between foot bottoms and the ground surface which can affect the final results to some extent. Thus the two human models in Fig. 61 and Fig. 62 have almost the same touching areas.

All simulations in this section were performed using the stationary current solver of CST EM STUDIO®. As a field solver, its direct results are electric field and current density field. The values of the current through human body can be calculated by integrating the calculated current density field over some predefined faces during the post process stage. There are in total three layers including six surfaces defined in each human body model to realize this function: three surfaces through the right leg and another three through the left leg as Fig. 63 and Fig. 64 show. This arrangement was aimed to verify body current values flowing through different positions of the same leg and compare the body current values through different legs. Because the background material of these two step voltage models was set as air with zero electrical conductivity, integral values of the current density field are exactly the values of body current flowing through the leg.

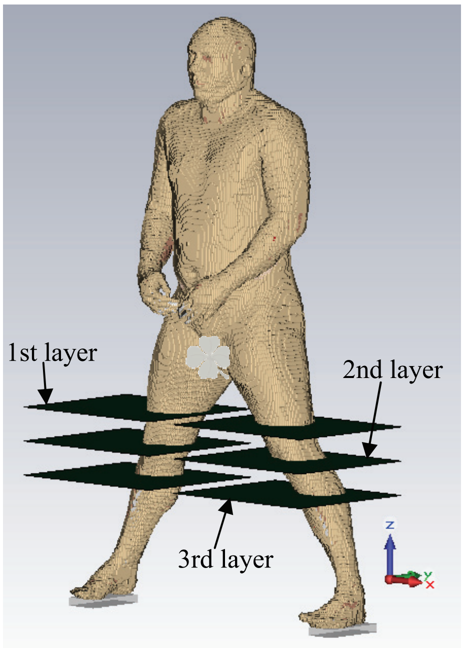

Fig. 63 Six surfaces defined in the standing human model used to calculate current values

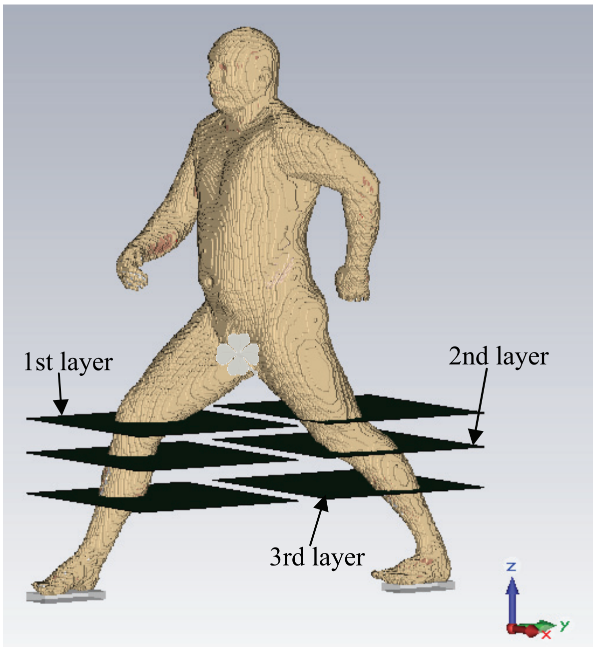

Fig. 64 Six surfaces defined in the walking human model used to calculate body current values

In these two models the step voltage values were calculated based on the effective values of the common power lines. The material properties of human tissues were calculated based on the Cole-Cole dispersive model at 50 Hz which are listed in Table 2 on page 13. With the parameter sweeping function of CST EM STUDIO®, the distance parameter was swept from 1 m to 20 m with 1 m interval. At the same time, the step voltage values, which were defined as a function of the distance parameter, would be changed automatically in accordance.

Before the simulation is performed formally, it’s necessary to perform the convergence calculation firstly to study the influence of the voxel size and mesh cells to the final results. Table 14 and Fig. 65 show how whole body current changes with the voxel size and the number of mesh cells, while the step voltage is fixed to be 220 V. It can be seen that four mm voxel size and around 14.5 million mesh cells are already accurate enough for this simulation. Using three mm or four mm voxel size human body model requires much more mesh cells, and then needs much more memory.

Table 14 Convergence study based on 220 V step voltage between two feet

Voxel size / mm	8	6	5	4	3	2
Num. of mesh cells	11,476,290	11,674,530	12,072,489	14,479,368	35,123,088	116,385,060
Body current / mA	49.3	56.3	58.5	65.5	66.6	65.8

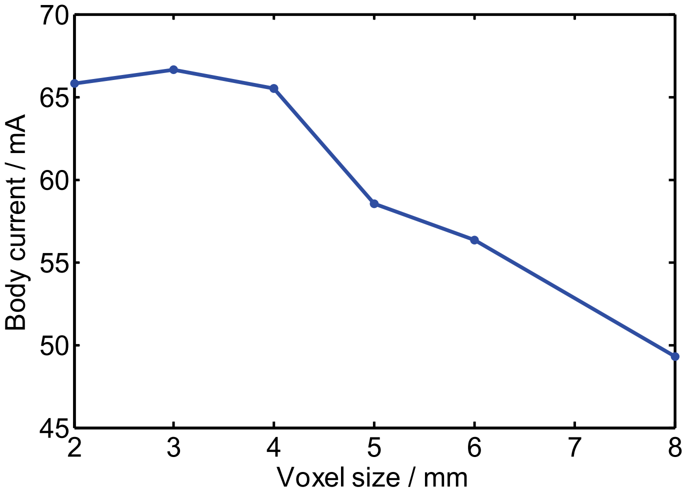

Fig. 65 Relationship between the body current and the voxel size for convergence study

After the simulation was finished, the relationship between the whole body current and the distance between the victim and the touching point of the power line was calculated and shown in Fig. 66. Positions and serial numbers of corresponding surfaces can be found in Fig. 63 and Fig. 64.

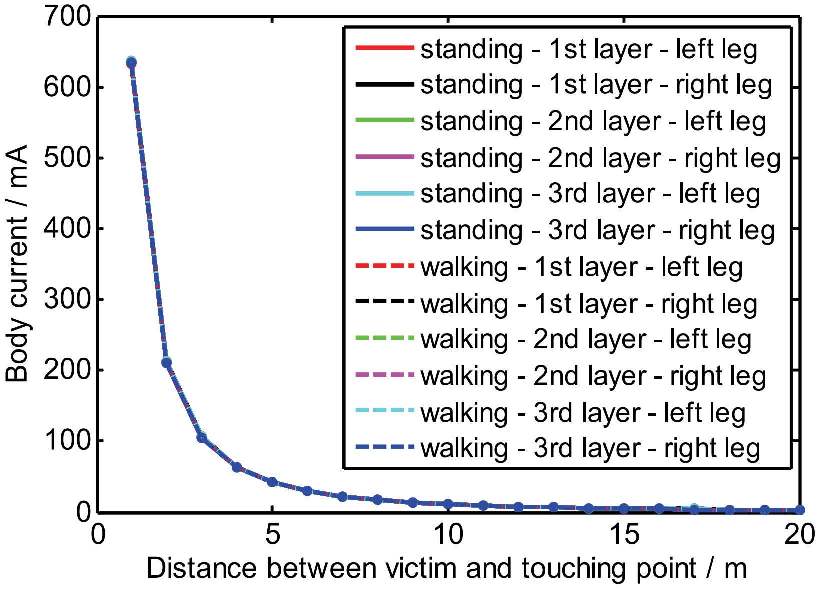

Fig. 66 The relationship between the whole body current through different layer surfaces and the distance between the victim and the touching point

Fig. 66 shows that all twelve result curves superpose each other completely, and all data points at the same x coordinate also superpose each other. When the distance between the victim and the touching point is 1m, comparing with the data calculated under the condition “standing – 1st layer – left leg”, the relative errors of the other data were calculated as Fig. 67 shows. It can be seen that all relative errors are below 0.6%, which is a very low level. The other values of the distance between the victim and the touching point have similar relative error levels.

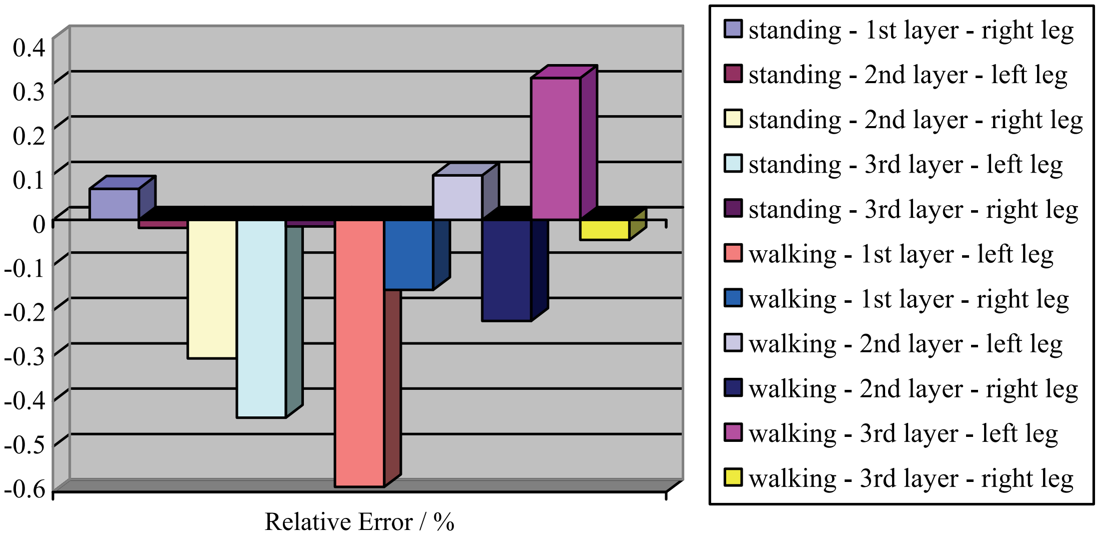

Fig. 67 Relative errors of the whole body current when the distance between the victim and the touching point is 1m, the reference value is the whole body current calculated under the condition “standing – 1st layer – left leg”

The results shown in Fig. 66 and Fig. 67 indicate following three points: firstly the values of body current through different positions of the same leg are identical; secondly the values of body current through right leg equals that through left leg as it should be, thus the first two points above have also verified the validity of these two simulation models; thirdly the value of body current through the human body model with standing posture is the same as that through the human body model with walking posture, which means that human body models with different postures have almost the same electrical resistance.

In conclusion, the whole human body model itself can be considered as a conductive wire, the current excited by the step voltage flows from the PEC patch below right foot bottom which is loaded with high electric potential, passes right leg, abdomen, left leg, at last flows to the PEC patch below left foot bottom which has zero electric potential value. The whole model can be simplified as a simple electric circuit including only one wire loaded with different electric potentials at two ends. The current in this equivalent circuit through any cross section has the same value, and the posture of the human body can hardly influence the electrical resistance or current value of the equivalent circuit. Detail body current values in Fig. 66 through the first layer faces are listed in Table 15.

The electrical resistance of the human body model at 50 Hz frequency calculated from the data in Table 15 is around 3.46 kΩ, which falls in the range from 3 kΩ to 8 kΩ provided by reference [85]. This resistance range was measured between two hands of the volunteers whose dry hands contacted the meter with palm of hands.

In reference [11], the restriction values of the touching current at frequency range below 2.5 kHz are 1 mA and 0.5 mA for occupational and general public case respectively. In order to reach these two safe current values, the calculation results until now show that the distance between the victim and the touching point of the 220 kV downed power line should be further than 35 m and 50 m respectively.

Table 15 Current values corresponding to different distances between victim and touching point (in mA)

Distance / m	Step voltage / V	Standing human model		Walking human model	
		Left leg	Right leg	Left leg	Right leg
1	2200.0	635.6	636.1	631.9	634.6
2	733.3	211.9	212.0	210.6	211.5
3	366.6	105.9	106.0	105.3	105.8
4	220.0	65.6	65.6	65.2	65.5
5	146.7	42.4	42.4	42.1	42.3
6	104.7	30.3	30.3	30.1	30.2
7	78.6	22.7	22.7	22.6	22.7
8	61.1	17.7	17.7	17.6	17.6
9	48.9	14.1	14.1	14.0	14.1
10	40.0	11.6	11.6	11.5	11.5
11	33.3	9.6	9.6	9.6	9.6
12	28.2	8.1	8.2	8.1	8.1
13	24.2	6.9	6.9	6.9	6.9
14	20.9	6.1	6.1	6.0	6.0
15	18.3	5.3	5.3	5.3	5.3
16	16.2	4.7	4.7	4.6	4.7
17	14.4	4.2	4.2	4.1	4.1
18	12.9	3.7	3.7	3.7	3.7
19	11.6	3.3	3.3	3.3	3.3
20	10.5	3.0	3.0	3.0	3.0

As it has been mentioned before, the restriction values in reference [11] all have a safe factor around 10. It means for normal healthy person in normal conditions, the restriction value of a safe touching current can reach around 10 mA for occupational case, which corresponds to around 11 m distance based on the data in Table 15. The data in Table 10 and Table 11 both show that 10 mA touching current at 50 or 60 Hz frequency is the let-go threshold and the victim shocked by such level current will feel pain. Thus 10 mA is really a dangerous current level that cannot be exceeded.

Apart from the values of touching current through whole human body, to master more information about current density distribution in the human body, two cut-plane drawings in Fig. 68 and Fig. 69 were created to display the current density distribution in legs and trunk of the standing and walking human body model. The results shown in these two figures were both calculated from the same models above with 11 m distance between the victim and touching point of the downed power line.

Fig. 68 shows that in the human body, the current excited by the step voltage mainly concentrates in two legs and abdomen, which is mainly because the excitation sources (two PEC patches loaded with electric potentials) were located below feet and were relatively far away from the upper part of the human body. It can be also observed that the current density field is much stronger near the joints of the leg such as knee or ankle, which is caused mainly by human body structure and different conductivity values of different tissues. At 50 Hz frequency, the conductivities of bone and marrow are 0.02 and 0.0016 S/m respectively, which are much lower than those of muscle (0.23 S/m) or blood (0.7 S/m). In the human leg, except for fat and skin, the calf and thigh mainly consist of muscles, blood and comparatively thin bone, while most part of the knee or ankle joint is bone and marrow. Apart from that, the calf and thigh are much thicker than the part of leg near the knee or ankle joint. It means that the cross sections of the calf or thigh are much larger than that of the knee or ankle joint, at the same time they also include much more tissues with higher conductivity. Because the body current through any cross section of the leg is identical, the current density must be much stronger near the knee or ankle joint to get the same body current value with that passes the calf or thigh.

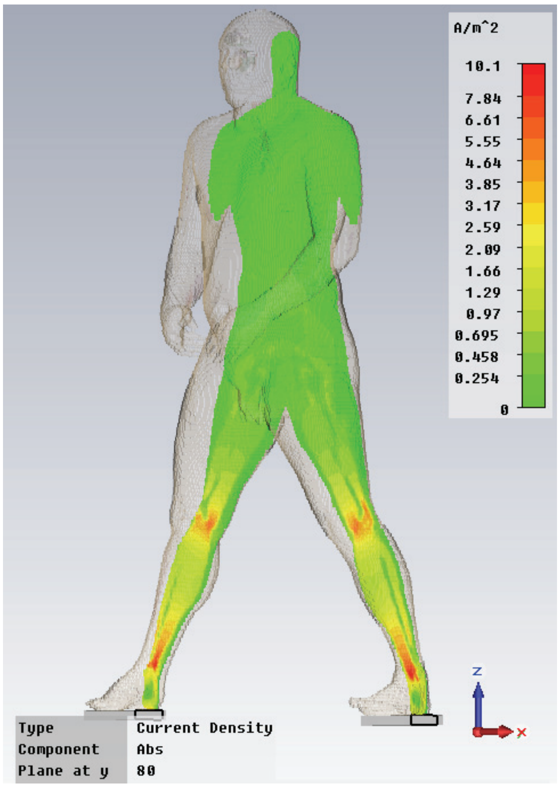

Fig. 68 Current density distribution in the standing human model with 11 m distance

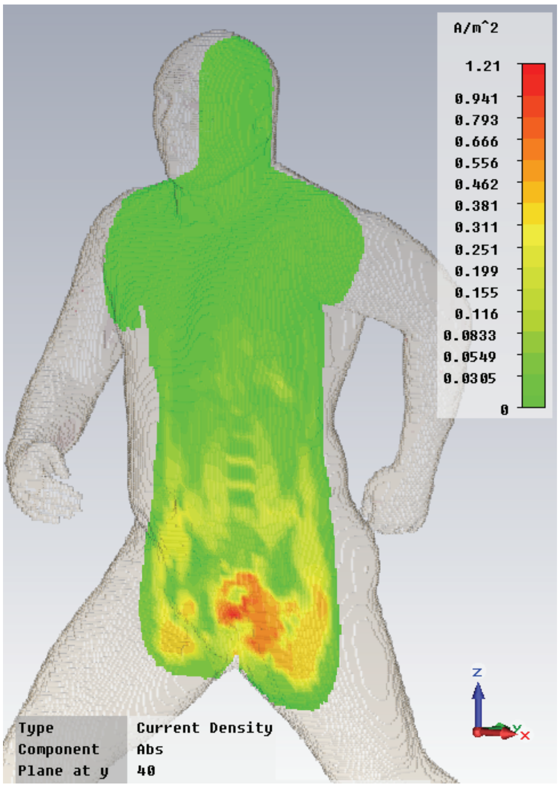

Fig. 69 Current density distribution in the trunk of the walking human model with 11 m distance

A relatively high value of the current density in Fig. 68, around 8 ~ 10 A/m^2, appears near the knee or ankle joint. This range exceeds the restriction current values or even all experimental data from the literature mentioned above by a great deal. This means that 11 m distance is not really a safe distance for the victim under the calculation conditions above. But fortunately the dangerous areas with such high current density values are not so large, they appear only near the knee or ankle joint. Values of the current density in other parts of the human body are much smaller, as Fig. 69 shows. The relatively high value of the current density in the abdomen is around 1 A/ m^2, which appears near the bladder, whose conductivity is also quite high, around 0.21 S/m.

Finally it should be also noticed that the fact that the comparatively larger current densities concentrate in the lower part of the human body, is a comparatively good situation, because the current doesn't pass any important organs of the victim. For example Fig. 70 and Fig. 71 display the current density distribution near the heart of standing and walking human model while distance parameter is 11 m. In these two figures the maximum values of the current density are 8.04 mA/m^2 and 9.75 mA/m^2 respectively. They are already lower than the restriction values of the current density (10 mA/m^2) of the ICNIRP guidelines for occupational case. Fig. 70 and Fig. 71 also show that in the blood of the aorta and ventricle, the current density is a little stronger, which is also because the blood has a much higher conductivity value. Apart from that, the flowing direction of the current is different between the standing and walking model because of different leg postures. As a result, the current density distribution near these two hearts is also a little different. In the heart of the walking human model as Fig. 71 shows, the position of the area with higher current density values is a little lower than that of the standing human model.

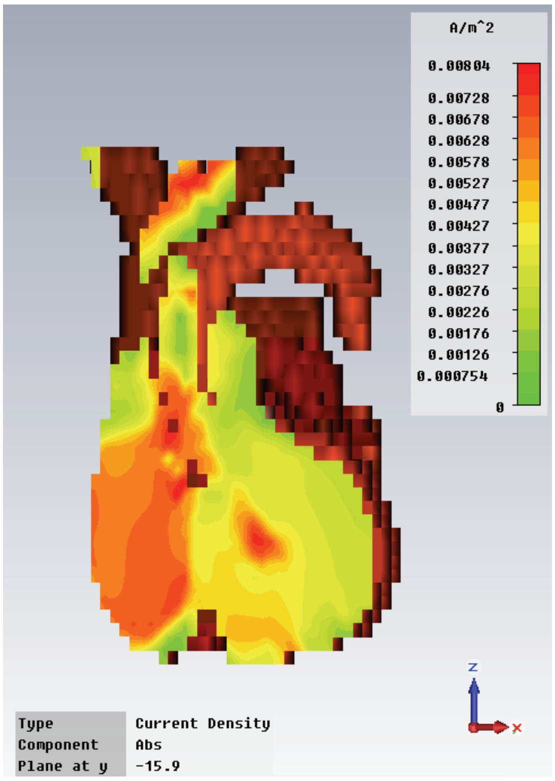

Fig. 70 Current density distribution near the heart of the standing human model with 11 m distance

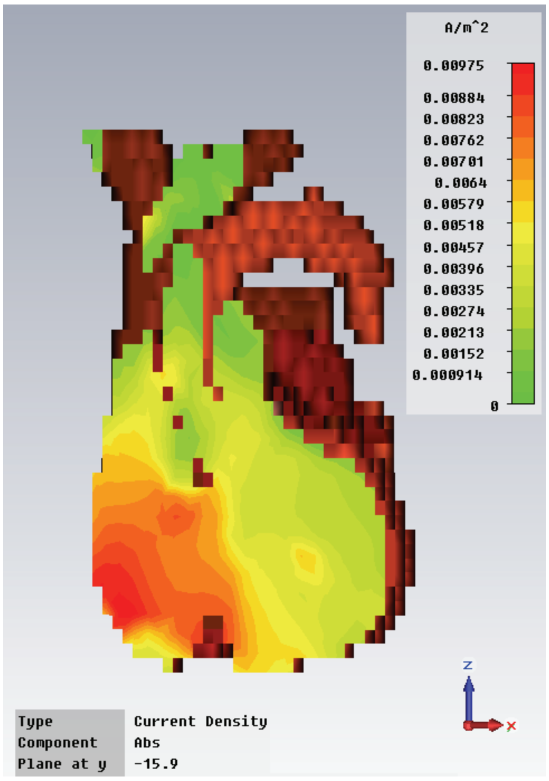

Fig. 71 Current density distribution near the heart of the walking human model with 11 m distance

Although the body current will not pass through most important organs at the very beginning, in reality often the human will fall onto the ground if he or she is shocked by the step voltage, and then the current will have the possibility to pass most organs of the victim, especially the heart. So if any person happens to stand or walk in the region with the step voltage, jumping out of it with single foot or just running away to a safe place is the safest way to save him or herself.

5.1.5. Influence of the Body Current Path

In 1965, Sam measured the electric voltage around the heart with 220 V excitation voltage along different body current paths of a dead body [86]. Fig. 72 shows the electric field distribution near the heart of the walking human model with 220 V, 50 Hz voltage excited between left hand and left foot. Sam's measurement result shows the electric voltage around the heart is 12.9 V/m for left hand to left foot current path. This value falls very well in the value range shown in Fig. 72, and is very near the average value. From the simulation results, the electric voltages are 658.12 mV, 624.10 mV and 572.43 mV respectively for left upper to right down side, right upper to left down side, and front upper to back down side of the heart. These three values are also very near Sam's measurement results, which are 660 mV, 600 mV and 580 mV respectively.

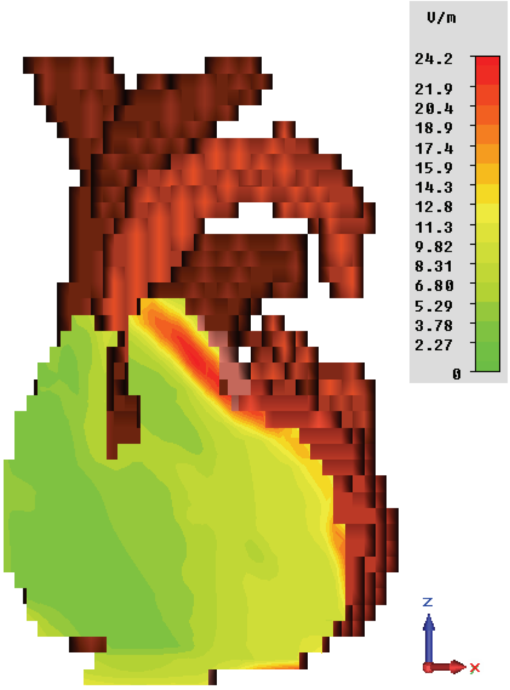

Fig. 72 Electric field distribution near the heart of the walking human model with 220 V voltage between left hand and left foot

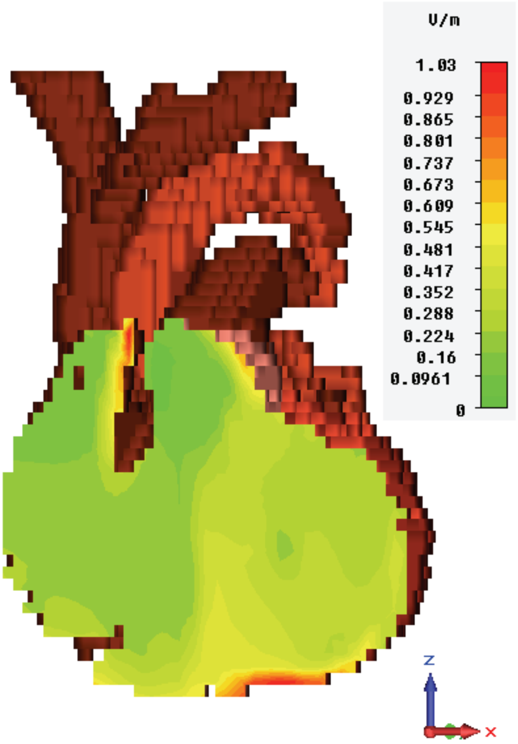

Fig. 73 Electric field distribution near the heart of the walking human model with 220 V voltage between two feet

Fig. 73 shows the electric field distribution near the heart of the walking human model with 220 V step voltage between two feet. Comparing with the body current path from left hand to left foot, the heart is far away from the excitation source for the body current path between two feet. As a result, the value range of the electric field strength shown in Fig. 73 is nearly only around 1 / 25 = 0.04 of the value range shown in Fig. 72. This ratio matches very well with the heart current correction factor F = 0.04, which is defined by the standard IEC 60479 [87], and will be used in following section.

5.2.Step Voltage Caused by Lightning Current

Besides the downed power line introduced above, a lightning-stroke can also lead to the dangerous step voltage. Thunderstorms and lightning flashes are natural weather phenomena and until now no available devices can prevent them. Lightning flashes striking structures or earth nearby are hazardous to people, structures and internal contents of the structures. As one of the main harmful effects of the lightning current, the step voltage will be simulated and analyzed in this section.

When a lightning flash strikes the earth, structures or buildings, the lightning current can flow into the ground through any grounded conductive object such as a metal rod as Fig. 74 shows, and then the discharged current in the ground will cause electric field in the ground near the metal rod. This electric field can produce electric potential difference between different places on the ground around the metal rod. If a human happens to stand or walk in this region, an electric potential difference between his or her legs exists – the so-called step voltage, whose value is an important reference parameter that must be considered in designing lightning protection equipment. It will be very dangerous if the lightning current is very strong and the human or animal is very near to the metal rod because of possible very high step voltage.

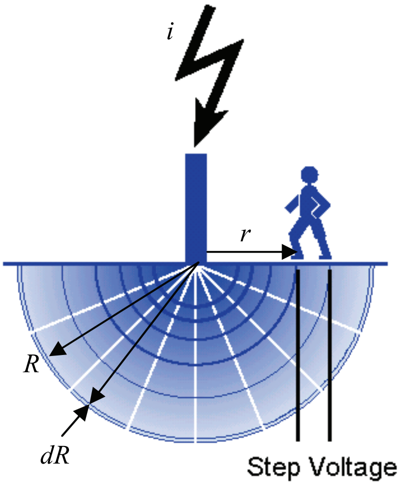

Fig. 74 Step voltage caused by lightning current [84]

Similar to the step voltage caused by the downed power line discussed above, a simple analytical model can be also built here for the step voltage caused by the lightning current as Fig. 74 shows. It's assumed that the discharged lightning current in the ground flows along all directions homogeneously, value of the lightning current is *i* A, and the conductivity of the ground is σ S/m. Thus based on the electric resistance formula $R = l/\sigma S$, the voltage between two sides of a thin spherical-shell with thickness of dR at a distance R away from the metal rod can be calculated as follows:

$$dU = \frac{idR}{2\pi R^2 \sigma} \tag{5-7}$$

Then when the human is r m away from the metal rod, and his or her step distance is $s = 1$ m, the step voltage applied between two feet of the victim can be calculated as:

$$U_r = \int_r^{r+s} dU = \int_r^{r+s} \frac{idR}{2\pi R^2\sigma} = \frac{is}{2\pi r(r+s)\sigma} = \frac{i}{2\pi r(r+1)\sigma} \tag{5-8}$$

A common value of dry soil's electrical conductivity is $\sigma = 0.001$ S/m, and the value of lightning current changes with time, $i = i(t)$, thus equation (5-8) becomes

$$U_r = U_r(t) = \frac{1000}{2\pi r(r+1)} i(t) . \tag{5-9}$$

5.2.1. Time Domain Lightning Current Signal

The time function of the lightning current is different for each lightning strike, and most researchers can use their own special equipments to measure and record these current signals. For analysis purpose, the International Electro-technical Commission (IEC) suggests to use following formulation to express the current wave shape of the short stroke which is one kind of lightning flash corresponding to an impulse current, while a long stroke corresponds to a continuing current [88].

$$i(t) = \frac{I}{k} \cdot \frac{(t/\tau_1)^{10}}{1+(t/\tau_1)^{10}} \cdot e^{(-t/\tau_2)} \tag{5-10}$$

with $I = 200$ kA	peak current,
$k = 0.93$	correction factor for the peak current,
t	time,
$\tau_1 = 19$ µs	front time constant,
$\tau_2 = 485$ µs	tail time constant.

The plot of function in equation (5-10) is shown in Fig. 75.

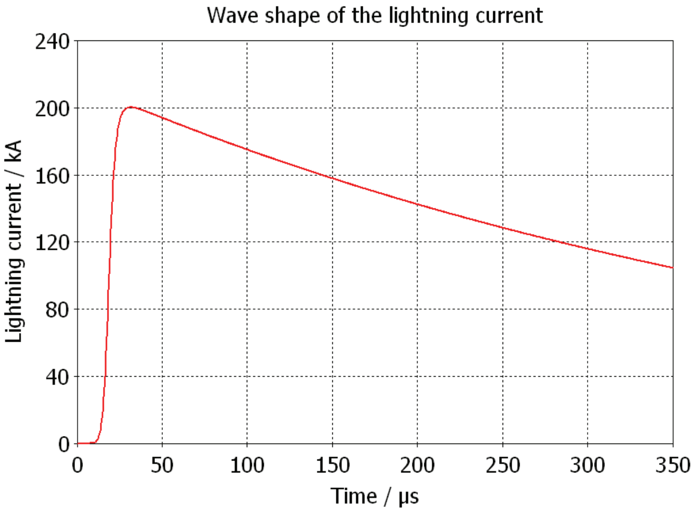

Fig. 75 Current wave shape of the lightning current of the short stroke 10/350 µs model

All values selected above for the parameters in equation (5-10) are based on the first lightning protection level (LPL I) which means the values of the lightning current parameters will not be exceeded with a probability of 99%.

Fig. 75 shows that in this signal, the lightning current will start from zero and increase rapidly to its peak value that is around 200 kA and then decrease slowly and almost linearly to half of the peak value. In this lightning current signal model, the front time of short stroke current (T_1), which is an important virtual parameter in the lightning protection technique and defined as 1.25 times the time interval between the instants when 10% and 90% of the peak value are reached, is 10 µs. The time to half value of short stroke current (T_2), which is another virtual parameter defined as the time interval between the virtual origin and the instant at which the current has decreased to half of the peak value, is 350 µs. So generally this model is called the short stroke 10/350 µs model.

In order to analyze the frequency spectrum of the lightning current signal above, the fast Fourier transformation (FFT) was applied on this signal to obtain its frequency spectrum shown in Fig. 76 and Fig. 77.

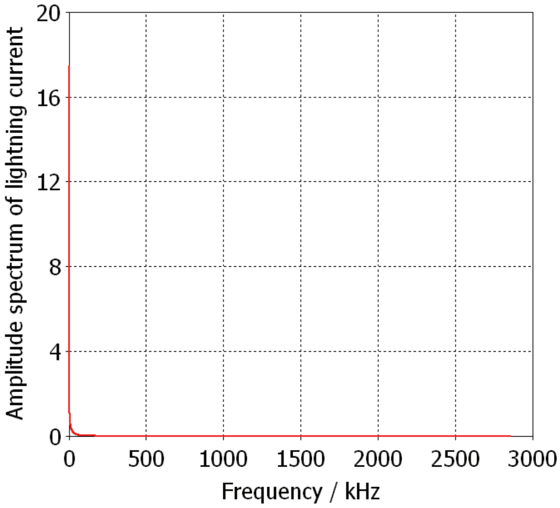

Fig. 76 FFT calculation result of the lightning current signal

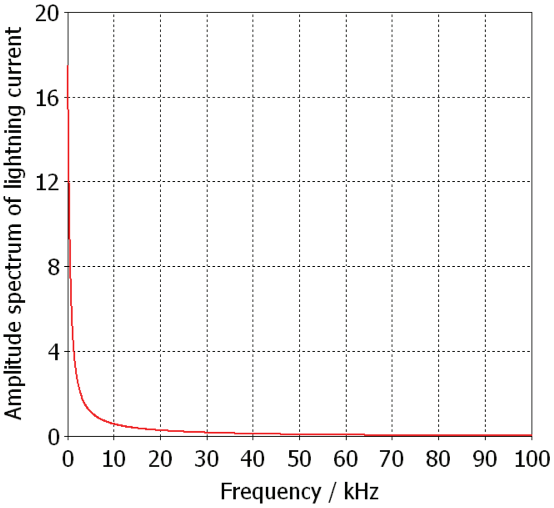

Fig. 77 Enlarged FFT calculation result of the lightning current signal

Fig. 76 shows that the lightning current signal expressed by equation (5-10) has very low frequency spectrum, and its low frequency part is shown in Fig. 77, which indicates that most part of the frequency content of the lighting current signal is below 100 kHz. Thus the shortest wave length of this signal in vacuum can be calculated approximately as:

$$\lambda = \frac{c}{f} = \frac{3\times10^{8}\ \text{m/s}}{100\times10^{3}\ \text{Hz}} = 3000\ \text{m} \tag{5-11}$$

Because 3000 m is much greater than the dimension of the step voltage model, which is almost the same as the height of the human body model, around 1.8 m, the simulation of the step voltage caused by the lightning current is then proved to be a typical electro quasi-static (EQS) problem, and can be speeded up with the reduced *c* technique explained in Chapter 3.

5.2.2. Error Analysis of Reduced *c* Technique

As discussed above in the last sub-section, the step voltage caused by the lightning current is a low frequency transient time domain simulation, which in principle can be solved by the FIT technique introduced in Chapter 3. However, because of restriction of the Courant limit for stability, even for the coarsest voxel size eight mm, in all calculations the length of the stable time step in air cannot exceed

$$\Delta t \le \frac{1}{c\sqrt{\left(\frac{1}{\Delta x}\right)^2+\left(\frac{1}{\Delta y}\right)^2+\left(\frac{1}{\Delta z}\right)^2}} = \frac{1}{3\times10^8\times\sqrt{3\times\left(\frac{1}{0.008}\right)^2}} \approx 1.54\times10^{-5}\ \mu\text{s}. \tag{5-12}$$

In order to sweep the complete lightning current signal length 350 µs, there will be in total 2.27×10^7 time steps needed to finish the whole simulation. With the computer author uses (Intel® Xeon® CPU: E5430, 2.66GHz, 2.66GHz; 16.0 GB of RAM), this calculation can last around 45 days, which is a very long simulation time. And if a smaller voxel size, such as six or four mm, is needed to get a finer anatomic structure, the simulation time will increase several times, which has already exceeded calculation ability of the computer available now.

In order to speed up the simulation, the reduced *c* technique, which was firstly introduced by Holland and then used by several authors to solve magnetic-quasistatic problem (MQS) [53] [54], was studied to be applied into all simulations here. The step voltage model studied here is very different from Holland's magnetic diffusion simulation, which is in principle a MQS problem. To our knowledge, the reduced *c* technique has still not been previously applied to EQS simulations. In EQS, it is not the relative permittivity but rather the materials' relative permeability that can be increased to artificially reduce the speed of the light and thus to obtain a much larger stable time step.

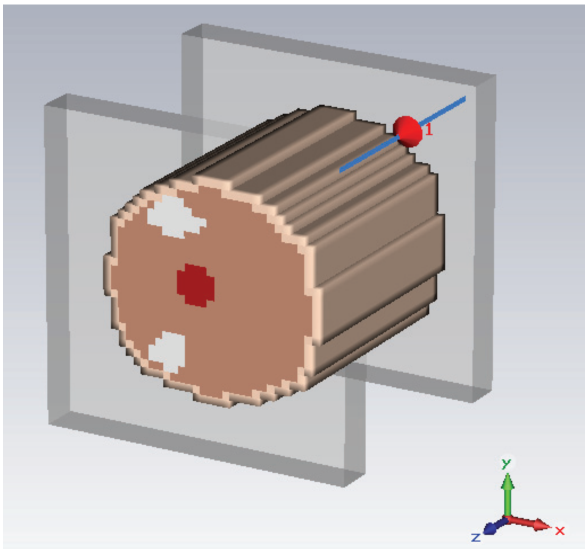

Fig. 78 Simplified model used to test algorithm and analyze error

In all step voltage models, the relative permeability μ_r of all human tissues, organs and background material (air) equals unity. And because of inconvenience of scaling relative permittivity, scaling relative permeability of all materials finally became the strategy here used to reduce the speed of light mathematically and then speed up this typical EQS simulation calculation. To test the performance of the algorithm and analyze the possible error caused by scaling relative permeability, a simplified step voltage model including a simple voxel model was built as Fig. 78 shows.

This simplified model includes similar functional elements and working principle as the full step voltage model which will be introduced in following sub-section. In the middle of the model, there is a simple voxel model including four typical human tissues: blood (red material), muscle (dark brown material), bones (white material) and skin layer (light brown material). At each end of the voxel model, there is one PEC patch touching the voxel model. A discrete voltage port with 10 V electric voltage value was set between the two PEC patches to define the voltage between these two PEC patches. The voxel size is two mm and there are 31 × 32 × 32 voxels along *x*-, *y*- and *z*- direction respectively. The material properties of all human tissues were calculated based on the Cole-Cole dispersive model introduced in Chapter 2. The excitation signal of this model was also defined from the lightning current signal equation (5-10), but in order to decrease calculation time, the signal length was changed to be 100 μs instead of 350 μs as Fig. 79 shows.

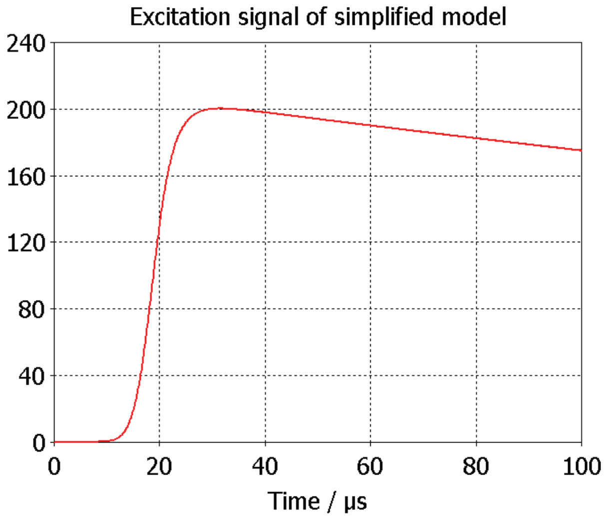

Fig. 79 Excitation signal of the simplified model

It can be seen that the excitation signal shown in Fig. 79 has already included rising, peak, and partial decreasing part of the original signal. Actually after 100 μs the original signal will decrease almost linearly as Fig. 75 shows. Thus, for the purpose of testing the effects of the algorithm and analyzing error of the reduced *c* technique, this signal is accurate enough as reference. Because the original voltage value of the discrete voltage port defined in the model was set to be 10 V, during the simulation, concrete voltage values of the discrete voltage port will be calculated by multiplying 10 V with the excitation signal, and then the peak voltage value is around 2 kV at $t = 31.4$ μs.

It can be deduced from equation (3-52) that increasing relative permeability n^2 times can reduce the speed of light *n* times mathematically and then increase the maximum stable time step of the FIT *n* times. In this simulation, the relative permittivity and conductivity are defined by the Cole-Cole dispersive functions and have no fixed numbers. Increasing the relative permeability of all tissues and background material of the air from 1 to 100 can speed up the original calculation 10 times, similarly increasing it to 400 can speed up the original calculation 20 times and so on.

In order to record electric field strength values at different times, two electric field probes were defined in the model, the first one is located in the center of the model (in the blood tissue) and the other one is in the muscle as Fig. 80 and Fig. 81 show. Because the electric field excited by the voltage between two PEC patches will distribute mainly along *z*-direction, these two probes were also both defined along the *z*-direction.

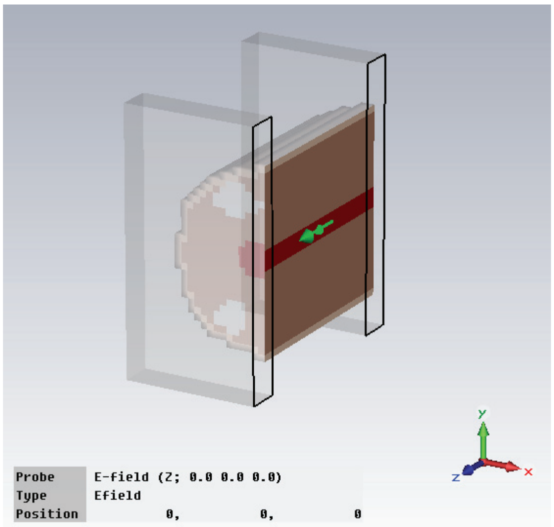

Fig. 80 Probe (green arrow) defined in the center of the model

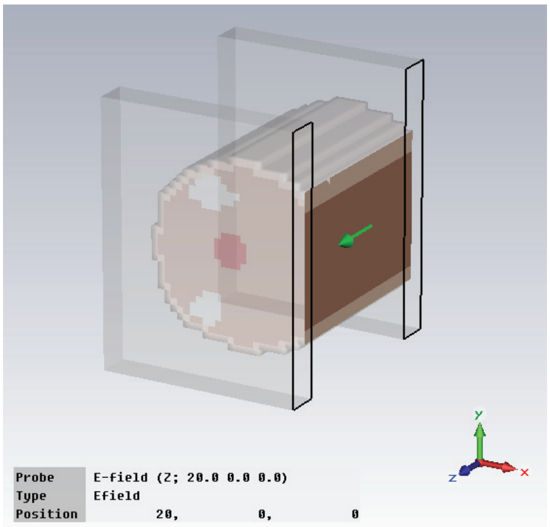

Fig. 81 Probe (green arrow) defined in the muscle of the model

After all calculations were finished, the electric field strength time signals recorded by the two electric field probes defined above with different modified relative permeability values are shown in Fig. 82 and Fig. 83.

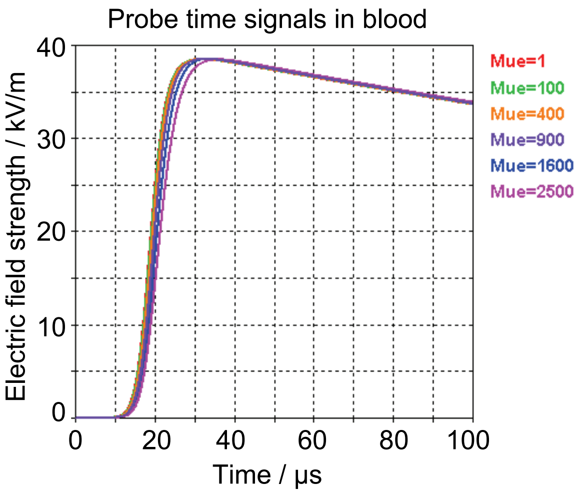

Fig. 82 Time signals of electric field probe defined in the center of the simplified model

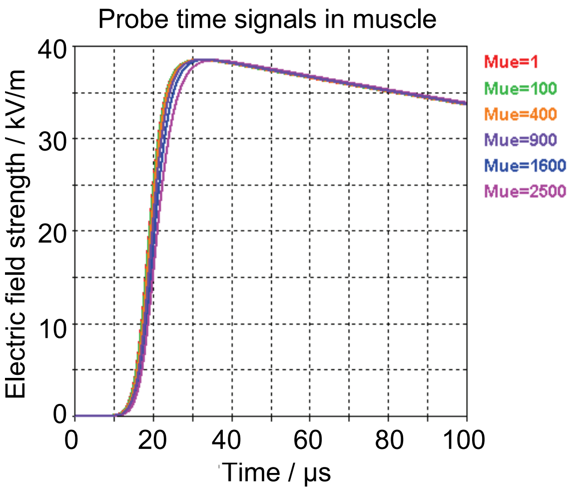

Fig. 83 Time signals of electric field probe defined in the muscle of the simplified model

It can be seen that the electric field strength in the center part (blood) of the simplified model is almost the same as that in the muscle. With the increase of the relative permeability values, in the time range before the peak value t < 31.4 µs, the electric field strength becomes smaller and smaller compared with the reference results (named “Mue = 1”), and the errors increase. In the center part (blood) of the simplified model, the relative errors of the electric field strength introduced by different modified relative permeability values at four typical time points are listed in Table 16. The formula used to calculate the relative error is as follows

$$\text{Relative error} = \frac{\text{Reference Value} - \text{Calculated Value}}{\text{Reference Value}} \times 100\%. \tag{5-13}$$

Table 16 Relative errors caused by using the reduced *c* technique (in the blood of simplified model)

Modified µ value	Speedup times	Relative error caused by the reduced *c* technique			
		t = 20 µs	t = 30 µs	t = 40 µs	t = 50 µs
100	10	1.6%	-0.03%	-0.04%	-0.02%
400	20	7.4%	0.04%	-0.1%	-0.1%
900	30	17.3%	0.2%	-0.2%	-0.2%
1600	40	29.7%	0.6%	-0.4%	-0.4%
2500	50	41.8%	2.5%	-0.6%	-0.7%

Fig. 82, Fig. 83 and all data in Table 16 show that the error caused by the reduced *c* technique is larger before reaching the peak values of the result curves but much smaller after the peak values. Because the rising part of the excitation signal before the peak value only occupies around 1 / 10 of whole signal length, and signal value of this part is much smaller than that of the part after the peak value, from the view of considering influence of the step voltage to human health, the error is acceptable until speeding up original calculation 20 times, where the error is around 7.5% in the middle of the rising part at $t = 20$ µs, and will decrease below 1% after the peak value. Fig. 84 shows electric field distribution on a two-dimensional cut plane through the center of the simplified model with different relative permeability values near the peak of the excitation signal at $t = 30$ µs. It shows that the electric field distribution are almost the same for different modified relative permeability values below $\mu_r = 1600$, and the peak value errors are also very small.

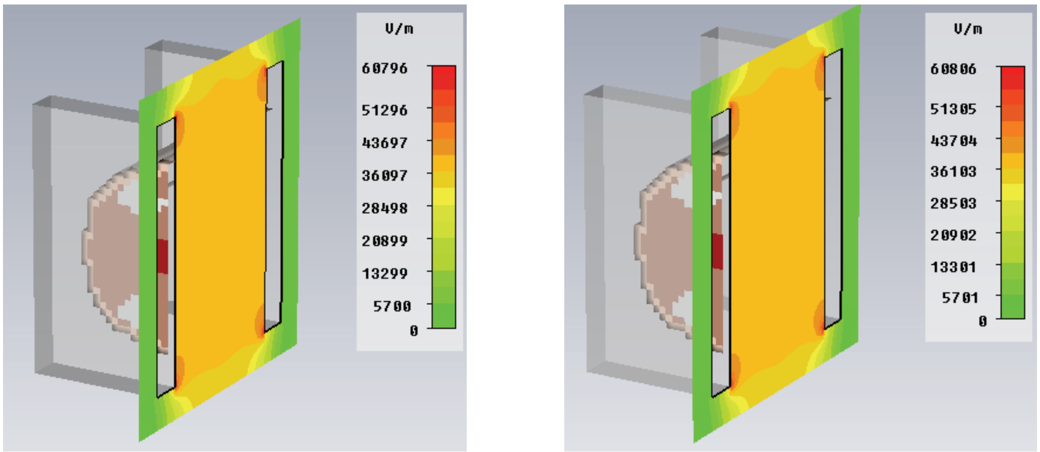

(a) $\mu_r = 1$ (b) $\mu_r = 100$

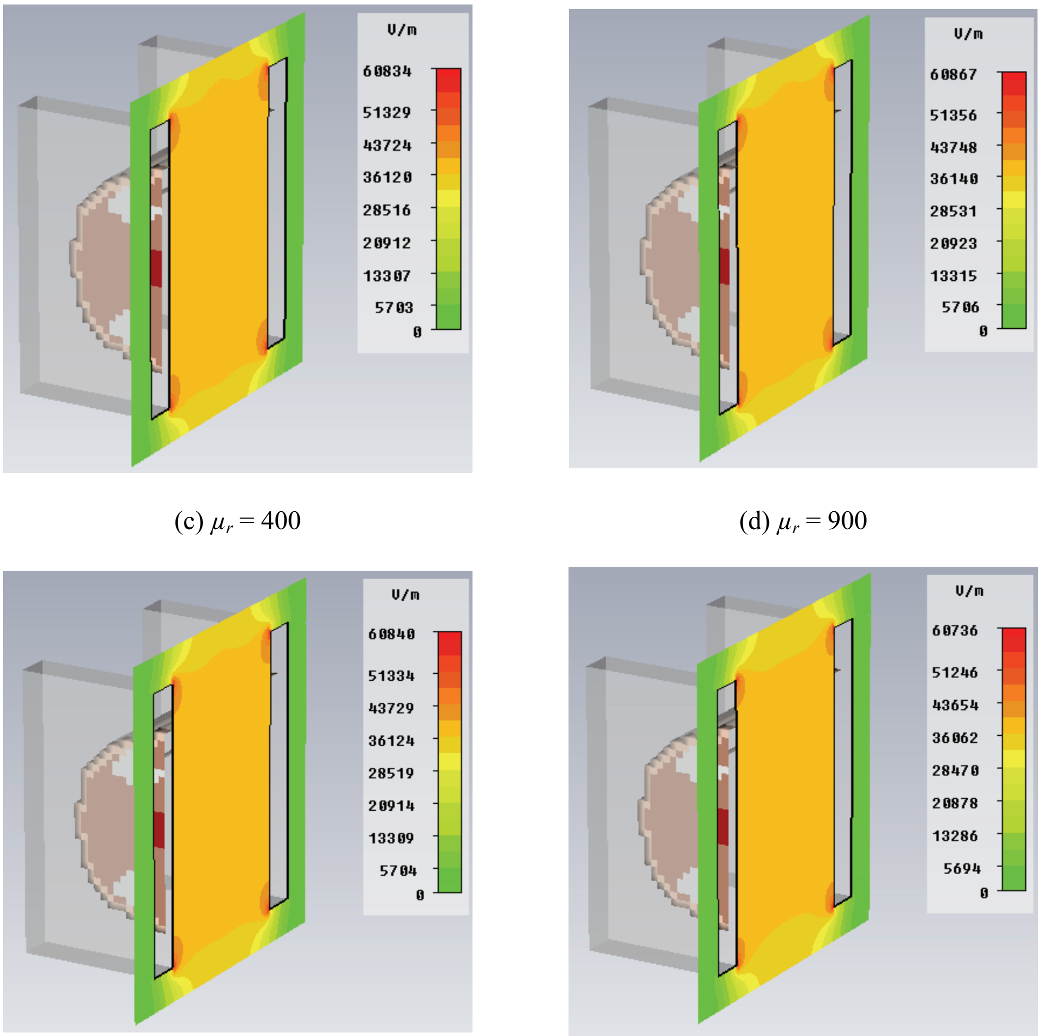

(c) $\mu_r = 400$

(d) $\mu_r = 900$

(e) $\mu_r = 1600$

(f) $\mu_r = 2500$

Fig. 84 Electric field distribution on the cut plane through center of the simplified model

5.2.3. Results Comparison and Discussion

The lightning current signal used in this dissertation is called 10/350 μs lightning current model, which means that this signal uses 10 μs to rise from 10% to 90% of the peak value, and 350 μs to decrease to its half peak value. Its amplitude starts from zero, rises to its peak value very fast and then decreases after reaching its peak value, which looks similar as a half sinusoidal period. Thus if the 10 μs rising time can be seen as 1/4 of a whole sinusoidal period, frequency of this sinusoidal function can be calculated as 25 kHz. In FIT, dealing with dispersive materials needs special algorithms, and non-dispersive materials are much easier to be adjusted while using the reduced c technique. In order to simplify simulations, all human tissues can use standard, non-dispersive material properties which are calculated from the Cole-Cole dispersive material function at $f = 25$ kHz.

To analyze the error caused by using non-dispersive material properties to replace the dispersive material properties, one more simulation was performed based on the same simplified model used above with non-dispersive material properties at *f* = 25 kHz. This calculation was not speeded up by the reduced *c* technique, which means all materials' relative permeability values equal unity. Fig. 85 compares the time signals of the electric field probes located in the center of the simplified model from these two different kinds of material properties. In this figure the red result curve is from the simulation based on the dispersive material properties and not speeded up by the reduced *c* technique, and the green curve is from the simulation mentioned above with the non-dispersive material properties. Apart from that, another blue curve, which was calculated by scaling the excitation signal to make it have the same peak value as that of the red result curve, is also displayed in this figure.

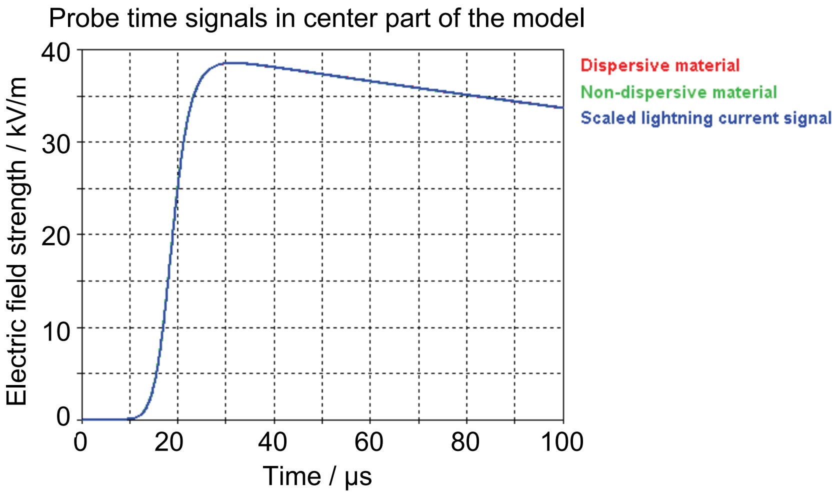

Fig. 85 Results comparison among different calculation conditions

Fig. 85 shows that three result curves superpose each other completely, which means the error caused by using non-dispersive materials instead of the dispersive materials is very small. Compared with the red result curve based on the dispersive materials, the relative errors of the result curves based on the non-dispersive materials and scaled excitation signal are listed in Table 17.

Table 17 Relative errors caused by using normal material properties

Result curves	Relative errors					
	t = 15 µs	t = 20 µs	t = 25 µs	t = 30 µs	t = 40 µs	t = 50 µs
Normal material	0.051%	-0.0013%	-0.0072%	-0.0038%	-0.020%	0.012%
Scaled signal	-0.51%	-0.0014%	-0.036%	-0.021%	-0.016%	-0.019%

All data in Table 17 show that the errors among these three curves are very small, below 1%. Thus both Fig. 85 and Table 17 indicate that in the transient time domain simulation excited by the lightning current with low frequency range, using the non-dispersive human tissue material properties to instead the dispersive material properties will not cause too large errors. From an engineering point of view, using the same model with unit step voltage value to perform one single stationary current calculation, and then scaling the result linearly based on the value of the lightning current signal can also get an acceptable result at different time points. This avoids a lengthy time-domain simulation.

It should be noticed that the second approximation method above, which means scaling the stationary current calculation result based on the value of excitation signal can get an acceptable transient time-domain result, is based on the lightning current signal equation (5-10) which has very low frequency spectrum. Another lightning current signal expression including higher frequency range will have a different performance and then the related transient simulations will not be able to be approximated as a similar way. To show this more clearly, two more simulations, which both used a Gauss impulse as the excitation source, were performed based on the same simplified model used above. The shape of the used Gauss impulse is shown in Fig. 86 and its frequency range is $0 \leq f \leq 200$ MHz which is much higher than that of the lightning current signal. Material properties of all human tissues were still defined by the Cole-Cole dispersive functions, and normal material properties were calculated from the Cole-Cole dispersive functions at middle frequency $f = 100$ MHz. All calculation results are shown in Fig. 87.

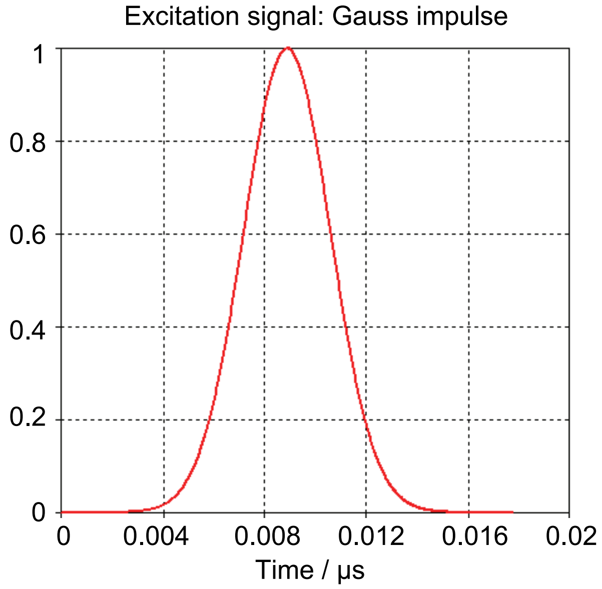

Fig. 86 Gauss impulse used as excitation signal

In Fig. 87 the red curve named "Scaled excitation signal" was generated by scaling the Gauss impulse in Fig. 86 to make it have the same peak value as that of the result curve calculated from the simulation with dispersive material properties. Fig. 87 shows that the peak value of the scaled excitation signal appears at a much earlier time point than that of the time signals of electric field probes, and the scaled excitation signal has completely different configuration as that of the probe time signals at around $t = 0.02$ µs. This means that the method scaling the result from stationary current calculation based on the value of the excitation signal cannot get an accurate enough transient time-domain result, if a lightning current signal including higher frequency range is used as the excitation signal. It can be also seen from Fig. 87 that two result curves from the simulation with the dispersive material properties have higher peak values than the two corresponding result curves from the simulation with non-dispersive material properties, which means using the non-dispersive material properties instead of the dispersive ones will result in some errors, if the excitation signal includes high frequency range.

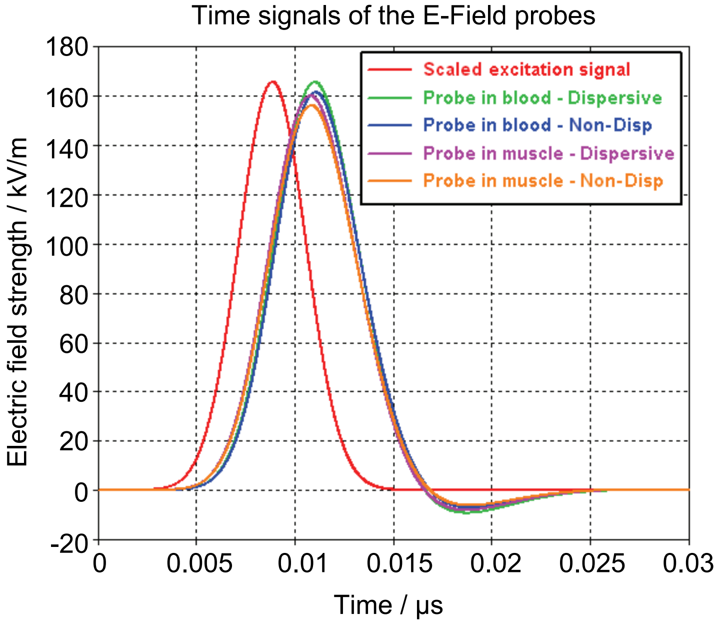

Fig. 87 Comparative analysis of the calculation results based on the Gauss impulse as the excitation source. Two probes were defined in the blood and the muscle respectively. Both dispersive and non-dispersive materials were considered. A scaled excitation signal is also shown here for reference.

5.2.4. Time Domain Calculation

Introduction to Simulation Models

Two full simulation models used to simulate the step voltage phenomenon caused by the lightning current are shown in Fig. 88 and Fig. 89 respectively. In these two models, two voxel-based human body models: one standing and one walking human body model, and the PEC patches below their feet are identical to those used in the simulation model of the step voltage excited by the downed power line in Section 5.1. However, in this simulation, the excitation source comes from the lightning current whose current values change with time. As a result, the step voltage value between two feet of the human body model is time-varying. The fixed electric potential source used in the model of the step voltage excited by the downed power line cannot be used here anymore. Instead, a discrete voltage port was set between the two PEC patches to define the step voltage between two feet of the human body models in the commercial software CST MICROWAVE STUDIO®.

For comparison convenience, the distance between the victim and the grounded metal rod that lighting flash strikes was still set to be r = 11 m. Based on equation (5-9), the step voltage value between two feet of the victim can be calculated as

$$U_r = U_r(t) = \frac{1000}{2\pi r(r+1)} i(t) = 1.206\ i(t)\ \text{(V)} \tag{5-14}$$

where *i(t)* is the time function of the lightning current as equation (5-10) shows, and it should be noticed here that the step distances of these two human models are still 1 m.

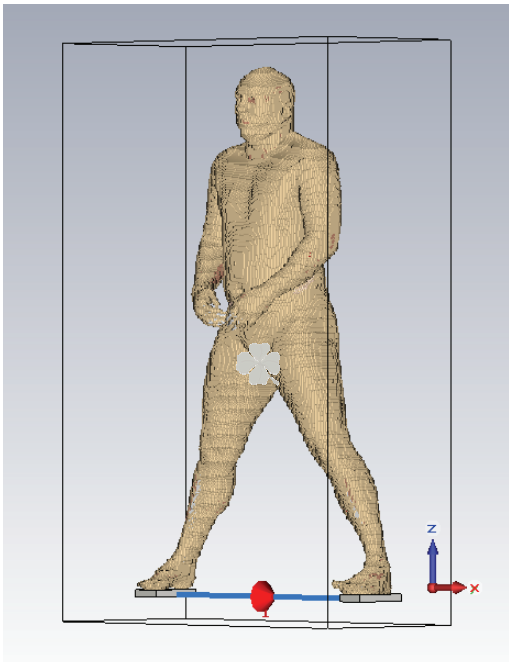

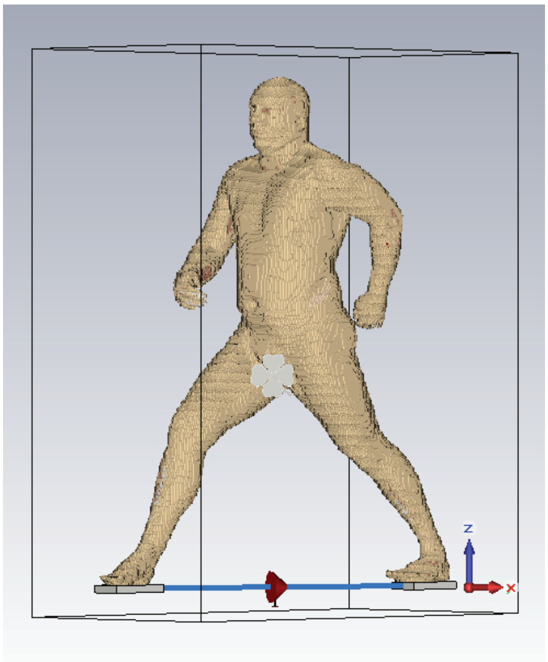

Fig. 88 The model of step voltage excited by lightning current including human model with standing posture

Fig. 89 The model of step voltage excited by lightning current including human model with walking posture

In equation (5-10), the unit of the lightning current is kA. During all simulations in this section, except for testing simulation calculations performed later to analyze possible errors of the reduced *c* technique in next sub-section, original voltage value defined for the discrete voltage port was 1.206 kV, and the excitation signal was defined based on equation (5-10) with a peak value 200, as Fig. 90 shows.

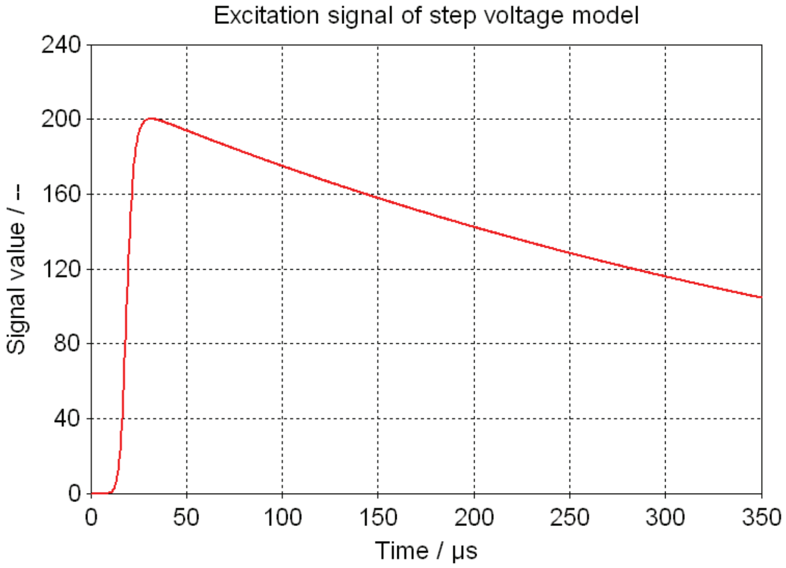

Fig. 90 Excitation signal of simulation model of step voltage excited by lightning current

Error Analysis of Reduced *c* Technique based on HUGO Model

Although the error caused by using the reduced *c* technique has already been analyzed in the last section, the shape of the whole-body human model is very different from the simplified voxel model, after all. Apart from that, because of complicated internal structure, the electric field distribution in the whole-body human model, excited by the step voltage, is much more complicated than that of the simple voxel model. As a result, in order to consider the influence of models' geometric difference and electric field direction, the error analysis of the reduced *c* technique was performed again based on the full step voltage model with standing human body model.

Because the purpose of the error analysis in this sub-section is to verify the error analysis results obtained in the last section, in order to decrease calculation time and for comparison convenience, the mesh cell size used in this sub-section is eight mm, the original voltage value defined for the discrete voltage port is 1 kV, and material properties of all human tissues, which are listed in Table 2 of Chapter 2, are calculated from the Cole-Cole dispersive model at 25 kHz. The length of the excitation signal is reduced to 1/7 of the original length, i.e. 50 μs, which already includes rising, peak, and partial decreasing part of the original signal, and has enough accuracy to analyze possible errors caused by the reduced *c* technique. In all simulations, open boundary conditions are used for all boundaries of the calculation domain.

From equation (3-52) or (5-12), it can be seen that the maximum stable time step, calculated from the Courant limit for stability, is determined by the minimum product of relative permeability and relative permittivity of all materials in the model. At 25 kHz frequency, relative permeability of all human tissues and organs is unity and relative permittivity of most human tissues and organs is greater than 1000, as shown in Table 2. There are only five tissues having a permittivity which is smaller or near 1000: marrow (μ_r = 311.27), fat (μ_r = 355.46), bones (μ_r = 330), skin (μ_r = 1130.8) and gall bladder (μ_r = 126.86). As a result, in the reference model, which was not speeded up by the reduced *c* technique, the maximum stable time step is determined by the relative permeability and relative permittivity of the background material air, which are both unity. Thus increasing only the relative permeability of the air from 1 to 100 can get a stable time step which is ten times greater than the original one, and material properties of all human tissues do not need to be changed. If the original calculation is needed to be speeded up 15 times, apart from increasing the relative permeability of the air from 1 to 225, the relative permeability of gall bladder should be also increased from 1 to 225 / 126.86 = 1.774, and material properties of all other tissues do not need to be changed. Other speeded up time numbers can be realized in an analogous way, and generally only increasing the permeability of the five materials mentioned above can just speed up the original calculation until 50 times (when minimum $\varepsilon_r \times \mu_r = 2500$), which is already fast enough for all simulations here.

With the purpose of recording electric field strength values at different times in different parts of the human body model along different directions, there were in total nine electric field probes defined in the whole body model as Fig. 91 and Fig. 92 shows. The first set including three probes along *x*-, *y*- and *z*- direction were defined in the heart, which is the most important organ. The second and the third set were defined in the bladder and the muscle of left thigh respectively.

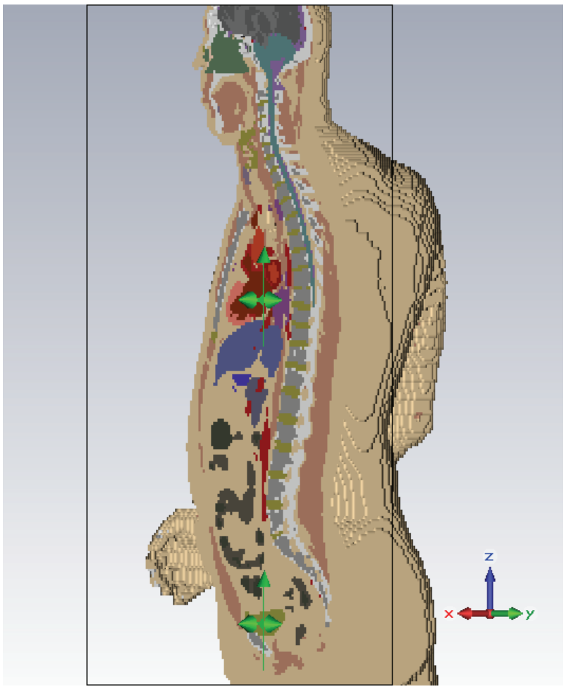

Fig. 91 6 E-Field probes (green arrows) defined in the heart and bladder

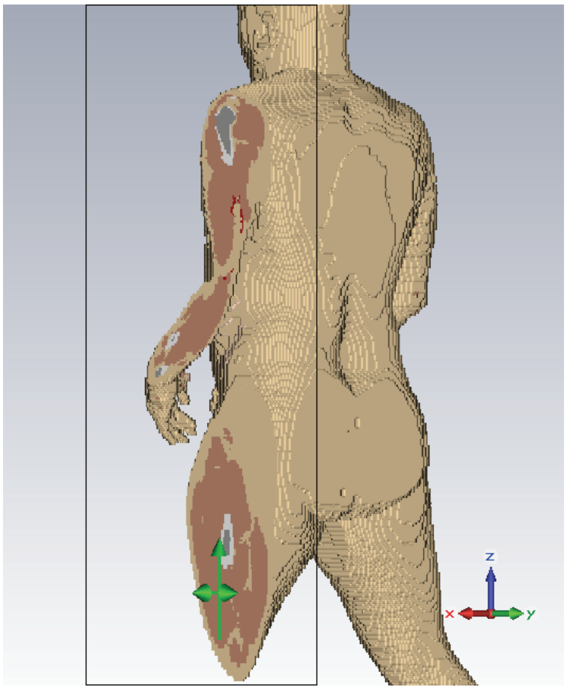

Fig. 92 3 E-Field probes (green arrows) defined in the muscle of thigh

The electric field strength time signals recorded by the nine electric field probes defined above with different modified relative permeability values are shown in Fig. 93. Generally, the higher the relative permeability is increased, the more the simulation will be speeded up. To analyze the errors caused by different speedup time numbers, all calculations above include five different modified relative permeability values. In Fig. 93, all red curves named "Mue = 1" stand for the standard calculation results for reference, which were not speeded up by the reduced *c* technique. The green curves named "Mue = 100" mean the relative permeability of the background material air was increased to 100, while the material properties of the human tissues were not modified. The blue curves named "Mue = 1600" mean the relative permeability of the air was increased to 1600, and relative permeability of the five human tissues mentioned above were also increased to some numbers that can make those material's minimum product $\varepsilon_r \times \mu_r = 1600$. The names of other result curves indicate similar meanings as the blue one.

All result curves in Fig. 93 include a wealth of information. Firstly, it's very convenient to see magnitude and direction of the electric field strength in these three parts of the human body model. Fig. 93 – (a), (b) and (c) show that in the heart, the *x*-component of the electric field strength is much stronger than the *y*- and *z*-component, and *y*-component is very weak and can be neglected. As a result, under the calculation conditions above, the peak value of the electric field strength in the heart is around 190 V/m, and the direction is from the right side of the human body model to the left side and slightly towards up.

Similarly, in the bladder, the peak value of the electric field strength is around 18 kV/m, and the direction is also from the right side to the left side and slightly towards upper front side. In the thigh, the peak value of the electric field strength is around 11 kV/m, and the direction is from top to bottom and slightly towards left back.

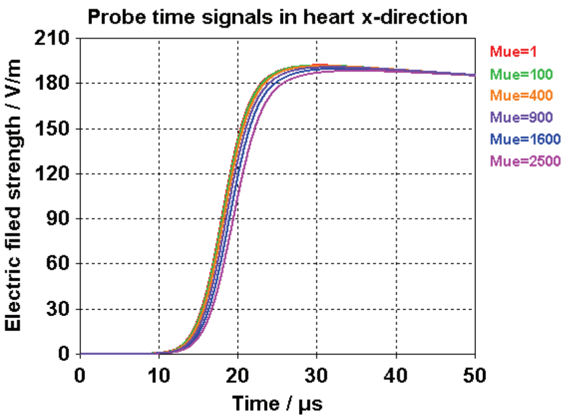

(a) Probe in heart, *x*-direction

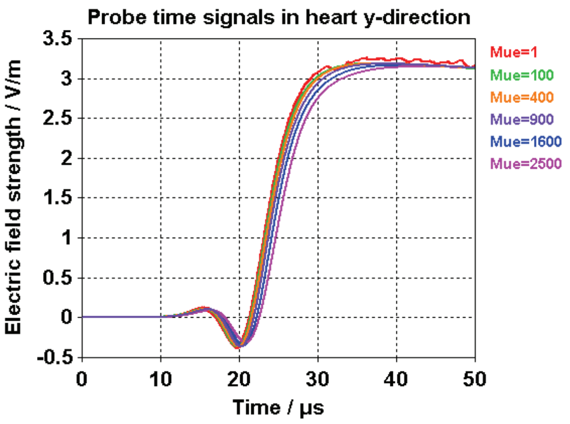

(b) Probe in heart, *y*-direction

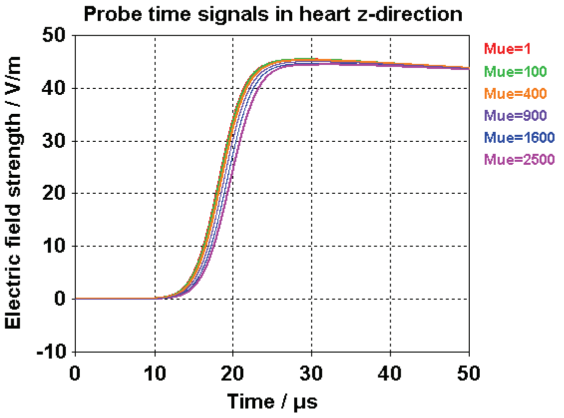

(c) Probe in heart, *z*-direction

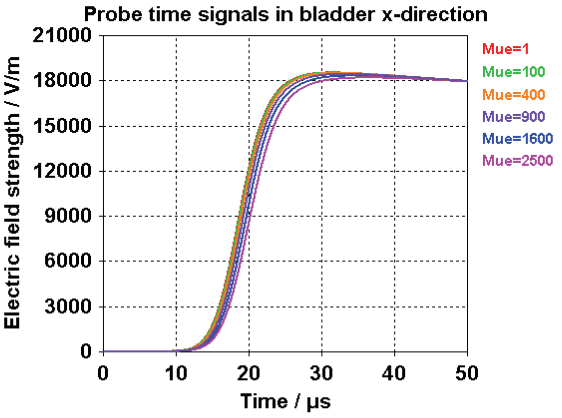

(d) Probe in bladder, *x*-direction

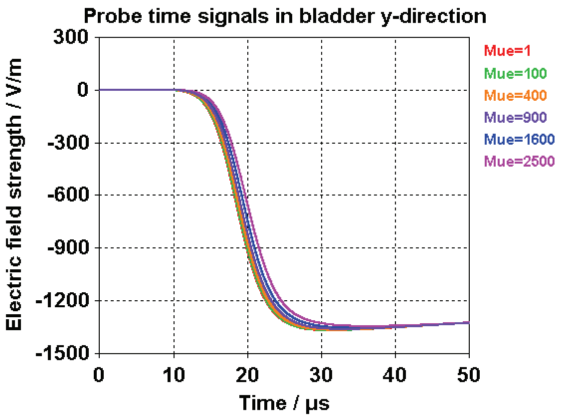

(e) Probe in bladder, *y*-direction

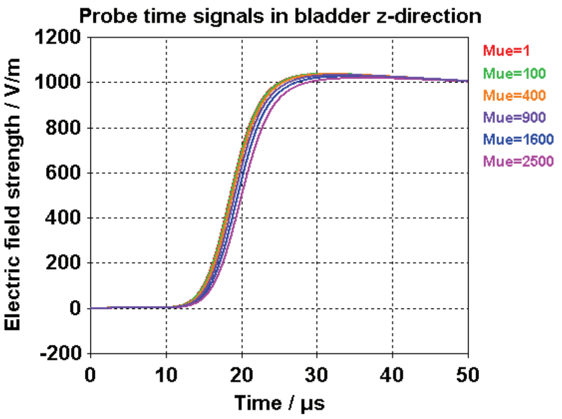

(f) Probe in bladder, *z*-direction

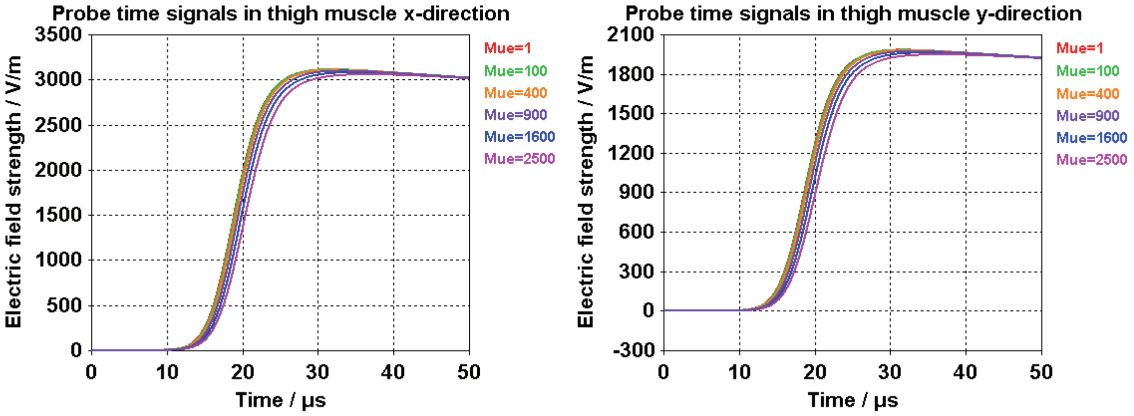

(g) Probe in muscle of thigh, *x*-direction (h) Probe in muscle of thigh, *y*-direction

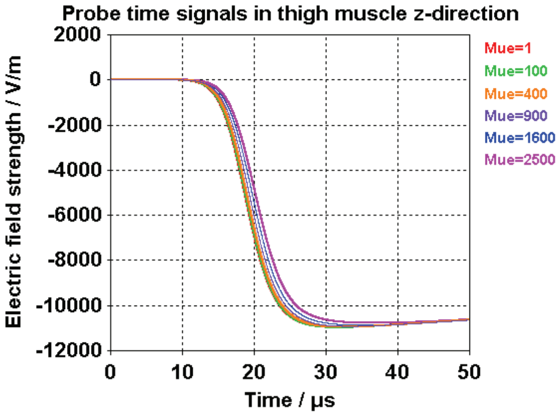

(i) Probe in muscle of thigh, *z*-direction

Fig. 93 Time signals of all E-Field probes defined in heart, bladder and muscle of thigh

From Fig. 93, it can be also seen that with the increase of the relative permeability values, especially in the time range t < 30 µs, the electric field strength becomes smaller and smaller compared to the reference results; therefore, at the same time point, the error between the result curves with modified relative permeability values and the standard result curves increase. In the three human body parts discussed above, the relative errors of main components of the electric field strength caused by different modified relative permeability values at four typical time points are listed in following three tables. The formula used to calculate the relative error is (5-13).

Table 18 Relative errors caused by using the reduced *c* technique (heart *x*-direction)

Modified µ value	Speedup times	Relative error caused by the reduced *c* technique			
		t = 20 µs	t = 30 µs	t = 40 µs	t = 50 µs
100	10	1.2%	0.07%	-0.09%	-0.07%
400	20	4.5%	0.3%	-0.1%	-0.1%
900	30	9.7%	0.7%	-0.01%	-0.2%
1600	40	17.4%	1.5%	0.2%	-0.1%
2500	50	27.1%	2.6%	0.7%	0.06%

Table 19 Relative errors caused by using the reduced *c* technique (bladder *x*-direction)

Modified μ value	Speedup times	Relative error caused by the reduced *c* technique			
		t = 20 μs	t = 30 μs	t = 40 μs	t = 50 μs
100	10	1.4%	0.03%	-0.02%	-0.02%
400	20	5.2%	0.3%	-0.04%	-0.07%
900	30	11.3%	0.8%	0.05%	-0.1%
1600	40	19.8%	1.7%	0.3%	-0.07%
2500	50	29.8%	2.9%	0.7%	0.08%

Table 20 Relative errors caused by using the reduced *c* technique (thigh muscle *z*-direction)

Modified μ value	Speedup times	Relative error caused by the reduced *c* technique			
		t = 20 μs	t = 30 μs	t = 40 μs	t = 50 μs
100	10	1.4%	-0.02%	-0.05%	-0.06%
400	20	5.4%	0.2%	-0.07%	-0.1%
900	30	11.8%	0.8%	0.02%	-0.2%
1600	40	20.6%	1.7%	0.3%	-0.1%
2500	50	30.8%	2.9%	0.7%	0.05%

The lightning current signal reaches its peak value at t = 31.4 μs. Fig. 93 and all data in the three tables above show that the error caused by the reduced *c* technique is comparatively larger before reaching the peak value but much smaller after the peak value. The reason for this is because the part of the signal before its peak value is a transient rising part, and after the peak value the signal will decrease almost linearly. In principle the reduced *c* technique is an approximate approach to solve the quasi-static problems, and then any simulation including lower frequency range can get a more accurate result.

Because the rising part of the excitation signal only occupies around 1 / 10 of the whole signal length, and signal value of this part is much smaller than that of the part after the peak value, from the view of considering influence of step voltage to human's health, the error is acceptable until speeding up original calculation 30 times, where the error is around 10% in the middle of the rising part at t = 20 μs, and will decrease below 1% after the peak value. In order to ensure an acceptable calculation accuracy, all calculations in next sub-section used the reduced *c* technique to speed up calculations around 20 times, where the error is only around 5% at t = 20 μs, and decreases below 0.5% near and after the peak value.

Error Correction through Parameter Modification

From Fig. 93, it can be seen that with the increase of the relative permeability from 1 to 2500, the result curves are all shifted towards right side, which is the main error source of the rising part of all result curves. The reason for this phenomenon is the reduced speed of light, because the electromagnetic fields, which travel with the reduced speed of light, will take a little longer time to reach the same point from the excitation sources.

The idea here is to use some new methods to shift back the result curves, which were calculated based on the reduced *c* technique, towards left side to decrease the errors of the rising part of the result curves.

Based on the results of the simulation involving a simplified voxel model, section 5.2.3 has proved that the scaled stationary current simulation results can be used to approximate the transient simulation results at different time points. This conclusion is proved again now by following Fig. 94, which shows the time signal recorded by the E-Field probe defined in the bladder along *x*-direction during the transient simulation.

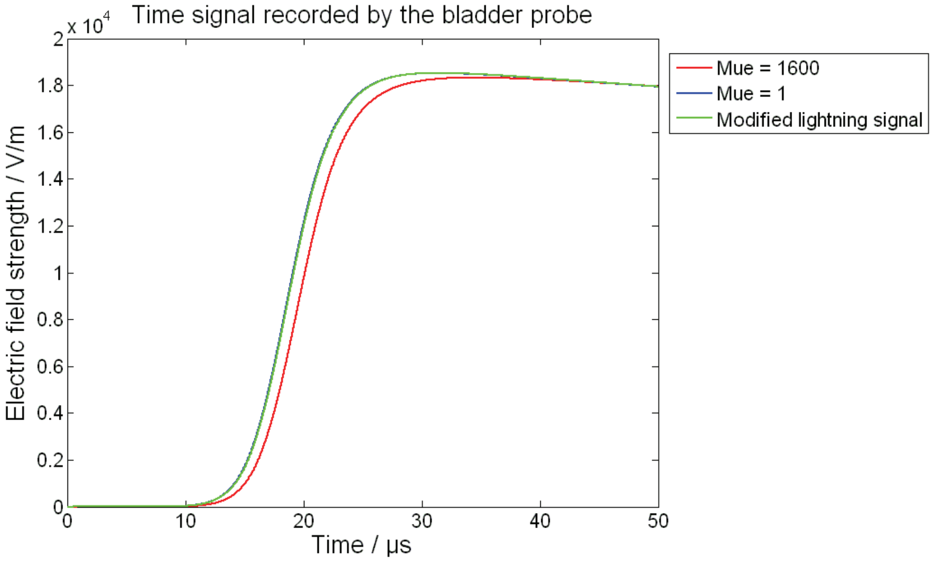

Fig. 94 Time signals recorded by the E-Field bladder probe based on two different relative permeability values, the modified lightning current signal is also shown for reference.

In Fig. 94, the green lightning current signal, whose peak value was modified to be the same as the blue signal recorded by the E-Field bladder probe, superposes completely with the blue curve. Because of the influence of the reduced *c* technique with relative permeability $\mu_r = 1600$, the red result curve, which was also recorded by the same E-Field bladder probe, is shifted a little towards right side.

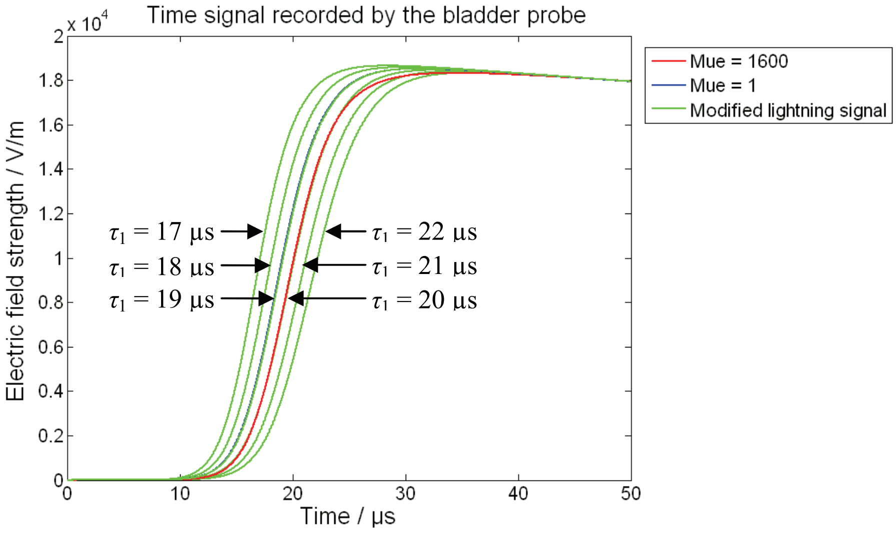

Fig. 95 The modified lightning current signal with front time constant τ_1 = 17, 18, 19, 20, 21 and 22 µs, the time signals recorded by the E-Field bladder probe based on two different relative permeability values are also shown for reference.

Equation (5-10) shows that the lightning current signal has three important parameters: the correction factor for the peak current $k = 0.93$, the front time constant $\tau_1 = 19$ µs and the tail time constant $\tau_2 = 485$ µs. In these three parameters, the front time constant τ_1 mainly influences current wave shape of the rising part of the lightning current signal as Fig. 95 shows.

Fig. 95 shows that with the increment of the front time constant τ_1, the green modified lightning current signals will be shifted from left to right side little by little. When τ_1 is changed from the standard value 19 µs into 20 µs, the green modified lightning current signal will be shifted a little towards right side and then superpose with the red time signal recorded by the E-Field bladder probe, which was calculated based on reduced c technique with modified relative permeability $\mu_r = 1600$.

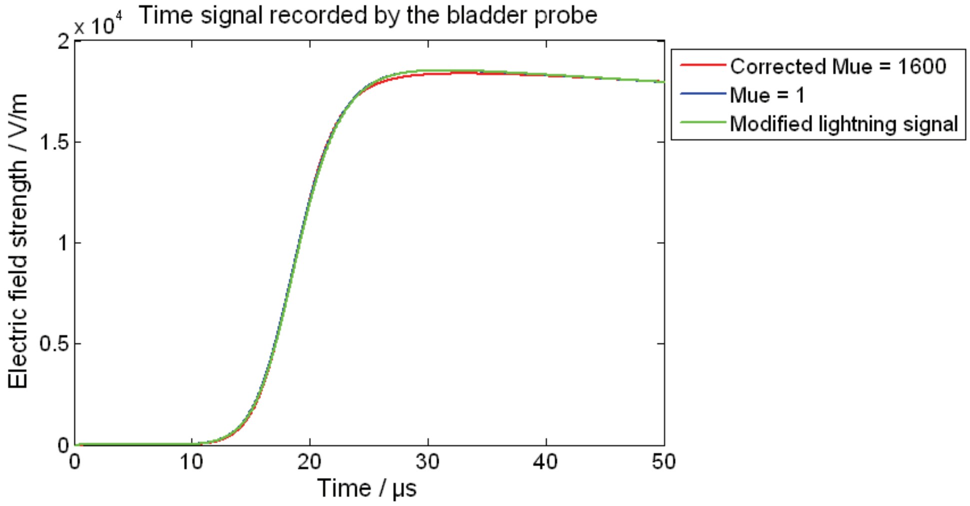

Fig. 96 Corrected time signal recorded by the E-Field bladder probe, which was calculated from the simulation speeded up by the reduced c technique with relative permeability $\mu = 1600$.

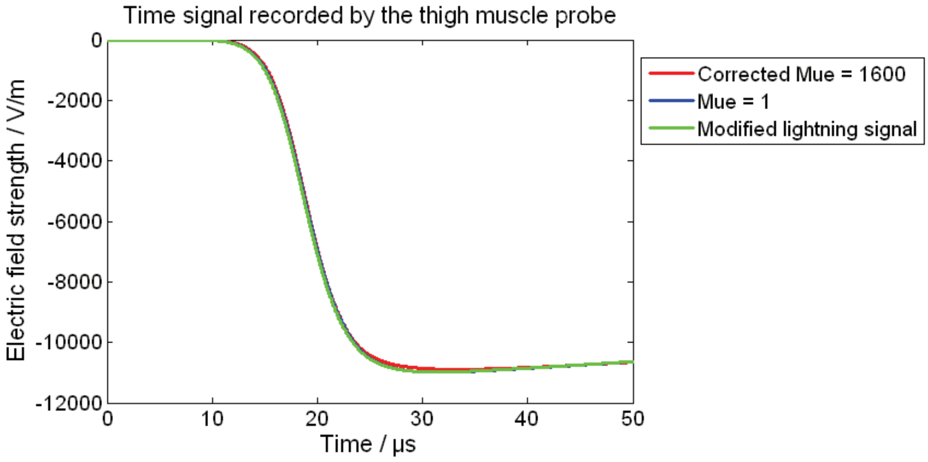

Fig. 97 Corrected time signal recorded by the E-Field thigh muscle probe, which was calculated from the simulation speeded up by the reduced c technique with relative permeability $\mu_r = 1600$.

Now in order to shift the red result curve “Mue = 1600” to the standard blue result curve “Mue = 1”, the red result curve “Mue = 1600” can be firstly divided by the modified lightning current signal with modified front time constant $\tau_1 = 20$ µs, and then multiplied by the modified lightning current signal with standard front time constant τ_1 = 19 µs. After this modification process, the red result curves calculated with the reduced *c* technique will be superposed with the standard blue result curves as Fig. 96 shows, and then the error in the rising part of these result curves can be decreased a lot.

Applying the same procedure to the other time signals, which were recorded by the other E-Field probes during the transient simulation speeded up by the reduced *c* technique, can correct them to the standard results. Fig. 97 shows the corrected results of the time signal recorded by the E-Field probe defined in the thigh muscle along *z*-direction.

In order to use this method to correct the calculated result curves, the modified values of the front time constant τ_1 should be determined firstly. For the reduced *c* technique with different relative permeability values, the front time constant τ_1 should also use different values. Through many simulation experiments, corresponding to several typical relative permeability values, the values of the front time constant τ_1 can be determined as Table 21 shows.

Table 21 Values of the front time constant corresponding to different relative permeability values

Modified µ value / --	1	100	400	900	1600	2500
Modified τ_1 value / µs	19	19	19.2	19.5	20	20.5

A fitting of the data listed in Table 21 (Fig. 98) shows that the relationship between the modified relative permeability μ_r and the modified front time constant τ_1 is almost linear, and the interpolated linear function can be calculated as

$$\tau_1 = 0.00063\mu_r + 18.9 \text{ (µs)}. \tag{5-15}$$

Based on this formulation, the value of the modified front time constant can be calculated conveniently from the value of the modified relative permeability, which is used in the reduced *c* technique to speed up original simulations.

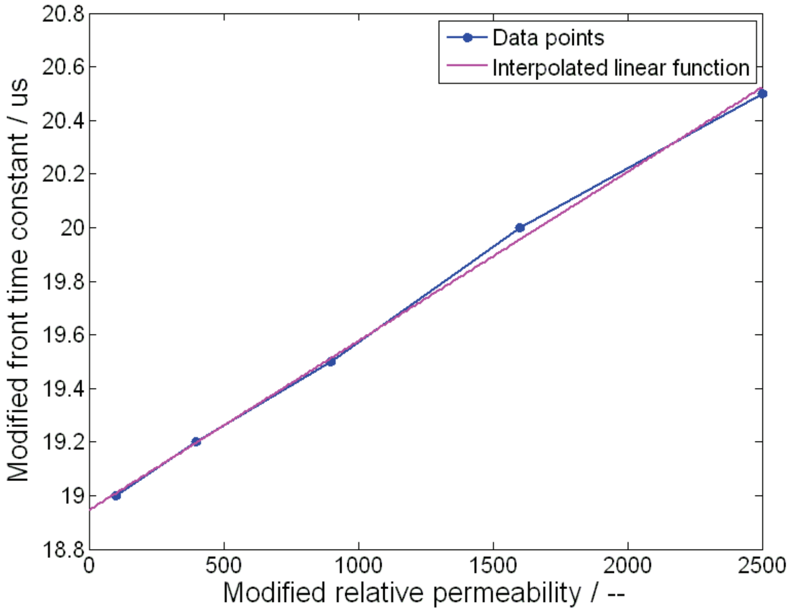

Fig. 98 Relationship between modified relative permeability µ and modified front time constant τ_1

At last, it should be noticed that even after correction, the result curves cannot superpose with the standard results completely, especially near the peak value such as Fig. 96 and Fig. 97 show. Apart from that, the error around the peak value will increase with the increment of the modified relative permeability. So generally it's not suggested to use the modified relative permeability more than $\mu_r = 2500$, where the peak value error is around 3%.

Time Domain Calculation Results and Discussion

At last transient time domain simulations were performed based on the two step voltage models described at beginning of this sub-section. The two deformed human body models both used four mm voxel size, material properties of the human tissues and organs were calculated from the Cole-Cole dispersive functions at 25 kHz, which has already been proved that this simplification in material properties will not cause two much errors. The excitation signal used in the simulations was the complete lightning current signal. Open boundary conditions were used for all boundaries of the calculation domain. Calculation results of these simulations can generate some animations to show variation process of the internal current density distribution at different time points very clearly as Fig. 99 and Fig. 100 show. All simulations were speeded up around 20 times by using the reduced *c* technique, which results in around one week calculation time (Computer hardware: Intel® Xeon® CPU: E5430, 2.66GHz, 2.66GHz; 16.0 GB of RAM).

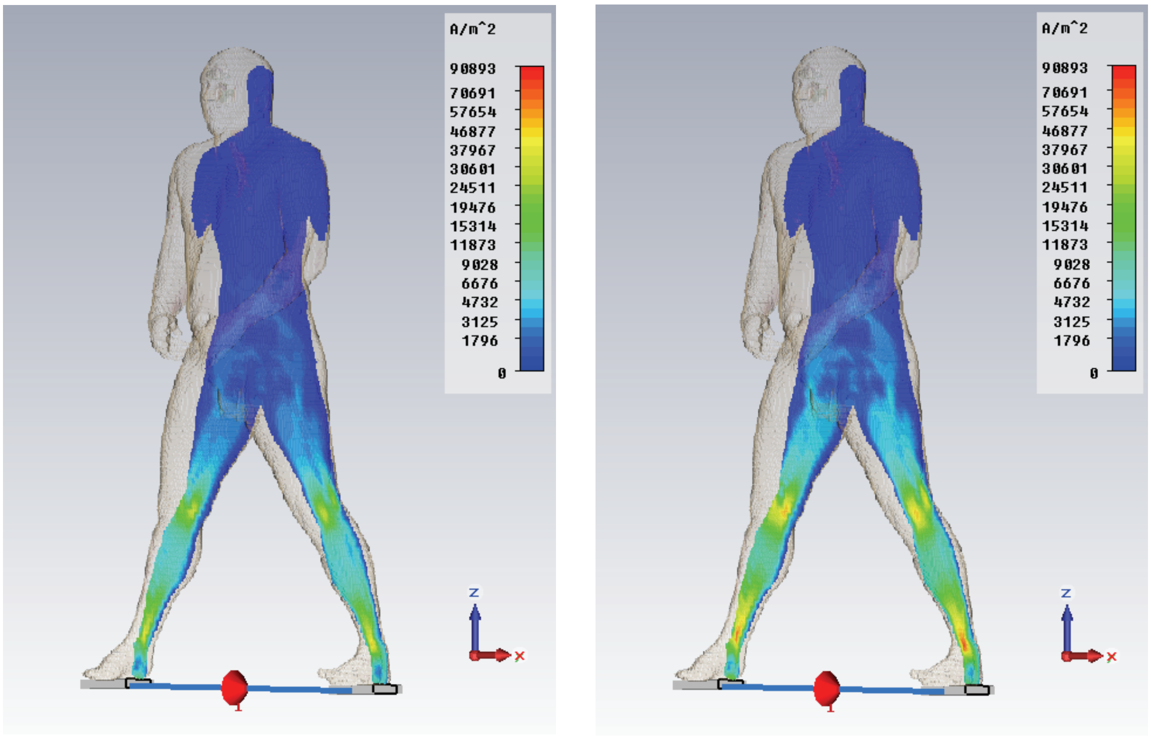

(a) t = 20 µs (b) t = 30 µs

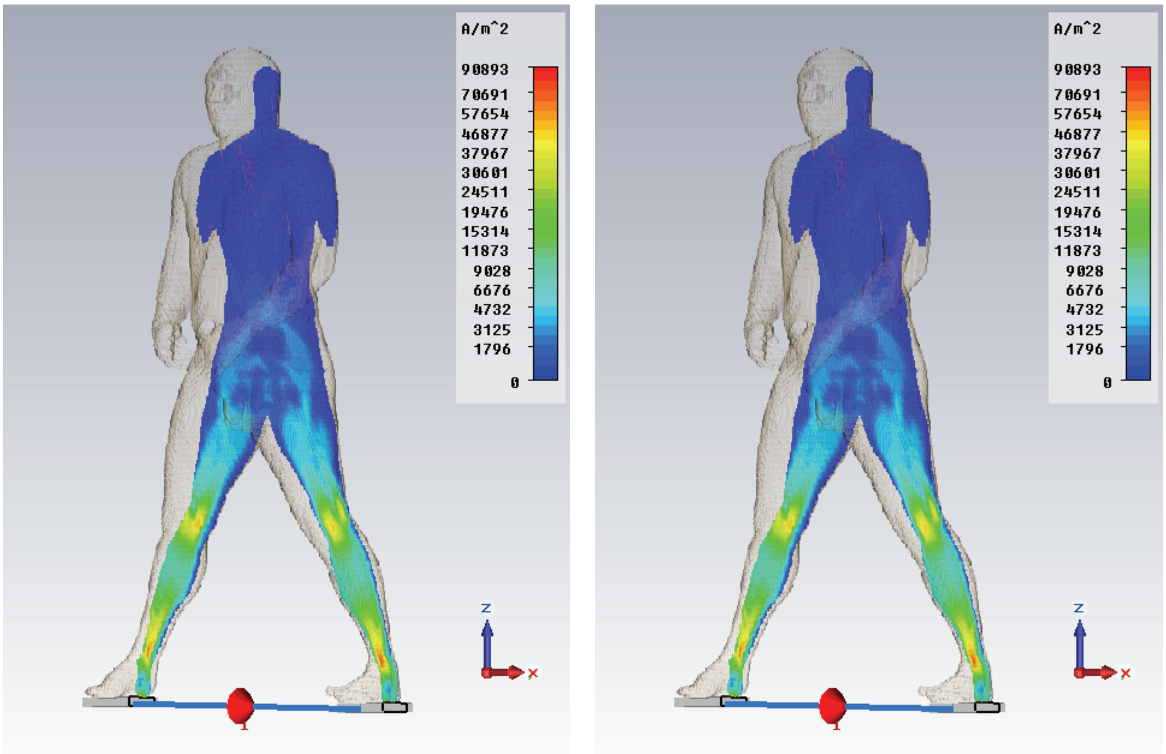

(c) t = 40 μs (d) t = 50 μs

Fig. 99 Current density distribution in standing human body at different times

Simulation results including the walking human body model are shown in Fig. 100.

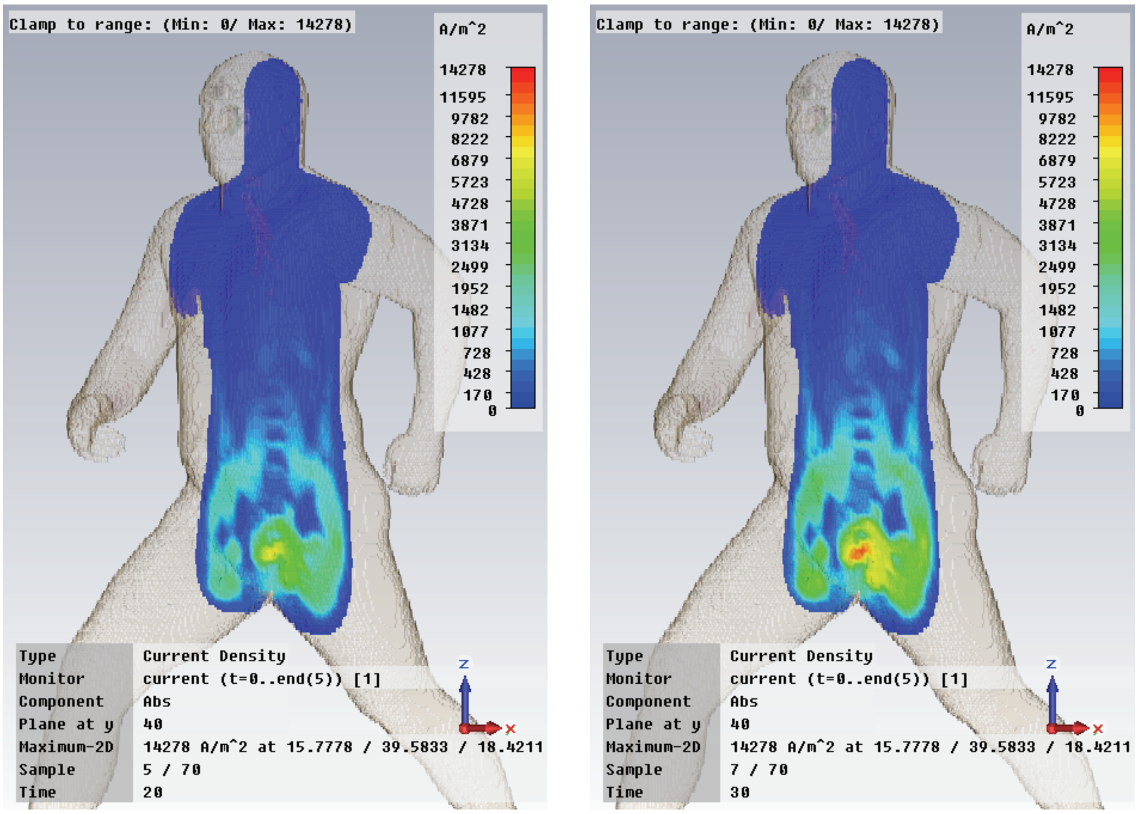

Clamp to range: (Min: 0/ Max: 14278)

Type Current Density
Monitor current (t=0..end(5)) [1]
Component Abs
Plane at y 40
Maximum-2D 14278 A/m^2 at 15.7778 / 39.5833 / 18.4211
Sample 5 / 70
Time 20

Clamp to range: (Min: 0/ Max: 14278)

Type Current Density
Monitor current (t=0..end(5)) [1]
Component Abs
Plane at y 40
Maximum-2D 14278 A/m^2 at 15.7778 / 39.5833 / 18.4211
Sample 7 / 70
Time 30

(a) t = 20 μs (b) t = 30 μs

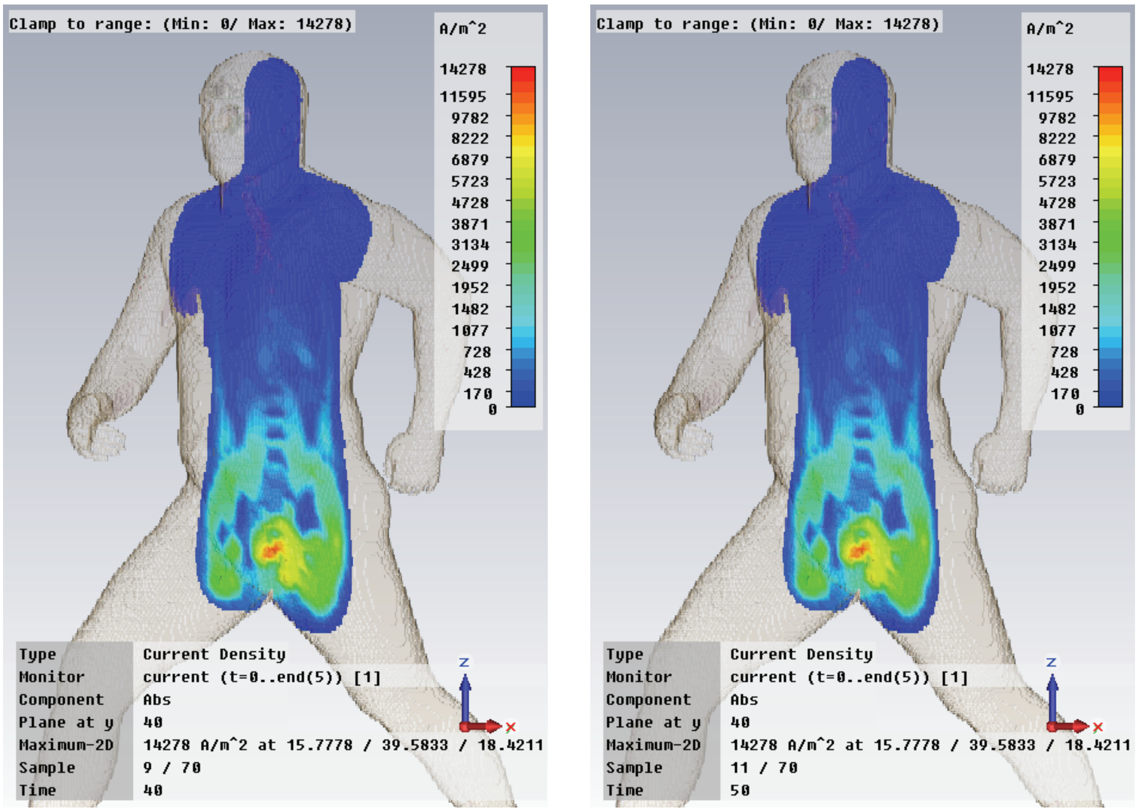

(c) t = 40 µs (d) t = 50 µs

Fig. 100 Current density distribution in walking human body at different times

In Fig. 99, to make all result figures clearer, text information about monitor, cut plane, maximum values, etc. were skipped. In both Fig. 99 and Fig. 100, the current density field in figure (b) is stronger than that in figure (a), but almost the same as that in figure (c) and (d), which means that the internal current density field in the human body will start from zero, increase very fast to its peak value at around t = 30 µs, and then decrease very slowly, which is almost the same as configuration of the lightning current signal.

Besides, it can be seen that the areas with higher current density values appear mainly in the muscles of two legs, especially near the knee and ankle joint. Similar as the simulation results which study the step voltage caused by the downed power line, this distribution situation is caused by the human body structure and different conductivity values of the different tissues. In the human body, the conductivities of the bone and marrow are much smaller than those of the muscle or blood. In the human leg, except for the fat and skin, the calf and thigh mainly consist of muscles, blood and comparatively thin bone, while most parts of the knee or ankle joint are bone and marrow. Meanwhile, the cross sections of the calf or thigh are much larger than those of the knee or ankle joint, and the calf and thigh also include much more tissues with higher conductivity. Because the body current through any cross section of the leg is identical, the current density must be much stronger near the knee or ankle joint to get the same body current value as that passes the calf or thigh. The organs and tissues in the abdomen also have comparatively higher current density values, especially the area near the bladder, because the conductivity of the bladder is also a little bigger than most other tissues. The current density is much weaker in bones and upper part of the human body. This is mainly because conductivity of the bone is very small, and upper part of the human body is far away from the excitation sources, which are located below two feet.

In order to verify the conclusion that scaling stationary current calculation results based on concrete step voltage values at different time points can also get an accurate enough transient simulation results at different time points, two more stationary current simulations were performed. In these two simulations, the fixed electric potential value defined on the right PEC patch was 241.233 kV which was calculated from formula (5-14) at *t* = 30 μs, and the fixed electric potential value defined on the left PEC patch was 0 V. Current density field results of the stationary current simulations are shown in Fig. 101.

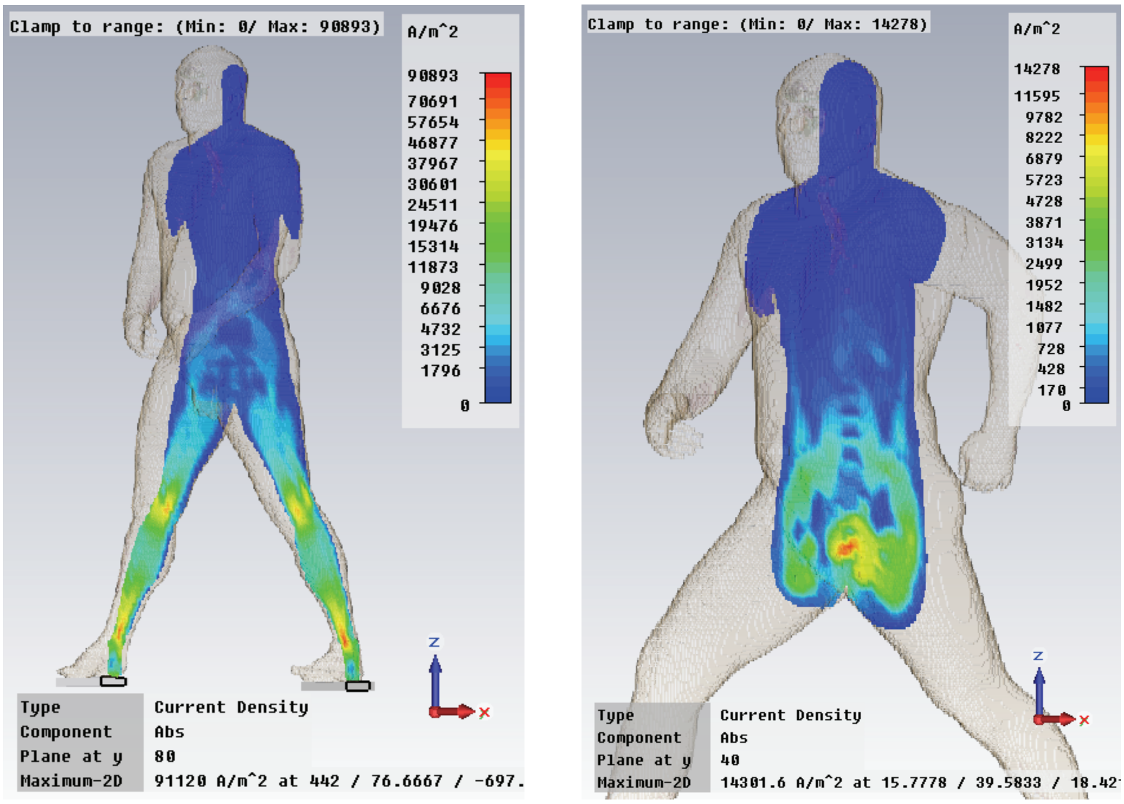

(a) Standing human body model (d) Walking human body model

Fig. 101 Current density distribution results calculated from stationary current simulations

In Fig. 101 – (a), the range of current density value is set as (0 ~ 90893 A/m^2) which is the same as that in Fig. 99 – (b). It can be seen that the current density distribution in Fig. 101 – (a) is almost the same as the result shown in Fig. 99 – (b) which indicates the current density field result of the transient time domain simulation at *t* = 30 μs. The relative error of the maximum value is (91120 - 90893) / 90893 × 100% = 0.25%. Similarly, the result shown in Fig. 101 – (b) is also almost the same as that in Fig. 100 – (b), and relative error of the maximum value is also only 0.20%. Thus it is proved again that, because of low frequency content of the 10/350 μs lightning current signal, scaling stationary current calculation result based on the step voltage values at different time points can lead to an accurate enough simulation results at corresponding time point.

As a very important organ in the whole human body, safety of the heart is always of great concern. Because the conductivities of the muscle and blood, which the heart is composed of, are comparatively higher than that of other human tissues, and from the view of medical aspect, a high enough electric field near the heart or strong enough current through the heart will cause ventricular fibrillation, which is fatal to victims, it' necessary to verify whether the heart is safe or not in the simulation. Fig. 102 shows the time signal of the electric field probe defined in the heart of the standing human body model along the *x*-direction which is the main direction of the electric field strength there. Like the excitation signal, electric field strength in the heart will start from zero, increase rapidly to its peak value around 223.12 V/m, and then decrease very slowly and almost linearly.

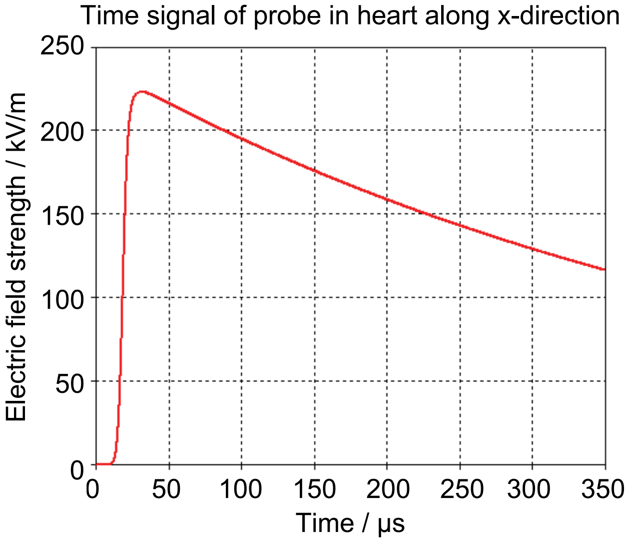

Fig. 102 Time signal of the E-Field probe defined in the heart along *x*-direction

The standard IEC 60479 uses a figure to show the threshold of ventricular fibrillation corresponding to different whole body currents and excitation impulse durations as Fig. 103 shows [89]. The curve in the figure indicates the probability of fibrillation risks for a current flowing along the path from left hand to feet. For a path from left foot to right foot, the value should be divided by a heart current correction factor F = 0.04 [87]. In Fig. 103, the white area below the curve indicates no fibrillation, while the gray area above the curve will have risk of fibrillation with different probabilities. Fig. 103 shows that the threshold of ventricular fibrillation should be greater than 5 000 / 0.04 mA = 125 A for impulse duration 350 µs = 0.35 ms along the path from one foot to another foot.

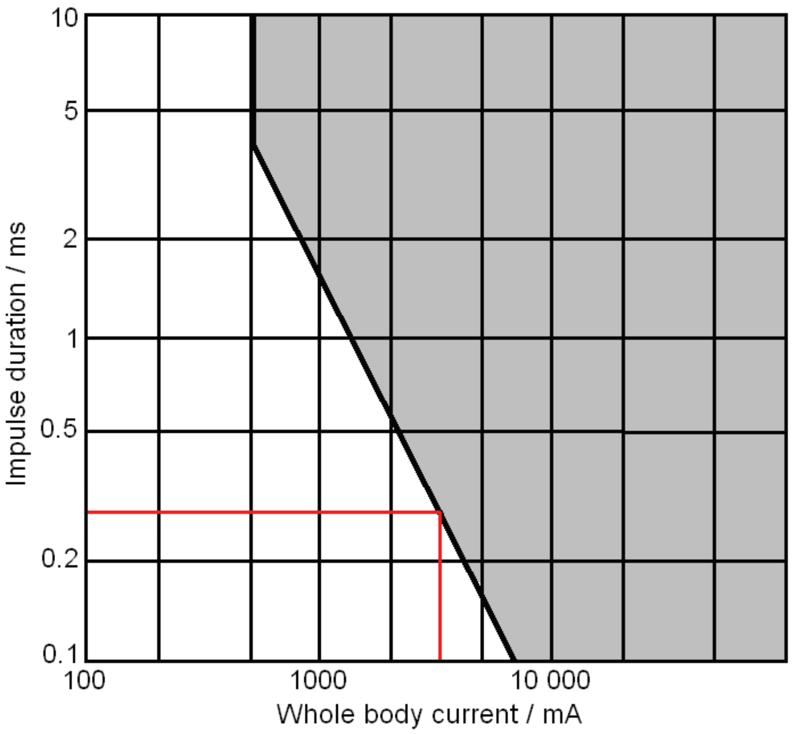

Fig. 103 Threshold of ventricular fibrillation with different body current and impulse duration

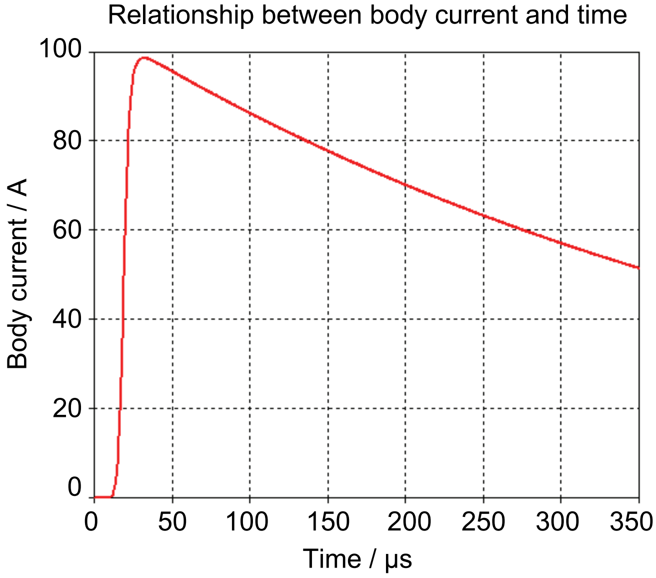

Fig. 104 Relationship between the current through whole human body and time

Fig. 104 shows the body current values at different times. It should be noticed that the value shown in Fig. 103 is rms value, but it can be seen that in Fig. 104 even the peak value of the body current, 98.6 A, is smaller than the threshold. Thus it means that because the heart is far away from the excitation sources which are located below two feet, victim’s heart is safe under the simulation conditions defined above, and then more attention should be paid on the safety of the leg muscles and the organs in abdomen.

6. Application of Postured Human Models on SAR Calculations

In recent years, the continuing spread of radio frequency (RF) electromagnetic wave applications makes the high frequency electromagnetic fields (EMF) exist in variety of places. At the same time there has been increasing concern about the safety of these applications, especially the possible effects on the human body close to operating wireless telecommunication devices. This research domain belongs to the electromagnetic dosimetry, which mainly studies the biological effects of the human body exposed directly in high frequency EMF, calculates induced internal fields within the exposed structures, and tries to prevent possible adverse health effects. In this situation, although a human does not touch the electromagnetic sources directly, the exposure to EMF can also lead to heating effects and make the human body temperature increase.

In 1998, based on a large literature survey including electromagnetic, medical laboratory and epidemiological studies, the International Commission on Non-Ionizing Radiation Protection (ICNIRP) released the guidelines used to restrict human body exposure to electromagnetic fields to ensure safety [11]. In the frequency range from 100 kHz to 10 GHz, these guidelines are based on the heat effects due to electromagnetic energy absorption in the human body, and the metric used to judge the safety of human body exposure to electromagnetic fields is the specific absorption rate (SAR). Since directly measuring the SAR in a living person is very difficult or even almost impossible, the most popular and accurate way to evaluate SAR now is numerical calculation using voxel-based human model such as HUGO.

In a realistic exposure scenario, people may have different postures and the electromagnetic wave may be irradiated from different directions. With the purpose of considering these two influential factors, in this section, after a general introduction to the basic knowledge about SAR and physiological effects of human body exposed to the high frequency electromagnetic fields, the SAR of a sitting human model and a standing human model exposed to radio frequency electromagnetic fields ranging from 30 MHz to 300 MHz, which includes the resonance frequency of the human body, is calculated, including both whole body averaged SAR and localized SAR distribution. The influence of human posture on SAR calculations is discussed, and fourteen kinds of irradiation directions are considered and compared with each other. All calculations in this section were performed based on 4 mm voxel resolution, and the human models were assumed to be in a free space or in a semi-closed enclosure, such as a car. The commercial software CST MICROWAVE STUDIO® was used to calculate the internal electric and magnetic fields of the human body model, which implements the Finite Integration Technique (FIT).

6.1. Introduction to Specific Absorbing Rate

Exposure to time-varying EMF will lead to induced internal body currents and energy absorption in human tissues, which depends on the coupling mechanisms and the frequency involved. In ICNIRP guidelines, the dosimetric quantities, corresponding to different frequency ranges, are used as follows: current density in the frequency range up to 10 MHz, electric current in the frequency range up to 110 MHz, SAR in the frequency range 100 kHz – 10 GHz, power density in the frequency range 10 – 300 GHz. The frequency range considered in this section is 30 MHz – 300 MHz, which falls in the range of SAR.

SAR is a measure of the rate at which energy is absorbed by the human body when exposed to a RF-EMF. It is defined as the power absorbed per mass of tissue and has unit of watts per kilogram (W/kg). SAR is usually averaged either over the whole body, or over a small sample volume (typically 1 g or 10 g of tissue), and commonly used to measure power absorbed from mobile phones and during MRI scans. Its definition formulation can be expressed as

$$SAR = \frac{d}{dt}\left(\frac{dW}{dm}\right) = \frac{d}{dt}\left(\frac{dW}{\rho \cdot dV}\right) \tag{6-1}$$

where dW is the absorbed incremental energy,

dm is the incremental mass,

dV is the volume element, and

ρ is the mass density.

It can be calculated from the electric field within the tissue as

$$SAR = \frac{\iiint_{sample} \frac{\sigma(\vec{r})\left|\vec{E}(\vec{r})\right|^2}{\rho(\vec{r})} dV}{V} \tag{6-2}$$

where σ is the electrical conductivity of the sample tissue,

E is the rms value of the electric field strength,

V is the volume of the sample tissue, and

ρ is the mass density of the sample tissue.

It can be seen that SAR is proportional to the square of the internal electric field strength in the tissue. Its values depend on mainly following three factors: the first one is the incident field, characterized by frequency, intensity, irradiation direction, polarization, etc.; the second one is the characteristics of the exposed human body, i.e. body dimension, posture, internal, external geometry, etc.; the last one includes ground effects and reflection effects of other objects near the exposed body. In this section, the irradiation direction of the incident field and the posture of the exposed body will be discussed in detail.

The research work of Chatterjee et al. demonstrated that, the dominant effect of exposure to an electromagnetic field below 100 kHz is nerve and muscle stimulation, while the energy absorption and related temperature rise can be negligible. However, exposure to electromagnetic fields at frequencies above 100 kHz can lead to significant energy absorption and temperature increases, which turns out to be the main effect of human body in this frequency range [90]. Electromagnetic fields can be divided into four ranges to consider how human body absorbs electromagnetic energy [91]:

1) From 100 kHz to 20 MHz, energy absorption in the trunk decreases rapidly with decreasing frequency, and significant absorption may occur in the neck and legs.

2) From 20 MHz to 300 MHz, which is also the main frequency range considered in this section, the whole human body will absorb relatively high electromagnetic energy. Resonance frequencies of most human bodies, despite small variations because of different body dimensions, appear in this range.

3) From 300 MHz to several GHz, energy absorption shows significantly local and uniform properties.

4) Above 10 GHz, energy absorption occurs primarily at the body surface.

In medical research, cellular and animal studies show that at levels of absorbed electromagnetic energy which can cause body temperature rise in excess of 1 – 2 °C, a large number of physiological effects have been characterized. These effects include alterations in neural and neuromuscular functions, increased blood-brain barrier permeability, ocular impairment and stress-associated changes in the immune system [92]. Volunteer studies also show that at frequencies from 10 MHz to 300 GHz, heating is the major effect of absorption of electromagnetic energy, and temperature rises of more than 1 – 2 °C can have adverse health effects such as heat exhaustion and heat stroke [93]. As a result, 1 °C has been suggested as the upper limit of temperature increase that has no adverse effects on human body.

Available experimental evidence demonstrates that the exposure of resting humans for approximately 30 min to EMF, producing a whole body averaged SAR of between 1 and 4 W/kg, results in a body temperature increase of less than 1 °C. Exposure to more intense fields, producing SAR values larger than 4 W/kg, can exceed the thermo-regulatory ability of human body and produce harmful levels of tissues heating [94] [95]. These data form the basis for an occupational exposure restriction of 0.4 W/kg with a safety factor of 10. Restriction values of SAR for time varying EMF for frequencies between 100 kHz and 10 GHz in ICNIRP guidelines are listed in Table 22.

Table 22 Restriction values of SAR for time varying EMF from 100 kHz to 10 GHz (W/kg)

Exposure characteristics	Whole body average SAR	Localized SAR (head and trunk)	Localized SAR (limbs)
Occupational exposure	0.4	10	20
General public exposure	0.08	2	4

Here the localized SAR averaging mass is any 10 g of contiguous tissue; the maximum SAR thus obtained should be the value used for the estimation of exposure. The general public exposure has an additional safety factor of 5 with respect to the occupational case.

6.2. Influence of Posture on the SAR of Human Body

If the irradiation direction of the incident electromagnetic wave is fixed, different postures of the human body will lead to different irradiation areas, and then result in different SAR values. In order to study the influence of human posture on the whole body averaged SAR and localized SAR distribution, two simulation models, including one sitting human body model and one standard standing human body model respectively, were built in the software CST MICROWAVE STUDIO® as Fig. 105 and Fig. 106 show.

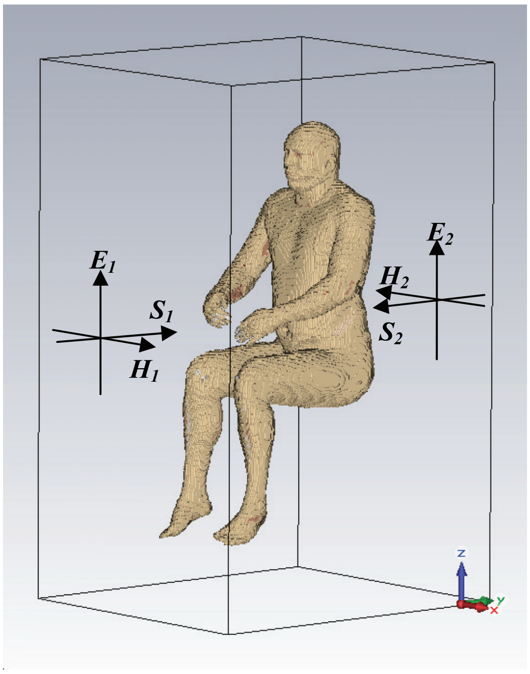

Fig. 105 SAR calculation model with sitting human body model

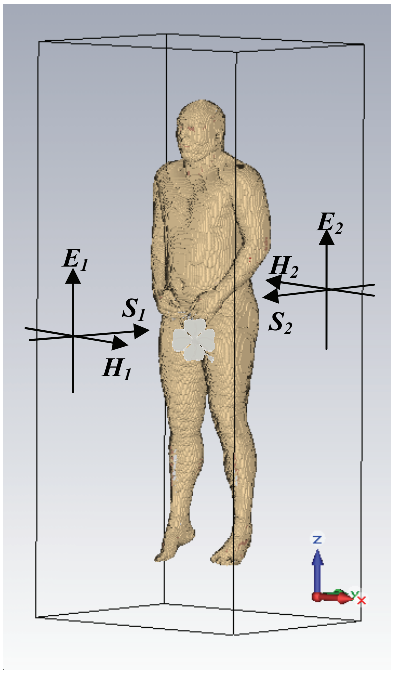

Fig. 106 SAR calculation model with standing human body model

In the first model as Fig. 105 shows, the original standing voxel-based human body model HUGO was deformed into a human body model with sitting posture with the help of the developed poser program. The voxel size is four mm and there are in total 150 × 193 × 372 voxels in *x*-, *y*- and *z*-direction respectively. The standing human body model in the second model is just the original undeformed HUGO model, the voxel size is also four mm and there are totally 148 × 85 × 468 voxels in *x*-, *y*- and *z*-direction respectively. The material properties of human tissues and organs used in the simulation are all calculated from the Cole-Cole dispersive material model.

In this sub-section, two electromagnetic wave irradiation directions are considered: from front side to back side and from back side to front side as the arrow sets in Fig. 105 and Fig. 106 show. Other irradiation directions were simulated and will be discussed in the next sub-section. The excitation sources in both models are plane waves which are good approximation of the electromagnetic field propagation in the far-field region. Based on the experience, under plane wave exposure conditions, when the long axis of the human body is parallel to the electric field vector, the whole body averaged SAR can reach its maximal values [11]. As a result, in both models above, the electric field vectors are all set along z-direction which is the long axis of the human body models. In simulation, the power density of the incident plane wave is 1 W/m^2, and open boundary condition is used for all boundaries of the calculation domain to realize an isolated, not grounded human body model.

Literature survey in ICNIRP guidelines shows that standard reference man (176 cm height, 73 kg mass [96]), if not grounded, has a resonant absorption frequency close to 70 MHz. For taller individuals the resonant absorption frequency is somewhat lower, and for shorter adults, children, babies, and seated individuals it will be higher and may exceed 100 MHz. Thus the frequency range studied in this sub-section is defined from 30 MHz to 300 MHz, which includes the possible resonant frequency and is convenient to be realized with four mm voxel size. Smaller voxel size will be needed if higher frequency range is wanted to be studied.

Fig. 107 shows the frequency characteristics of the whole body averaged SAR of the sitting human body model and standing human body model for the two irradiation directions of the incident plane wave.

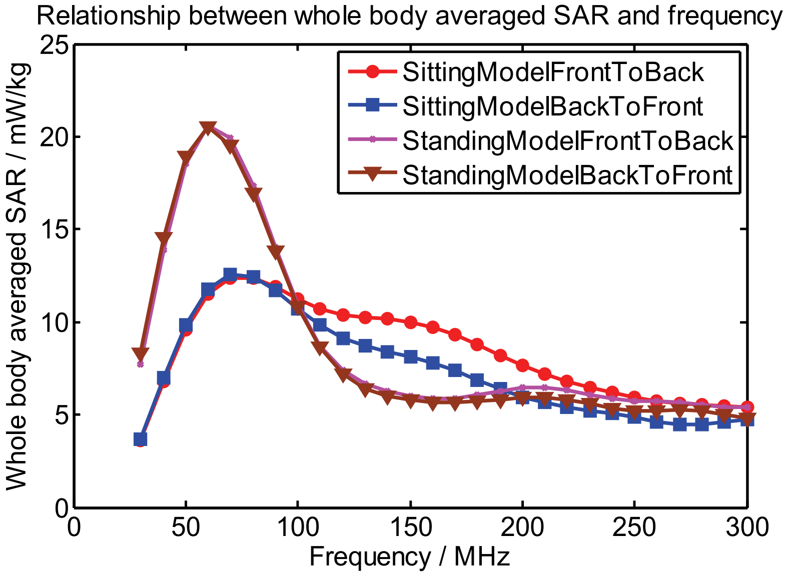

Fig. 107 Whole body averaged SAR of human models with standing and sitting posture, for irradiation direction from the front and from the back side

It can be seen that the maximum values of the whole body averaged SAR for the sitting model and standing model are both between 60 MHz and 80 MHz which corresponds to the resonant frequency of the human body. Because the height of the human model influences the resonance frequency of the human body [22] [23], Fig. 107 also shows that the resonant frequency of the sitting model is a little higher than that of the standing model. In addition, the whole body averaged SAR at the resonant frequency for the sitting model is about 37% lower than that of the standing model. Apart from the main resonance frequency, another apparent peak appears at around 150 MHz for the sitting model. All of these results agree with the results of Nagaoka [10], Findlay and Dimbylow [8].

Apart from that, the whole body averaged SAR when the incident plane wave propagates from the front side to the back side is higher than that with irradiation direction from back side to the front side. This phenomenon appears both in the sitting model and in the standing model, but it is more apparent in the sitting model. This is mainly because the back side of human model is much flatter than the front side. As a result, the front side of the human body has larger absorption area, which will result in higher SAR values.

For irradiation direction from front to back, the maximum whole body averaged SAR values in Fig. 107 are 0.0124 W/kg and 0.0206 W/kg, for sitting and standing human body model respectively. In ICNIRP guidelines, the restriction values for whole body averaged SAR are 0.4 W/kg for occupational case with 10 W/m^2 equivalent incident plane wave power density, and 0.08 W/kg for general public case with 2 W/m^2 equivalent incident plane wave power density. Because the power density of incident plane wave in the simulations is 1 W/m^2 and the SAR value is proportional to the power density of the incident plane wave, for an incident plane wave with 10 W/m^2 power density, the whole body averaged SAR can be calculated as 0.124 W/kg and 0.206 W/kg for sitting and standing human body model respectively. For 2 W/m^2 power density, the related whole body averaged SAR results are 0.0248 W/kg and 0.0412 W/kg. All calculated results are below the restriction values of ICNIRP guidelines showing that the guidelines provide a reasonable and a little conservative restriction values for SAR.

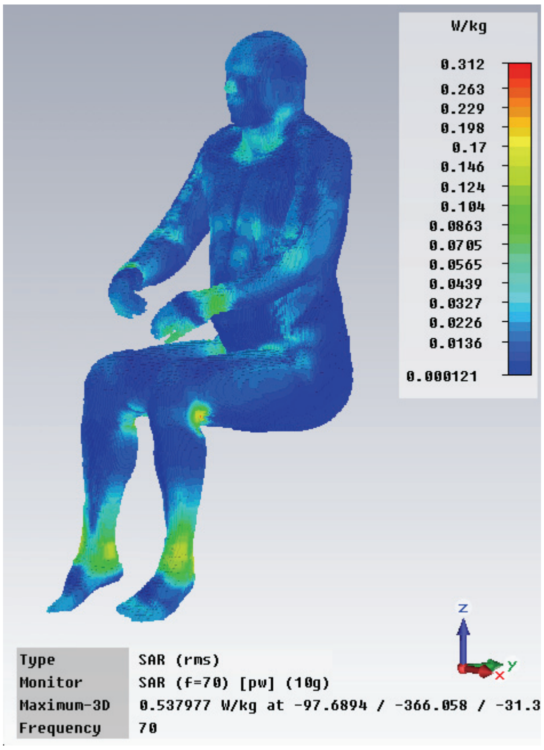

Type SAR (rms)
Monitor SAR (f=70) [pw] (10g)
Maximum-3D 0.537977 W/kg at -97.6894 / -366.058 / -31.3
Frequency 70

Fig. 108 Localized SAR distribution of the human body with sitting posture at *f* = 70 MHz

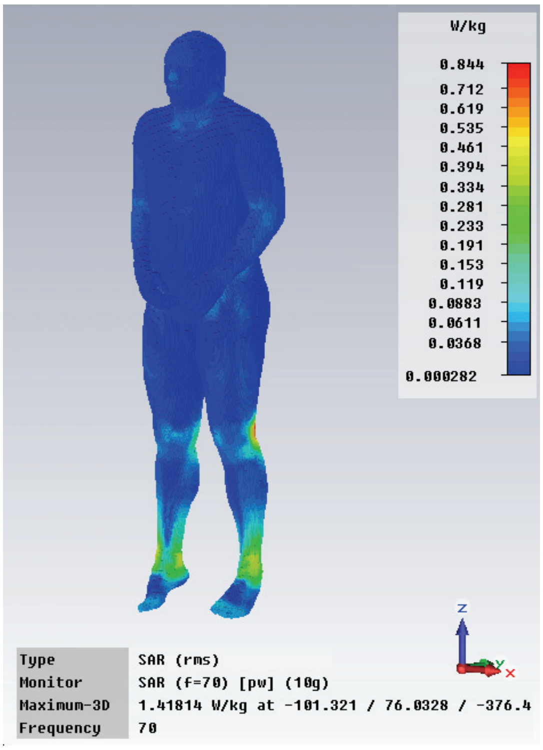

Type SAR (rms)
Monitor SAR (f=70) [pw] (10g)
Maximum-3D 1.41814 W/kg at -101.321 / 76.0328 / -376.4
Frequency 70

Fig. 109 Localized SAR distribution of the human body with standing posture at *f* = 70 MHz

Fig. 108 and Fig. 109 show the localized SAR (averaged on 10 g mass) distribution in the human body with sitting and standing posture at 70 MHz which is near the resonance frequency of human body. The irradiation direction is still from front to back. For the human body with sitting posture in Fig. 108, most of the electromagnetic energy is absorbed near different kinds of joints such as ankle, knee, hip joint, wrist, elbow and neck. The area near the nose and the fingers also has a little higher localized SAR. For the human body with standing posture in Fig. 109, higher SAR values mainly appear in the legs, especially near ankle and knee joint.

The maximum localized SAR values in these two figures are 0.538 W/kg and 1.418 W/kg respectively and are both located in the legs. In ICNIRP guidelines, the restriction values for localized SAR in limbs are 20 W/kg for the occupational case with 10 W/m^2 equivalent incident plane wave power density, and 4 W/kg for the general public case with 2 W/m^2 equivalent incident plane wave power density. For incident plane wave with 10 W/m^2 power density, the maximum localized SAR can be calculated as 5.38 W/kg and 14.18 W/kg for sitting and standing human body model respectively. For 2 W/m^2 power density, related localized SAR results are 1.046 W/kg and 2.836 W/kg. All calculation results are still smaller than the restriction values of ICNIRP guidelines.

6.3. Influence of Irradiation Direction on SAR of Human Body

Apart from the posture, the irradiation direction of the incident plane wave can also influence the way a human body absorbs electromagnetic energy significantly. Here twenty four simulation calculations were performed to study the influence of this factor including twelve irradiation directions which are not from front or back side of the studied human body models. All irradiation directions studied in this sub-section are shown in Fig. 110.

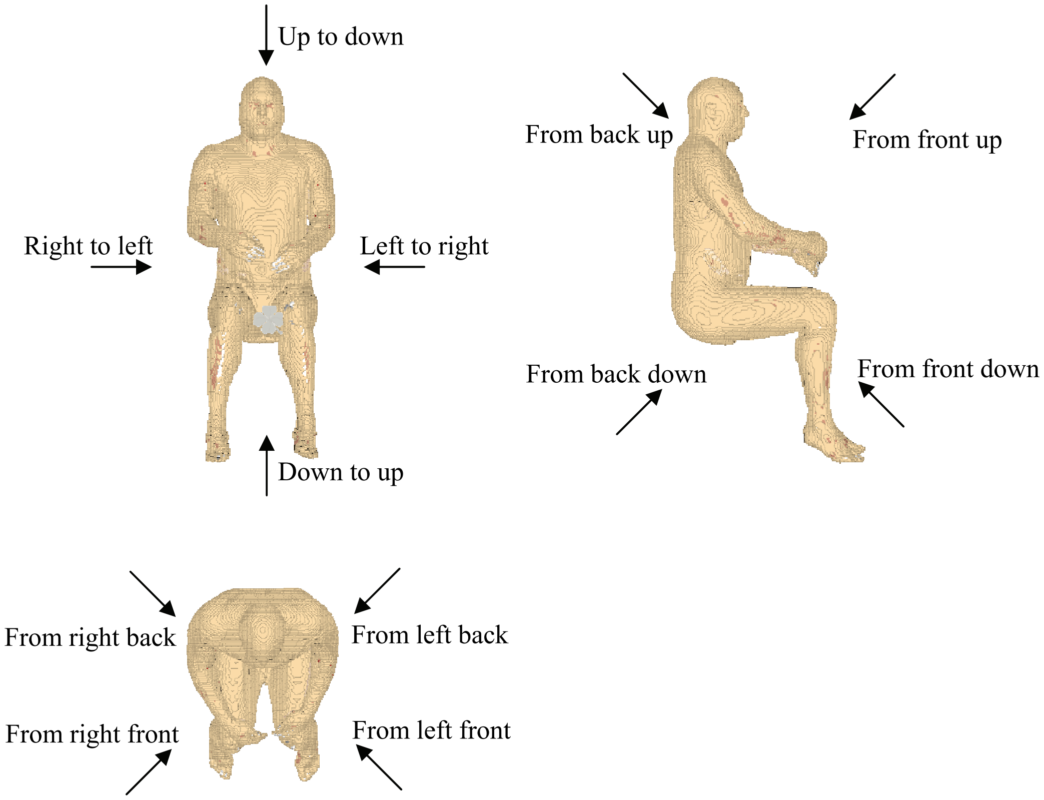

Fig. 110 Different irradiation directions of incident plane wave to study the influence of irradiation direction on whole body averaged SAR of human body

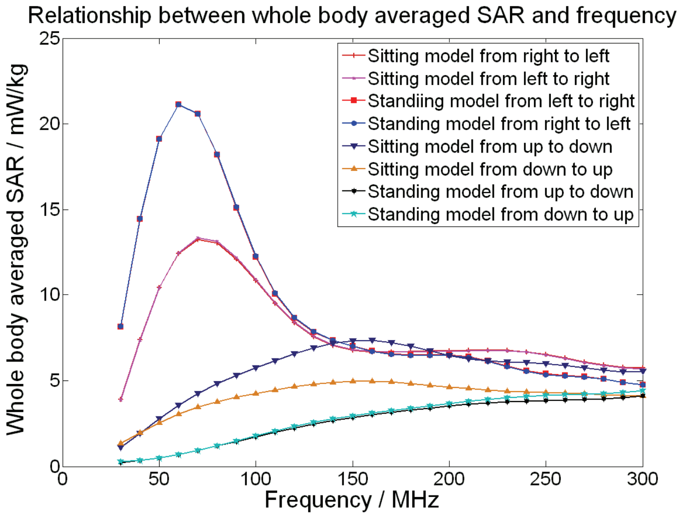

Fig. 111 Whole body averaged SAR of human models with standing and sitting posture, for irradiation directions from right to left, from left to right, from up to down and from down to up.

Fig. 111 shows the frequency characteristics of whole body averaged SAR of the sitting model and standing model including four different irradiation directions among right, left, up and down side. It can be seen that because either sitting model or standing model is symmetrical along left and right side, the incident plane wave irradiating from right side to left side or from left side to right side will result in almost the same whole body averaged SAR values both for sitting or standing models. The general trend of these four curves is similar to the result curves in Fig. 107 except that the sitting model here doesn't have an apparent second peak near 150 MHz.

While irradiation directions are changed to be between upper side and down side, the trend of the result curves will be very different. Because the projection areas are much smaller for these two irradiation directions, the whole body averaged SAR values of these four curves are much smaller than that of the two irradiation directions explained above. The sitting model with irradiation direction from upper side to down side results in the highest whole body averaged SAR values because it has the largest projection area. For the standing model, irradiation directions from upper side to down side and from down side to upper side have almost the same projection area, which results in almost the same whole body averaged SAR values as Fig. 111 shows.

Fig. 112 shows the results of other four different irradiation directions surrounding the human body models. Because of symmetry of the standing human model, the incident plane wave irradiating from left front side, from right front side, from left back side and from right back side all get almost the same whole body averaged SAR results. Similarly for sitting human model, the incident plane wave irradiating from left front side and from right front side get almost the same results, while irradiation directions from left back side and from right back side also get the same results. Because the projection areas are a little bigger for directions from left front side and right front side, these two directions result in a little greater whole body averaged SAR values.

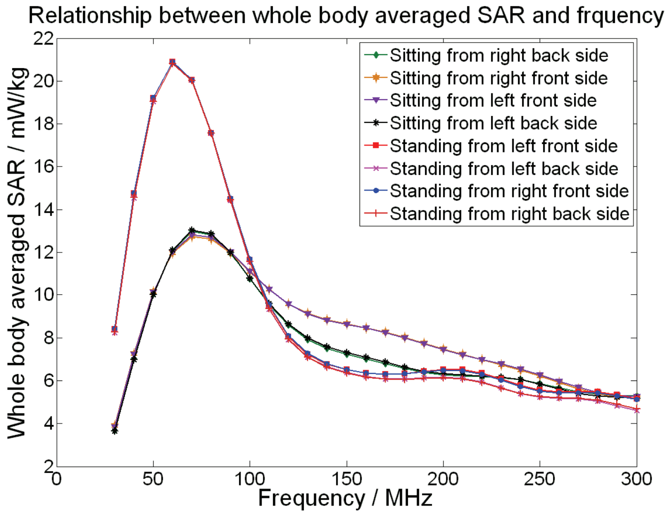

Fig. 112 Whole body averaged SAR of human models with standing and sitting posture, for irradiation directions from right front, from left front, from right back and from left back

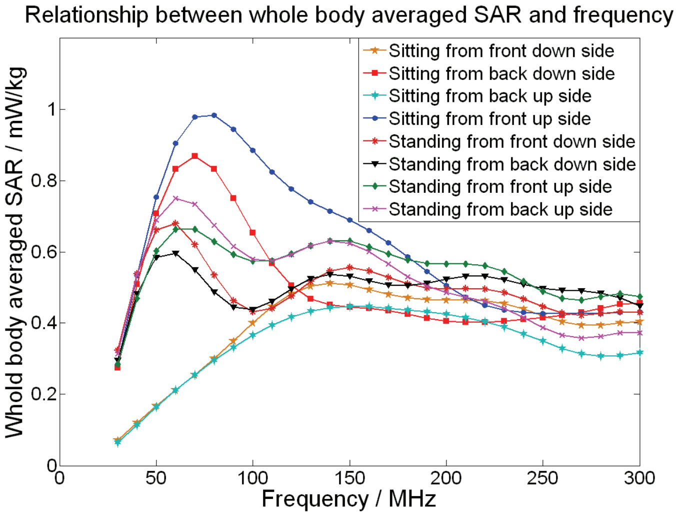

Fig. 113 Whole body averaged SAR of human models with standing and sitting posture, for irradiation directions from front down, from front up, from back down and from back up

Fig. 113 shows whole body averaged SAR results of the last four irradiation directions. Because these four directions are near the exactly upper side or down side, their whole body averaged SAR values are comparatively very small. Most of them still have a resonance frequency between 50 and 80 MHz, except for the irradiation directions from front down side and from back up side of the sitting human model. The sitting human model with irradiation direction from front upper side achieves the highest SAR values, while the second highest one is for the sitting human model with irradiation direction from back down side. The difference among the four result curves of the standing human model is not as big as that of the sitting human model. The standing human model with irradiation direction from back upper side results in a little higher whole body averaged SAR values, while the standing human model with irradiation direction from back down side gets a little lower values.

6.4. Electromagnetic Simulation of a Driver-Car Model

In order to put the postured human body model into an exposure scenario in real life, a new sitting human body model was generated and placed in a car model[1] as Fig. 114 shows. In this simulation, the calculation conditions are almost the same as the ones used before, the whole model including the car and the driver was exposed to a plane wave with 1 W/m^2 power density, open boundary condition was set for all boundaries of the calculation domain, and the irradiation direction of the plane wave was from front side to back side.

Fig. 114 One deformed human body model that sits in a car

Fig. 115 shows the electric field distribution inside and outside the car excited by the plane wave. It can be seen that because of the electromagnetic shielding effect of the metal car body, the electric field strength inside the car is much smaller than that outside the car.

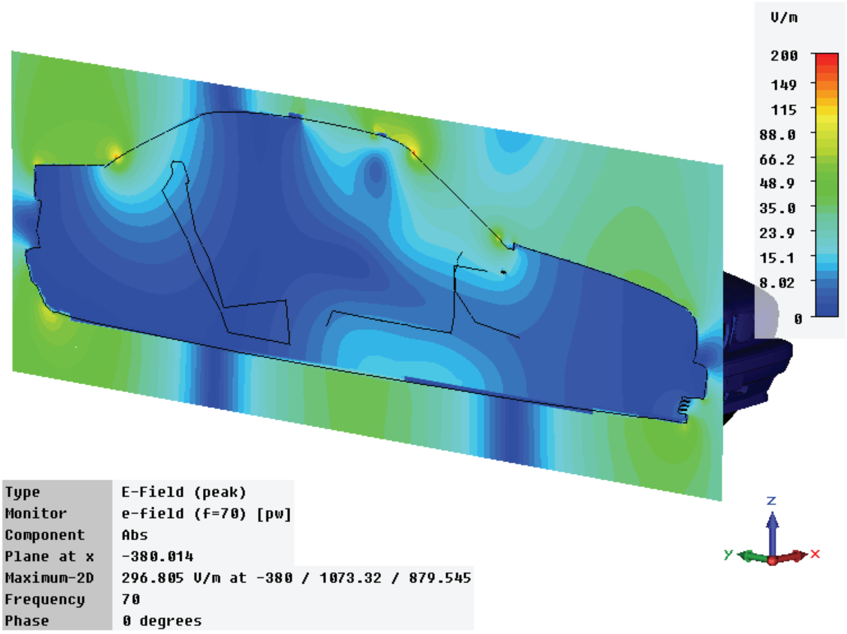

Type	E-Field (peak)
Monitor	e-field (f=70) [pw]
Component	Abs
Plane at x	-380.014
Maximum-2D	296.805 V/m at -380 / 1073.32 / 879.545
Frequency	70
Phase	0 degrees

Fig. 115 Electric field distribution of the drive-car model exposed to plane wave

---

[1] The car models used in this section were provided by CST – Computer Simulation Technology AG.

Fig. 116 shows the localized SAR (averaged on 10 g mass) distribution in the body of the driver at 70 MHz. Because of the protection of the car, the value of the localized SAR in this simulation (with 0.119 W/kg peak value) is much smaller than that of the sitting human model in Fig. 108 (with 0.538 W/kg peak value). Most of the electromagnetic energy is also absorbed near different kinds of joints such as wrist, knee, ankle, neck and hip joint. Areas near head top and right hand also have a little higher localized SAR.

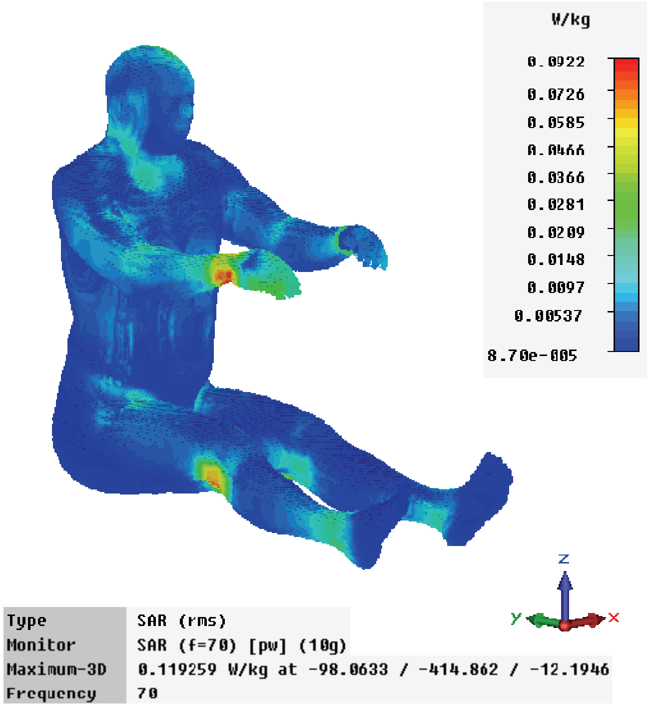

Type SAR (rms)
Monitor SAR (f=70) [pw] (10g)
Maximum-3D 0.119259 W/kg at -98.0633 / -414.862 / -12.1946
Frequency 70

Fig. 116 Localized SAR distribution of driver model exposed to plane wave

The plane wave excitation source in this simulation is located outside the car, thus the electromagnetic shielding effect of the metal car body can protect the driver, who is in the car, from the electromagnetic radiation outside. Similarly it can be deduced that if the electromagnetic excitation source is located inside the car, e.g. a wireless hand-free phone in the car, electromagnetic shielding effect of the metal car body will make the related electromagnetic wave to be reflected inside the car, and then the driver and passenger will take more electromagnetic radiation and have higher localized SAR if they were sitting outside of the car.

In the second simulation example as shown in Fig. 117, the whole driver-car model is struck by a lightning current on the top of the car. As the excitation source, the lightning current was defined through a discrete current port which is on the top of the car and touches the car. The whole driver-car model was placed on the ground which was defined by the combination of a PEC plate and a lumped electrical resistor element that represents the grounded resistance of the whole model. For comparison, two situations were considered: an open top window and a closed top window. Fig. 117 shows all detailed components of the whole simulation model, in which the top window is open.

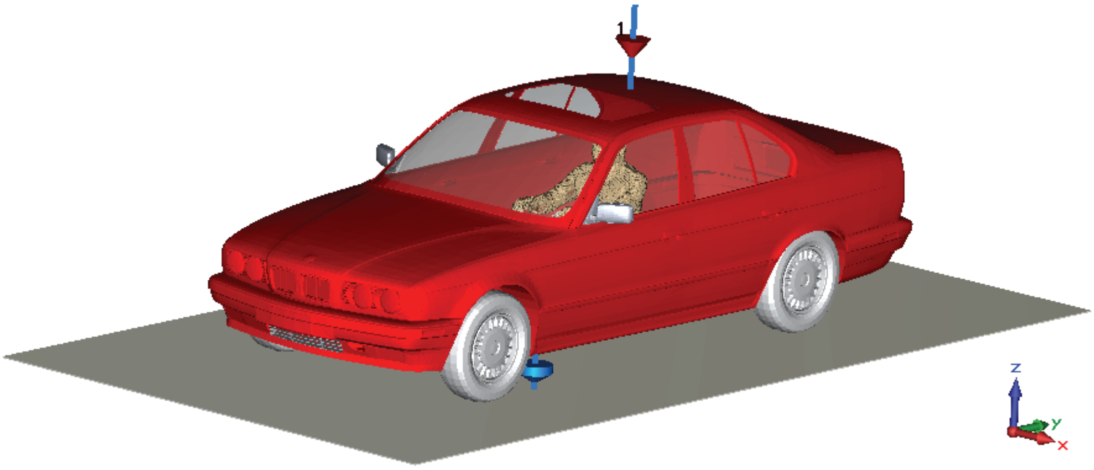

Fig. 117 A driver-car model used in the electromagnetic analysis where the car is struck by a lightning

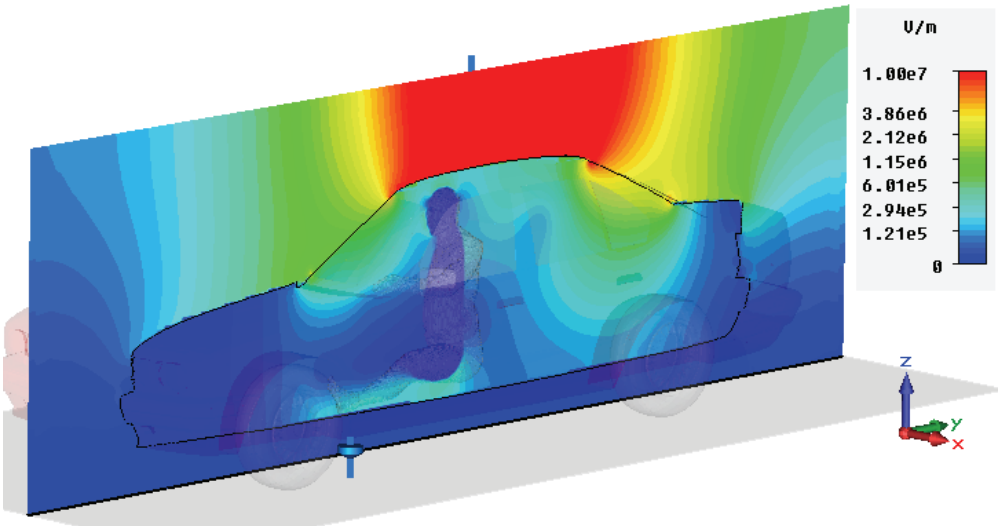

a) The top window of the car is closed

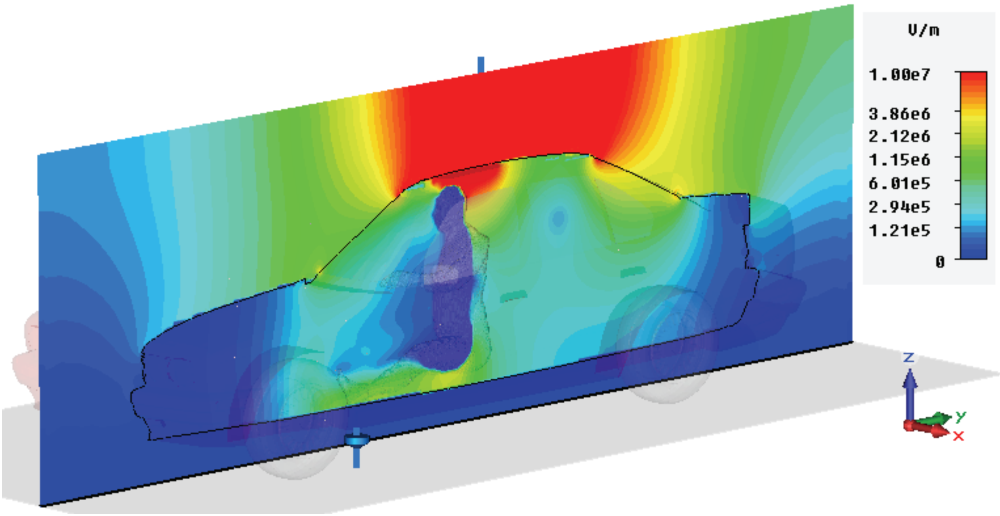

b) The top window of the car is open

Fig. 118 Electric field distribution inside and outside the car near the peak value of the lightning current signal, while the driver-car model is struck by a lightning current

Fig. 118 shows the electric field distribution inside and outside the car near the peak value of the lightning current signal, while the whole driver-car model is struck by the lightning current. In principle, when the car is struck by the lightning current, the related lightning current will be conducted into the ground through the metal car body. When the top window of the car is closed such as Fig. 118 – a) shows, because of the electromagnetic shielding effect of the metal car body, the electric field strength inside the car is much smaller than that outside the car. When the top window is open, the electromagnetic field excited by the lightning current has an opportunity to go inside the car, which will lead to higher electric field strength inside the car such as Fig. 118 – b) shows. Apart from that, because the top window of the car is very near to the driver's head, an open top window will lead to very strong electric field near the driver's head, which is very dangerous for the driver's health.

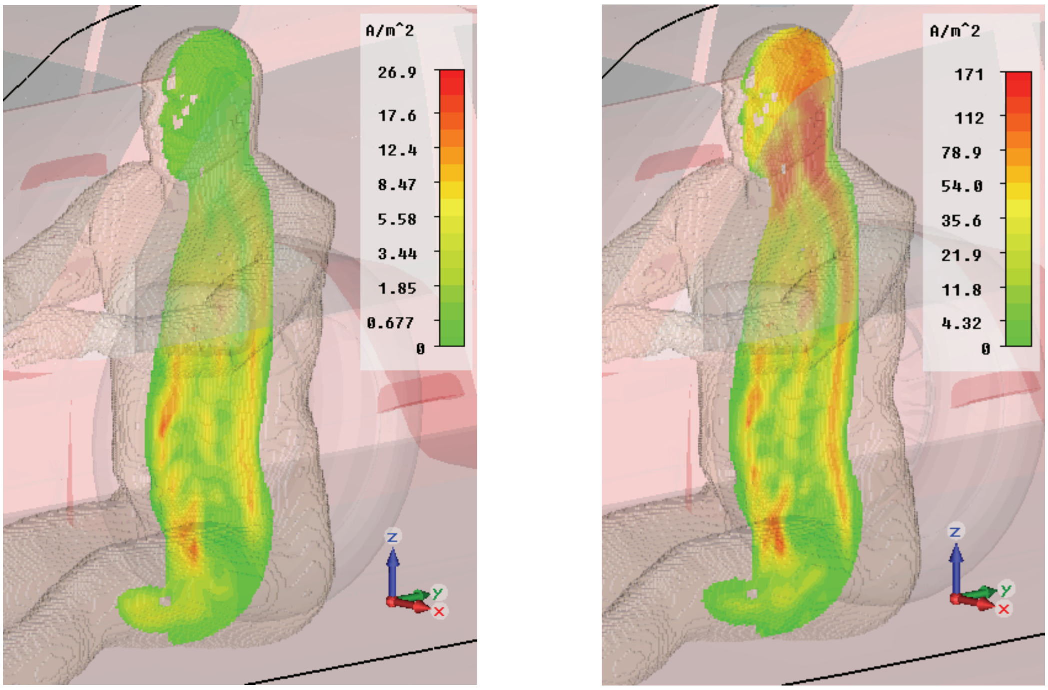

a) The top window of the car is closed

b) The top window of the car is open

Fig. 119 Current density distribution of the driver model near the peak value of the lightning current signal, while the driver-car model is struck by a lightning current

Fig. 119 shows the current density distribution inside the driver model near the peak value of the lightning current signal. It can be seen that the current density field inside the driver model is much stronger when the top window of the car is open, especially for the driver's head.

So, in order to ensure the health of the passengers in the car, especially the driver and co-driver because they are both very near away from the top window, the driver should close the top window of the car when driving the car by storm.

7. Summary and Outlook

This dissertation presents a poser program package with GUI, which was developed to deform the most popular voxel-based human body model HUGO into different postures. Three typical application examples of the postured human body models in electrical engineering were simulated and analyzed in detail. The present chapter gives a brief summary of the essential points and an outlook for possible future works.

Summary

In the frame of this work, the main achievement is the development of the poser program package. With the increasingly improvement and optimization, the whole program package includes in total eight function modules: importing and storing the original voxel dataset with ∗.raw file or ∗.lat file; rendering the original or the deformed human body model with the MC algorithm; rendering the other useful geometries for reference e.g. the simplified human model and the FFD control lattices; setting rotation angles of different joints with the help of the simplified human model; performing the FFD calculation to deform the original human body model; exporting the deformed human body model as a new dataset with ∗.raw file or ∗.lat file; mass calculation and comparison; moving, rotating or scaling all shown geometries. The GUI of the poser program has also been updated many times in order to ensure that the user can use the program package as conveniently as possible.

In order to build a consistent FFD control lattice system for the whole body human model, locations of all joint points were determined firstly by observing the internal anatomical structure of the finest 1 mm resolution HUGO model. Then all joint points were divided into three groups: (right / left) hip joint – knee – ankle – foot tiptoe, and waist – neck – (right / left) shoulder – elbow – fingertip. Thus when one joint point is adjusted by the user, some other joint points will be moved in accordance as the way actual human being uses. The configuration and deformation rules of the FFD control lattices were designed specifically for different joint points, based on different internal anatomical structures. As a result, the original human body model can be deformed as real person as possible.

Internal structure of the human body is very complicated. In order to deform the original voxel-based human body model as reasonable as possible, some specific problems were solved. Firstly, the arms were separated away from the trunk with the developed segmentation method, and then the arms can be moved independently and their deformations will not influence the trunk. The segmentation method also avoids the possible errors caused by the unreasonable manual cutting method, which was often used before for simplicity. Secondly, the muscles of the upper arm can be swelled to different extent by adjusting one independent FFD control point. This function can simulate the situation in which people bends his or her elbows, especially with great force. Thirdly, three sets of FFD control lattices were defined around the right and left knee joint: the first set is used for deforming the fat, muscle, skin and other flexible materials; the second set can move the femur and the tibia as a rigid body; and the third set is used to rotate the patella based on rotation angle of the knee joint. As a result, when the knee joint is bent, the patella can be moved to its right position and the unreasonable deformations of the femur and the tibia can be avoided.

In the poser program package, the MC algorithm and the FFD technique were combined together to deform the voxel-based human body model. The advantage of this combination is that the user can check the deformed human body model before it is exported as a new dataset file. This function can save the user a lot of time and ensure validity of the deformed human body model as earlier as possible.

The postured human body models can be exported as new voxel dataset files with $*$.raw file or $*$.lat file in an extended voxel space. One compensation algorithm was developed to fill in the possible 0 tissue ID voxels with reasonable tissues IDs to get a continuous internal anatomical structure and decrease memory requirement. The masses of each tissue, organ and the whole body of the deformed human body model can be calculated and compared with those of the original HUGO model. After testing and modifying the strategy of defining and moving the FFD control lattice system many times in detail, the poser program decreases the mass error below 5% for the three postured human body models used in the application examples of this dissertation. The mass errors of the whole body of the sitting, standing, and walking human models are even below 2%.

Besides the main goal of developing poser program package, some further achievements have been accomplished in three application examples.

In this dissertation, with the help of two postured voxel-based human body models with standing and walking posture respectively, two simulations were performed to study the distribution of the internal electric field and the current density field in the human body shocked by the step voltage, and their influences on human's health. For the step voltage, two excitation sources were considered: the downed power line which was simulated as a stationary current calculation; and the lightning current which was solved as a transient time-domain calculation. Simulation results showed dangerous areas in the human body with higher current densities and variation of the internal current density field with time, revealed the relationship between the whole body current and the distance between the point where the downed power line is located or the lightning strikes and the victim, and explained the influence of human's posture on human body's electrical resistance and the simulation results. Results of the whole body current and the internal current density field in the human body were both compared with related healthy criterions from IEC standards and other reference materials.

For the step voltage excited by the lightning current, because of very low frequency content of the lightning current signal, the simulation was in principle an electro-quasistatic problem. However, the dispersive nature of the biological materials required the use of a full-wave transient simulator, which can deal with such materials. Due to the Courant time step limitation and long during of the excitation signal, the simulation would require a huge number of time steps. To alleviate this problem, the reduced *c* technique, which was often applied to solve magneto-quasistatic simulations before, was studied to speed up the electro-quasistatic simulation. After an error analysis, the simulation was speeded up around 20 times, while the error can be decreased below 5% in the very short rising part of the lightning current signal, and even below 0.5% for time instants near and after the peak value. At last, a new error-correction approach was developed to modify and improve the simulation results calculated from the reduced *c* technique. With its help, the error introduced by using the reduced *c* technique can be decreased even for a much larger speed-up factor.

As a high frequency electromagnetic application, the influence of the human's posture and the irradiation direction of the incident wave were analyzed, when calculating the whole body averaged SAR and the localized SAR distribution of a sitting and a standing human body model exposed to radio frequency electromagnetic fields ranging from 30 MHz to 300 MHz. Simulation results showed variation of the whole-body averaged SAR with the frequency, revealed that the resonance frequency of the human body was around 70 MHz but influenced by the human's posture, showed the localized SAR distribution of the human body models near the resonance frequency and the areas with higher localized SAR values. At last, as two real scenario situations, the distributions of the electric field, current density field and localized SAR of a driver-car were simulated and analyzed while the whole model is exposed to a plane wave and struck by a lightning current.

Outlook

Some ideas and remarks about future work of this project are listed below:

- Use the same methodology in this dissertation to deform other voxel-based human body models, especially female and child models.
- With the FFD technique, scale the original voxel-based human models to some extent to make it match different individuals with different body dimensions.
- Use some improved deformation techniques, which are developed based on the FFD technique, to deform the voxel-based human body models. Such as the extended free form deformation technique (EFFD) [58] and the direct manipulation free form deformation technique (DFFD) [97].
- Use the skeleton-tree based deformation technique [98] [99], which is another very famous deformation technique in the computer graphics domain, to deform the voxel-based human body models, and compare its performance with that of the FFD technique.
- Apply the deformed human body models in other application examples, such as the influence of mobile phone to human's health.

Appendix A: Look-up Tables of Marching Cubes Algorithm

Edge table [256] = {

0x000, 0x109, 0x203, 0x30a, 0x406, 0x50f, 0x605, 0x70c, 0x80c, 0x905,0xa0f, 0xb06, 0xc0a, 0xd03, 0xe09, 0xf00, 0x190, 0x099, 0x393, 0x29a, 0x596, 0x49f, 0x795, 0x69c, 0x99c, 0x895, 0xb9f, 0xa96, 0xd9a, 0xc93, 0xf99, 0xe90, 0x230, 0x339, 0x033, 0x13a, 0x636, 0x73f, 0x435, 0x53c, 0xa3c, 0xb35, 0x83f, 0x936, 0xe3a, 0xf33, 0xc39, 0xd30, 0x3a0, 0x2a9, 0x1a3, 0x0aa, 0x7a6, 0x6af, 0x5a5, 0x4ac, 0xbac, 0xaa5, 0x9af, 0x8a6, 0xfaa, 0xea3, 0xda9, 0xca0, 0x460, 0x569, 0x663, 0x76a, 0x066, 0x16f, 0x265, 0x36c, 0xc6c, 0xd65, 0xe6f, 0xf66, 0x86a, 0x963, 0xa69, 0xb60, 0x5f0, 0x4f9, 0x7f3, 0x6fa, 0x1f6, 0x0ff, 0x3f5, 0x2fc, 0xdfc, 0xcf5, 0xfff, 0xef6, 0x9fa, 0x8f3, 0xbf9, 0xaf0, 0x650, 0x759, 0x453, 0x55a, 0x256, 0x35f, 0x055, 0x15c, 0xe5c, 0xf55, 0xc5f, 0xd56, 0xa5a, 0xb53, 0x859, 0x950, 0x7c0, 0x6c9, 0x5c3, 0x4ca, 0x3c6, 0x2cf, 0x1c5, 0x0cc, 0xfcc, 0xec5, 0xdcf, 0xcc6, 0xbca, 0xac3, 0x9c9, 0x8c0, 0x8c0, 0x9c9, 0xac3, 0xbca, 0xcc6, 0xdcf, 0xec5, 0xfcc, 0x0cc, 0x1c5, 0x2cf, 0x3c6, 0x4ca, 0x5c3, 0x6c9, 0x7c0, 0x950, 0x859, 0xb53, 0xa5a, 0xd56, 0xc5f, 0xf55, 0xe5c, 0x15c, 0x055, 0x35f, 0x256, 0x55a, 0x453, 0x759, 0x650, 0xaf0, 0xbf9, 0x8f3, 0x9fa, 0xef6, 0xfff, 0xcf5, 0xdfc, 0x2fc, 0x3f5, 0x0ff, 0x1f6, 0x6fa, 0x7f3, 0x4f9, 0x5f0, 0xb60, 0xa69, 0x963, 0x86a, 0xf66, 0xe6f, 0xd65, 0xc6c, 0x36c, 0x265, 0x16f, 0x066, 0x76a, 0x663, 0x569, 0x460, 0xca0, 0xda9, 0xea3, 0xfaa, 0x8a6, 0x9af, 0xaa5, 0xbac, 0x4ac, 0x5a5, 0x6af, 0x7a6, 0x0aa, 0x1a3, 0x2a9, 0x3a0, 0xd30, 0xc39, 0xf33, 0xe3a, 0x936, 0x83f, 0xb35, 0xa3c, 0x53c, 0x435, 0x73f, 0x636, 0x13a, 0x033, 0x339, 0x230, 0xe90, 0xf99, 0xc93, 0xd9a, 0xa96, 0xb9f, 0x895, 0x99c, 0x69c, 0x795, 0x49f, 0x596, 0x29a, 0x393, 0x099, 0x190, 0xf00, 0xe09, 0xd03, 0xc0a, 0xb06, 0xa0f, 0x905, 0x80c, 0x70c, 0x605, 0x50f, 0x406, 0x30a, 0x203, 0x109, 0x000 }

Triangular table [256][16] = {

{-1, -1, -1, -1, -1, -1, -1, -1, -1, -1, -1, -1, -1, -1, -1, -1},
{0, 8, 3, -1, -1, -1, -1, -1, -1, -1, -1, -1, -1, -1, -1, -1},
{0, 1, 9, -1, -1, -1, -1, -1, -1, -1, -1, -1, -1, -1, -1, -1},
{1, 8, 3, 9, 8, 1, -1, -1, -1, -1, -1, -1, -1, -1, -1, -1},
{1, 2, 10, -1, -1, -1, -1, -1, -1, -1, -1, -1, -1, -1, -1, -1},
{0, 8, 3, 1, 2, 10, -1, -1, -1, -1, -1, -1, -1, -1, -1, -1},
{9, 2, 10, 0, 2, 9, -1, -1, -1, -1, -1, -1, -1, -1, -1, -1},
{2, 8, 3, 2, 10, 8, 10, 9, 8, -1, -1, -1, -1, -1, -1, -1},
{3, 11, 2, -1, -1, -1, -1, -1, -1, -1, -1, -1, -1, -1, -1, -1},
{0, 11, 2, 8, 11, 0, -1, -1, -1, -1, -1, -1, -1, -1, -1, -1},
{1, 9, 0, 2, 3, 11, -1, -1, -1, -1, -1, -1, -1, -1, -1, -1},
{1, 11, 2, 1, 9, 11, 9, 8, 11, -1, -1, -1, -1, -1, -1, -1},
{3, 10, 1, 11, 10, 3, -1, -1, -1, -1, -1, -1, -1, -1, -1, -1},
{0, 10, 1, 0, 8, 10, 8, 11, 10, -1, -1, -1, -1, -1, -1, -1},
{3, 9, 0, 3, 11, 9, 11, 10, 9, -1, -1, -1, -1, -1, -1, -1},
{9, 8, 10, 10, 8, 11, -1, -1, -1, -1, -1, -1, -1, -1, -1, -1},
{4, 7, 8, -1, -1, -1, -1, -1, -1, -1, -1, -1, -1, -1, -1, -1},
{4, 3, 0, 7, 3, 4, -1, -1, -1, -1, -1, -1, -1, -1, -1, -1},
{0, 1, 9, 8, 4, 7, -1, -1, -1, -1, -1, -1, -1, -1, -1, -1},
{4, 1, 9, 4, 7, 1, 7, 3, 1, -1, -1, -1, -1, -1, -1, -1},
{1, 2, 10, 8, 4, 7, -1, -1, -1, -1, -1, -1, -1, -1, -1, -1},
{3, 4, 7, 3, 0, 4, 1, 2, 10, -1, -1, -1, -1, -1, -1, -1},
{9, 2, 10, 9, 0, 2, 8, 4, 7, -1, -1, -1, -1, -1, -1, -1},

```
{2, 10, 9, 2, 9, 7, 2, 7, 3, 7, 9, 4, -1, -1, -1, -1},
{8, 4, 7, 3, 11, 2, -1, -1, -1, -1, -1, -1, -1, -1, -1, -1},
{11, 4, 7, 11, 2, 4, 2, 0, 4, -1, -1, -1, -1, -1, -1, -1},
{9, 0, 1, 8, 4, 7, 2, 3, 11, -1, -1, -1, -1, -1, -1, -1},
{4, 7, 11, 9, 4, 11, 9, 11, 2, 9, 2, 1, -1, -1, -1, -1},
{3, 10, 1, 3, 11, 10, 7, 8, 4, -1, -1, -1, -1, -1, -1, -1},
{1, 11, 10, 1, 4, 11, 1, 0, 4, 7, 11, 4, -1, -1, -1, -1},
{4, 7, 8, 9, 0, 11, 9, 11, 10, 11, 0, 3, -1, -1, -1, -1},
{4, 7, 11, 4, 11, 9, 9, 11, 10, -1, -1, -1, -1, -1, -1, -1},
{9, 5, 4, -1, -1, -1, -1, -1, -1, -1, -1, -1, -1, -1, -1, -1},
{9, 5, 4, 0, 8, 3, -1, -1, -1, -1, -1, -1, -1, -1, -1, -1},
{0, 5, 4, 1, 5, 0, -1, -1, -1, -1, -1, -1, -1, -1, -1, -1},
{8, 5, 4, 8, 3, 5, 3, 1, 5, -1, -1, -1, -1, -1, -1, -1},
{1, 2, 10, 9, 5, 4, -1, -1, -1, -1, -1, -1, -1, -1, -1, -1},
{3, 0, 8, 1, 2, 10, 4, 9, 5, -1, -1, -1, -1, -1, -1, -1},
{5, 2, 10, 5, 4, 2, 4, 0, 2, -1, -1, -1, -1, -1, -1, -1},
{2, 10, 5, 3, 2, 5, 3, 5, 4, 3, 4, 8, -1, -1, -1, -1},
{9, 5, 4, 2, 3, 11, -1, -1, -1, -1, -1, -1, -1, -1, -1, -1},
{0, 11, 2, 0, 8, 11, 4, 9, 5, -1, -1, -1, -1, -1, -1, -1},
{0, 5, 4, 0, 1, 5, 2, 3, 11, -1, -1, -1, -1, -1, -1, -1},
{2, 1, 5, 2, 5, 8, 2, 8, 11, 4, 8, 5, -1, -1, -1, -1},
{10, 3, 11, 10, 1, 3, 9, 5, 4, -1, -1, -1, -1, -1, -1, -1},
{4, 9, 5, 0, 8, 1, 8, 10, 1, 8, 11, 10, -1, -1, -1, -1},
{5, 4, 0, 5, 0, 11, 5, 11, 10, 11, 0, 3, -1, -1, -1, -1},
{5, 4, 8, 5, 8, 10, 10, 8, 11, -1, -1, -1, -1, -1, -1, -1},
{9, 7, 8, 5, 7, 9, -1, -1, -1, -1, -1, -1, -1, -1, -1, -1},
{9, 3, 0, 9, 5, 3, 5, 7, 3, -1, -1, -1, -1, -1, -1, -1},
{0, 7, 8, 0, 1, 7, 1, 5, 7, -1, -1, -1, -1, -1, -1, -1},
{1, 5, 3, 3, 5, 7, -1, -1, -1, -1, -1, -1, -1, -1, -1, -1},
{9, 7, 8, 9, 5, 7, 10, 1, 2, -1, -1, -1, -1, -1, -1, -1},
{10, 1, 2, 9, 5, 0, 5, 3, 0, 5, 7, 3, -1, -1, -1, -1},
{8, 0, 2, 8, 2, 5, 8, 5, 7, 10, 5, 2, -1, -1, -1, -1},
{2, 10, 5, 2, 5, 3, 3, 5, 7, -1, -1, -1, -1, -1, -1, -1},
{7, 9, 5, 7, 8, 9, 3, 11, 2, -1, -1, -1, -1, -1, -1, -1},
{9, 5, 7, 9, 7, 2, 9, 2, 0, 2, 7, 11, -1, -1, -1, -1},
{2, 3, 11, 0, 1, 8, 1, 7, 8, 1, 5, 7, -1, -1, -1, -1},
{11, 2, 1, 11, 1, 7, 7, 1, 5, -1, -1, -1, -1, -1, -1, -1},
{9, 5, 8, 8, 5, 7, 10, 1, 3, 10, 3, 11, -1, -1, -1, -1},
{5, 7, 0, 5, 0, 9, 7, 11, 0, 1, 0, 10, 11, 10, 0, -1},
{11, 10, 0, 11, 0, 3, 10, 5, 0, 8, 0, 7, 5, 7, 0, -1},
{11, 10, 5, 7, 11, 5, -1, -1, -1, -1, -1, -1, -1, -1, -1, -1},
{10, 6, 5, -1, -1, -1, -1, -1, -1, -1, -1, -1, -1, -1, -1, -1},
{0, 8, 3, 5, 10, 6, -1, -1, -1, -1, -1, -1, -1, -1, -1, -1},
{9, 0, 1, 5, 10, 6, -1, -1, -1, -1, -1, -1, -1, -1, -1, -1},
{1, 8, 3, 1, 9, 8, 5, 10, 6, -1, -1, -1, -1, -1, -1, -1},
{1, 6, 5, 2, 6, 1, -1, -1, -1, -1, -1, -1, -1, -1, -1, -1},
{1, 6, 5, 1, 2, 6, 3, 0, 8, -1, -1, -1, -1, -1, -1, -1},
{9, 6, 5, 9, 0, 6, 0, 2, 6, -1, -1, -1, -1, -1, -1, -1},
{5, 9, 8, 5, 8, 2, 5, 2, 6, 3, 2, 8, -1, -1, -1, -1},
{2, 3, 11, 10, 6, 5, -1, -1, -1, -1, -1, -1, -1, -1, -1, -1},
{11, 0, 8, 11, 2, 0, 10, 6, 5, -1, -1, -1, -1, -1, -1, -1},
{0, 1, 9, 2, 3, 11, 5, 10, 6, -1, -1, -1, -1, -1, -1, -1},
{5, 10, 6, 1, 9, 2, 9, 11, 2, 9, 8, 11, -1, -1, -1, -1},
{6, 3, 11, 6, 5, 3, 5, 1, 3, -1, -1, -1, -1, -1, -1, -1},
{0, 8, 11, 0, 11, 5, 0, 5, 1, 5, 11, 6, -1, -1, -1, -1},
{3, 11, 6, 0, 3, 6, 0, 6, 5, 0, 5, 9, -1, -1, -1, -1},
{6, 5, 9, 6, 9, 11, 11, 9, 8, -1, -1, -1, -1, -1, -1, -1},
{5, 10, 6, 4, 7, 8, -1, -1, -1, -1, -1, -1, -1, -1, -1, -1},
{4, 3, 0, 4, 7, 3, 6, 5, 10, -1, -1, -1, -1, -1, -1, -1},
```

```
{1, 9, 0, 5, 10, 6, 8, 4, 7, -1, -1, -1, -1, -1, -1, -1},
{10, 6, 5, 1, 9, 7, 1, 7, 3, 7, 9, 4, -1, -1, -1, -1},
{6, 1, 2, 6, 5, 1, 4, 7, 8, -1, -1, -1, -1, -1, -1, -1},
{1, 2, 5, 5, 2, 6, 3, 0, 4, 3, 4, 7, -1, -1, -1, -1},
{8, 4, 7, 9, 0, 5, 0, 6, 5, 0, 2, 6, -1, -1, -1, -1},
{7, 3, 9, 7, 9, 4, 3, 2, 9, 5, 9, 6, 2, 6, 9, -1},
{3, 11, 2, 7, 8, 4, 10, 6, 5, -1, -1, -1, -1, -1, -1, -1},
{5, 10, 6, 4, 7, 2, 4, 2, 0, 2, 7, 11, -1, -1, -1, -1},
{0, 1, 9, 4, 7, 8, 2, 3, 11, 5, 10, 6, -1, -1, -1, -1},
{9, 2, 1, 9, 11, 2, 9, 4, 11, 7, 11, 4, 5, 10, 6, -1},
{8, 4, 7, 3, 11, 5, 3, 5, 1, 5, 11, 6, -1, -1, -1, -1},
{5, 1, 11, 5, 11, 6, 1, 0, 11, 7, 11, 4, 0, 4, 11, -1},
{0, 5, 9, 0, 6, 5, 0, 3, 6, 11, 6, 3, 8, 4, 7, -1},
{6, 5, 9, 6, 9, 11, 4, 7, 9, 7, 11, 9, -1, -1, -1, -1},
{10, 4, 9, 6, 4, 10, -1, -1, -1, -1, -1, -1, -1, -1, -1, -1},
{4, 10, 6, 4, 9, 10, 0, 8, 3, -1, -1, -1, -1, -1, -1, -1},
{10, 0, 1, 10, 6, 0, 6, 4, 0, -1, -1, -1, -1, -1, -1, -1},
{8, 3, 1, 8, 1, 6, 8, 6, 4, 6, 1, 10, -1, -1, -1, -1},
{1, 4, 9, 1, 2, 4, 2, 6, 4, -1, -1, -1, -1, -1, -1, -1},
{3, 0, 8, 1, 2, 9, 2, 4, 9, 2, 6, 4, -1, -1, -1, -1},
{0, 2, 4, 4, 2, 6, -1, -1, -1, -1, -1, -1, -1, -1, -1, -1},
{8, 3, 2, 8, 2, 4, 4, 2, 6, -1, -1, -1, -1, -1, -1, -1},
{10, 4, 9, 10, 6, 4, 11, 2, 3, -1, -1, -1, -1, -1, -1, -1},
{0, 8, 2, 2, 8, 11, 4, 9, 10, 4, 10, 6, -1, -1, -1, -1},
{3, 11, 2, 0, 1, 6, 0, 6, 4, 6, 1, 10, -1, -1, -1, -1},
{6, 4, 1, 6, 1, 10, 4, 8, 1, 2, 1, 11, 8, 11, 1, -1},
{9, 6, 4, 9, 3, 6, 9, 1, 3, 11, 6, 3, -1, -1, -1, -1},
{8, 11, 1, 8, 1, 0, 11, 6, 1, 9, 1, 4, 6, 4, 1, -1},
{3, 11, 6, 3, 6, 0, 0, 6, 4, -1, -1, -1, -1, -1, -1, -1},
{6, 4, 8, 11, 6, 8, -1, -1, -1, -1, -1, -1, -1, -1, -1, -1},
{7, 10, 6, 7, 8, 10, 8, 9, 10, -1, -1, -1, -1, -1, -1, -1},
{0, 7, 3, 0, 10, 7, 0, 9, 10, 6, 7, 10, -1, -1, -1, -1},
{10, 6, 7, 1, 10, 7, 1, 7, 8, 1, 8, 0, -1, -1, -1, -1},
{10, 6, 7, 10, 7, 1, 1, 7, 3, -1, -1, -1, -1, -1, -1, -1},
{1, 2, 6, 1, 6, 8, 1, 8, 9, 8, 6, 7, -1, -1, -1, -1},
{2, 6, 9, 2, 9, 1, 6, 7, 9, 0, 9, 3, 7, 3, 9, -1},
{7, 8, 0, 7, 0, 6, 6, 0, 2, -1, -1, -1, -1, -1, -1, -1},
{7, 3, 2, 6, 7, 2, -1, -1, -1, -1, -1, -1, -1, -1, -1, -1},
{2, 3, 11, 10, 6, 8, 10, 8, 9, 8, 6, 7, -1, -1, -1, -1},
{2, 0, 7, 2, 7, 11, 0, 9, 7, 6, 7, 10, 9, 10, 7, -1},
{1, 8, 0, 1, 7, 8, 1, 10, 7, 6, 7, 10, 2, 3, 11, -1},
{11, 2, 1, 11, 1, 7, 10, 6, 1, 6, 7, 1, -1, -1, -1, -1},
{8, 9, 6, 8, 6, 7, 9, 1, 6, 11, 6, 3, 1, 3, 6, -1},
{0, 9, 1, 11, 6, 7, -1, -1, -1, -1, -1, -1, -1, -1, -1, -1},
{7, 8, 0, 7, 0, 6, 3, 11, 0, 11, 6, 0, -1, -1, -1, -1},
{7, 11, 6, -1, -1, -1, -1, -1, -1, -1, -1, -1, -1, -1, -1, -1},
{7, 6, 11, -1, -1, -1, -1, -1, -1, -1, -1, -1, -1, -1, -1, -1},
{3, 0, 8, 11, 7, 6, -1, -1, -1, -1, -1, -1, -1, -1, -1, -1},
{0, 1, 9, 11, 7, 6, -1, -1, -1, -1, -1, -1, -1, -1, -1, -1},
{8, 1, 9, 8, 3, 1, 11, 7, 6, -1, -1, -1, -1, -1, -1, -1},
{10, 1, 2, 6, 11, 7, -1, -1, -1, -1, -1, -1, -1, -1, -1, -1},
{1, 2, 10, 3, 0, 8, 6, 11, 7, -1, -1, -1, -1, -1, -1, -1},
{2, 9, 0, 2, 10, 9, 6, 11, 7, -1, -1, -1, -1, -1, -1, -1},
{6, 11, 7, 2, 10, 3, 10, 8, 3, 10, 9, 8, -1, -1, -1, -1},
{7, 2, 3, 6, 2, 7, -1, -1, -1, -1, -1, -1, -1, -1, -1, -1},
{7, 0, 8, 7, 6, 0, 6, 2, 0, -1, -1, -1, -1, -1, -1, -1},
{2, 7, 6, 2, 3, 7, 0, 1, 9, -1, -1, -1, -1, -1, -1, -1},
{1, 6, 2, 1, 8, 6, 1, 9, 8, 8, 7, 6, -1, -1, -1, -1},
{10, 7, 6, 10, 1, 7, 1, 3, 7, -1, -1, -1, -1, -1, -1, -1},
```

```
{10, 7, 6, 1, 7, 10, 1, 8, 7, 1, 0, 8, -1, -1, -1, -1},
{0, 3, 7, 0, 7, 10, 0, 10, 9, 6, 10, 7, -1, -1, -1, -1},
{7, 6, 10, 7, 10, 8, 8, 10, 9, -1, -1, -1, -1, -1, -1, -1},
{6, 8, 4, 11, 8, 6, -1, -1, -1, -1, -1, -1, -1, -1, -1, -1},
{3, 6, 11, 3, 0, 6, 0, 4, 6, -1, -1, -1, -1, -1, -1, -1},
{8, 6, 11, 8, 4, 6, 9, 0, 1, -1, -1, -1, -1, -1, -1, -1},
{9, 4, 6, 9, 6, 3, 9, 3, 1, 11, 3, 6, -1, -1, -1, -1},
{6, 8, 4, 6, 11, 8, 2, 10, 1, -1, -1, -1, -1, -1, -1, -1},
{1, 2, 10, 3, 0, 11, 0, 6, 11, 0, 4, 6, -1, -1, -1, -1},
{4, 11, 8, 4, 6, 11, 0, 2, 9, 2, 10, 9, -1, -1, -1, -1},
{10, 9, 3, 10, 3, 2, 9, 4, 3, 11, 3, 6, 4, 6, 3, -1},
{8, 2, 3, 8, 4, 2, 4, 6, 2, -1, -1, -1, -1, -1, -1, -1},
{0, 4, 2, 4, 6, 2, -1, -1, -1, -1, -1, -1, -1, -1, -1, -1},
{1, 9, 0, 2, 3, 4, 2, 4, 6, 4, 3, 8, -1, -1, -1, -1},
{1, 9, 4, 1, 4, 2, 2, 4, 6, -1, -1, -1, -1, -1, -1, -1},
{8, 1, 3, 8, 6, 1, 8, 4, 6, 6, 10, 1, -1, -1, -1, -1},
{10, 1, 0, 10, 0, 6, 6, 0, 4, -1, -1, -1, -1, -1, -1, -1},
{4, 6, 3, 4, 3, 8, 6, 10, 3, 0, 3, 9, 10, 9, 3, -1},
{10, 9, 4, 6, 10, 4, -1, -1, -1, -1, -1, -1, -1, -1, -1, -1},
{4, 9, 5, 7, 6, 11, -1, -1, -1, -1, -1, -1, -1, -1, -1, -1},
{0, 8, 3, 4, 9, 5, 11, 7, 6, -1, -1, -1, -1, -1, -1, -1},
{5, 0, 1, 5, 4, 0, 7, 6, 11, -1, -1, -1, -1, -1, -1, -1},
{11, 7, 6, 8, 3, 4, 3, 5, 4, 3, 1, 5, -1, -1, -1, -1},
{9, 5, 4, 10, 1, 2, 7, 6, 11, -1, -1, -1, -1, -1, -1, -1},
{6, 11, 7, 1, 2, 10, 0, 8, 3, 4, 9, 5, -1, -1, -1, -1},
{7, 6, 11, 5, 4, 10, 4, 2, 10, 4, 0, 2, -1, -1, -1, -1},
{3, 4, 8, 3, 5, 4, 3, 2, 5, 10, 5, 2, 11, 7, 6, -1},
{7, 2, 3, 7, 6, 2, 5, 4, 9, -1, -1, -1, -1, -1, -1, -1},
{9, 5, 4, 0, 8, 6, 0, 6, 2, 6, 8, 7, -1, -1, -1, -1},
{3, 6, 2, 3, 7, 6, 1, 5, 0, 5, 4, 0, -1, -1, -1, -1},
{6, 2, 8, 6, 8, 7, 2, 1, 8, 4, 8, 5, 1, 5, 8, -1},
{9, 5, 4, 10, 1, 6, 1, 7, 6, 1, 3, 7, -1, -1, -1, -1},
{1, 6, 10, 1, 7, 6, 1, 0, 7, 8, 7, 0, 9, 5, 4, -1},
{4, 0, 10, 4, 10, 5, 0, 3, 10, 6, 10, 7, 3, 7, 10, -1},
{7, 6, 10, 7, 10, 8, 5, 4, 10, 4, 8, 10, -1, -1, -1, -1},
{6, 9, 5, 6, 11, 9, 11, 8, 9, -1, -1, -1, -1, -1, -1, -1},
{3, 6, 11, 0, 6, 3, 0, 5, 6, 0, 9, 5, -1, -1, -1, -1},
{0, 11, 8, 0, 5, 11, 0, 1, 5, 5, 6, 11, -1, -1, -1, -1},
{6, 11, 3, 6, 3, 5, 5, 3, 1, -1, -1, -1, -1, -1, -1, -1},
{1, 2, 10, 9, 5, 11, 9, 11, 8, 11, 5, 6, -1, -1, -1, -1},
{0, 11, 3, 0, 6, 11, 0, 9, 6, 5, 6, 9, 1, 2, 10, -1},
{11, 8, 5, 11, 5, 6, 8, 0, 5, 10, 5, 2, 0, 2, 5, -1},
{6, 11, 3, 6, 3, 5, 2, 10, 3, 10, 5, 3, -1, -1, -1, -1},
{5, 8, 9, 5, 2, 8, 5, 6, 2, 3, 8, 2, -1, -1, -1, -1},
{9, 5, 6, 9, 6, 0, 0, 6, 2, -1, -1, -1, -1, -1, -1, -1},
{1, 5, 8, 1, 8, 0, 5, 6, 8, 3, 8, 2, 6, 2, 8, -1},
{1, 5, 6, 2, 1, 6, -1, -1, -1, -1, -1, -1, -1, -1, -1, -1},
{1, 3, 6, 1, 6, 10, 3, 8, 6, 5, 6, 9, 8, 9, 6, -1},
{10, 1, 0, 10, 0, 6, 9, 5, 0, 5, 6, 0, -1, -1, -1, -1},
{0, 3, 8, 5, 6, 10, -1, -1, -1, -1, -1, -1, -1, -1, -1, -1},
{10, 5, 6, -1, -1, -1, -1, -1, -1, -1, -1, -1, -1, -1, -1, -1},
{11, 5, 10, 7, 5, 11, -1, -1, -1, -1, -1, -1, -1, -1, -1, -1},
{11, 5, 10, 11, 7, 5, 8, 3, 0, -1, -1, -1, -1, -1, -1, -1},
{5, 11, 7, 5, 10, 11, 1, 9, 0, -1, -1, -1, -1, -1, -1, -1},
{10, 7, 5, 10, 11, 7, 9, 8, 1, 8, 3, 1, -1, -1, -1, -1},
{11, 1, 2, 11, 7, 1, 7, 5, 1, -1, -1, -1, -1, -1, -1, -1},
{0, 8, 3, 1, 2, 7, 1, 7, 5, 7, 2, 11, -1, -1, -1, -1},
{9, 7, 5, 9, 2, 7, 9, 0, 2, 2, 11, 7, -1, -1, -1, -1},
{7, 5, 2, 7, 2, 11, 5, 9, 2, 3, 2, 8, 9, 8, 2, -1},
```

```
    {2, 5, 10, 2, 3, 5, 3, 7, 5, -1, -1, -1, -1, -1, -1, -1},
    {8, 2, 0, 8, 5, 2, 8, 7, 5, 10, 2, 5, -1, -1, -1, -1},
    {9, 0, 1, 5, 10, 3, 5, 3, 7, 3, 10, 2, -1, -1, -1, -1},
    {9, 8, 2, 9, 2, 1, 8, 7, 2, 10, 2, 5, 7, 5, 2, -1},
    {1, 3, 5, 3, 7, 5, -1, -1, -1, -1, -1, -1, -1, -1, -1, -1},
    {0, 8, 7, 0, 7, 1, 1, 7, 5, -1, -1, -1, -1, -1, -1, -1},
    {9, 0, 3, 9, 3, 5, 5, 3, 7, -1, -1, -1, -1, -1, -1, -1},
    {9, 8, 7, 5, 9, 7, -1, -1, -1, -1, -1, -1, -1, -1, -1, -1},
    {5, 8, 4, 5, 10, 8, 10, 11, 8, -1, -1, -1, -1, -1, -1, -1},
    {5, 0, 4, 5, 11, 0, 5, 10, 11, 11, 3, 0, -1, -1, -1, -1},
    {0, 1, 9, 8, 4, 10, 8, 10, 11, 10, 4, 5, -1, -1, -1, -1},
    {10, 11, 4, 10, 4, 5, 11, 3, 4, 9, 4, 1, 3, 1, 4, -1},
    {2, 5, 1, 2, 8, 5, 2, 11, 8, 4, 5, 8, -1, -1, -1, -1},
    {0, 4, 11, 0, 11, 3, 4, 5, 11, 2, 11, 1, 5, 1, 11, -1},
    {0, 2, 5, 0, 5, 9, 2, 11, 5, 4, 5, 8, 11, 8, 5, -1},
    {9, 4, 5, 2, 11, 3, -1, -1, -1, -1, -1, -1, -1, -1, -1, -1},
    {2, 5, 10, 3, 5, 2, 3, 4, 5, 3, 8, 4, -1, -1, -1, -1},
    {5, 10, 2, 5, 2, 4, 4, 2, 0, -1, -1, -1, -1, -1, -1, -1},
    {3, 10, 2, 3, 5, 10, 3, 8, 5, 4, 5, 8, 0, 1, 9, -1},
    {5, 10, 2, 5, 2, 4, 1, 9, 2, 9, 4, 2, -1, -1, -1, -1},
    {8, 4, 5, 8, 5, 3, 3, 5, 1, -1, -1, -1, -1, -1, -1, -1},
    {0, 4, 5, 1, 0, 5, -1, -1, -1, -1, -1, -1, -1, -1, -1, -1},
    {8, 4, 5, 8, 5, 3, 9, 0, 5, 0, 3, 5, -1, -1, -1, -1},
    {9, 4, 5, -1, -1, -1, -1, -1, -1, -1, -1, -1, -1, -1, -1, -1},
    {4, 11, 7, 4, 9, 11, 9, 10, 11, -1, -1, -1, -1, -1, -1, -1},
    {0, 8, 3, 4, 9, 7, 9, 11, 7, 9, 10, 11, -1, -1, -1, -1},
    {1, 10, 11, 1, 11, 4, 1, 4, 0, 7, 4, 11, -1, -1, -1, -1},
    {3, 1, 4, 3, 4, 8, 1, 10, 4, 7, 4, 11, 10, 11, 4, -1},
    {4, 11, 7, 9, 11, 4, 9, 2, 11, 9, 1, 2, -1, -1, -1, -1},
    {9, 7, 4, 9, 11, 7, 9, 1, 11, 2, 11, 1, 0, 8, 3, -1},
    {11, 7, 4, 11, 4, 2, 2, 4, 0, -1, -1, -1, -1, -1, -1, -1},
    {11, 7, 4, 11, 4, 2, 8, 3, 4, 3, 2, 4, -1, -1, -1, -1},
    {2, 9, 10, 2, 7, 9, 2, 3, 7, 7, 4, 9, -1, -1, -1, -1},
    {9, 10, 7, 9, 7, 4, 10, 2, 7, 8, 7, 0, 2, 0, 7, -1},
    {3, 7, 10, 3, 10, 2, 7, 4, 10, 1, 10, 0, 4, 0, 10, -1},
    {1, 10, 2, 8, 7, 4, -1, -1, -1, -1, -1, -1, -1, -1, -1, -1},
    {4, 9, 1, 4, 1, 7, 7, 1, 3, -1, -1, -1, -1, -1, -1, -1},
    {4, 9, 1, 4, 1, 7, 0, 8, 1, 8, 7, 1, -1, -1, -1, -1},
    {4, 0, 3, 7, 4, 3, -1, -1, -1, -1, -1, -1, -1, -1, -1, -1},
    {4, 8, 7, -1, -1, -1, -1, -1, -1, -1, -1, -1, -1, -1, -1, -1},
    {9, 10, 8, 10, 11, 8, -1, -1, -1, -1, -1, -1, -1, -1, -1, -1},
    {3, 0, 9, 3, 9, 11, 11, 9, 10, -1, -1, -1, -1, -1, -1, -1},
    {0, 1, 10, 0, 10, 8, 8, 10, 11, -1, -1, -1, -1, -1, -1, -1},
    {3, 1, 10, 11, 3, 10, -1, -1, -1, -1, -1, -1, -1, -1, -1, -1},
    {1, 2, 11, 1, 11, 9, 9, 11, 8, -1, -1, -1, -1, -1, -1, -1},
    {3, 0, 9, 3, 9, 11, 1, 2, 9, 2, 11, 9, -1, -1, -1, -1},
    {0, 2, 11, 8, 0, 11, -1, -1, -1, -1, -1, -1, -1, -1, -1, -1},
    {3, 2, 11, -1, -1, -1, -1, -1, -1, -1, -1, -1, -1, -1, -1, -1},
    {2, 3, 8, 2, 8, 10, 10, 8, 9, -1, -1, -1, -1, -1, -1, -1},
    {9, 10, 2, 0, 9, 2, -1, -1, -1, -1, -1, -1, -1, -1, -1, -1},
    {2, 3, 8, 2, 8, 10, 0, 1, 8, 1, 10, 8, -1, -1, -1, -1},
    {1, 10, 2, -1, -1, -1, -1, -1, -1, -1, -1, -1, -1, -1, -1, -1},
    {1, 3, 8, 9, 1, 8, -1, -1, -1, -1, -1, -1, -1, -1, -1, -1},
    {0, 9, 1, -1, -1, -1, -1, -1, -1, -1, -1, -1, -1, -1, -1, -1},
    {0, 3, 8, -1, -1, -1, -1, -1, -1, -1, -1, -1, -1, -1, -1, -1},
    {-1, -1, -1, -1, -1, -1, -1, -1, -1, -1, -1, -1, -1, -1, -1, -1}
}
```

Appendix B: Applied Notations and Symbols

General mathematical symbols

f	frequency	Hz
λ	wave length	m
ω	angular frequency	rad Hz
Δt	time step	s
$\vec{r}$	spatial vector	
$\vec{g}$,$Grad$	gradient vector	
$\vec{n}$	vector normal to an area	

M	matrix	
M^{T}	transpose of matrix M	
M^{-1}	inverse matrix M	

$d\vec{s}$	edge element	m
$d\vec{A}$	area element	m^2
$d\vec{V}$	volume element	m^3
∂A	boundary of the area	
∂V	boundary of the volume	

Classical electromagnetic field theory

$\vec{E}$	electric field strength	V/m
$\vec{H}$	magnetic field strength	A/m
$\vec{D}$	electric flux density	$\mathrm{C/m^2}$
$\vec{B}$	magnetic flux density	T
$\vec{J}$	total current density	$\mathrm{A/m^2}$
$\vec{J}_i$	imposed current density	$\mathrm{A/m^2}$
$\vec{J}_k$	conduction current density	$\mathrm{A/m^2}$
$\vec{J}_c$	convection current density	$\mathrm{A/m^2}$
q	charge density	$\mathrm{C/m^3}$
c	speed of light	m/s
A	magnetic vector potential	Wb/m
Φ	electric scalar potential	V

μ	permeability	H/m
μ_r	relative permeability	1
μ_0	permeability of vacuum	H/m
$\hat{\varepsilon}$	complex relative permittivity	F/m

ε	permittivity	F/m
ε_r	relative permittivity	1
ε_0	permittivity of vacuum	F/m
σ	conductivity	S/m
σ_i	static ionic conductivity	S/m
τ	time constant used for different dispersion regions	µs
ε_∞	permittivity at field frequencies where $\omega\tau >> 1$	F/m
ε_s	permittivity at field frequencies where $\omega\tau << 1$	F/m

Finite Integration Technique

G	primary grid cell complex	
$\tilde{G}$	dual grid cell complex	
P_n	primary grid nodes	
$\tilde{P}_n$	dual grid nodes	
L	primary grid edges	m
$\tilde{L}$	dual grid edges	m
A	primary grid facets	m^2
$\tilde{A}$	dual grid facets	m^2
V	primary grid cell	m^3
$\tilde{V}$	dual grid cell	m^3
$\widehat{\mathrm{e}}$	electric edge voltage	V
$\widehat{\mathrm{h}}$	magnetic edge voltage	A
$\widehat{\widehat{\mathrm{d}}}$	electric facet flux	C
$\widehat{\widehat{\mathrm{b}}}$	magnetic facet flux	Wb
$\widehat{\widehat{\mathrm{j}}}$	vector of grid currents	A
$\mathrm{C}, \tilde{\mathrm{C}}$	curl discrete operator on the primary / dual grid	
$\mathrm{S}, \tilde{\mathrm{S}}$	divergence operator on the primary / dual grid	
M_ε	material matrix of permittivity	
M_σ	material matrix of conductivity	
$\mathrm{M}_{\mu^{-1}}$	material matrix of inverse permeability	

Free Form Deformation Technique

P_0-STU	local coordinate system used for FFD calculation
$\vec{P}_0$	position vector of origin of the P_0-STU
$\vec{S}, \vec{T}, \vec{U}$	three coordinate axis vectors of the P_0-STU
$\vec{P}$	position vector of any point in the original object
$\vec{P}_{\mathrm{ffd}}$	position vector of any point in the deformed object
$\vec{P}_L$	position vector of the object point in the P_0-STU

$\vec{P}_{ijk}$	position vector of any FFD control point
$\vec{P}'_{ijk}$	position vector of any FFD control point in the P_0-STU
B_i^n	Bernstein basis function
l, m, n	subdivision numbers of the FFD control lattice
(s, t, u)	local coordinates in the P_0-STU
$(s_\mathrm{d}, t_\mathrm{d}, u_\mathrm{d})$	local coordinates of any point in the deformed object
(x, y, z)	global coordinates

Abbreviations

CT	Computer Tomography
EFFD	Extended Free Form Deformation
EMF	Electromagnetic Field
EQS	Electro-quasistatic
FDTD	Finite Difference Time Domain
FFD	Free Form Deformation
FFT	Fast Fourier transformation
FIT	Finite Integration Technique
GCS	Global Coordinate System
GUI	Graphical User Interface
ICNIRP	International Commission on Non-ionizing Radiation Protection
IEC	International Electrotechnical Commission
LCS	Local Coordinate System
MC	Marching Cubes
MFC	Microsoft Foundation Class
MQS	Magneto-quasistatic
MR	Magnetic Resonance
MRI	Magnetic Resonance Imaging
NURBS	Non-Uniform Rational B-Spline
PEC	Perfect Electrical Conductor
RF	Radio Frequency
rms	root mean square
SAR	Specific Absorption Rate
SPECT	Single-Photon Emission Computed Tomography
VHP	Visible Human Project

Bibliography

[1] M. Caon, “Voxel-based computational models of real human anatomy: a review,” *Radiation and Environmental Biophysics*, vol. 42, no. 4, pp. 229-235, Feb. 2004.

[2] T. Weiland, “A discretization model for the solution of Maxwell's equations for six-component fields,” *Archiv Elektronik und Uebertragungstechnik*, vol. 31, no. 3, pp. 116–120, 1977.

[3] T. Weiland, “Lossy waveguides with arbitrary boundary contour and distribution of material,” *AEU Archiv füer Elektrotechnik und Ubertragungstechnik*, vol. 33, pp. 170–174, 1979.

[4] T. W. Dawson, K. Caputa, and M. A. Stuchly, “Numerical evaluation of 60 Hz magnetic induction in the human body in complex occupational environments,” *Physics in Medicine and Biology*, vol. 44, pp. 1025–1040, 1999.

[5] S. J. Allen, E. R. Adair, K. S. Mylacraine, W. Hurt, and J. Ziriax, “Empirical and theoretical dosimetry in support of whole body resonant RF exposure (100 MHz) in human volunteers,” *Bioelectromagnetics*, vol. 24, no. 7, pp. 502-509, 2003.

[6] S. J. Allen, E. R. Adair, K. S. Mylacraine, W. Hurt, and J. Ziriax, “Empirical and theoretical dosimetry in support of whole body radio frequency (RF) exposure in seated human volunteers at 220 MHz,” *Bioelectromagnetics*, vol. 26, no. 6, pp. 440-447, 2005.

[7] R. P. Findlay and P. J. Dimbylow, “Effects of posture on FDTD calculations of specific absorption rate in a voxel model of the human body,” *Physics in Medicine and Biology*, vol. 50, no. 16, pp. 3825-3835, 2005.

[8] R. P. Findlay and P. J. Dimbylow, “FDTD calculations of specific energy absorption rate in a seated voxel model of the human body from 10 MHz to 3 GHz,” *Physics in Medicine and Biology*, vol. 51, no. 9, pp. 2339-2352, 2006.

[9] T. W. Dawson, K. Caputa, and M. A. Stuchly, “Magnetic field exposures for UK live-line workers,” *Physics in medicine and biology*, vol. 47, pp. 995–1012, 2002.

[10] T. Nagaoka and S. Watanabe, “Postured voxel-based human models for electromagnetic dosimetry,” *Physics in Medicine and Biology*, vol. 53, no. 24, pp. 7047-7061, 2008.

[11] ICNIRP, “Guidelines for limiting exposure to time-varying electric, magnetic, and electromagnetic fields (up to 300 GHz),” *Health Phys*, vol. 74, no. 4, pp. 494–522, 1998.

[12] H. L. Fisher and W. S. Snyder, *Annual progress report for period ending*. Oak Ridge TN, USA: Health Physics Division, Oak Ridge National Laboratory, 1966.

[13] J. M. L. Hwang, R. L. Shoup, G. G. Warner, and J. W. Poston, *Mathematical descriptions of a one-and five-year old child for use in dosimetry calculations*. Tenn. USA: Oak Ridge National Laboratory, 1976.

[14] W. L. Chen, J. W. Poston, and G. G. Warner, *Evaluation of the distribution of absorbed dose in child phantoms exposed to diagnostic medical x rays*. Tenn. USA: Oak Ridge National Laboratory, 1978.

[15] M. Cristy, *Mathematical phantoms representing children of various ages for use in estimates of internal dose*. Tenn. USA: Oak Ridge National Laboratory, 1980.

[16] Valentin J, *Reference man: anatomical, physiological and metabolic characteristics*. Pergamon, Oxford, UK: ICRP Publication, 1975.

[17] N. I. Badler and S. W. Smoliar, "Digital representations of human movement," *ACM Computing Surveys (CSUR)*, vol. 11, no. 1, pp. 19 - 38, Mar. 1979.

[18] K. Komatsu, "Human skin model capable of natural shape variation," *The visual computer*, vol. 3, no. 5, pp. 265–271, 1988.

[19] L. P. Nedel and D. Thalmann, "Modeling and deformation of the human body using ananatomically-based approach," in *Computer Animation 98. Proceedings*, pp. 34–40, 1998.

[20] The National Library of Medicine, "Visible Human Project." [Online]. Available: http://www.nlm.nih.gov/research/visible/visible_human.html. [Accessed: 19-Aug-2010].

[21] S. J. Gibbs, A. Pujol, and others, "Patient risk from interproximal radiography," *Oral Surgery, Oral Medicine, Oral Pathology*, vol. 58, no. 3, pp. 347–354, 1984.

[22] T. Nagaoka et al., "Development of realistic high-resolution whole-body voxel models of Japanese adult males and females of average height and weight, and application of models to radio-frequency electromagnetic-field dosimetry," *Physics in Medicine and Biology*, vol. 49, no. 1, pp. 1-15, 2004.

[23] P. J. Dimbylow, "Fine resolution calculations of SAR in the human body for frequencies up to 3 GHz," *Physics in Medicine and Biology*, vol. 47, no. 16, pp. 2835-2846, 2002.

[24] P. Dimbylow, W. Bolch, and C. Lee, "SAR calculations from 20 MHz to 6 GHz in the University of Florida newborn voxel phantom and their implications for dosimetry," *Physics in Medicine and Biology*, vol. 55, no. 5, pp. 1519-1530, 2010.

[25] T. W. Dawson, K. Caputa, and M. A. Stuchly, "Influence of human model resolution on computed currents induced in organs by 60-Hz magnetic fields," *Bioelectromagnetics*, vol. 18, no. 7, pp. 478–490, 1998.

[26] T. W. Dawson, K. Caputa, and M. A. Stuchly, "Electric fields induced in humans and rodents by 60 Hz magnetic fields," *Physics in Medicine and Biology*, vol. 47, no. 14, pp. 2561-2568, 2002.

[27] A. J. Neal, G. Sivewright, and R. Bentley, "Evaluation of a region growing algorithm for segmenting pelvic computed tomography images during radiotherapy planning," *British Journal of Radiology*, vol. 67, no. 796, pp. 392 - 395, 1994.

[28] M. Zankl, R. Veit, G. Williams, K. Schneider, H. Fendel, and N. Petoussi, "The construction of computer tomographic phantoms and their application in radiology and radiation protection," *Radiation and Environmental Biophysics*, vol. 27, no. 2, pp. 153–164, 1988.

[29] M. Caon, G. Bibbo, and J. Pattison, "Monte Carlo calculated effective dose to teenage girls from computed tomography examinations," *Radiation Protection Dosimetry*, vol. 90, no. 4, pp. 445 - 448, 2000.

[30] R. Kramer, J. W. Vieira, H. J. Khoury, F. R. A. Lima, and D. Fuelle, "All about MAX: a male adult voxel phantom for Monte Carlo calculations in radiation protection dosimetry," *Physics in medicine and biology*, vol. 48, no. 10, pp. 1239 - 1262, 2003.

[31] P. J. Mountford and D. H. Temperton, "Recommendations of the International Commission on Radiological Protection (ICRP) 1990," *European Journal of Nuclear Medicine and Molecular Imaging*, vol. 19, no. 2, pp. 77–79, 1992.

[32] P. J. Dimbylow, "FDTD calculations of the whole-body averaged SAR in an anatomically realistic voxel model of the human body from 1 MHz to 1 GHz," *Physics*

in Medicine and Biology, vol. 42, no. 3, pp. 479 - 490, 1997.

[33] M. Zankl and A. Wittmann, “The adult male voxel model "Golem" segmented from whole-body CT patient data,” *Radiation and Environmental Biophysics*, vol. 40, no. 2, pp. 153–162, 2001.

[34] M. J. Ackerman, “The visible human project,” *Proceedings of the IEEE*, vol. 86, no. 3, pp. 504–511, 1998.

[35] R. H. T. Bates and L. GARDEN, “Overview of computerized tomography with emphasis on future developments,” *Proceedings of the IEEE*, vol. 71, no. 3, 1983.

[36] W. S. Hinshaw and A. H. Lent, “An introduction to NMR imaging: From the Bloch equation to the imaging equation,” *Proceedings of the IEEE*, vol. 71, no. 3, 1983.

[37] S. S. Trivedi, G. T. Herman, and J. K. Udupa, “Segmentation into three classes using gradients,” *IEEE Transactions on Medical Imaging*, vol. 5, no. 2, pp. 116–119, 1986.

[38] J. K. Udupa, “Interactive segmentation and boundary surface formation for 3-D digital images,” *Computer Graphics and Image Processing*, vol. 18, no. 3, pp. 213–235, 1982.

[39] S. W. Zucker and R. Hummel, “Three-Dimensional Edge Operator,” *IEEE Transactions on Pattern Analysis and Machine Intelligence*, vol. 3, no. 3, pp. 324–331, 1981.

[40] G. B. Aboutanos, J. Nikanne, N. Watkins, and B. M. Dawan, “Model creation and deformation for the automatic segmentation of the brain in MR images,” *IEEE Transactions on biomedical engineering*, vol. 46, no. 11, pp. 1346–1356, 1999.

[41] Dipp GmbH, “Anatomical volume data sets.” [Online]. Available: http://www.vr-laboratory.com/. [Accessed: 08-Nov-2010].

[42] E. Gjonaj, M. Bartsch, M. Clemens, S. Schupp, and T. Weiland, “High-resolution human anatomy models for advanced electromagnetic field computations,” *IEEE Transactions on Magnetics*, vol. 38, no. 2, pp. 357–360, 2002.

[43] A. Barchanski, H. D. Gersem, E. Gjonaj, and T. Weiland, “Impact of the displacement current on low-frequency electromagnetic fields computed using high-resolution anatomy models,” *Physics in Medicine and Biology*, vol. 50, no. 19, pp. 243-249, 2005.

[44] A. Barchanski, M. Clemens, E. Gjonaj, H. De Gersem, and T. Weiland, “Large-scale calculation of low-frequency-induced currents in high-resolution human body models,” *IEEE Transactions on Magnetics*, vol. 43, no. 4, pp. 1693–1696, 2007.

[45] A. Barchanski, T. Steiner, H. De Gersem, M. Clemens, and T. Weiland, “Local grid refinement for low-frequency current computations in 3-D human anatomy models,” *IEEE Transactions on Magnetics*, vol. 42, no. 4, pp. 1371–1374, 2006.

[46] A. Barchanski, M. Clemens, H. De Gersem, T. Steiner, and T. Weiland, “Using domain decomposition techniques for the calculation of low-frequency electric current densities in high-resolution 3D human anatomy models,” *COMPEL: The International Journal for Computation and Mathematics in Electrical and Electronic Engineering*, vol. 24, no. 2, pp. 458–467, 2005.

[47] C. Gabriel, S. Gabriel, and E. Corthout, “The dielectric properties of biological tissues: I. Literature survey,” *Physics in Medicine and Biology*, vol. 41, pp. 2231 - 2249, 1996.

[48] S. Gabriel, R. W. Lau, and C. Gabriel, “The dielectric properties of biological tissues: II. Measurements in the frequency range 10 Hz to 20 GHz,” *Physics in Medicine and Biology*, vol. 41, pp. 2251 - 2269, 1996.

[49] C. Gabriel, *Compilation of the Dielectric Properties of Body Tissues at RF and Microwave Frequencies.* London, UK: Physics Department King's College London,

1996.

[50] S. Gabriel, R. W. Lau, and C. Gabriel, "The dielectric properties of biological tissues: III. Parametric models for the dielectric spectrum of tissues," *Physics in Medicine and Biology*, vol. 41, pp. 2271 - 2293, 1996.

[51] CST AG, "CST - Computer Simulatin Technology." [Online]. Available: http://www.cst.com/. [Accessed: 20-Aug-2010].

[52] K. Yee, "Numerical solution of initial boundary value problems involving Maxwell's equations in isotropic media," *IEEE Transactions on antennas and propagation*, vol. 14, no. 3, pp. 302–307, 1966.

[53] R. Holland, "Finite-difference time-domain (FDTD) analysis of magnetic diffusion," *IEEE Transactions on Electromagnetic Compatibility*, vol. 36, no. 1, pp. 32–39, 1994.

[54] R. Holland, "FDTD analysis of nonlinear magnetic diffusion by reduced c," *IEEE Transactions on Antennas and Propagation*, vol. 43, no. 7, pp. 653–659, 1995.

[55] S. R. Parry, "Free-form deformations in a constructive solid geometry modeling system," Doctoral Dissertation, Brigham Young University, 1986.

[56] T. W. Sederberg and S. R. Parry, "Free-form deformation of solid geometric models," *Proceedings of the 13th annual conference on computer graphics and interactive techniques (ACM Siggraph 86)*, vol. 20, no. 4, pp. 151 - 160, 1986.

[57] J. E. Chadwick, D. R. Haumann, and R. E. Parent, "Layered construction for deformable animated characters," in *Proceedings of the 16th annual conference on computer graphics and interactive techniques (ACM Siggraph 89)*, vol. 23, pp. 243 - 252, 1989.

[58] S. Coquillart, "Extended free-form deformation: a sculpturing tool for 3 D geometric modeling," in *Proceedings of the 17th annual conference on computer graphics and interactive techniques (ACM Siggraph 90)*, vol. 24, pp. 187 - 196, 1990.

[59] J. Griessmair and W. Purgathofer, "Deformation of solids with trivariate B-splines," in *Proceedings of Eurographics*, vol. 89, pp. 137–148, 1989.

[60] P. Kalra, A. Mangili, N. M. Thalmann, and D. Thalmann, "Simulation of facial muscle actions based on rational free form deformations," in *Computer Graphics Forum*, vol. 11, pp. 59–69, 1992.

[61] H. J. Lamousin and N. N. Waggenspack Jr, "NURBS-based free-form deformations," *IEEE Computer Graphics and Applications*, vol. 14, no. 6, pp. 59–65, 1994.

[62] G. E. Farin, *Curves and Surfaces for Computer-Aided Geometric Design: A Practical Code*. Orlando, FL, USA: Academic Press, Inc., 1996.

[63] J. D. Foley, *Computer graphics: principles and practice*, 2nd ed. MA, USA: Addison-Wesley Publishing Company, Inc., 1995.

[64] J. D. Foley, A. Van Dam, S. K. Feiner, J. F. Hughes, and R. L. Phillips, *Introduction to computer graphics*. MA, USA: Addison-Wesley Publishing Company, Inc., 1994.

[65] P. V. Suhocki, "Say it with multimedia: new presentation tools for the radiologist," *American Journal of Roentgenology*, vol. 171, no. 2, pp. 313 - 319, 1998.

[66] W. E. Lorensen and H. E. Cline, "Marching cubes: A high resolution 3D surface construction algorithm," in *Proceedings of the 14th annual conference on Computer graphics and interactive techniques (ACM Siggraph 87)*, vol. 24, pp. 163-169, 1987.

[67] H. E. Cline, W. E. Lorensen, S. Ludke, C. R. Crawford, and B. C. Teeter, "Two algorithms for the three-dimensional reconstruction of tomograms.," *Medical physics*, vol. 15, no. 3, pp. 320–327, 1988.

[68] E. Keppel, "Approximating complex surfaces by triangulation of contour lines," *IBM Journal of Research and Development*, vol. 19, no. 1, pp. 2–11, 1975.

[69] H. Fuchs, Z. M. Kedem, and S. P. Uselton, “Optimal surface reconstruction from planar contours,” *Communications of the ACM*, vol. 20, no. 10, pp. 693–702, 1977.

[70] M. W. Jones and M. Chen, “A new approach to the construction of surfaces from contour data,” in *Computer Graphics Forum*, vol. 13, pp. 75–84, 1994.

[71] G. T. Herman and J. K. Udupa, “Display of 3-D digital images: Computational foundations and medical applications,” *IEEE Computer Graphics and Applications*, vol. 3, no. 5, pp. 39–46, 1983.

[72] L. S. Chen, G. T. Herman, and R. Reynolds, “Surface shading in the cuberille environment.,” *IEEE Computer Graphics and Applications*, vol. 5, no. 12, pp. 33–43, Dec. 1985.

[73] D. Meagher, “Geometric modeling using octree encoding,” *Computer Graphics and Image Processing*, vol. 19, no. 2, pp. 129–147, 1982.

[74] P. Bourke, “Polygonising a scalar field (Marching Cubes).” [Online]. Available: http://local.wasp.uwa.edu.au/~pbourke/geometry/polygonise/. [Accessed: 25-Aug-2010].

[75] U. Van Rienen and T. Weiland, “Triangular discretization method for the evaluation of RF-fields in waveguides and cylindrically symmetric cavities,” *Particle Accelerators*, vol. 20, no. 3, pp. 239–266, 1987.

[76] R. Schuhmann and T. Weiland, “A stable interpolation technique for FDTD on non-orthogonal grids,” *International Journal of Numerical Modelling: Electronic Networks, Devices and Fields*, vol. 11, no. 6, pp. 299–306, 1998.

[77] P. Thoma and T. Weiland, “A consistent subgridding scheme for the finite difference time domain method,” *International Journal of Numerical Modelling: Electronic Networks, Devices and Fields*, vol. 9, no. 5, pp. 359–374, 1996.

[78] M. Clemens and T. Weiland, “Discrete electromagnetism with the finite integration technique,” *Progress in Electromagnetic Research, PIER*, vol. 32, pp. 65–87, 2001.

[79] T. Weiland, “On the unique numerical solution of Maxwellian eigenvalue problems in three dimensions,” *Particle Accelerators*, vol. 17, pp. 227-242, 1985.

[80] T. Weiland, “Time domain electromagnetic field computation with finite difference methods,” *International Journal of Numerical Modelling: Electronic Networks, Devices and Fields*, vol. 9, no. 4, pp. 295–319, 1996.

[81] R. Schuhmann and T. Weiland, “Conservation of discrete energy and related laws in the finite integration technique,” *Progress in Electromagnetic Research, PIER*, vol. 32, pp. 301–316, 2001.

[82] A. Taflove and M. E. Brodwin, “Numerical solution of steady-state electromagnetic scattering problems using the time-dependent Maxwell's equations,” *IEEE transactions on Microwave Theory and Techniques*, vol. 23, no. 8, pp. 623–630, 1975.

[83] H. Gable, “Anatomical structure of the Knee.” [Online]. Available: http://www.imageinterpretation.co.uk/knee.html. [Accessed: 03-Jun-2010].

[84] Stuetzpunkt Feuerwehr Meilen, “Blitz und Gewitter.” [Online]. Available: http://www.feuerwehr-meilen.ch/default.asp?navig=558. [Accessed: 26-Feb-2011].

[85] T. R. Kuphaldt, *Lessons In Electric Circuits, Volume I–DC*. E-book, 2002.

[86] U. Sam, “Untersuchungen über die elektrische Gefährdung des Menschen bei Teildurchströmungen, insbesondere bei Arbeiten in Kesseln, Behältern und Rohrleitungen (2. Teil),” *Biomedizinische Technik / Biomedical Engineering*, vol. 12, no. 1, pp. 29–37, 1967.

[87] IEC, “IEC 60479-1: Effects of current on human beings and livestock - Part 1: General aspects,” International Electrotechnical Commission, 2005.

[88] IEC, “IEC 62305-1: Protection against lighting - Part 1: General principles,” Interna-

tional Electrotechnical Commission, 2003.

[89] IEC, “IEC 60479-2: Effects of current passing through the human body - Part 2: Special aspects,” International Electrotechnical Commission, 2006.

[90] I. Chatterjee, D. Wu, and O. P. Gandhi, “Human body impedance and threshold currents for perception and pain for contact hazard analysis in the VLF-MF band,” *IEEE transactions on Biomedical Engineering*, vol. 33, pp. 486–494, 1986.

[91] C. H. Durney, H. Massoudi, and M. F. Iskander, *Radiofrequency Radiation Dosimetry Handbook*. Salt Lake City, Utah, USA: Electrical Engineering Department, The University of Utah, 1986.

[92] S. M. Michaelson and E. C. Elson, “Modulated fields and "window" effects,” in *CRC Handbook of Biological Effects of Electromagnetic Fields*, Boca Raton, Fl: CRC Press, 1996.

[93] ACGIH, *Threshold limit values for chemical substances and physical agents and biological exposure indices*, 2nd ed. Cincinati, OH, USA: American Conference of Government Industrial Hygienists, 1996.

[94] F. G. Shellock and J. V. Crues, “Temperature, heart rate, and blood pressure changes associated with clinical MR imaging at 1.5 T,” *Radiology*, vol. 163, no. 1, pp. 259-262, 1987.

[95] S. Tofani, G. d'Amore, G. Fiandino, A. Benedetto, O. P. Gandhi, and J. Y. Chen, “Induced foot-currents in humans exposed to VHF radio-frequency EM fields,” *IEEE Transactions on Electromagnetic Compatibility*, vol. 37, no. 1, pp. 96–99, 1995.

[96] J. Valentin, “Basic anatomical and physiological data for use in radiological protection: reference values: ICRP Publication 89,” *Annals of the ICRP*, vol. 32, no. 3, pp. 1-277, 2002.

[97] W. M. Hsu, J. F. Hughes, and H. Kaufman, “Direct manipulation of free-form deformations,” in *Proceedings of the 19th annual conference on Computer graphics and interactive techniques (ACM Siggraph92)*, vol. 26, pp. 177-184, 1992.

[98] N. Cornea, D. Silver, and P. Min, “Curve-Skeleton Applications,” in *VIS 05. IEEE Visualization 2005*, pp. 95-102, 2005.

[99] N. D. Cornea, D. Silver, and P. Min, “Curve-Skeleton Properties, Applications, and Algorithms,” *IEEE Transactions on Visualization and Computer Graphics*, vol. 13, no. 3, pp. 530-548, 2007.

Acknowledgements

At this point of completing this dissertation, I would like to express my gratitude to all the people, who directly or indirectly helped me throughout the whole time of this Ph.D. work.

First of all, I want to thank Prof. Dr.-Ing. Thomas Weiland for giving me the excellent opportunity to work in his group TEMF and Graduate School of Computational Engineering, and his kind scientific supervision. Without his support in science and finance, it would have been impossible for me to complete this Ph.D. work in TU Darmstadt.

Then I would like to thank Prof. Dr.-Ing. Volker Hinrichsen for kindly providing me the step voltage project and cooperation opportunity with his group.

Special thanks to Prof. Dr.-Ing. Irina Munteanu for her scientific guidance and for her carefully reviewing and correcting this dissertation until the last version. I have learned a lot from her. Her diligent work spirit impressed me a lot and will guide me to the future career.

Other special thanks to Dr.phil.nat Wolfgang F.O. Müller and Dr.-Ing Alexander Prokop for helping me to initialize my poser preprogram project.

During the research activities at TEMF and Graduate School of Computational Engineering, my present and former colleagues provided the pleasant and friendly atmosphere. It is impossible to express my thanks in so few words.

At last I want to express my deep thanks to my parents for their supporting throughout all of my life. Especially thank my wife Mrs. Zhihua Dai, who gave me a lot of help in working and living, making me feel understood.

Thanks to all of you!

Curriculum Vitae

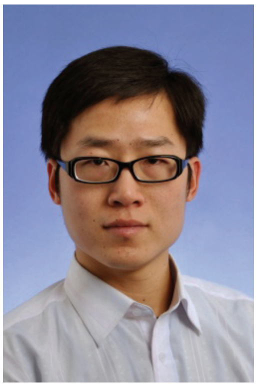

Jing Gao

born on 22nd December 1982 in Handan city, Hebei province, China

1989-1995 Beidashe primary school in Handan city, Hebei province

1995-1998 Shucun junior middle school in Handan city, Hebei province

1998-2001 Wuan no.3 senior middle school in Handan city, Hebei province

2001-2005 Bachelor degree study at Department of Mechanical Engineering of University of Science and Technology Beijing in Beijing city

2005-2008 Master degree study at Department of Automotive Engineering of Tsinghua University in Beijing city

2008-2011 PhD student at Department of Electrical Engineering and Information Technology of Darmstadt University of Technology in Darmstadt